Physical characterization of engineered aerosol particles

Ludvigsson, Linus

2017

[Link to publication](#)

Citation for published version (APA):
Ludvigsson, L. (2017). *Physical characterization of engineered aerosol particles* (1:a uppl.). [Doktorsavhandling (sammanläggning), Fasta tillståndets fysik]. Solid State Physics.

Total number of authors:
1

Physical characterization of engineered aerosol particles

Linus Ludvigsson

LUND
UNIVERSITY

DOCTORAL DISSERTATION
by due permission of the Faculty of Engineering, Lund University, Sweden.
To be defended on Friday, September 22 at 09.15 in Rydbergssalen Sölvegatan 14, Lund

Faculty opponent
Lutz Mädler

Evaluation Committee
Oliver F Bischof, Ulla Vogel, Thomas Willum Hansen

Organization LUND UNIVERSITY	Document name DOCTORAL DISSERTATION	
	Date of issue	
Author(s) LINUS LUDVIGSSON	Sponsoring organization	

Title and subtitle Physical Characterization of Engineered Nanoparticles

Abstract

This thesis will explore parts of the life of engineered nanoparticles, from generation in research environments and process monitoring, to emissions in an industrial setting. The aim is to give insights into how the particles can be characterized in different settings and how different characterization methods can be applied depending on need or demand.

Airborne nanoparticles have been around forever but the use of them in specialized materials has increased dramatically during the past decades. The new materials bring improvements to old applications, and brand new uses as the world of nanotechnology expands. It is, however, not only one-sided positive effects from this increase in use; some of these materials have properties previously experienced as health hazards. The physical size and amounts of material handled during the production can be different from what has been experienced before and with that, new hazards might arise. In order to assess these hazards, careful characterization of the particle behavior can be utilized in controlled environments to further the knowledge on how the particles might behave out in the real world during use and application. Particles can be characterized in many different ways and aspects. Finding out which path that suits a certain situation is a key to make a successful measurement campaign or experiment. The systems used to produce these particles also need to be well characterized. In addition to safe handling, well characterized generation systems will also allow for new uses and exploration of materials previously not investigated.

In this thesis, I have characterized the initial stages of particles generated with spark discharge discovering how the particles evolve depending on process parameters milliseconds after generation. I further dive deeper into the spark discharge characterization and show how the emitted light from the discharge can be correlated with the particles being produced and show how the input power doesn't linearly correlate with particles produced in this process. In the same system, I successfully generate particles of InSb. It is demonstrated how a reducing atmosphere during generation is critical for the formation of pure particles of this material. Several different characterization techniques to determine the properties of the generated particles are described.

One of the most interesting properties of nanoparticles from a toxicological view point is surface area. Knowing the surface area of complex particles is, however, not always straightforward and is often difficult to measure directly. I present an overview of a set of models that can be used to estimate the surface area of agglomerated particles generated from different particle sources. The input to the methods relies on online measurements of mobility diameter, mass, and offline characterization of morphology via microscopy samples.

No matter how harmful particles with specific properties are to humans, there is no harm unless people get exposed to the particles. I present results from an extensive workplace campaign in which we utilized online aerosol instruments to characterize the emissions. A new method for classifying carbon nanotube materials via electron microscopy from filter samples, as well as from surface sampling with adhesive tape, is further introduced.

From this campaign release of engineered nanoparticles at several occasions during the work day was found. It was evident that online methods alone would not enable us to discern carbon nanotubes from other particles but with the combination of online time resolved characterization of emissions and extensive microscopy analysis emission events were identified. It was also revealed that the surface contamination of engineered particles were extensive. Several sampled surfaces showed contamination by not only carbon nanotubes but also of nanomaterial which were not handled during the time of the measurements.

From this thesis it is clear that measuring nanoparticles is as difficult as you make it. It is possible to measure with simple means to yield results that are sufficient to give an indication that some things needs to improve. In this thesis I will also show that an extensive arsenal of equipment can yield results which complement and build upon each other. While it is possible to measure all kinds of data on the same aerosol given enough time and resources, it is clear that the optimization and tailoring of a study might be the real challenge.

Key words

Classification system and/or index terms (if any)

Supplementary bibliographical information	Language English
ISSN and key title	ISBN 978-91-7753-407-5 (print) 978-91-7753-408-2 (pdf)

Recipient's notes	Number of pages 189	Price
	Security classification	

Signature _____ Date 21/8 2017

Physical characterization of engineered aerosol particles

Linus Ludvigsson

LUND UNIVERSITY

Till A.

Content

Abstract

This thesis will explore parts of the life of engineered nanoparticles, from generation in research environments and process monitoring, to emissions in an industrial setting. The aim is to give insights into how the particles can be characterized in different settings and how different characterization methods can be applied depending on need or demand.

Airborne nanoparticles have been around forever but the use of them in specialized materials has increased dramatically during the past decades. The new materials bring improvements to old applications, and brand new uses as the world of nanotechnology expands. It is, however, not only one-sided positive effects from this increase in use; some of these materials have properties previously experienced as health hazards. The physical size and amounts of material handled during the production can be different from what has been experienced before and with that, new hazards might arise. In order to assess these hazards, careful characterization of the particle behavior can be utilized in controlled environments to further the knowledge on how the particles might behave out in the real world during use and application. Particles can be characterized in many different ways and aspects. Finding out which path that suits a certain situation is a key to make a successful measurement campaign or experiment. The systems used to produce these particles also need to be well characterized. In addition to safe handling, well characterized generation systems will also allow for new uses and exploration of materials previously not investigated.

In this thesis, I have characterized the initial stages of particles generated with spark discharge discovering how the particles evolve depending on process parameters milliseconds after generation. I further dive deeper into the spark discharge characterization and show how the emitted light from the discharge can be correlated with the particles being produced and show how the input power doesn't linearly correlate with particles produced in this process. In the same system, I successfully generate particles of InSb. It is demonstrated how a reducing atmosphere during generation is critical for the formation of pure particles of this material. Several different characterization techniques to determine the properties of the generated particles are described.

One of the most interesting properties of nanoparticles from a toxicological view point is surface area. Knowing the surface area of complex particles is, however, not always straightforward and is often difficult to measure directly. I present an overview

of a set of models that can be used to estimate the surface area of agglomerated particles generated from different particle sources. The input to the methods relies on online measurements of mobility diameter, mass, and offline characterization of morphology via microscopy samples.

No matter how harmful particles with specific properties are to humans, there is no harm unless people get exposed to the particles. I present results from an extensive workplace campaign in which we utilized online aerosol instruments to characterize the emissions. A new method for classifying carbon nanotube materials via electron microscopy from filter samples, as well as from surface sampling with adhesive tape, is further introduced.

From this campaign release of engineered nanoparticles at several occasions during the work day was found. It was evident that online methods alone would not enable us to discern carbon nanotubes from other particles but with the combination of online time resolved characterization of emissions and extensive microscopy analysis emission events were identified. It was also revealed that the surface contamination of engineered particles were extensive. Several sampled surfaces showed contamination by not only carbon nanotubes but also of nanomaterial which were not handled during the time of the measurements.

From this thesis it is clear that measuring nanoparticles is as difficult as you make it. It is possible to measure with simple means to yield results that are sufficient to give an indication that some things needs to improve. In this thesis I will also show that an extensive arsenal of equipment can yield results which complement and build upon each other. While it is possible to measure all kinds of data on the same aerosol given enough time and resources, it is clear that the optimization and tailoring of a study might be the real challenge.

Acknowledgements

I have been fortunate to get to work with a crowd of talented persons during my years in research. I would like to thank my main supervisors Knut Deppert and Maria Messing. You two are some of the kindest and hardest working persons I have had the fortune to meet and work with.

I would also like to thank my co-supervisors at the division of Aerosol Technology, Joakim Pagels and Jenny Rissler, for great discussions and for making my introduction to aerosol science a quite pleasant experience.
Bengt Meuller both for building an awesome particle generator, for helping to fix it on the rare occasions that it's not doing what it should. For all the discussion within the growing aerosol group at FTF with Robert, Calle and Sara. Christina Isaxon, Christian Svensson, and Patrik Nilsson at EAT for diligent work during our measurement campaigns, both in Norway and in the aerosol lab, and for being great role models for how a PhD students and researchers should be.

Big thanks should also be given to the people at Arbets- och Miljömedicin, in particular Maria Hedmer and Håkan Tinnerberg for valuable input in the field of occupational health, and for showing that science can be done with common office supplies. To the technical staff both at Lund Nanolab and at nCHREM, for keeping both lab and microscopes in great condition, in particular Gunnel Karlsson and Crispin Hetherington at Centre for Analysis and Synthesis, and Håkan Lapovski, George Rydnemalm, Anders Kvennefors and Ivan Maximov at Lund Nanolab. My colleagues, the management and administration and the rest of the ever growing number of Solid State Physics employees, thank you for all practical and technical assistance and for making this division a such a great place to work in.

Last but not least I would like thank my family; Per, Jeanette, Simon, and my friends back in Trelleborg.

Linus Ludvigsson August 2017

Populärvetenskaplig sammanfattning

Den här avhandlingen handlar om luftburna designade nanopartiklar och hur man tar reda på vilka egenskaper de har. Luftburna partiklar eller aerosoler är något som människan alltid har haft omkring sig. Oavsett om det varit i form av pollen, rök från eldstaden, eller från astmainhalatorn så har de alltid varit där och påverkat oss. I varje andetag drar vi in flera tusen partiklar, men vilken typ de är beror på var någonstans man är. I många fall är partiklarna inte något som gynnar kroppen men just eftersom inandning av partiklar inte är något nytt har flera olika system i kroppen utvecklats för att ta hand om de partiklar som fastnar i lungorna, andra partikeltyper är svårare för kroppen att hantera. Ett historiskt exempel är asbestfibrer som när de används till isolering har många goda egenskaper, men som när de blir luftburna och andas in orsakar cancer. Genom att studera hur asbestfibrer påverkar kroppen och varför de är farliga kom man fram till att det till stor del berodde på att de var olösliga i lungorna. Med den vetskapen designade man nya material som inte hade de oönskade effekterna som asbestfibrer. Kolnanorör är en ny typ av material som nu börjat användas med till synes liknande egenskaper som asbestfibrer men där användningsområdena skiljer sig. För att undvika liknande problem som uppstod för asbest vidtar man idag betydligt grundligare undersökningar, speciellt vid tillverkningen för att minimera riskerna att någon kommer till skada.

För att kunna avgöra vilka som är skadliga och vilka som vi kan dra nytta av behöver vi veta vad som gör en partikel god eller ond. Till detta behövs tekniker från många olika fält som inte naturligt varit en del av samma område inom naturvetenskapen eller tekniken. När det dessutom handlar om nya material som används inom nya områden är behovet av nya grepp för att förstå dessa partiklar uppenbart.

I detta arbete visar jag på flera olika angreppsvinklar som kan användas för att få en helhetsbild av luftburna nanopartiklar. Partiklarna som studerats har haft sitt ursprung både i faktiska tillämpningar ute på arbetsplatser och medvetet genererade i labbet. Jag har undersökt vad som sker från själva tillblivelsen av partiklar i gnisturladdningar, till fundamentala egenskaper som hur de växer till under de första ögonblicken efter sitt skapande, samt när och var partiklar släpps ut under industriell produktion. Genom att förstå hela processen kan man enklare designa partiklar med de egenskaper man vill ha, och undvika de man inte vill ha. En god kontroll över vad man producerar hjälper

också till när man ska ta reda på vad som faktiskt spelar roll när man studerar vilka effekter partiklarna har på, till exempel, levande celler.

Beroende på i vilket sammanhang partiklarna förekommer och anledningen till att man vill undersöka dem måste man göra en avvägning i hur pass noggrann man kan vara. Det hade varit bäst om man kunde undersöka allt men oftast är det inte fallet. Omfattande undersökningar kräver resurser både i form av tid och pengar, och dessa är ofta begränsade. I fallet med arbetsmiljö är det oftare av intresse att, i alla fall till en början, kunna peka på om det finns en uppenbar fara för de som vistas i miljön än att ge detaljerad information som skulle ta längre tid att få fram. Ibland kan förvånansvärt enkla metoder ge goda och relevanta resultat. För grundforskning i en kontrollerad miljö ges möjligheten att kunna studera betydligt mindre delar av en process så som partikelbildning. De upptäckter man gör i det steget kan senare användas för till exempel diagnostik av processen under produktion eller för optimering av egenskaper hos partiklarna.

Jag har i mina studier tagit fram metoder för att identifiera och klassificera nanomaterial som släpps ut under produktion genom att använda analysmetoder som tidigare inte använts i fältet. Jag har genom mina studier kunnat kartlägga partikelbildning från de allra första ögonblicken till processade nanopartiklar under partikelbildning och genom detta möjliggjort optimering av gnisturladdnings-generering av nanopartiklar. Jag har också lyckats producera nanopartiklar av material som tidigare aldrig gjorts.

Publication List

This thesis is based on the following papers listed and referred to paper I-VII

    I.   **Linus Ludvigsson**, Bengt O. Meuller, Maria E. Messing **Investigations of initial particle stages during spark discharge** J. Phys. D: Appl. Phys. 48 (2015) 314012 (9pp) doi:10.1088/0022-3727/48/31/314012 (2015)

I had a major part in planning the study, I carried out the experiments and analysis, I wrote major parts of the paper

    II.   Christian R. Svensson, **Linus Ludvigsson**, Bengt O. Meuller, Maximillian L. Eggersdorfer, Knut Deppert, Mats Bohgard, Joakim H. Pagels, Maria E. Messing, Jenny Rissler **Characteristics of airborne gold aggregates generated by spark discharge and high temperature evaporation furnace: mass-mobility relationship and surface area** Journal of Aerosol Science Volume 87, September 2015, Pages 38–52 doi:10.1016/j.jaerosci.2015.05.004

I generated the particles, performed the TEM analysis, and took part in writing the paper

    III.   **Linus Ludvigsson**, Knut Deppert, Maria E. Messing. **Spark discharge generation of InSb nanoparticles** (2017) *Manuscript*

I initiated the study, I had a major part in planning the study, I carried out the experiments and analysis, I wrote the paper

    IV.   Attila Kohut**, Linus Ludvigsson**, Gábor Galbács, Maria E. Messing, Bengt O. Meuller, Knut Deppert and Zsolt Geretovszky. **Optical- and particle emission of a spark discharge nanoparticle generator** (2017) *Submitted*

I had a major part in the initial design of the study; I generated the particles, performed the TEM analysis, and took part in writing the paper

V. **Linus Ludvigsson**, Christina Isaxon, Patrik T. Nilsson, Håkan Tinnerberg, Maria E. Messing, Jenny Rissler, Vidar Skaug, Anders Gudmundsson, Mats Bohgard, Maria Hedmer, Joakim H. Pagels **Carbon nanotube emissions from arc discharge production: Classification of particle types with electron microscopy and comparison with direct reading techniques** Ann Occup Hyg (2016) 60 (4): 493-512. doi: 10.1093/annhyg/mev094 First published online: January 8, 2016 (2016)

I participated during the sample collection, I performed the SEM preparation and developed the analysis method, I wrote major parts of the paper

VI. Maria Hedmer, Christina Isaxon, Patrik T. Nilsson, **Linus Ludvigsson**, Maria E. Messing, Johan Genberg, Vidar Skaug, Mats Bohgard, Håkan Tinnerberg, Joakim H. Pagels **Exposure and emission measurements during production, purification, and functionalization of arc discharge-produced multi-walled carbon nanotubes**. Annals of Occupational Hygiene 58 (3): 355-379 first published online January 3, 2014 doi:10.1093/annhyg/met072 (2015)

I participated during the sample collection, I performed the SEM preparation and analysis, I wrote parts of the paper

VII. Maria Hedmer, **Linus Ludvigsson**, Christina Isaxon, Patrik Nilsson P, Vidar Skaug, Mats Bohgard, Maria E. Messing, Joakim H. Pagels, Håkan Tinnerberg **Detection of carbon nanotubes and carbon nanodiscs on workplace surfaces in a small-scale producer** Ann Occup Hyg (2015) 59 (7): 836-852. doi: 10.1093/annhyg/mev036 First published online: June 29, 2015 (2015)

I participated during the sample collection, I performed the SEM preparation and analysis, I wrote parts of the paper

Papers not included in this thesis

i. Christian R. Svensson, Shegufta S. Ameer, **Linus Ludvigsson**, Neserin Ali, Ayman Alhamdow, Maria E. Messing, Joakim H. Pagels, Anders Gudmundsson, Mats Bohgard, Elodie Sanfins, Monica Kåredal, Karin Broberg, Jenny Rissler **Validation of an air–liquid interface toxicological set-up using Cu, Pd, and Ag well-characterized nanostructured aggregates and spheres** J Nanopart Res (2016) 18:86 DOI 10.1007/s11051-016-3389-y

ii. Jicheng Feng, Luyi Huang, **Linus Ludvigsson**, Maria E. Messing, Anne Maisser, George Biskos, and Andreas Schmidt-Ott **General approach to the evolution of singlet nanoparticles from a rapidly quenched point source** J. Phys. Chem. C, 2016, 120 (1), pp 621–630 DOI: 10.1021/acs.jpcc.5b06503

iii. Patrik T. Nilsson, Axel C. Eriksson, **Linus Ludvigsson**, Maria E. Messing, Erik Z. Nordin, Anders Gudmundsson, Bengt O. Meuller, Knut Deppert, Edward C. Fortner, Timothy B. Onasch, Joakim H. Pagels **In-situ characterization of metal nanoparticles and their organic coatings using laser-vaporization aerosol mass spectrometry** Nano Res. (2015) 8: 3780. doi:10.1007/s12274-015-0877-9

iv. Patrik T. Nilsson, Christina Isaxon, Axel C. Eriksson, Maria E. Messing, **Linus Ludvigsson**, Jenny Rissler, Maria Hedmer, Håkan Tinnerberg, Anders Gudmundsson, Knut Deppert, Mats Bohgard, Joakim H. Pagels **Nano-objects emitted during maintenance of common particle generators: direct chemical characterization with aerosol mass spectrometry and implications for risk assessments** J Nanopart Res (2013) 15: 2052. doi:10.1007/s11051-013-2052-0

1. Introduction

In the world of aerosol research the main focus for a long time has been on what's going on above our heads, in the atmosphere. Sophisticated techniques have been developed to determine the finest properties of matter in size ranges far below what our eyes can see, or even what our minds can grasp. Once the potential of the properties of aerosols began to unravel a new line of research in the field of aerosol science sparked. Several applications were improved by what was learned from the fundamental investigations of airborne particles. This thesis will deal with the effort to further the knowledge of engineered particles, by different physical characterization techniques.

The applications of engineered particles vary and so does the techniques needed to understand the processes that govern the final properties of the particles. As in the atmosphere the particles floating around are seldom static in nature and changes over time, both in size and composition. Characterization of the particles must be relevant to the application in mind. Certain conventional ways are not applicable to the new materials that are used and because of that, new characterization techniques must be developed or transferred from other fields of research to be applied to the new and fascinating materials emerging form research on engineered particles. In some cases what is conventional in one field is next to groundbreaking in another.

Characterization of airborne particles began with the discovery that the air around us is not empty, there is actually something that floats around us. Some of these particles have always been around and therefore it might not be a simple task to actually evaluate their effects on our daily lives. However, particles in the air do have an impact on us, now more than ever in some areas. The health effects that airborne particles cause are indeed something that needs to be dealt with. One of the first major events that caused a public interest and put air pollution onto the map of the public was the London smog of 1910. During a few days the concentration of particles skyrocketed and the populous city had to breathe what their plentiful coal furnaces spewed out. The event lead to an elevated prevalence of asthma, lung effects and the long term effects could be seen as the number of deaths spiked some weeks after as a direct cause of the exposure to the particles[1]. Even earlier than that, in ancient Greece miners working with extraction of asbestos or stone masons were known to have a shorter lifespan and a much higher rate of lung disease compared to the general public[2]. One would think that these historic examples would give insights in how to avoid these events of exposure. However, as history has taught us that is not the case.

The epidemic of cancer caused by asbestos exposure during the 1900s[3] and the present pollution in major cities around the world, especially in East Asia, shows that we have not learned enough from history. One path to a better approach to deal with these issues is to learn more about the particles themselves. What causes the health issues related to the exposure? Is it possible to design particles in a fashion that makes them less harmful if there is an exposure? Even more so, can the exposure be prevented completely? The answer to all of these questions can be found in the characterization of the properties and how the particles behave.

As stated before, in this thesis I will describe different aspects of physical characterization of aerosol particles and the outline will be the following. In Chapter 2, I will give a brief overview of the main topics important for the papers included in this thesis. In Chapter 3, I will introduce different characterization methods, and how they can be used. In Chapter 4, I will describe the main findings of my work and give a short summary of each paper. Finally, in Chapter 5, I will give a conclusion to summarize this thesis as well as give an outlook into what I think are some challenges and opportunities that arise from the findings of my work.

2. Background

This chapter will describe some general concepts of the themes important to all of the included articles. It is intended to give a short overview of each important topic.

2.1 Aerosols

A mixture of particles suspended in a gas is considered as an aerosol. The system needs to be stable for a prolonged period of time, i.e. the particles must stay airborne for a longer period and they must not evaporate. This is of course a bit ambiguous, the composition of the particles will change over time and new particles can be formed from precursors in the gas phase[4]. Likewise, particles can agglomerate and accumulate mass to the point that they settle on a surface. The size range that is generally considered when dealing with aerosols ranges from about 1 nm to 10000 nm. Matter smaller can still be airborne and stable but at that point the term atomic clusters are more often used[5]. Particles larger than 10 µm are often too heavy to be able to stay airborne for an extended period of time.

Particles can become airborne following two different routes. Either they start from something big and, by some process, lose matter which in turn can make them light enough, or particles are formed from gaseous species that form larger entities to the point that they are considered particles. In both these cases the particles can either be liquid or solid. One way of classifying airborne particles are by their size. In the order from small to large, common classes are ultrafine (1-100 nm), fine (1-2500 nm), and coarse (2500-10000 nm)[6]. Ultrafine particles can also be called nanoparticles (NPs). However, nanoparticles can also be defined as particles with features or at least one dimension smaller than 100 nm[7].

2.2 Generation of nanoparticles

The methods of generating airborne particles are diverse. A broad division can be made as top down or bottom up, i.e. generation based on dividing material into smaller and smaller entities or growing them from some gaseous or liquid precursor. Nanoparticles are generally produced in a bottom up process.

Methods using electrical discharges are a group of nanoparticle generation techniques which has gained attraction the past few years[8]. These methods can be made efficient in terms of both energy and material consumption compared to thermal evaporation-condensation processes. The scalability of these methods have in the past been limited but in recent years efforts have made it possible to achieve mass production of particles generated by electrical discharges[9,10].

One type of method using electrical discharges are spark discharge generators (SDG). The method have proven to be both energy efficient and material efficient as they often can be run without any external cooling and with simple electrical setups[8]. This method utilizes an electric discharge between two solid electrodes. One setup that can be used is a simple circuit consisting of a capacitance bank charged with a high voltage (HV) power source, and a chamber with one electrode connected to the high voltage of the capacitance bank and one electrode being grounded. As long as the distance between the electrodes is smallest between the electrode tips the discharge will occur there. A schematic of this setup including aerosol processing stages can be seen in figure 2.1.

The discharge is initiated via a Townsend avalanche once the voltage between the electrodes reaches a breakdown voltage[11]. This voltage depends on the pressure of the gas between the electrodes, the ion concentration in the gas, and the gas mixture. The avalanche is a process where ambient ions get accelerated by the increasing voltage. As they collide with molecules they will in turn create more ions. More and more ions are created until a conducting channel is formed and the current dramatically increase. This causes the temperature to locally rise to several thousand degree C. As these processes happen during a few µs there will be an offset in charge distribution between the electrodes as charge is transported from the HV electrode to the ground electrode. This will reverse the polarity and charge will start to travel back and strike the previous HV electrode. Depending on capacitance, electrode gap distance, and impedance of the circuit this oscillation will continue until the charge has dissipated. The discharge ablates and evaporates material at each strike on the electrodes. This material condenses into nanoparticles as the vapor is quenched by the carrier gas which flows through the generation chamber.

4
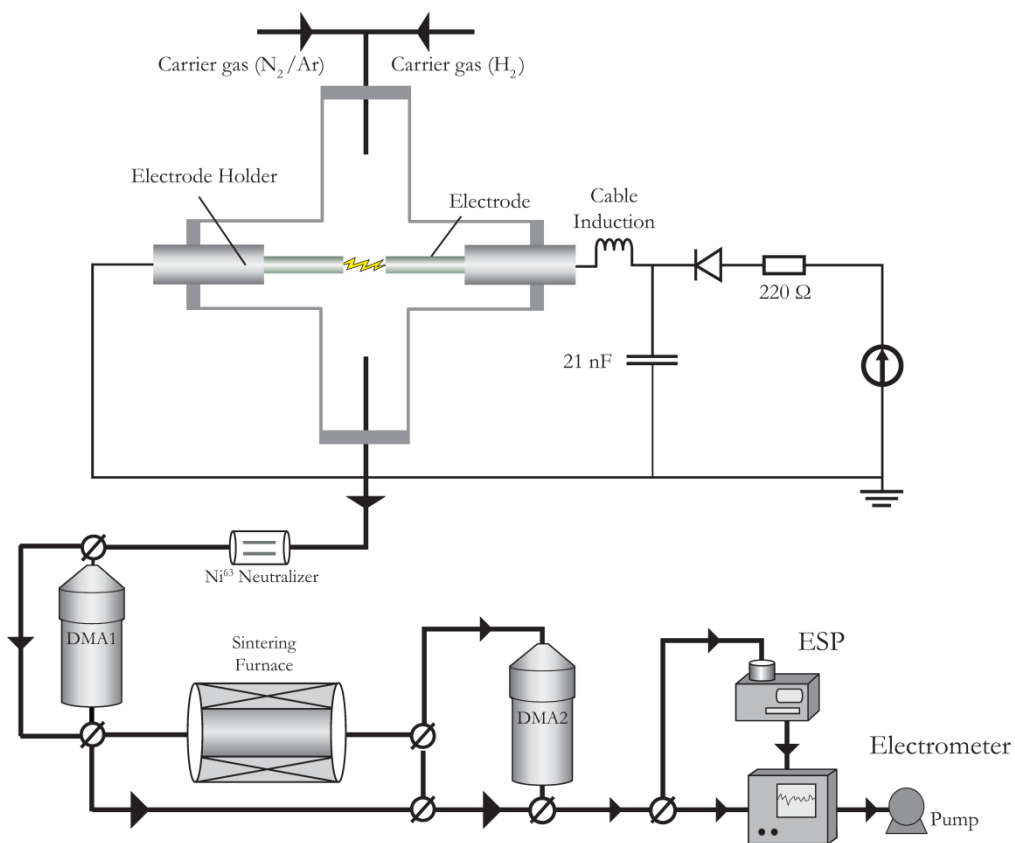
Figure 2. 1 A schematic of the SDG system used in Papers I, II, III, and IV. Particles are generated via discharges between the electrodes and transported by a carrier gas. The aerosol is given a charge distribution in the neutralizer. Size selection of the particles based on electrical mobility can be performed in the differential mobility analyzers (DMA), and att agglomerated particles can be reshaped in the sintering furnace. The particles can then either be measured in the electrometer, or be deposited on substrates in the electrostatic precipitator (ESP)

2.3 Adverse effects of (nano)particle exposure

There is a darker side to nanoparticles, namely exposure effects, that needs to be addressed in order to reach a general trust for the technology. Adverse health effects are nothing desirable but something that can occur if new materials are used without any deeper consideration. There are many examples in history where occupational exposure and the following health effects affected a majority of the workers. The main route of exposure is in most cases inhalation. The most significant example in history that shares some characteristics with modern materials is the case of pneumoconiosis. This family of disease affects the lung function of the patients and is almost always related to occupational exposure. The family contains subtypes related to the different materials that the patients were exposed to and they have slightly different onset and progress.

Silicosis and chalicosis are two types of pneumoconiosis that have a long history, the latter one has been known at least since ancient Greece, since they appear in workers exposed to mineral dust mainly from cutting and processing stone and ceramics[2,3]. There are different routes depending on the level of exposure, with acute silicosis being a result of extreme exposure during, for example, sandblasting. In this case huge amounts of material are deposited in the lung and trigger an acute response from the body. This is perhaps more related to accidents or bad safety routines at the workplace and the more worrying type is the chronic silicosis. This type appears after several years (~20) of exposure to crystalline silica (SiO_2) dust leading to severely reduced lung capacity and a progressive buildup of scar tissue in the lung due to a chronic inflammation state caused by the silica particles. The toxicity of silica particles is believed to arise from a chemical reaction on the surface of the deposited material. The size of the particles in this case is of less importance to the actual effects but rather the total deposited surface area is of importance.

Another disease in this family is asbestosis. Asbestosis occurs only in persons that have been exposed to asbestos fibers during an extended period of time. However the onset can be several decades after the actual exposure occurred. It is a more severe condition compared to silicosis. The shape of the asbestos fibers makes it difficult to remove them effectively if they are deposited in the alveolar region of the lung[12]. Their presence will in a similar fashion as for silica and other minerals cause a chronic inflammation but in the case of asbestos there is a severely elevated risk for cancer to develop.

The above mentioned occupational lung diseases are a result of inhaled particles being deposited in the lung. It is in that sense a small task to reduce the diseases by removing the particles or hindering the particles from entering the lung. In the actual situation, completely eliminating the risk of exposure has been shown to be a much greater challenge.

3. Characterization

Nanoparticles can have plenty of different properties that can be investigated to increase the knowledge about different types of particles. In this chapter, I will describe the main characterization techniques that were used in our studies.

A common concept in aerosol science is equivalent diameters[4,6]. As particles can have many sources, shapes, consist of different materials etc. there is a need to have some common ways to describe them. The particles can be described in terms of how they behave and then be compared to a common standard. Such standards could be a spherical particle with unit density. Particles that behave in a similar fashion to that of a standard particle with a certain diameter would be denoted as having the same equivalent diameter.

The properties of the particles can also be used as a base for determine an equivalent diameter such as the Sauter mean diameter, described in the next section.

3.1 Size distributions

Particle size is not a trivial metric to determine. There are many definitions used in different settings such as different mobility diameters (which will be discussed in more depth later), equivalent diameters based on circularity, projected area, Feret's diameter, or Martin diameter. No matter which diameter is used looking at one particle is often not enough. The different distributions used to describe a certain particle property is built up by a large amount of particles often to the point where the ensemble of particles, for all practical reasons, turns into a continuous distribution on which probability distributions can be fitted.

Number

Number size distributions without any discrimination or weights on the data could be considered the baseline distribution, as simple as it gets. There are however still caveats about this as the diameter is still needed to be defined by the method and sample loss during the measurement could still skew the data if that is not considered. Sampling a static aerosol a distribution of diameters will eventually occur. The shape of the distribution is dependent on the source but some general traits of this distribution could still be stated even without knowing too much about the source. By

definition the diameter of particles cannot be negative and the distribution of aerosol particles is often skewed towards smaller diameters. A good candidate model to describe the distribution is the log-normal distribution. When plotted on a logarithmic x-scale the distribution will appear as a standard Gaussian distribution with the same characteristics.

Mass

Particle mass was one of the first metrics to be used as a standard metric for pollution and still is an important guidance for policy making when it comes to health related issues. Generally the total mass or mass of fraction based on particle diameter is used. The very nature of mass will skew the distribution towards larger particle sizes making mass weighted size distributions less interesting in the case of nanoparticles.

However, to measure the mass of nanoparticles can still be of interest. Gravimetric analysis is not an option for single particles but there are instruments such as Aerosol Particle Mass analyzers (APM) which can achieve data on the mass of particles[13,14] in similar fashion as electrical mobility.

Surface area

Surface area has been linked to toxicity of particles in a number of cases[15-17]. One way to measure the surface area is by analysis of the total charge that can be put onto the particles. The total possible surface charge is proportional to the surface area as equation 3.1[4] with n_L as the number of negative charges, d as diameter, e as the elemental charge, and E_L as the surface field strength for spontaneous electron emission.

$$n_L = \frac{d^2 E_L}{4e} \quad (3.1)$$

This is valid for solid spherical particles which would give yet another equivalent metric, surface area equivalent diameter. As surface area is argued to be important for toxicology and even more so in the case of nanoparticles this metric has been utilized in instruments such as the nanoparticle surface area monitor[18]. The surface area can also be used to describe the Sauter diameter which is defined as the fraction of volume and surface. It is more often used as mean Sauter diameter, d_{va}, defined as equation 3.2[4].

$$d_{va} = \frac{\sum n_i d^3}{\sum n_i d^2} \quad (3.2)$$

3.2 Particle morphology

Morphology is in a sense an easy aspect in terms of characterization. It is usually simple to describe a particle based on an image and in some cases that is good enough. However, when statistics are needed there needs to be better defined metrics. Metrics like projected surface area or aspect ratio can be used. A straight forward method for morphology analysis of deposited particles is electron microscopy[19]. Generally two types of electron microscopy are utilized for nanoparticles, scanning electron microscopy (SEM) and transmission electron microscopy (TEM). Both methods are true workhorses in material science but they differ in some key aspects; generally SEM will use the secondary and/or backscattered electrons emitted from the surface of the material, while TEM will use electrons transmitted through the sample to create the respective image. In both methods electrons are accelerated and focused onto the sample. The electrons interact with the sample which will send out, apart from electrons of different origins, characteristic X-rays from which chemical composition of the analyzed area can be analyzed with energy dispersive X-ray spectroscopy (XEDS).

Scanning electron microscopy

SEM is often suited for overview imaging as the physical sample size can be relatively large making it an ideal method for analysis of filter samples or bulk analysis of particle sizes. A SEM works on the principle of a focused electron beam that raster scan an area of the sample and dwell for a certain time on each point. Secondary electron emission will occur at the surface of the sample and these electrons are collected. This signal can be converted to an image of the area. Resolution of this image is determined by the size of the electron beam and by how small steps are taken at each point of the scan. Some sample preparation is needed for SEM analysis if the sample is insulating or has poor conductivity. A common preparation method is coating the whole sample with a thin layer of conductive material. While this allows for easier imaging it also reduces the possibility to get relevant chemical information with XEDS. High detail images can still be achieved as the resolution can be down to a few nm. In Figure 3.1 a structure sampled during the cleaning of a reactor used for material synthesis can be seen. The smooth filter surface makes identification of deposited particles easy. It is, however, still a manual task as reliable image analysis of this type of random structures is difficult to implement.
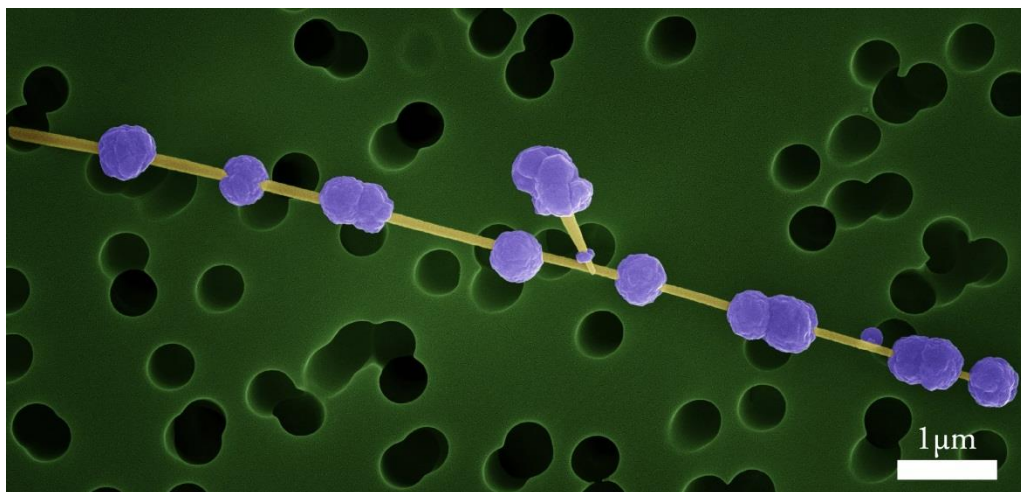
Figure 3. 1 A colorized SEM image of a semiconductor structure sampled on a porous polycarbonate filter

Transmission electron microscopy

TEM is often used for detailed particle analysis. Single particles can be investigated, under optimal conditions, on an atomic level[20]. A high resolution image of a gold particle is shown in Figure 3.2. A TEM can be operated in a range of ways. The electron probe can be shaped into a broad coherent beam which allows for phase contrast imaging of larger areas of the sample with high resolution. The beam can also be focused down to a sharp probe and be scanned in the same fashion as in an SEM which allows for, among other things, detailed elemental analysis.

The TEM samples consist of thin metal grids onto which particles can be deposited. Sample collection and preparation can be a harder task compared to the preparation of SEM samples. While the TEM samples generally don't need any additional coating to allow good analysis, the collection of enough particles while not overloading the sample, can still be a challenge, especially during fieldwork.

While TEM analysis lacks the sample throughput speed of an SEM it is still one of the most versatile methods in terms of nanoparticle characterization.

10

Figure 3. 2 A High Resolution TEM image of a gold nanoparticle

3.3 Particle mobility

In essence, mobility describes how easy a particle moves depending on which forces that acts on it. As the forces can have different origins the mobility related to them will differ from each other. When mobility is defined it is often described in the basic form as how a spherical particle moves. Relating the mobility of an ambiguously shaped particle to that of a sphere will give it its equivalent mobility diameter[4].
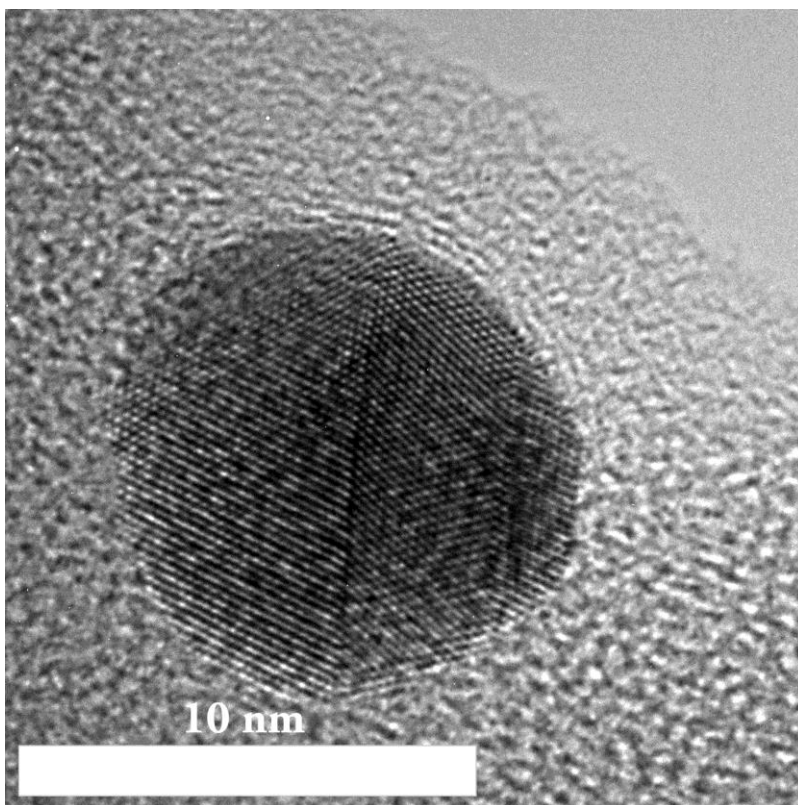
Electrical mobility

A common metric is the electrical mobility diameter that describes how a particle moves in an electric field. The electrical mobility, Z, describes the velocity of a particle with a number, n, of charges, e, when it is placed in a electric field with unit field strength eq. 3.3[4]. The electrical mobility also depends on the diameter of the particle, which is introduced as the Cunningham slip correction factor, C_c, as the electrostatic force is countered by a drag force and the viscosity, η, of the gas surrounding the particle. These two forces balance as the particle reaches terminal velocity.

$$Z = \frac{neC_c}{3\pi\eta d} \quad (3.3)$$

The number of charges on a particle can vary and can give the same mobility for different diameters. This multiple charging is important to account for in a differential mobility analyzer (DMA), a device analyzing particles by selecting a certain electrical mobility, when analyzing large particles. As described previously the number of charges which are capable to reside on a particle is proportional to its size. A schematic of a DMA is shown in Figure 3.3. The basic principle is to select particles with a certain Z and relate this to a d and denote that as the mobility diameter of the selected particle. A DMA can easily be connected to a particle counter such as a condensation particle counter or an electrometer to measure the mobility size distribution. This configuration is usually called a scanning mobility particle sizer (SMPS).
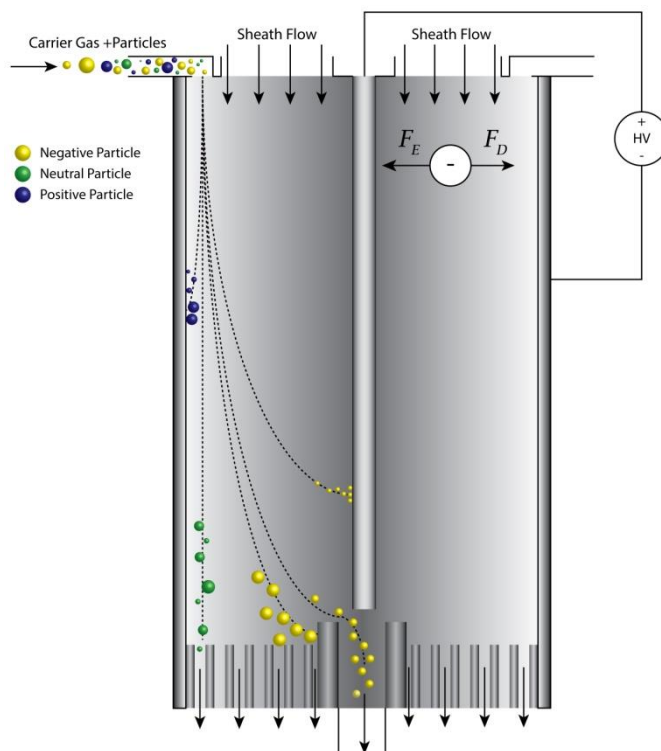
Figure 3. 3 Schematic of a DMA selecting negative paricles

Aerodynamic mobility

The motion of large aerosol particles in a gas with low Reynolds number (no turbulence or rapid gas motion) is called aerodynamic mobility. The aerodynamic mobility diameter of a particle is defined as the diameter of a sphere with unit density which has the same settling velocity as the particle[4]. Comparing two particles of the same material with the same mass, a compact particle will have a smaller aerodynamic diameter compared to an agglomerated particle. An issue with the aerodynamic diameter is that as particle diameter decreases, the settling velocity which originates from gravity becomes less important to the overall motion of the particle as Brownian motion takes over. Instruments such as inertial impactors and aerodynamic particle sizers (APS) will be able to collect or sample particles with diameters of a few hundred nanometers, but will have difficulties with smaller sized particles.

3.4 Emission spectroscopy of electrical discharges

During the electrical discharge in the SDG process energy is dissipated in a range of routes, via ionization, excitation, heating and evaporation. During the process the atoms involved will undergo a set of state changes which will emit light characteristic of that species. Depending on the amount of energy and type of discharge the emitted light can reveal some of the processes on an atomic level. In the scope of characterization of particle generation the intensity of the emitted light of certain atomic species are of higher interest than others. Their temporal evolution is also of interest. Emission spectroscopy is a fairly simple method as it only requires optical access to the generation chamber that allows the collection of light. Spatial resolution can also be achieved by limiting the angle from which the light is collected.

Analysis of the light can be performed in varied complexity by spectrometers which will determine the energy resolution and temporal resolution. Temporal analysis of individual discharges requires some sort of triggering to determine the start of the discharge. This can be achieved by measuring the voltage or current through the electrode gap. Initiation of the discharge will occur without or with only weak optical signal and evolve into the bright characteristic flash of an electrical discharge. An integrated spectrum from Paper IV can be seen in Figure 3.4 which shows some of the species that occur over time during discharge between copper electrodes in a nitrogen atmosphere. As nitrogen is most abundant in this setting most of the peaks will originate from nitrogen, but copper is also present.
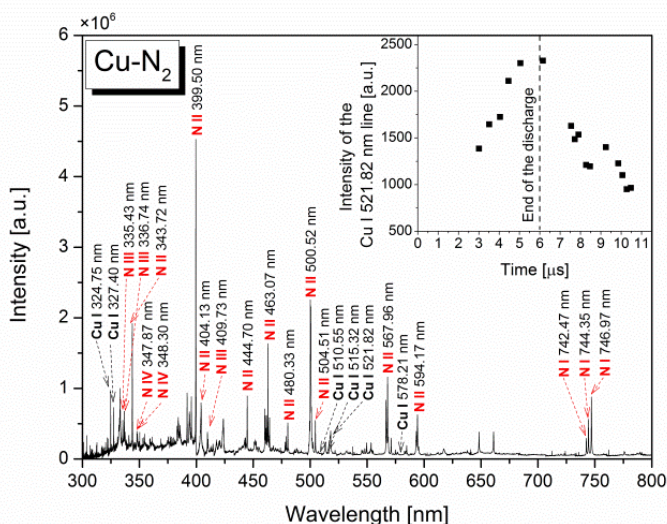

Figure 3. 4 Temporally and spatially integrated emission spectrum of the spark acquired during the generation of Cu NPs in nitrogen atmosphere Inset: temporal evolution of the intensity of the Cu I 521.82 nm line (Paper IV)

3.5 Adverse health effects

Importance of surface area

As previously mentioned, surface area can be a key metric to understand the toxicity of nanoparticles[21,22]. Insoluble materials will exhibit their toxic action with interactions on the surface; the bulk of the material will be of less importance. As for particles smaller radii yields a higher surface to volume ratio and becomes important for fractal structures composed of many smaller entities such as primary particles in agglomerates. An example is titanium dioxide, a common material in consumer products. Oberdörster *et al.*[22] show that toxicity correlates with deposited surface area rather than deposited mass. Similar trends have been shown for other materials such as Carbon Black[23]. The difficulties in measuring surface area in a direct way are many but it can be estimated from other metrics of the particles[24,25].

The properties of particles discussed in this chapter can be used to determine plenty of what a particle will do in any given situation. But in order to have any adverse health effects people has to be exposed to be able to get an effect. With the development of new materials new potential risks are introduced. Studies have shown that the critical period during the lifecycle of a particle used in a product or as part of a material is the production of the particles themselves or tasks related to the handling of the unfinished product or material[26]. It is also during these processes that the amount of material is the highest and most concentrated. Investigating the environment for the workers dealing with these materials is of great importance as some effects, like cancer, won't show itself until several years later.

Some materials are perhaps more of an issue then others as they share properties with materials already proven to be dangerous. However, the answer is seldom black and white, materials looking the same may not behave the same, and even within families of materials there is a vast range of health effect from seemingly similar materials.

A common morphological trait that is known to cause adverse health effects are particles that fall under the fiber paradigm[27-32]. Long, thin, and rigid particles have prevalence in inducing for example frustrated phagocytosis[29,33]. This was one of the problems with asbestos and has now been invigorated with the introduction of carbon nanotubes (CNT).

The case of carbon nanotubes

Carbon nanotubes are a group of engineered materials that has been around since their invention in the early 90's [34,35]. The material itself is based on rolled-up sheets of carbon but there is a vast range of CNT types in terms of physical, and chemical properties, including different types of residues from catalytic material used in the production.

The common structure of all CNTs is the rolled-up layers of carbon that forms the backbone of all CNT materials. This core structure of large single molecules grants properties hard to find in other materials. One of the more prominent ones is the strength of the CNTs, both tensile and ductile. It is uncommon that they are used as a solo material in the final product but they are rather used in composites where the actual content is low in terms of mass or volume.[26]

The aggregation form of the CNTs varies a lot. This comes down to the means of production and the fundamental structure of the individual CNT. Some types will be tangled balls while others will be stiff fibers. If the CNT material is raw from production depending on the production method it may contain large amounts of impurities, both carbonaceous and other elements, while, however, the purified material can be pure CNTs. In terms of toxicity the origin of the CNT material will be important to determine any possible toxic hazards. Fibre toxicity in general can be visualized as shown in Figure 3.5 from Donaldson et al 2006[29]. CNTs are biopersistent and long CNTs will follow the right hand path in the diagram which can explain their toxicity. There are, however, indications that even short CNTs can have toxic effects[36] making CNTs a special case which needs to be assessed with a broader set of techniques compared with other fibre hazards. These types of particles are difficult to assess with indirect methods as the fibers are hard to separate from other particles. In the past phase contrast microscopy has been a standard in asbestos and fiber analysis[37,38], however, the resolution is limited. To circumvent the limitation in resolution, electron microscopy can be used. In Papers VI and VII we use electron microscopy to assess the CNT concentrations.
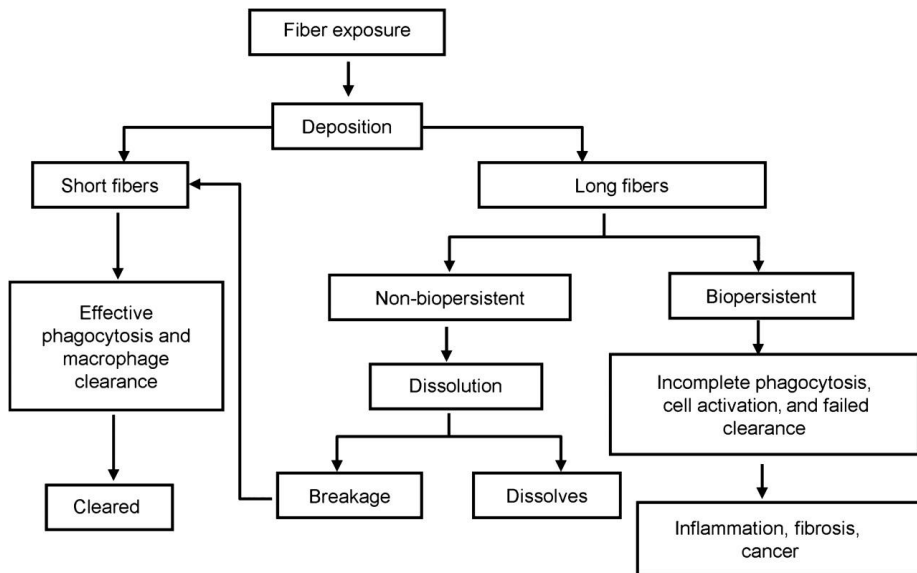
Figure 3. 5 Possible paths of airborne fiber exposure

4. Results

In this chapter, I will describe the main results and their implications from each paper. The chapter is divided into themes related to the main objective of the characterization.

4.1 Characterization related to generation (Papers I, II, and III)

As the need for more specialized materials increases so does the need to understand the processes that governs the generation of the particles during production. SDG production has advantages such as scalability and versatility in the materials which can be produced using the same basic platform. In order to optimize the process and tune the properties of the generated particles, investigations of the initial stages of the production are of interest. There are a number of characterization methods available for nanoparticle generation.

In situ proximity TEM sampling

In Paper I a custom build *in situ* proximity TEM sampler was used to collect particles from within the generation chamber. In Figure 2.1. a schematic of the SDG system is shown. The method of *in situ* sampling has previously been used in other studies to sample soot from flames to study the evolution of particle formation[39-41] and similar piston based samplers utilizing thermophoresis have been used in flame spray pyrolysis[42-44]. In our case the temperature gradient is much smaller due to the rapid quenching of the plasma/vapor plume and the distance to the sampler from the discharge.

The setup was operated using N_2 as carrier gas and gold electrodes with diameter of 3 mm as this configuration has been in used in previous studies[46,47]. The sampling head could be adjusted relative to the electrode gap and achieve a sampling distance of 5-15 mm from the gap center. As the sampler were on the same ground as the counter electrode there was a risk that the discharge would ignite between the HV electrode

and the sampler. This behavior was not consequent but rather erratic with a lower rate with large sampler distance as expected. A distance of 9 mm were chosen as this distance proved to yield acceptable numbers of erroneous discharges. If a discharge struck the sampler that sample was discarded. Discharge frequencies were set to 1.5 Hz and 500 Hz and carrier gas flow 0.5 and 8 lmin^{-1}. These settings were chosen as they were at the extremes of what could be achieved with the setup. TEM grids were aligned vertical and parallel to the carrier gas flow just below the electrodes in Figure 2.1. Particles were also collected downstream in the electrostatic precipitator (ESP). To compare the *in situ* sampled particles all samples were analyzed using TEM and the particle diameters were measured. The downstream particles had undergone agglomeration and the primary particle size was measured on those particles. On the samples acquired *in situ* the particles showed a high degree of crystallinity as can be seen in Figure 4.1.
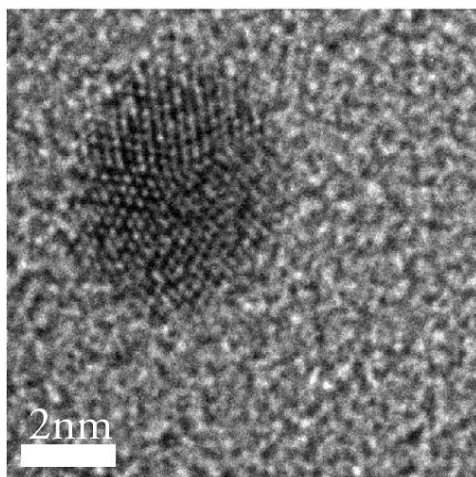
Figure 4. 1 An *in situ* sampled gold particle

Samples were collected at carrier gas flows of 0.5 and 8 lmin^{-1} sampling with 5, 20, 50 and 100 discharges per TEM grid. It became clear that the sampling time did not influence the particle size as there were no significant differences in mean diameter which can be seen in Figure 4.2. The data from the same carrier gas flow were pooled and used when comparing diameters between each flow and the primary particles from the downstream sampled agglomerates. There were significant differences in
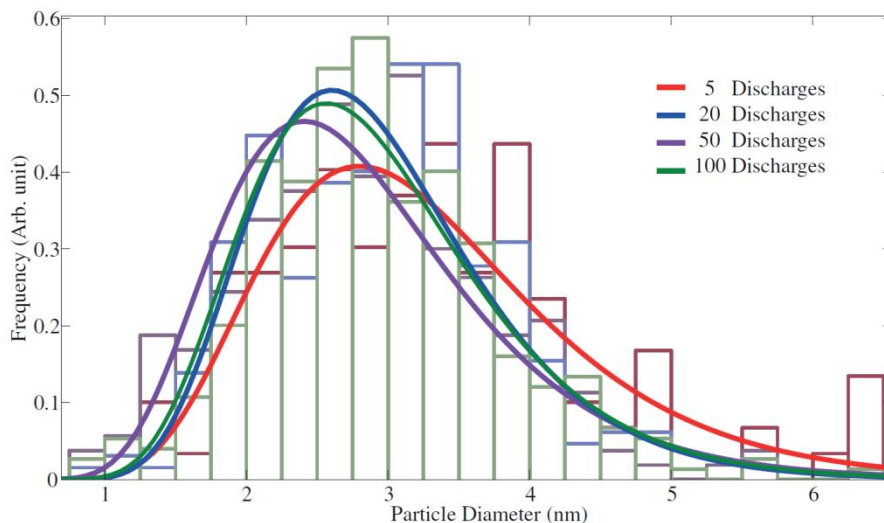
Figure 4. 2 Particle size distributions for varied number of discharges. The curves are fitted log-normal distributions and the bars are the bar plot of the measured particles

diameters comparing the two flows in the proximity sampled particles. Particles generated at a flow of 0.5 lmin^{-1} had a mean diameter of 2.97 nm and at 8 lmin^{-1} the particles had a mean diameter of 2.58 nm. The downstream sampled particles had mean primary particle diameters of 5.90 nm and 4.50 nm for 0.5 lmin^{-1} and 8 lmin^{-1} respectively. The size distributions of these particles can be seen in Figure 4.3.

From this study it was concluded that the particles grow or coalesce further downstream as the size difference was significant under the same generation conditions. It was shown that already deposited particles did not grow or in any other way got affected by an increased sampling time in the timeframe that we investigated. The decrease in particle size with increased carrier flow supports the route of particle size depending on dilution rate.
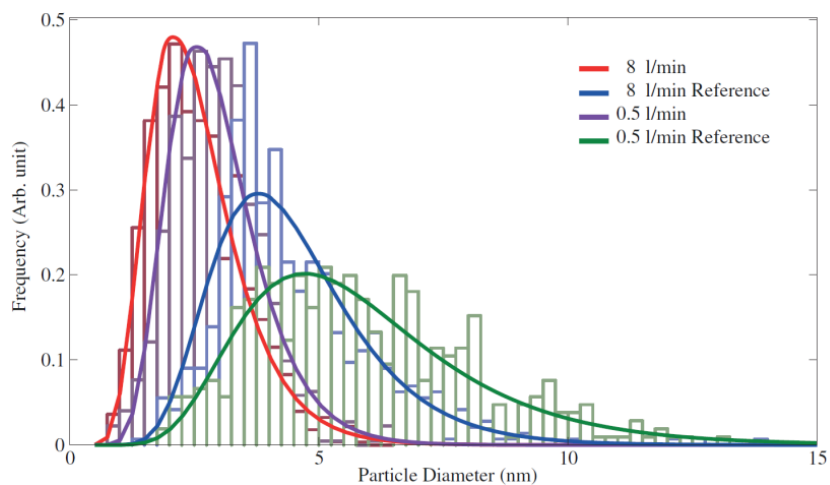
Figure 4. 3 Size distributions (fit and data) for sampled particles and deposited reference particles. The curves are fitted log-normal

Comparison of agglomerate structure between method of particle generation

As well as understanding the initial particle formation it is also of interest to investigate different methods of producing the same type of particles. In addition, as an important factor in the toxicity of nanoparticles, surface area is a property that needs to have easier methods for estimation. A comparison of three methods of generation was performed in Paper II. Gold agglomerates were chosen as model particles and the three sources were two SDGs (one custom made previously described and one commercial (Palas GFG 1000)), and one high temperature (HT) furnace. These three methods all produce gold agglomerates in roughly the same mobility size range without any additional material added to the particles, they are as pure as the gold used as input material. The aim of this study was to compare the methods in terms of number, mass, and surface area output, as well as comparing different methods of surface area estimation. These metrics were measured using set semi-empirical and theoretical models using inputs from DMA-APM, SMPS, and TEM measurements.

The surface area were estimated using five different methods, each relying on certain assumptions of the aerosol set by the model and input data

(I)	Mass-mobility data in combination with TEM imagery[25].
(II)	Theory describing the mass of aggregates in combination with TEM imagery[48].
(III)	Mass-mobility data in combination with semi-empirical theory[24].
(IV)	Lall and Friedlander (2006)[49].
(V)	Assumption of spherical particles.

In addition to these methods, methods (I) and (II) assumes point contacts between primary particles in the agglomerates. In the real agglomerates primary particles are often bridged and thus reducing the surface area to volume ratio of the combined structure. The impact of considering the bridging was also investigated in this study.

The HT furnace had the highest output of particles in terms of mass; by a factor of 8 compared to the commercial SDG, 48.1 vs. 6.08 mg/m^3. The primary particles were larger and thus the HT method produces effectively denser agglomerates. Agglomerates generated with the SDG had smaller primary particles compared to the HT furnace which leads to a lower effective density for a given mobility diameter of the agglomerates when comparing the generation methods. The SDGs had the highest number concentration output with a smaller average mean diameter compared to the HT furnace. However, as the HT furnace had a broader size distribution the lowest effective density of 0.80 g/cm^3 of all sampled settings was measured on 400 nm agglomerates generated with the HT furnace. Comparing the two SDG setups the custom made had a higher output both in terms of number and surface area.

Depending on application the proper generation method should be used as the properties of the particles clearly differ.

When choosing a method to estimate the surface area it is important to consider limitations, pros and cons, and of course the instruments that are available. Regarding (II) and (IV) an advantage is that a DMA–APM measurement is not needed. It does, however, require a primary particle image analysis. In contrast, (III) does not require a primary particle analysis, while it does require DMA–APM measurements of the aerosol. Method (II) is strictly limited to aggregates formed by DLCA with no following restructuring occurring. Method (III) is limited to aggregates formed by DLCA and sintered by viscous flow, grain boundary or lattice diffusion. Many aerosol aggregate distributions have large portions that are not in the free molecular regime, for example combustion soot or welding fume, making Approach IV unsuitable. Approach I requires both DMA–APM and primary particle image analysis. However, it is not limited to the shape of the aggregates and thus applies to aggregates of all forms and not only to aggregates formed by DLCA. Thus, the method can be used for all types of aggregates. It was evident that the bridging between primary particles played an important role and needs to be considered regardless of method.

Generation of new compound materials

With a well characterized and versatile system exploring new materials becomes more accessible. In Paper III we investigated the generation of indium antimonide (InSb) nanoparticles using our custom SDG system. InSb particles have been synthesized using inert gas condensation[50] or via colloid formation[51]. These methods lack the range of options available to the SDG setup and aerosol processing has shown to be promising in fields previously exclusive to epitaxial methods[52]. Aerosol production of compound materials has been explored before[53-55] but to our knowledge InSb has never before been synthesized using the SDG method.

As input materials pure indium and antimony electrodes were used. These materials are prone to oxidize. This was experienced as particles would not compact during sintering at the expected temperature range when using only nitrogen as carrier gas. Addition of 5% hydrogen to the carrier gas flow drastically reduced the sintering temperature at which the particles compacted. A complication of the material is the large difference in equilibrium vapor pressure of In and Sb. Sb is prone to leave the particles at elevated temperatures. This is to some extent a good thing as the initial particles contains an excess of Sb and compacting particles causes the ratio between In and Sb to get close to 1:1. Compacted particles show crystal structure with lattice parameters as expected compared with bulk InSb, an example can be seen in Figure 4.4.

Since it is a simple task to change material in the system pure In and Sb particles were also produced with similar results, limited compaction without the addition of hydrogen but with hydrogen compaction occurred at much lower temperatures. I show in this paper the importance of the composition of the carrier gas, not only for the properties of the discharge but for the generation and the properties of the particles themselves. The reducing atmosphere present already at the generation stage was shown to be a requirement for the compound particles to form.
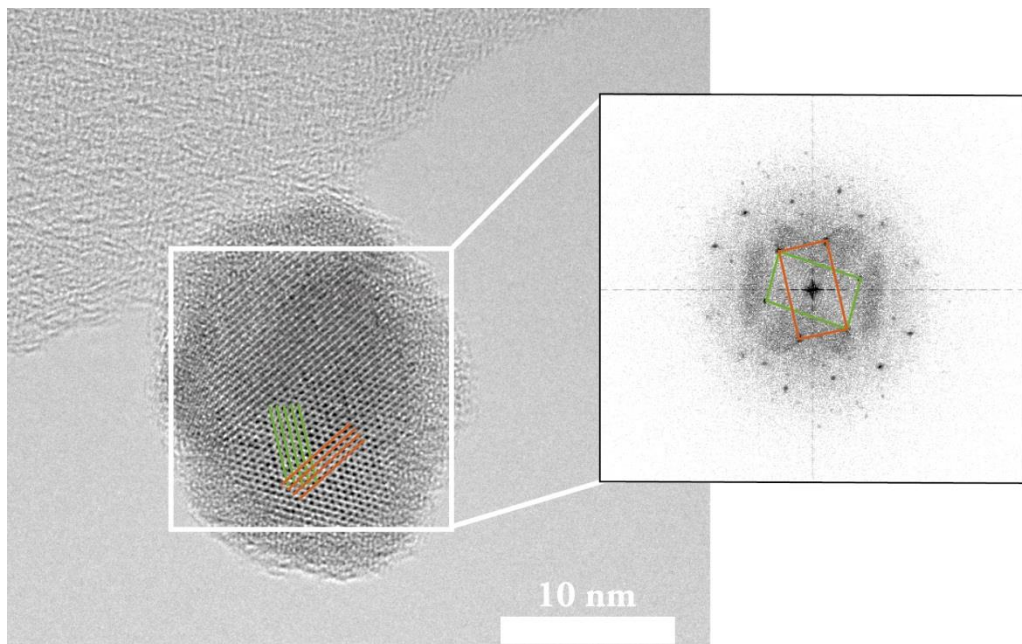
Figure 4. 4 A compacted InSb particle. The FFT indicates lattice distances of {111} in InSb

4.2 Process monitoring (Paper IV)

Process characterization becomes more vital when the demand on the product increases. Online monitoring of aerosol processes is more difficult as the common methods are invasive and or destructive, such as filter sampling or mobility measurements. Even if these methods can be incorporated in the production, online and real-time monitoring is sometimes preferable.

In Paper IV we show that the emitted light during particle generation via spark discharge can be correlated to the amount of material produced. The relationship is from our findings not trivial and differs between materials. In our study copper and gold particles were produced with varied electrode gap distance and charging current.

These two parameters effectively vary the breakdown voltage and the total energy in a single discharge, and the frequency of the discharges. An optical fiber was mounted in front of an observation window on the generation chamber and the collected light was analyzed via a spectrograph.

Triggering of the collection of light is crucial and this was achieved by probing the high voltage drop caused by the discharge. The latency from discharge to collection was on the order of 100 ns which is acceptable as the total discharge lasts a few µs. Time resolution were set to 50 ns and several hundred discharges were measured for each setting. When the energy of the discharge increases, and hence more material is produced, so does the intensity of characteristic wavelengths of the carrier gas. This is expected as more excitations occur with an increased energy. However, the intensity of gold or copper wavelength did not increase at the same rate and were saturated for discharges at a gap distance of 3 mm. This saturation in emission matched well with the particle generation rate with also showed the same trend. This means that this type of online monitoring could be a viable way to monitor continuous particle generation using the SDG method.

4.3 Workplace emission characterization (Papers V, VI, and VII)

A situation that can push the limits of measurement techniques are workplace measurements. A campaign in a real setting is often limited both in time and in accessibility. These campaigns also tend to be resource intensive in terms of people involved. All of the above requires careful planning of the campaign. Papers V, VI, and VII are all based on the same field measurement campaign. The location was a small scale producer of CNTs and we wanted to investigate both acute emissions as well as historic emissions in the form of settled dust sampled of surfaces. It gave us a great opportunity to test standardized and common methods of characterization of workplace emission measurements as well as adapting and comparing new methods.

Sampling was performed during two days where filter samples were collected in the breathing zone (Paper VI) and the emission zone (Paper V) during normal work. Tasks that could be of interest or that were naturally divided during the work was identified before the campaign and a sample were acquired for each one. These samples were also used when comparing results between measurement methods.

In these studies I developed a SEM method for the filter analysis where individual CNT particles were identified and classified into three classes as can be seen in Figure 4.5 from Paper V. In this case we were interested in describing the CNT-containing

particles while still giving a metric on the released concentrations. The analysis was made by hand which limited the complexity of the characteristics that could be used for classification. However, it made the identification process more versatile as the CNTs embedded in the particles would be difficult to identify using other techniques such as automatic image analysis. Single CNTs were rare and particles that would be considered typical fibers in the context of asbestos[56] were few. Instead the particles resembling fibers consisted of several parallel strands of CNTs. Even more so, this class, Type 1, was only 37 % of all the CNT-containing particles found in total. Using the same classification and reporting as is convention for asbestos would miss these particles as they do not fulfill the standard criteria set by, for example, the World Health Organization[56] or the Swedish Work Environment Agency[26].
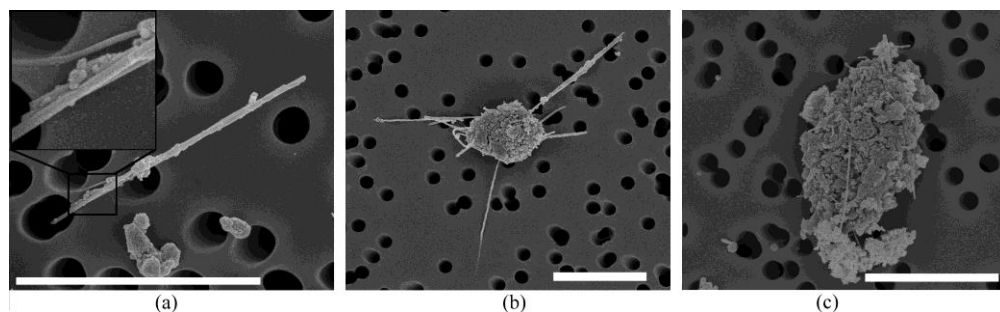
Figure 4. 5 SEM images of different types of airborne CNT-containing particles: (a) type 1 insert shows several strands of CNTs building up the larger structure, (b) type 2, and (c) type 3. The scale bar in each image equals 3 µm. The overall time weighted distribution of the different types was as follows: type 1: 37 %; type 2: 22 %; type 3: 41 %.

Airborne particle sampling

Several methods can be used to collect airborne samples and in that fashion several metrics can be of importance. The full picture requires a set of different sampling methods and instruments. In Papers V and VI we present results from air samples from a range of instruments. Paper VI focuses on the personal samples collected in the breathing zone of the workers and Paper V focus on the local emission zone measurements. Both papers include extensive microscopy analysis of filter samples collected in both zones. An aim of the campaign was to be able to analyze a wide range of particle sizes and this required a range of instruments. It was also of interest to test hand held personal monitors against more advanced aerosol instruments.

Measurements were performed at several locations around the facility and during the days of measurements a background station sampled ambient air a few meters from the closest identified potential source. The background station contained an Aerodynamic particle sizer (APS 3321 TSI) and a Scanning mobility particle sizer (SMPS Model 3071 TSI). Local emission was sampled via probes by an APS (identical to the unit as in the background), a Condensation particle counter (CPC 3022 TSI), and a filter sampler. The filter samplers were fitted with a cyclone (BGI4L, BGI Inc., Waltham, USA) to sample respirable dust to be able to compare with occupational limit values for respirable dust[57,58]. Samples for elemental carbon (EC) were also collected for each work task as EC has been proposed as a proxy metric for CNT[58].

Results from SEM analysis of the filter samples showed release of CNT particles from several of the sampled work tasks at concentrations well above current limit values (<0.01 fibers/cm^3)[59,60]. In no samples were the majority of the CNT particles considered fibers (Type 1) but were classified as either Type 2 or 3. Particles of Type 2 or 3 would have visible CNTs and Type 2 would have a large visible part consisting of CNTs. As these particle were preselected as respirable they would have had the possibility to enter the airways and potentially cause damage as CNTs has shown negative health effects at a range of lengths below that of what generally is considered toxic for asbestos exposure[36]. Using the conventional methods for asbestos counting would result in missing most of the Type 1 particles and all of the Type 2 and 3 particles.

Personal sampling also showed CNT particles to an extent that was above the limit value of 0.01 #cm^{-3} with the lowest measured full day respirable CNT concentration in the breathing zone of 0.04 #cm^{-3} and as high as 2.0 #cm^{-3}. It should be noted that the workers wore personal protective equipment during the tasks with the highest release of material measured form the local emission probes and by that limited the actual exposure to CNT particles.

Impactor samples were also analyzed by SEM and confirmed the presence of CNTs in all stages of the impactor. The impactor sampled without any preselection and it was clear that there were plenty of huge CNT particles that were discarded by the respirable selector. An oddity found in the impactor samples can be seen in Figure 4.6. The SEM image shows a particle from the end stage of the impactor which ideally just should function as end filter to remove anything left after the previous stages and is not a filter that is usually analyzed in the standard gravimetric method. However, the particle found on this stage is much larger than what would be expected and even more so it contains both plenty of CNTs but also Carbon nanodiscs. The latter ones were not handled during our campaign.

As the filter samples shows the integrated sampling during the work task the online instruments proved to be a useful source when estimating when emissions occurred.

From the APS measurements it was clear that the characteristics of the emissions differed between sources and in the case of the work task with the highest CNT emissions there were several sharp peaks of emissions. As a monitoring tool online instruments have an obvious advantage over filter samples. However, when used in combination it makes it possible to gain both detailed information on the emitted particles in aspects of chemical composition shape and number, and a high time resolution of the emissions.
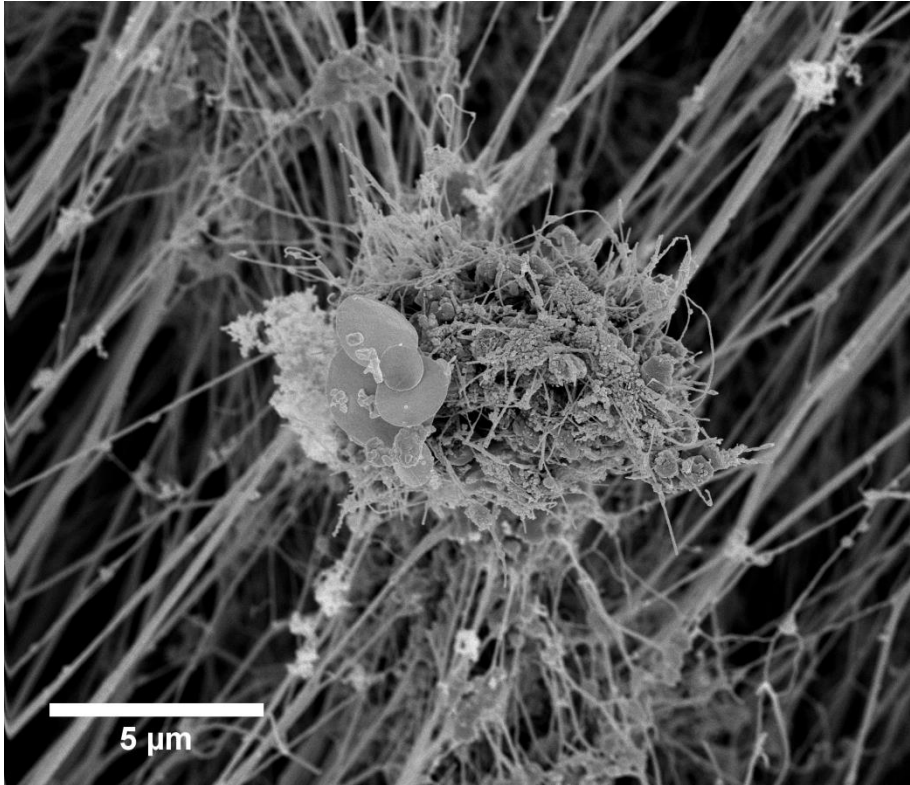
Figure 4. 6 A bundle of CNTs and carbon nanodiscs found on the final stage of a Sioutas cascade impactor. The fibers in the backgroudn belongs to the Teflon filter

Surface sampling

In Paper VII the results from surface sampling are discussed. The method used is not exclusive to nanoparticles or aerosols but will sample all deposited particles. It was a simple method where a strip of adhesive tape was pushed against a surface and then peeled off. The strip was then placed face down on a clean plastic film to protect the sample. The adhesive side of the tape was later analyzed with SEM. The results from this investigation showed contamination of CNTs and carbon nanodiscs from several sites at the facility, some of them outside the area where one would expect contamination. Figure 4.7 shows a set of carbon nanodiscs embedded in a carbon matrix which is part of a large chunk of material found on one of the sampled surfaces. As mentioned before there was no handling of carbon nanodiscs during our campaign. This shows that the risk of cross contamination is something that needs to be considered, especially if there are many users of the same laboratory or production facility. The sampling is in essence a simple method but reveals information which would be hard to find by other methods.
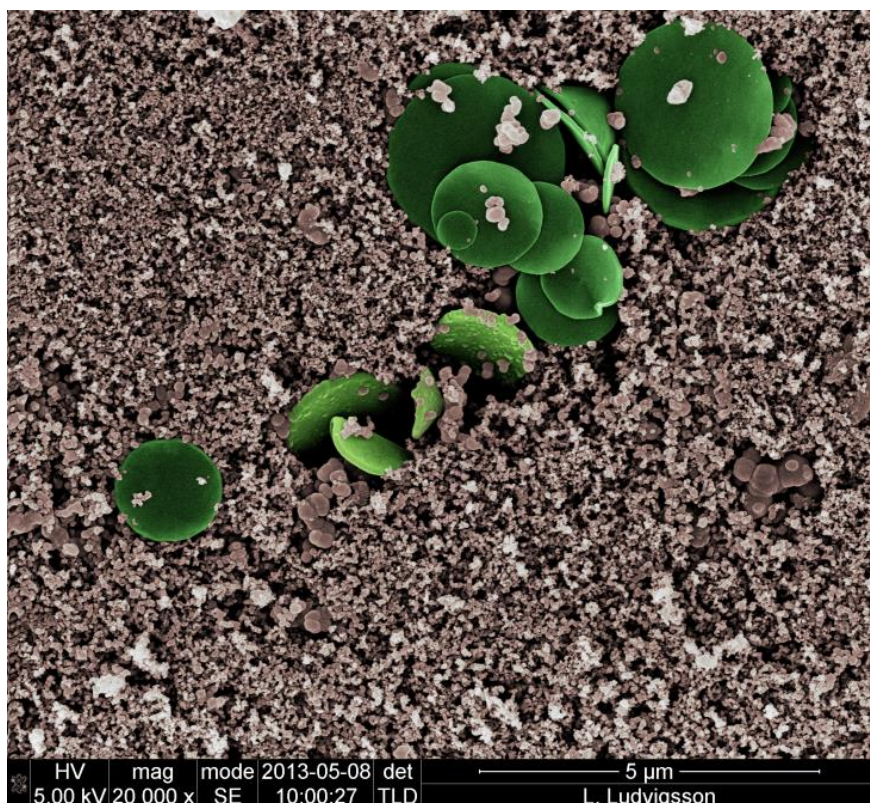
Figure 4. 7 Carbon nano discs (green) embedded in a carbon matrix

5. Conclusions

With a greater understanding of details of a generation process it gives opportunities to explore recently unvisited areas. I have produced InSb nanoparticles which previously have not been achieved in SDG setups. I have successfully sampled initial stages of particles before they have grown into their final size in agglomerates and by that shined a light on particle formation processes which occur under extreme conditions. I have performed spectroscopic characterization of the spark discharge process and correlated spectroscopic data with particle production making a base on which process monitoring could be build. I have compared generation methods of gold agglomerates in terms of particle output and compared methods of estimating the particle surface area output.

Measuring nanoparticles is as difficult as you make it. I have presented that it is possible to measure with simple means as the surface sampling, yet yield results that are sufficient to give an indication that some things needs to improve. I have also shown that an extensive arsenal of equipment can yield results which complement and build upon each other. By just using online instruments it will not be possible to get a complete picture of the emission situation when particle shape are of that importance as it is in the case of CNTs. With the use of only filter sampling and offline analysis temporal variance in the emissions would be difficult to assess without having a large number of samples, which would be ineffective.

I have shown that certain characterization methods can be used in a wide range of applications. Electron microscopy has proven to be essential in all of our studies. The same instrument can be utilized in quantitative and qualitative studies and yield data on a range of properties of the analyzed materials. While microscopy is an offline methods it complements online instrumentation as it can acquire data that can confirm online measurements as well as give additional insights in terms of morphology and chemical composition.

While it is possible to measure all kinds of data on the same aerosol given enough time and resources, the optimization and tailoring of the study might be the real challenge.

Outlook

Spark discharge generators have possibilities to expand as a source of nanoparticles for many applications. The far most interesting aspect of the method is the versatility of the choice of materials available and the rapidness that the material can be exchanged. This opens up to specialty production where quantity might not be the first priority. The system can be used as a source of otherwise hard to produce material combinations at the nanoscale.

With nanotechnology being a truly interdisciplinary science it is not farfetched to assume that the techniques needed to analyze these materials in different settings must also be interdisciplinary. Certain methods are underused in some fields while being standard in others. As fields come closer to each other it is natural that the knowledge within them will spread and spark new ideas on how to utilize combinations of methods. It might even be required to develop new standards or characterization methods to meet the demand from industry and public. While it's still too early to tell if precautions taken now is enough to limit any adverse effects of exposure there are signs that industry and government take actions that gives hope for the future of nanosafety.

References

1 Bates, D. V. Recollections of the London Fog. *Environmental health perspectives* **110**, A735-A736 (2002).

2 Corn, J. K. Historical Aspects of Industrial Hygiene—II. Silicosis. *American Industrial Hygiene Association Journal* **41**, 125-133, doi:10.1080/15298668091424474 (1980).

3 Wagner, G. R. Asbestosis and silicosis. *The Lancet* **349**, 1311-1315, doi:10.1016/S0140-6736(96)07336-9.

4 Hinds, W. C. *Aerosol Technology: Properties, behavior, and measurement of airborne particles*. 2 edn, 53 (Wiely, 1999).

5 Boyen, H. G. *et al.* Oxidation-resistant gold-55 clusters. *Science* **297**, 1533-1536 (2002).

6 Kulkarni, P., Baron, P. A. & Willeke, K. *Aerosol measurement: principles, techniques, and applications*. (John Wiley & Sons, 2011).

7 European Comission. Comission Recommendation on the definition of nanomaterial. Report No. 2011/696/EU, (2011).

8 Meuller, B. O. *et al.* Review of Spark Discharge Generators for Production of Nanoparticle Aerosols. *Aerosol Science and Technology* **46**, 1256-1270, doi:10.1080/02786826.2012.705448 (2012).

9   Stein, M. & Kruis, F. E. Optimization of a transferred arc reactor for metal nanoparticle synthesis. *J Nanopart Res* **18**, 258, doi:10.1007/s11051-016-3559-y (2016).

10   Feng, J. *et al.* Scalable and Environmentally Benign Process for Smart Textile Nanofinishing. *ACS Applied Materials & Interfaces* **8**, 14756-14765, doi:10.1021/acsami.6b03632 (2016).

11   Raizer, Y. P., Kisin, V. I. & Allen, J. E. *Gas Discharge Physics*. (Springer Berlin Heidelberg, 2011).

12   Lippmann, M. Effects of fiber characteristics on lung deposition, retention, and disease. *Environmental health perspectives* **88**, 311-317 (1990).

13   Ehara, K., Hagwood, C. & Coakley, K. J. Novel method to classify aerosol particles according to their mass-to-charge ratio—Aerosol particle mass analyser. *J Aerosol Sci* **27**, 217-234, doi:http://dx.doi.org/10.1016/0021-8502(95)00562-5 (1996).

14   Charvet, A., Bau, S., Paez Coy, N. E., Bémer, D. & Thomas, D. Characterizing the effective density and primary particle diameter of airborne nanoparticles produced by spark discharge using mobility and mass measurements (tandem DMA/APM). *J Nanopart Res* **16**, 2418, doi:10.1007/s11051-014-2418-y (2014).

15   Aitken, R. J., Chaudhry, M. Q., Boxall, A. B. A. & Hull, M. Manufacture and use of nanomaterials: current status in the UK and global trends. *Occupational Medicine-Oxford* **56**, 300-306, doi:10.1093/occmed/kq1051 (2006).

16   Donaldson, K. & Borm, P. J. A. The quartz hazard: A variable entity. *Ann Occup Hyg* **42**, 287-294, doi: 10.1016/S0003-4878(98)00044-1 (1998).

17   Waters, K. M. *et al.* Macrophage Responses to Silica Nanoparticles are Highly Conserved Across Particle Sizes. *Toxicological Sciences* **107**, 553-569, doi:10.1093/toxsci/kfn250 (2009).

18   Asbach, C., Fissan, H., Stahlmecke, B., Kuhlbusch, T. A. J. & Pui, D. Y. H. Conceptual limitations and extensions of lung-deposited Nanoparticle Surface Area Monitor (NSAM). *J Nanopart Res* **11**, 101-109, doi:10.1007/s11051-008-9479-8 (2009).

19   David B. Williams, Carter C. Barry,. *Transmission Electron Microscopy - Textbook for Materials Science*. (Springer, 2008).

20   Pyrz, W. D. & Buttrey, D. J. Particle Size Determination Using TEM: A Discussion of Image Acquisition and Analysis for the Novice Microscopist. *Langmuir* **24**, 11350-11360, doi:10.1021/la801367j (2008).

21   Schmid, O. & Stoeger, T. Surface area is the biologically most effective dose metric for acute nanoparticle toxicity in the lung. *J Aerosol Sci* **99**, 133-143, doi:http://dx.doi.org/10.1016/j.jaerosci.2015.12.006 (2016).

22   Oberdorster, G., Oberdorster, E. & Oberdorster, J. Nanotoxicology: an emerging discipline evolving from studies of ultrafine particles. *Environmental health perspectives* **113**, 823-839 (2005).

23   Sager, T. M. & Castranova, V. Surface area of particle administered versus mass in determining the pulmonary toxicity of ultrafine and fine carbon black: comparison to ultrafine titanium dioxide. *Particle and Fibre Toxicology* **6**, 15, doi:10.1186/1743-8977-6-15 (2009).

24   Eggersdorfer, M. L., Gröhn, A. J., Sorensen, C. M., McMurry, P. H. & Pratsinis, S. E. Mass-Mobility Characterization of Flame-made ZrO(2) Aerosols: Primary Particle Diameter & Extent of Aggregation. *J Colloid Interf Sci* **387**, 12-23, doi:10.1016/j.jcis.2012.07.078 (2012).

25   Rissler, J. *et al.* Experimental determination of deposition of diesel exhaust particles in the human respiratory tract. *J Aerosol Sci* **48**, 18-33, doi:10.1016/j.jaerosci.2012.01.005 (2012).

26   Per Gustavsson, Maria Hedmer, Jenny Rissler. Kunskapsöversikt Kolnanorör – Exponering, toxikologi och skyddsåtgärder i arbetsmiljön. Report No. 2011:1, 70 (Arbetsmiljöverket, 2011).

27   Bernstein, D. M. *et al.* The pathological response and fate in the lung and pleura of chrysotile in combination with fine particles compared to amosite asbestos following short-term inhalation exposure: interim results. *Inhal Toxicol* **22**, 937-962, doi:10.3109/08958378.2010.497818 (2010).

28   Bolton, R. E., Davis, J. M. G., Donaldson, K. & Wright, A. Variations in the Carcinogenicity of Mineral Fibers. *Ann Occup Hyg* **26**, 569-582, doi:10.1093/annhyg/26.5.569 (1982).

29   Donaldson, K. *et al.* Carbon nanotubes: a review of their properties in relation to pulmonary toxicology and workplace safety. *Toxicol Sci* **92**, 5-22, doi:10.1093/toxsci/kfj130 (2006).

30   Donaldson, K., Brown, G. M., Brown, D. M., Bolton, R. E. & Davis, J. M. Inflammation generating potential of long and short fibre amosite asbestos samples. *Occupational and Environmental Medicine* **46**, 271-276, doi:10.1136/oem.46.4.271 (1989).

31   Miller, B. G. *et al.* Influence of fibre length, dissolution and biopersistence on the production of mesothelioma in the rat peritoneal cavity. *Ann Occup Hyg* **43**, 155-166, doi:10.1016/S0003-4878(99)00018-6 (1999).

32   Tran, C. L. *et al.* A hypothetical model for predicting the toxicity of high aspect ratio nanoparticles (HARN). *J Nanopart Res* **13**, 6683-6698, doi:10.1007/s11051-011-0575-9 (2011).

33   Poland, C. A. *et al.* Carbon nanotubes introduced into the abdominal cavity of mice show asbestos-like pathogenicity in a pilot study. *Nat Nano* **3**, 423-428, doi:10.1038/nnano.2008.111 (2008).

34   Iijima, S. Carbon nanotubes: past, present, and future. *Physica B-Condensed Matter* **323**, 1-5, doi:10.1016/S0921-4526(02)00869-4 (2002).

35   Iijima, S. Helical microtubules of graphitic carbon. *Nature* **354**, 56-58, doi:10.1038/354056a0 (1991).

36   Kostarelos, K. The long and short of carbon nanotube toxicity. *Nat Biotech* **26**, 774-776 (2008).

37   Burdett, G. A comparison of historic asbestos measurements using a thermal precipitator with the membrane filter-phase contrast microscopy method. *Ann Occup Hyg* **42**, 21-31, doi:10.1016/S0003-4878(97)00048-3 (1998).

38   Cely-Garcia, M. F., Sanchez, M., Breysse, P. N. & Ramos-Bonilla, J. P. Personal Exposures to Asbestos Fibers During Brake Maintenance of Passenger Vehicles. *Ann Occup Hyg* **56**, 985-999, doi:10.1093/annhyg/mes030 (2012).

39   Cai, J., Lu, N. & Sorensen, C. M. Comparison of size and morphology of soot aggregates as determined by light scattering and electron microscope analysis. *Langmuir* **9**, 2861-2867, doi:10.1021/la00035a023 (1993).

40   Cho, J. & Choi, M. Determination of number density, size and morphology of aggregates in coflow diffusion flames using light scattering and local sampling. *J Aerosol Sci* **31**, 1077-1095, doi:http://dx.doi.org/10.1016/S0021-8502(99)00574-1 (2000).

41   Arabi–Katbi, O. I., Pratsinis, S. E., Morrison, P. W. & Megaridis, C. M. Monitoring the flame synthesis of TiO2 particles by in-situ FTIR spectroscopy and thermophoretic sampling. *Combustion and Flame* **124**, 560-572, doi:http://dx.doi.org/10.1016/S0010-2180(00)00227-3 (2001).

42   Dobbins, R. A. & Megaridis, C. M. Morphology of flame-generated soot as determined by thermophoretic sampling. *Langmuir* **3**, 254-259, doi:10.1021/la00074a019 (1987).

43   Gröhn, A. J., Eggersdorfer, M. L., Pratsinis, S. E. & Wegner, K. On-line monitoring of primary and agglomerate particle dynamics. *J Aerosol Sci* **73**, 1-13, doi:http://dx.doi.org/10.1016/j.jaerosci.2014.03.001 (2014).

44   Kammler, H. K., Jossen, R., Morrison, P. W., Pratsinis, S. E. & Beaucage, G. The effect of external electric fields during flame synthesis of titania. *Powder Technology* **135**, 310-320, doi:http://dx.doi.org/10.1016/j.powtec.2003.08.023 (2003).

45   Messing, M. E. *et al.* A comparative study of the effect of gold seed particle preparation method on nanowire growth. *Nano Res* **3**, 506-519, doi:DOI 10.1007/s12274-010-0011-y (2010).

46   Messing, M. E., Dick, K. A., Wallenberg, L. R. & Deppert, K. Generation of size-selected gold nanoparticles by spark discharge - for growth of epitaxial nanowires. *Gold Bull* **42**, 20-26 (2009).

47   Nilsson, P. T. *et al.* In-situ characterization of metal nanoparticles and their organic coatings using laser-vaporization aerosol mass spectrometry. *Nano Res* **8**, 3780-3795, doi:10.1007/s12274-015-0877-9 (2015).

48   Sorensen, C. M. The Mobility of Fractal Aggregates: A Review. *Aerosol Science and Technology* **45**, 765-779, doi:10.1080/02786826.2011.560909 (2011).

49   Lall, A. A., Seipenbusch, M., Rong, W. & Friedlander, S. K. On-line measurement of ultrafine aggregate surface area and volume distributions by electrical mobility analysis: II. Comparison of measurements and theory. *J Aerosol Sci* **37**, 272-282, doi:http://dx.doi.org/10.1016/j.jaerosci.2006.01.006 (2006).

50   Pandya, S. G. & Kordesch, M. E. Characterization of InSb Nanoparticles Synthesized Using Inert Gas Condensation. *Nanoscale Res Lett* **10**, 1-7, doi:10.1186/S11671-015-0966-4 (2015).

51   Liu, W., Chang, A. Y., Schaller, R. D. & Talapin, D. V. Colloidal InSb Nanocrystals. *Journal of the American Chemical Society* **134**, 20258-20261, doi:10.1021/ja309821j (2012).

52   Heurlin, M. *et al.* Continuous gas-phase synthesis of nanowires with tunable properties. *Nature* **492**, 90-94, doi:10.1038/Nature11652 (2012).

53   Deppert, K. *et al.* Aerosol fabrication of nanocrystals of InP. *Japanese Journal of Applied Physics Part 1-Regular Papers Brief Communications & Review Papers* **38**, 1056-1059, doi:10.1143/Jjap.38.1056 (1999).

54   Deppert, K. *et al.* Size-selected nanocrystals of III-V semiconductor materials by the aerotaxy method. *J Aerosol Sci* **29**, 737-748, doi:10.1016/S0021-8502(97)10017-9 (1998).

55   Deppert, K. *et al.* Aerosol fabrication of nanocrystals of InP and related materials. *1998 International Conference on Indium Phosphide and Related Materials - Conference Proceedings*, 765-768, doi:10.1109/Iciprm.1998.712771 (1998).

56   World Health Organization. *Determination of airborne fibre number concentrations: A recommended method, by phasecontrast optical microscopy (membrane filter method)* (1997)

57   Jones, A. D. *et al.* Thoracic size-selective sampling of fibres: Performance of four types of thoracic sampler in laboratory tests. *Ann Occup Hyg* **49**, 481-492, doi:10.1093/annhyg/mei004 (2005).

58   NIOSH. *Occupational exposure to carbon nanotubes and nanofibres.* , <http://www.cdc.gov/niosh/docs/2013-145/pdfs/2013-145.pdf> (2013).

59   British Standards Institute. *Nanotechnologies – part 2: guide to safe handling and disposal of manufactured nanomaterials* (2007)

60   IFA. *Criteria for assessment of the effectiveness of protective measures.*, <http://www.dguv.de/ifa/Fachinfos/Nanopartikel-am-Arbeitsplatz/Beurteilung-von-Schutzma%C3%9Fnahmen/index-2.jsp> (2013).

Paper I

Investigations of initial particle stages during spark discharge

Linus Ludvigsson, Bengt O Meuller and Maria E Messing

Solid State Physics, Lund University, Box 118, 221 00 Lund, Sweden

E-mail: Linus.Ludvigsson@ftf.lth.se

Abstract

The number of nanoparticle-based products on the market is expected to increase considerably during the coming decades. This forces the industry to have highly meticulous manufacturing of large amounts of nanoparticles using cheap and environmentally friendly methods. For the production of metal nanoparticles spark discharge generation is a promising route to fulfill these demands. The spark discharge generator can be easily scaled-up for mass production due to its simple design solely by placing several units in parallel. Before doing so, one first needs to optimize a single spark discharge generator unit. To optimize the spark discharge generator in a controlled way the first stage of nanoparticle formation needs to be understood. To improve this understanding we have constructed a customized nanoparticle sampler to enable sampling of the initial stages of particle formation for imaging in a TEM. In this article we present the design of the sampler and discuss optimal sampling parameters. We also present how the generation parameters can be tuned in order to affect the first stages of particle formation and hence the final nanoparticles.

(Some figures may appear in colour only in the online journal)

1. Introduction

Nanoparticles are nowadays integrated in a variety of different products that can be found on the market [1]. The ability to manufacture large amounts of nanoparticles with controlled characteristics is a requirement for the continued development of nanoparticle containing products. One method to produce nanoparticles with controlled properties is by colloid chemistry. This is useful in some cases but for a number of products cleanliness of the particles is of major importance and one wants to avoid the use of chemicals. Instead, it might also be cheaper, easier to scale up to mass production and more environmentally friendly to use physical generation methods.

A well-established method for production of metal oxide particles is flame spray pyrolysis (FSP) that is widely used in industry today [2, 3]. The drawback of this method is that generation of pure metal particles is highly challenging. No perfect physical method for large scale manufacturing of pure metal particles with tailored properties is used today but there is a strong belief that the so-called spark discharge generator

(SDG) could be a suitable option. In the SDG nanoparticles are created due to the formation of a plasma channel that leads to a discharge between two conducting electrodes and hence evaporation of electrode material.

The SDG has a very simple design and consist of an electrode pair and a power supply. By placing several electrode pairs in parallel the generation process could be easily scaled up at low cost and with minimal impact on the environment, due to high energy efficiency in the conversion of electrodes into particles and the possibility to recycle the non-heated carrier gas. In the EU-project BUONAPART-E, 21 partners from both industry and academia work on this up scaling to reach a production rate of $100\,kg\,d^{-1}$ [4]. To reach such high production rates the first step is to optimize the production of a SDG containing a single electrode pair. It is of utmost importance that the fundamental mechanisms taking place during the short discharge is carefully investigated and understood in order to enable controlled design optimization of the SDG. Although the SDG has been around since 1988 [5], is commercially available [6] and used by several groups [7–12],

these mechanisms are still poorly investigated. One major reason for this is that it is not completely straightforward to perform measurements really close to the region where the discharge takes place. A few examinations using conventional aerosol methods [13] and laser spectroscopy [14] have been performed but to our knowledge no investigations to actually image the particles in the vicinity of the discharge has been performed.

In this article we therefore describe a custom-made sampler with the capability to collect transmission electron microscopy (TEM) samples in the vicinity of the spark, very close to the electrode pair. We refer to this sampler as the proximity sampler. Several groups have performed TEM sampling of particles in flames and combustion engines previously using different techniques [15–18]. This is, however, to the authors' knowledge the first time such investigations have been conducted for spark discharge generated nanoparticles. Sampling for TEM of the first stages of nanoparticle formation using flame spray pyrolysis (FSP) has been achieved using another type of sampler also equipped with a piston [19–21]. Both samplers build on thermophoresis of particles towards the lower side of the temperature gradient as the deposition mechanism. However, the temperature gradient between the particles and the sampler is much higher in the case of FSP. This is due to the very localized heating of the spark and rapid cooling of the aerosol. In the case of spark discharge generation one cannot rule out that there also might be a difference in electrical potential between the spark and the sample and/or the charged particles and the sample although the sample is not biased. In both the FSP and SDG cases the residence time can be controlled but in the SDG case the time span is much longer since sampling can be performed for prolonged times. If a TEM grid is kept too long in a flame the grid will be burned and useless, but this is not the case for the SDG. The major difference between our custom-made sampler and samplers used for FSP is the demand of a completely leak tight connection of the sampler to the SDG. When producing metal particles no oxygen can be introduced to the system since even the smallest amount affect particle formation and metal oxides might be produced instead.

Another route to image particle formation is to generate or alter particles inside the TEM while imaging, which has been done for colloidal particles [22] and particles formed by sputtering of a thin film [23]. Although this provides important information about the particle formation processes it does not image a 'real' process and the requirements of the TEM are rather high. Therefore, conventional TEM sampling is still typically done on a filter or using an electrostatic precipitator [24], which means that the samples are collected a fair distance downstream of the spark. By adding this extra distance the particles have time to grow and agglomerate, and imaging of these particles do not reveal their size upon formation. Since the sampling with the custom build sampler is done very close to the actual discharge region we conducted measurements at optimal parameters for sampling in order not to destroy the delicate TEM grid and compared to particle samples collected a fair distance downstream with a conventional electrostatic precipitator. Finally, we show that for generation

of gold particles the tuning of different generation parameters have a significant influence on the particle size in the very first stages of particle growth, and hence also the final size of the produced nanoparticles.

2. Experimental

2.1. Particle formation theory

A spark discharge particle generator forms nanoparticles via ablation of electrode material. As the sparks are discrete, the material will undergo rapid cooling leading to super saturation with subsequent nucleation and to the formation of singlet particles as described by Schmidt-Ott *et al* [25, 26]. Singlet particles are defined as the stage between fully grown primary particles and the initial nuclei. The dimension of the first particles are determined by the critical cluster radii, r_p^*, described by the Kelvin equation (1) [27], were σ is the surface tension of the material, ν is the molecular volume, T is the absolute temperature and S is the saturation ratio.

$$r_p^* = \frac{2\sigma\nu}{k_bT\ln S} \tag{1}$$

With the start of the formation of stable particles, the saturation in the gas will drastically drop and will in turn limit the potential for new particles to form. Instead condensation onto and growth of the initial particles would increase until the vapor reaches equilibrium partial pressure. At this stage the particles are traditionally considered as primary particles with a monodisperse size distribution as described by Friedlander [27] and Pratsinis [28].

Due to their small size, the Brownian motion will cause the newly formed particles to collide if the concentration is high. This process will form agglomerate particles and reduce the total number concentration of particles. Their final dimensions are limited by diffusion and amount of available vapor according to diffusion-limited aggregation (DLA) [29], and this has been described in the context of spark discharge generators by Meuller *et al* [30] and Pfeiffer *et al* [13].

The small size of the initial primary particles can lead to coalescence due to energy reduction from the decrease in surface area as described by Lehtinen *et al* [31], resulting in larger primary particles or partially fused primary particles measured in the final agglomerates.

The primary particle diameter could be affected by a rapid reduction of available material during the growth after nucleation leading to smaller primary particles, and also a reduction in the degree of agglomeration. In a spark discharge generator system this would be expected to occur with an increasing carrier gas flow rate.

2.2. The spark discharge generator

A spark discharge generator is basically a capacitance charger loading a capacitance bank that discharges in a controlled manner between two electrodes of the material being produced. A schematic view of the electrical system is shown in figure 1.
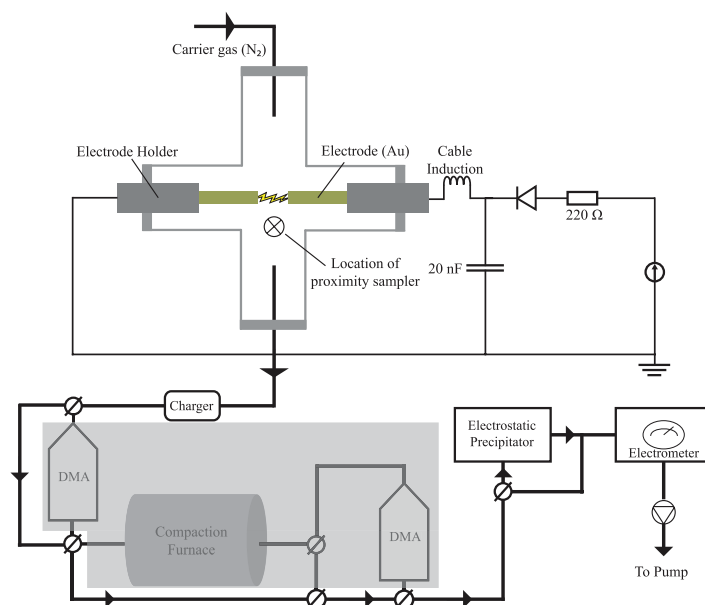
Figure 1. Schematic view of the spark discharge system. Thick lines represent pipes, thin lines represents electrical wiring. The grayed out portion is part of the entire nanoparticle generation system but was bypassed during these experiments and is included in the images to show that the electrostatic precipitator used for the reference samples are located downstream the actual SDG where the proximity sampler is used.

To be able to handle the produced particles the electrodes need to be placed in a chamber. A carrier gas is used to transport the produced particles from the chamber. Control over the gas flows is necessary to enable controlled production and measurements of the particles. For this purpose mass flow controllers (MFC) are used to regulate the in and out flow of gases. An electronic pressure controller (EPC) regulates the system pressure by regulating its outflow of gas.

After the particles are formed in the spark chamber there is a possibility for size classification, e.g. using differential mobility analyzers (DMA), of the agglomerate particles that form from the primary particles directly in the chamber and even to compact them in the compaction furnace. This however is outside the scope of this paper but is well described in [32, 33]. The system also contains an electrostatic precipitator (ESP) for deposition of nanoparticles which were used in these experiments for deposition of reference samples. These samples could be considered the product of the system. The reference samples are samples containing the final agglomerate particles for a certain gas flow. The difference between the samples from close to the spark, sampled with the proximity sampler, and the reference samples attained in the ESP is one of the targets of this study.

The nanoparticles in the experiments described here were produced using a Technix CCR15-P-150 capacitance charger charging a bank of 20 nF high voltage capacitors. The high voltage is carried to the anode electrode via a high voltage cable with the grounded return in the coaxial shielding braid. The spark chamber consists of a standard 6-way KF40 vacuum cross with gas inlets and outlets on the top and bottom flanges respectively. Two opposing flanges are used for the anode and cathode feedthroughs. For the anode feedthrough a 20 kV high voltage feedthrough from MDC Vacuum Products LLC was used and for the grounded anode a linear motion manipulator for high vacuum also from MDC Vacuum Products LLC. For gas control an AERA FC-7700CU MFC was used. Pressure control was achieved with the use of a Bronkhorst P-702CV EPC. Control over the system is sustained with an in-house LabView™ program through a National Instruments cDAQ with a NI-9205 module for Analog Input, a NI-9264 for Analog Output and a NI-9403 for Digital Input and Output.

2.3. The TEM proximity sampler

The unit consists of three main components: the control system, the pneumatics, and the sample holder. Assembled, it is mounted on the spark chamber and oriented as seen in figure 2.

The first component is the electronics and mechanics, as schematically shown in figure 2, consisting of a PLC, pneumatic actuators, power supply and proximity sensors. The PLC is a 24 V FESTO FC30 Front End Controller controlling a FESTO CPE10 5/2-way Solenoid valve regulating the
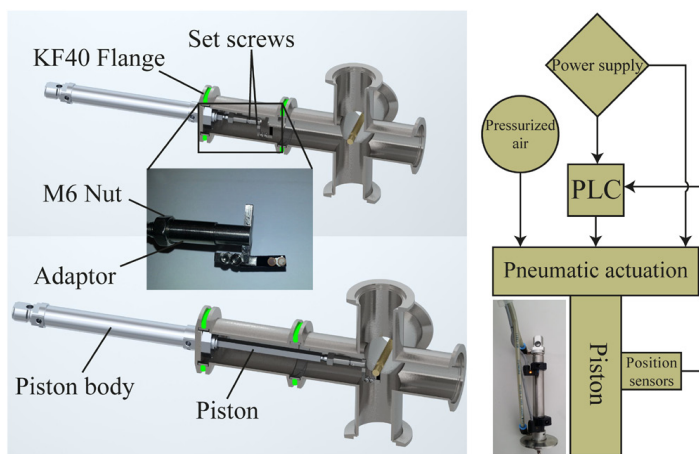
Figure 2. The proximity sampler mounted to the spark chamber. The chamber and one of the electrodes has been cut out to see inside the chamber. Top left image shows the retracted state so that no contamination occurs. Bottom left shows the extended state where sampling occurs. To the right, the schematic for the sampling platform is shown. The right photograph shows the pneumatic system with proximity sensors and connected gas lines.

movement of the pneumatic piston. The platform uses two SMEO-4 proximity sensors to determine and give feedback on the position of the piston rod shown in the right photo inset of figure 2.

Programing of the PLC gives the opportunities through the input panel to select the residence time of the sample holder in the extended position. This can be varied from 1 ms up to 70 s. It also permits the setting of a failsafe time. Failsafe time is the time after which the piston is retracted if the forward sensor does not detect the piston in the extended state due to sensor problems or problems with the piston.

The second component of the platform is the pneumatic part that consists of a FESTO DSNU piston with a diameter of 16 mm, 80 mm stroke length, PPV cushioning and square profile piston rod. The diameter and length of the piston is chosen to be the minimum needed to minimize stroke time and weight. The sample holder needs to be far from the electrodes when not sampling so not to contaminate the sample with particles remaining in the vicinity of the spark due to eddies and non-laminar flow. A cushioned piston was chosen (although this increases the stroke time) to reduce percussions from the piston to translate into the SDG system. The one-way stroke time with this setup and at 5 bar pneumatic pressure was about 80 ms. The 5 bar working pressure is the nitrogen working pressure used for the SDG. The pneumatic piston is mounted on a KF40 flange with a cylindrical O-ring seal to maintain a vacuum tight system.

The third component of the platform is the sample holder. For this project the sample holder is made to be able to hold a strip of silicon to which TEM-grids are fastened with a silver emulation. The holder consists of, as shown in the left photo inset in figure 2, an adaptor fastened to the piston rod directly and secured with a M6 nut. The adaptor acts as an extension

of the rod to make coarse corrections of the lengthwise position of the sample holder. It also acts as a simple mean to be able to keep the sample at the desired rotational angle. Onto the adaptor the holder body is attached and secured with a set screw. The threads connecting the adaptor and holder body allows for finer length adjustments. In the slit in the front of the holder body the holder arm is placed and secured with a set screw. In this way it is possible to adjust the sample in the radial direction. The arm is shaped as an 'L' and holds the pincers in place with two M2 screws. The holder arm and pincers are constructed in such a way that the sample is held in the centerline of the whole piston-holder assembly. For extra stability in holding the sample the holder arm and pincers can be mounted backwards as shown in the left photo inset of figure 2.

2.4. Nanoparticle sampling and analysis procedure

In the SDG system we have possibilities to change electrode material, carrier gas, carrier gas flow rate, discharge energy, discharge frequency, sampling time and sampling distance from the electrode gap. For the experiments in this study we choose to keep the carrier gas, sampling distance, and electrode material constant and to vary the carrier gas flow rate, the spark discharge frequency, and the sampling time. The following settings were investigated: nitrogen carrier gas, gold electrodes (99.999%) with a diameter of 3 mm, a capacitance of 20 nF, a sampling distance of 5–15 mm from the electrode gap, discharge frequencies of 1.5 and 500 Hz, and carrier gas flow rates of 0.5–8 l min^{-1}.

The TEM grids were mounted vertically aligned to the carrier gas flow onto a piece of silicon wafer, which in turn was clamped to the pneumatic arm. The positioning of the TEM
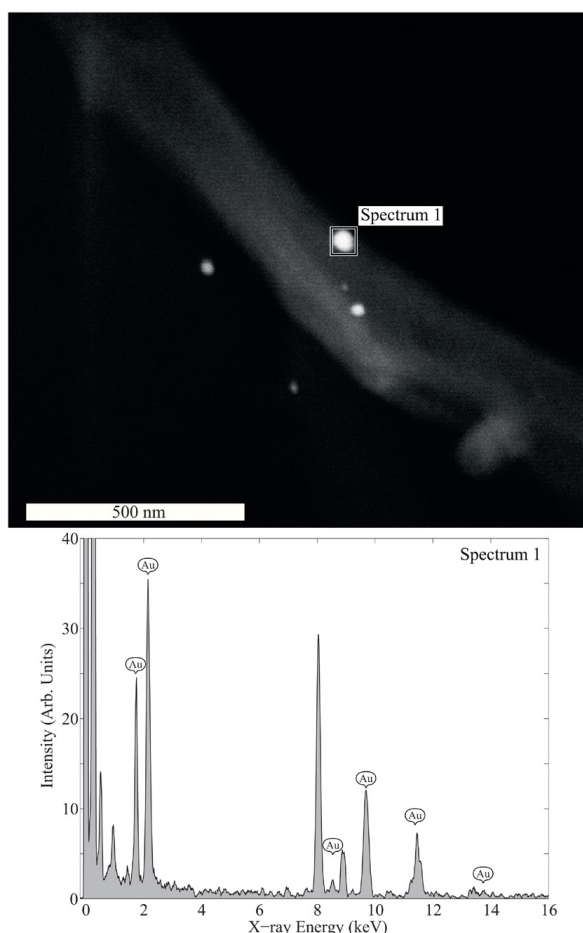
Figure 3. STEM micrograph and EDX spectra.

grid was adjusted to match a set distance from the center of the electrodes to the center of the TEM grid. As soon as the spark was ignited the arm was inserted beneath the electrode gap and stayed in the extended position for a set number of discharges. Afterwards the arm was retracted and the spark was immediately turned off. The particle diameter and composition were measured.

Reference particles produced under the same conditions were deposited on TEM grids placed inside the electrostatic precipitator placed far downstream in the system (figure 1) for 1 h for 0.5 lpm and 8 lpm gas flow. The primary particle diameter in the deposited agglomerate particles was measured, and compared to the measured singlet particles on the TEM samples collected using the proximity sampler.

Analysis of the TEM samples was performed with a 300 kV high resolution TEM (JEOL 3000F) equipped with a field emission gun and an x-ray energy dispersive spectrometer (XEDS) for elemental analysis. The composition of the sampled particles was confirmed using XEDS to make sure that nothing but gold particles was deposited on the TEM grids. High-resolution images of the collected particles were acquired and the images were analyzed using ImageJ. On the order of 250 particles were measured for each sample.

3. Results and discussion

The custom-made proximity sampler proved highly useful for collecting TEM samples displaying the initial stages of particle formation. To find optimal sampling conditions several settings were tested. The distances to the electrodes were adjusted to assure a good yield on the samples. The counter electrode and sampler were both kept grounded which means that the distance

from the sampling arm to the high voltage electrode must be greater than from the high voltage electrode to the counter electrode. In all experiments an inter electrode distance of 2 mm was used with electrodes of 3 mm in diameter. If the sampler were perfectly aligned in the center of the electrodes this would give an approximated minimum vertical distance of 1.73 mm to the top of the inserted sampling arm. The total distance to the center of the TEM grid would then be 4.73 mm.

In order to find conditions where striking sparks do not destroy the TEM grid, we tested different distances. A 5 mm distance was tested but it was clear that the spark sometimes struck the TEM grid, which destroyed the sample. Physical limitations of the chamber gave a maximum distance of 15 mm but at this distance some agglomerates were deposited on the grid, possibly due to recirculation of material in the chamber. A distance of 9 mm (electrode center to TEM grid center) was found to be a good compromise with the spark striking the sampler only on rare occasions while maintaining a homogeneous sample.

Sampling during a high frequency discharge made it difficult to get controllable amount of particles deposited on the TEM grid. At discharge rates around 500 Hz the deposited numbers of particles was often far too low or in some cases even too high for proper analysis of the samples. The sampling time in these cases were on the order of 500 ms. Going up in sampling time to increase the deposition often resulted in a spurious spark hitting the sampler destroying the TEM grid. This was more common at higher discharge frequencies. The short sampling time made it difficult to accurately determine how many discharges that occurred during the sampling period, something that might be crucial in order to be able to correctly interpret the results.

In order to study the influence of the number of sampled discharges a lower frequency but with much longer sampling times, 5–70 s, were found to suit the purpose of getting manageable amounts of particles deposited while keeping track of the number of sampled discharges. Even at as low as 5 sampled discharges there was still enough material deposited on the grid to perform analysis of the particle size. At 100 sampled discharges on the same grid we did not observe an overloading of particles.

The composition of the sampled particles were verified by EDX analysis in STEM mode and confirmed to be 100% gold, as seen in figure 3. High resolution TEM was performed to investigate the crystallinity of the sampled particles, a 3 nm particle sampled at a carrier gas flow of 8 lpm can be seen in figure 4.

No significant difference was found comparing singlet diameter for a varied sampling time. Means of singlet diameter between samples collected during varied sampling time, i.e. number of discharges, but otherwise the same sampling conditions shows no significant difference when comparing samples from between 5, 20, 50, and 100 sparks, equal to a sampling time range from 1.4 to 70 s. Using this knowledge, samples from different sampling times were combined together to form a sample size of about 1000 measured particles for 0.5 and 8 lpm carrier flow rate to get a better estimate of the carrier flow effect on the mean diameter. This was compared to the mean diameter of the reference samples, i. e. the particles deposited
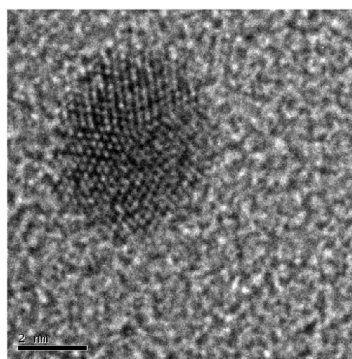
Figure 4. HR-TEM of proximity sampled Au particle.

downstream in the electrostatic precipitator (see figure 1). Significant difference was found comparing mean of the diameter for combined samples of proximity sampled particles and particles deposited downstream under the same generation conditions. For 0.5 lpm the diameter of the proximity-sampled particles were measured to 2.97 nm compared to the deposited reference sample where the primary particles had a diameter of 5.90 nm. Comparing samples from 8 lpm, the average diameter of the singlets were 2.58 nm and the reference measured an average primary particle diameter of 4.50 nm. Examples of sampled particles from $0.5 \, l \, min^{-1}$ and $8 \, l \, min^{-1}$ can be seen in figure 5, and of reference particles in figure 6. Measured size distributions for both sampled particles and reference particles can be seen in figure 7. The fitted curves in figure 7 are based on the histograms in the same figure. They are all normalized to have an integrated area of 1, therefore the height difference indicate a difference in polydispersity and not necessarily a decreased concentration.

No significant growth of the particle diameter could be seen with an increasing number of sampled discharges indicating that the particles mainly form before depositing on the TEM grid, see figure 8. A difference in particle diameter with an increasing carrier flow could be related to two effects. It could be a result of an increased quenching rate and dilution of the metal vapor. It could also be related to the fact that the gas and particles are transported more rapidly to the sampling site and thus have less time to gather material resulting in a decrease in particle diameter. By changing the carrier flow rate the size of the primary particles in the final agglomerates can be tuned, via the tuning of singlet diameter. This is highly useful for certain applications where particle size play an important role, one example being for catalysis.

4. Conclusions

In this article we present a TEM sampler that gives the possibility to sample material from the initial stage of nanoparticle formation in a spark discharge generator. The sampler is constructed to have a controlled and variable residence time to enable sampling of a set number of discharges. It
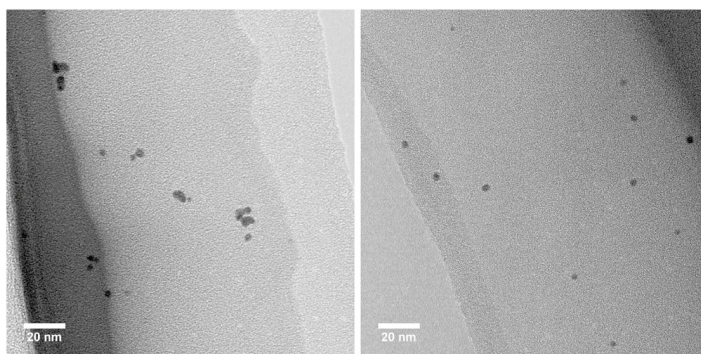
Figure 5. TEM images of sampled gold particles at carrier gas flow of $0.5\,l\,min^{-1}$ (left) and $8\,l\,min^{-1}$ (right).
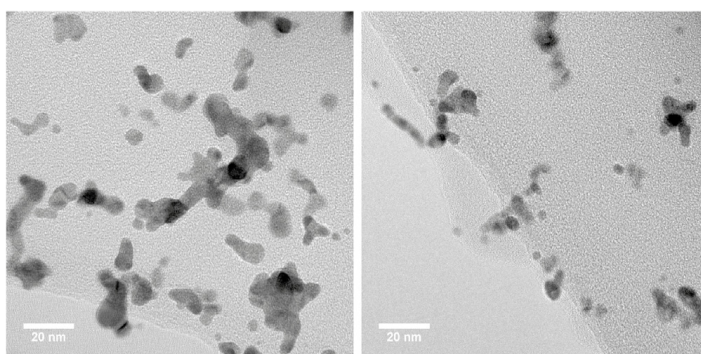
Figure 6. Overview TEM images of deposited reference samples at carrier gas flow of $0.5\,l\,min^{-1}$ (left) and $8\,l\,min^{-1}$ (right).
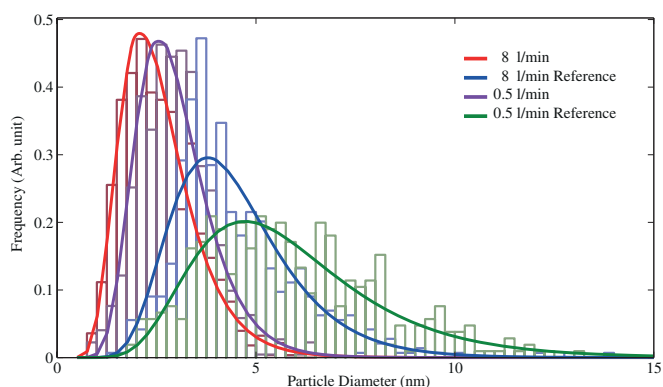
Figure 7. Size distributions (fit and data) for sampled particles and deposited reference particles. The curves are fitted log-normal distributions and the bars are the binned raw data from the TEM analysis.

is also constructed to have a leak-tight connection to the SDG, something that is highly important for the production of metal nanoparticles. We believe this sampler will be useful for sampling in other particle-generation systems as well, with only minor adjustments to for example the connection parts.
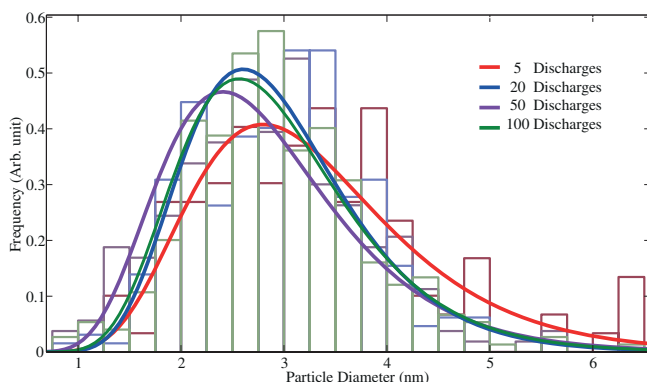
Figure 8. Particle size distributions for varied number of discharges. The curves are fitted log-normal distributions and the bars are the binned raw data from the TEM analysis.

Optimal sampling parameters have been discussed and the first images of singlet nanoparticles sampled in the vicinity of the spark have been shown. It is clear that there is a significant difference between the diameter of the singlet particles and the resulting primary particles. By tuning the generation parameters the size of the singlet particles can be tuned which in turn enables tweaking of the final particle diameter.

To really understand these first steps of particle formation is crucial in order to further develop the SDG for optimal particle production. Experimental results, such as the ones presented here, should be combined with theoretical calculations to make sure the optimization is done in a controlled manner. When this is achieved up-scaling of the SDG by positioning several units in parallel is a promising route to mass production of metal nanoparticles in a cheap and environmentally friendly way.

References

[1] Braakhuis H M *et al* 2014 Physicochemical characteristics of nanomaterials that affect pulmonary inflammation. *Part. Fibre Toxicol.* **11** 18
[2] Schimmoeller B, Pratsinis S E and Baiker A 2011 Flame aerosol synthesis of metal oxide catalysts with unprecedented structural and catalytic properties *ChemCatChem* **3** 1234–56
[3] Wegner K and Pratsinis S E 2003 Scale-up of nanoparticle synthesis in diffusion flame reactors *Chem. Eng. Sci.* **58** 4581–9
[4] Buonapart-e 2012 Available from: www.buonapart-e.eu/
[5] Schwyn S, Garwin E and Schmidt-Ott A 1988 Aerosol generation by spark discharge *J. Aerosol Sci.* **19** 639–42
[6] Helsper C *et al* 1993 Investigations of a new aerosol generator for the production of carbon aggregate particles *Atmos. Environ.* **27** 1271–5
[7] Seipenbusch A *et al* 2003 Influence of the gas atmosphere on restructuring and sintering kinetics of nickel and platinum aerosol nanoparticle agglomerates *J. Aerosol Sci.* **34** 1699–709
[8] Borra J P 2006 Nucleation and aerosol processing in atmospheric pressure electrical discharges: powders production, coatings and filtration *J. Phys. D: Appl. Phys.* **39** R19–54
[9] Hontanon E *et al* 2013 The transition from spark to arc discharge and its implications with respect to nanoparticle production *J. Nanopart. Res.* **15** 1957
[10] Kreyling W G *et al* 2011 Generation and characterization of stable, highly concentrated titanium dioxide nanoparticle aerosols for rodent inhalation studies *J. Nanopart. Res.* **13** 511–24
[11] Roth C *et al* 2004 Generation of ultrafine particles by spark discharging *Aerosol Sci. Technol.* **38** 228–35
[12] Tabrizi N S *et al* 2009 Generation of nanoparticles by spark discharge *J. Nanopart. Res.* **11** 315–32
[13] Pfeiffer T V, Feng J and Schmidt-Ott A 2014 New developments in spark production of nanoparticles *Adv. Powder Technol.* **25** 56–70
[14] Palomares J M *et al* 2014 A time-resolved imaging and electrical study on the operation of a spark discharge nanoparticle generator *J Phys D: Appl Phys* (under review)
[15] Cai J, Lu N and Sorensen C M 1993 Comparison of size and morphology of soot aggregates as determined by light-scattering and electron-microscope analysis *Langmuir* **9** 2861–7
[16] Cho J and Choi M 2000 Determination of number density, size and morphology of aggregates in coflow diffusion flames using light scattering and local sampling *J. Aerosol Sci.* **31** 1077–95

J. Phys. D: Appl. Phys. **48** (2015) 314012

L Ludvigsson *et al*

[17] Arabi-Katbi O I *et al* 2001 Monitoring the flame synthesis of TiO₂ particles by *in situ* FTIR spectroscopy and thermophoretic sampling *Combust. Flame* **124** 560–72

[18] Lee J, Altman I and Choi M 2008 Design of thermophoretic probe for precise particle sampling *J. Aerosol Sci.* **39** 418–31

[19] Dobbins R A and Megaridis C M 1987 Morphology of flame-generated soot as determined by thermophoretic sampling *Langmuir* **3** 254–9

[20] Gröhn A J *et al* 2014 On-line monitoring of primary and agglomerate particle dynamics *J. Aerosol Sci.* **73** 1–13

[21] Kammler H K *et al* 2003 The effect of external electric fields during flame synthesis of titania *Powder Technol.* **135–136** 310–20

[22] Zheng H M *et al* 2009 Observation of single colloidal platinum nanocrystal growth trajectories *Science* **324** 1309–12

[23] Tai K *et al* 2013 Integration of microplasma with transmission electron microscopy: real-time observation of gold sputtering and island formation *Sci. Rep.* **3** 1325

[24] Krinke T J *et al* 2002 Microscopic aspects of the deposition of nanoparticles from the gas phase *J. Aerosol Sc.* **33** 1341–59

[25] Feng J *et al* 2014 A Simple Model for Nanoparticle Formation by Spark Ablation *Int. Aerosol Conf. (Busan, Korea)*

[26] Schmidt-Ott A 2015 *Sci. Rep.* Submitted

[27] Friedlander S K 1983 Dynamics of aerosol formation by chemical reaction *Ann. New York Acad. Sci.* **404** 354–64

[28] Pratsinis S E 1988 Simultaneous nucleation, condensation, and coagulation in aerosol reactors *J. Colloid Interface Sci.* **124** 416–27

[29] Witten T A and Sander L M 1983 Diffusion-limited aggregation *Phys. Rev.* B **27** 5686–97

[30] Meuller B O *et al* 2012 Review of spark discharge generators for production of nanoparticle aerosols *Aerosol Sci. Technol.* **46** 1256–70

[31] Lehtinen K E J, Windeler R S and Friedlander S K 1996 Prediction of nanoparticle size and the onset of dendrite formation using the method of characteristic times *J. Aerosol Sci.* **27** 883–96

[32] Messing M E *et al* 2009 Generation of size-selected gold nanoparticles by spark discharge - for growth of epitaxial nanowires *Gold Bulletin* **42** 20–6

[33] Messing, M E *et al* 2013 Gas-borne particles with tunable and highly controlled characteristics for nanotoxicology studies *Nanotoxicology* **7** 1052–63

Paper II

Characteristics of airborne gold aggregates generated by spark discharge and high temperature evaporation furnace: Mass–mobility relationship and surface area

C.R. Svensson [a,*], L. Ludvigsson [b], B.O. Meuller [b], M.L. Eggersdorfer [c], K. Deppert [b], M. Bohgard [a], J.H. Pagels [a], M.E. Messing [b], J. Rissler [a]

[a] Ergonomics and Aerosol Technology, Lund University, Box 118, SE-22100 Lund, Sweden
[b] Solid State Physics, Lund University, Box 118, SE-22100 Lund, Sweden
[c] Experimental Soft Condensed Matter, Harvard University, Cambridge, MA 02138, USA

ARTICLE INFO

ABSTRACT

The properties of gas-borne aggregates are important in nano-technology and for potential health effects.

Gold aggregates from three generators (one commercial and one custom built spark discharge generator and one high-temperature furnace) have been characterized. The aggregate surface areas were determined using five approaches – based on aggregation theory and/or measured aggregate properties. The characterization included mass–mobility relationships, effective densities (assessed by an Aerosol Particles Mass analyzer), primary particle analysis (based on Transmission Electron Microscopy), as well as total mass and number concentration outputs.

The relationships between mass and mobility are well described by power-law functions with exponents of 2.18–2.35. For all generators, the primary particles of the aggregates were fused together by a bridge with a diameter typically ~60–70% of the primary particle diameter (5–10 nm). The total mass outputs were 6.1–48.1 mg/m3 and the predicted surface area outputs in the range 0.9×10^{-3}–17×10^{-3} cm^2/cm^3.

The aggregate effective densities differed considerably between generators. The difference could partly be explained by the differences in primary particle diameter, but not fully. This in turn may be explained either by a varying primary particle size with aggregate size, or by that there are slight differences in the morphology of the aggregates from the generators.

1. Introduction

The properties of airborne agglomerates and aggregates are important for many reasons. It is known that exposure to airborne particulates, which often includes agglomerates/aggregates, can have adverse health effects (Barath et al., 2010; Dockery et al., 1993). To understand the toxicological effect of inhaling aggregates it is important to (I) have robust but variable methods available for controlled generation of airborne aggregates (for controlled toxicological tests) and (II) methods assessing the critical properties of the aggregated particles. Studies have shown that for various particle types the surface areas of the particles produce coherent dose-response relations, suggesting that the promoter of toxicity is the surface area rather than the mass or particle number inhaled (Aitken, Chaudhry, Boxall, & Hull, 2006; Donaldson et al., 2008; Waters et al., 2009). Hence it is of great importance to have readily available tools and models for calculating the surface area dose for aggregated particles, be it in a lab during toxicological studies, occupational exposure setting, or for other applications.

Apart from surface area of the aggregates/agglomerates, produced by for example flame spray pyrolysis, high temperature evaporation condensation or spark discharge, there are several other aggregate properties that needs to be thoroughly characterized such as the mass–mobility relationships, number/mass output, primary particle size (Dillon, Copley, Koos, Bishop, & Grobert, 2013; Heurlin et al., 2012; Messing, Dick, Wallenberg, & Deppert, 2009; Shin et al., 2009).

In this study, the term "agglomerates" is used when primary particles are held together by weak van der Waals forces, and "aggregates" is use for primary particles more strongly bound together by partial melting (DFG, 2013; Lövestam et al., 2010). We here let aggregate include agglomerates if we do not know which nomenclature if most descriptive. Note that the nomenclature of the structures is not used unambiguously in the literature and the two terms can be used interchangeably depending on the research field.

Assessing the surface area of non-spherical nanoparticles is not straightforward, and as of today there few ways of performing direct measurements. For most methods used the measured surface area will be intimately related to the method by which it was determined. Although methods that measure surface area on-line are available (Asbach, Fissan, Stahlmecke, Kuhlbusch, & Pui, 2009; Fierz, Houle, Steigmeier, & Burtscher, 2011; Ntziachristos, Giechaskiel, Ristimäki, & Keskinen, 2004; Wang et al., 2010), these were typically not developed for non-spherical and porous particles, and thus do not work in an optimal way for all types of aggregates (LeBouf et al., 2011). Also there is data suggesting that the techniques based on unipolar diffusion charging does not relate directly to the surface area of the aerosol particles as suggested (Gopalakrishnan, Thajudeen, Ouyang, & Hogan, 2013; Ku & Kulkarni, 2012; Ku & Maynard, 2005). Transmission electron microscopy (TEM) imagery is often used to characterize primary particle size (d_{pp}) of aggregates. On-line techniques such as the aerosol particle mass analyzer (APM) that coupled in a series after a differential mobility analyzer (DMA) determines the mass–mobility relationship, as well as particle effective density (ρ_{effd}), with a relatively high resolution in both time and size (Ehara, Hagwood, & Coakley, 1996; Olfert, Symonds, & Collings, 2007). This technique also allows one to distinguish between externally mixed particles of different effective densities (McMurry, Wang, Park, & Ehara, 2002; Rissler et al., 2014). Various techniques have been used for specific surface area characterization, whereof nitrogen adsorption, or Brunauer Emmett Teller (BET) is the most common (Brunauer, Emmett, & Teller, 1938). BET has been successfully used for nanoparticle surface area characterization (Eggersdorfer, Groehn, Sorensen, McMurry, & Pratsinis, 2012; Ku & Kulkarni, 2012). However, the technique can prove challenging for many applications and nanoparticle sources since it is offline and a relatively large amount of material is needed (min. ~10 mg). Furthermore, the whole particle population collected over a long period of time is characterized, as a whole.

TEM imagery has also been compared to BET measurements and suggested as a stand-alone off-line method for determining specific surface area (Bau, Witschger, Gensdarmes, Rastoix, & Thomas, 2010). A combination of on-line and off-line techniques have also been suggested for the determination of surface area of aggregates, such as that of combining aerosol particle mass measurements (DMA–APM) and basic TEM imagery (Rissler et al., 2012, 2013; Thajudeen, Jeon, & Hogan, 2015).

Another approach to assess surface area is from a theoretical point of view, combined with on-line or off-line techniques. An extensive effort have been made in the area of modeling properties of fractal structures formed by diffusion limited cluster aggregation (DLCA), mainly focusing on number of primary particles in aggregates in relation to the aggregate radius of gyration or mobility size (Chan & Dahneke, 1981; Eggersdorfer, Groehn, Sorensen, McMurry, & Pratsinis, 2012; Meakin, Donn, & Mulholland, 1989; Sorensen, 2011). Furthermore, effort has also been devoted to linking the mobility of aggregates to results from image analysis using TEM (Thajudeen et al., 2015). Eggersdorfer, Groehn, Sorensen, McMurry, and Pratsinis (2012) suggest predicting surface area from DMA–APM measurements solely – for aggregates formed by DLCA. There is also considerable work put into describing the properties of aggregates by using a purely theoretical approach (Chan & Dahneke, 1981; Dahneke, 1982).

The aim of this study is to compare number, mass and surface area output concentrations of gold aggregates generated by three methods. These methods were a high temperature furnace (HT), a commercial spark discharge generator (SDG_P), and a novel in-house constructed spark discharge generator (SDG_C). This was accomplished by a detailed characterization regime in combination with theory and semi-empirical models. The instruments used for characterization were: a transmission electron microscopy (TEM), a Differential mobility analyzer – aerosol particle mass analyzer (DMA–APM), and a differential mobility particle sizer (DMPS).

Fig. 1. Overview of the generation and characterization system for the Au aerosols by spark discharge and high temperature evaporation.

The measured particle characteristics were used in combination with 5 approaches to estimate the total surface area output of the generators. The approaches are based on the combination of on-line and off-line techniques and aggregation models:

(I) Mass–mobility data in combination with TEM imagery.
(II) Theory describing the mass of aggregates in combination with TEM imagery.
(III) Mass–mobility data in combination with semi-empirical theory.
(IV) Lall and Friedlander (2006) theory in combination with TEM imagery.
(V) Assumption of spherical particles.

In addition to the primary aim, size dependent properties of the aerosols were determined and compared. These properties include primary particle diameter, bridging between the primary particles, the size dependent effective density, the mass–mobility relationship, and aggregate number size distributions.

The systems have been applied in several biological applications such as deposition in biological fluids studying aggregation and protein corona (Svensson et al., 2013). The HT and SDG$_P$ has also been evaluated with regards to surface area and mass output for air liquid interface studies (Messing et al., 2012). The SDG$_C$ has recently been used in in vivo inhalation studies (manuscript).

The data that this study is based upon is publicly available through Swedish National Data Service (SND, www.SND.gu.se/en) by doi:10.5878/002624.

2. Material and methods

2.1. System setup

The particles were generated using three different systems: a commercially available spark discharge unit, SDG$_P$ (Palas CFG 1000), a custom built spark discharge unit, SDG$_C$, and a high temperature evaporation/condensation furnace (HT) (Scheibel & Porstendorfer, 1983). The setup included a β-emitting ^{63}Ni source (Neutralizer) (Wiedensohler, 1988); two differential mobility analyzers (one long TSI Inc. model 3081) and a custom built Vienna type DMA (Knutson & Whitby, 1975) allowing the selection of a quasi-monodisperse aerosol; a sintering tube furnace (Karlsson et al., 2005) for sintering of aggregates into spherical particles (SINT); an aerosol particle mass analyzer (APM, Kanomax model APM-3600) (Ehara et al., 1996) in series after a DMA; an electrometer (TSI Inc. model 3068B) and a condensation particle counter (CPC) (model 3760, TSI Inc.) for particle detection; and an electrostatic precipitator (ESP)(Deppert, Schmidt, Krinke, Dixkens, & Fissan, 1996) for collection of the particles unto TEM grids. An overview of the generation system is presented in Fig. 1.

The aerosol flow rate was held constant throughout the main part of the system at 1.7 l/min. The flow rate through the SDG$_C$ is variable but here kept at 1.7 l/min and for SDG$_P$ set at either 2.9 or 3.7 l/min. The excess flow rate over 1.7 l/min was released into the atmosphere through a filter. The flow rate for the HT was constant at 1.7 l/min. The aerosol flow through the APM and the CPC was 0.85 l/min and the remaining flow was led through the electrometer and/or ESP. At any given time during experiments aggregates where only characterized or sampled from one of the generation methods i.e. HT, SDG$_C$ or SDG$_P$.

2.2. Particle generation

The SDG$_P$ system was originally designed for the controlled generation of soot particles using graphite electrodes. The systems has a variable carrier gas flow rate and the spark generation frequency can be varied between 0 and 300 Hz (Schwyn, Garwin, & Schmidtott, 1988). For the course of our experiment the system was refitted with gold electrodes and the carrier gas flow was nitrogen gas, $> 99.9\%$ in purity (Messing et al., 2009), the carrier gas was the same for the SDG$_C$ and HT experiments. During operation, the inter electrode distance in SDG$_P$ are controlled automatically via the discharge voltage, which may change with a changed carrier gas flow. For the SDG$_P$ two different carrier gas flows were used (2.9 and 3.7 l/min).

The SDG$_C$ was designed based on the principle of the SDG$_P$ but with implementations from previous work (Meuller et al., 2012; Tabrizi, Xu, van der Pers, Lafont, & Schmidt-Ott, 2009; Tabrizi, Xu, van der Pers, & Schmidt-Ott, 2010; Tabrizi, Ullmann, Vons, Lafont, & Schmidt-Ott, 2009). The SDG$_C$ was designed to be able to deliver oxide free metal nanoparticles and has therefore a need to be more leak tight compared to the SDG$_P$, and hence, was designed with all vacuum compatible parts made of stainless steel. The chamber and power feed were redesigned to increase control over generation parameters, such as electrode distance, charging current, electrical capacitance, and gas flows. The inter-electrode distance control was improved in SDG$_C$ by the adding a manual linear actuator to the ground electrode. This enables electrode distance adjustments before and during operation. Furthermore, the energy per discharge was increased as well as discharge frequency, creating a larger particle output. In this study, the SDG$_C$ was not running on settings generating the maximal output. SDG$_C$ is a mobile, single unit instrument with all post particle production processing built in. The SDG$_C$ was fitted with gold electrodes for the course of this study.

The HT system utilizes high temperature evaporation of bulk material inside a graphite cylinder, followed by nucleation and aggregation as the temperature decreases. The HT system uses a constant carrier gas flow of 1.7 l/min while two different generation settings were achieved by using two different furnace temperatures of 1575 °C and 1625 °C, these two settings are in this study referred to as HT 1575 and HT 1625. For the course of the experiments in this study the bulk material in the HT was gold.

2.3. DMPS measurements

Differential mobility particle sizer (DMPS) measurements were performed on all aerosols generated. Scans were performed using DMA1 in the set-up in combination with an electrometer, Fig. 1. The aerosol particles were lognormal distributed and the count median diameter (CMD), geometrical standard deviation (GSTD) and total particle number were calculated.

2.4. DMA–APM measurements

The DMA–APM was used for on-line mass determination of mobility-classified particles. A DMA selects particles of one mobility diameter at a time and the mass distribution of the selected particles is determined by the APM. The APM consists of two concentric cylinders rotating at the same angular speed, where the particles are kept in orbit by an electric field (Ehara et al., 1996). Only particles of a specific mass to charge ratio passes the APM and is quantified by the CPC.

$$\frac{m}{q} = \frac{V}{r_c^2 \cdot \omega^2 \cdot \ln\left(\frac{r_2}{r_1}\right)} \tag{1}$$

where r_c is defined as

$$r_c = \frac{(r_1 + r_2)}{2} \tag{2}$$

here m is the particle mass, V is the voltage between the rotating cylinders, ω is the angular velocity, q is the elemental charge, and r_1 and r_2 are the inner and outer cylinder diameter, respectively.

During each APM scan, the mass distribution of the quasi mono disperse particles selected by the DMA was determined by stepping the APM voltage while keeping the rotational speed constant. The voltage at which the distribution peaks was determined by fitting a normal distribution function to the spectra. This is equivalent to how the analysis was done in previous studies of unimodal mass distributions (Rissler et al., 2012, 2013). The particle mass was determined by inserting the fitted voltage into Eq. (1), assuming singly charged particles. For aggregated particles doubly charged aggregates might lead to artifacts (Rissler et al., 2013). The effect of doubly charged particles was investigated prior to the analysis but proved not to be an issue, mainly due to the relatively small aggregate size distribution. The effects of doubly charged particles are mainly governed by the aggregate particle number size distribution and the size selected by the DMA.

For the SDG$_P$ and HT, the APM measurements were performed on monodisperse aerosol fractions in the size range 15–80 nm selected with DMA1. For the SDG$_C$ particles selected covered the size range 40–300 nm. For those measurements a DMA (Model 3071, TSI Inc.) was used for the selection of monodisperse size fractions.

Suspensions of spherical polystyrene latex particles (PSL, Duke Scientific Inc., USA) of sizes 50, 80, 150, 250 and 350 nm were nebulized with an atomizer (Model 3076, TSI Inc.) and used for calibrating the DMA–APM according to the procedure
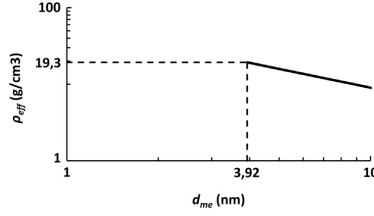
Fig. 2. Principle of the method for primary particle size determination from DMA–APM, as proposed in Charvet et al. (2014).

described by McMurry et al. (2002). During the calibration, the known inherent density of 1.05 g/cm^3 was used to determine the DMA–APM correction factor.

2.5. Primary particle analysis

The aggregate primary particles were analyzed concerning size and bridging/necking. Furthermore, the primary particle diameter was estimated from DMA–APM data according to methods described in Charvet, Bau, Paez Coy, Bémer, and Thomas (2014) and Eggersdorfer, Groehn, Sorensen, McMurry, and Pratsinis (2012).

2.5.1. Primary particle size from TEM analysis

Monodisperse aggregates of mobility diameter (d_{me}) 60 nm were selected using a DMA for each of the generation method settings. The aggregates were deposited onto carbon coated Cu TEM grids glued onto semiconductor silicon substrates and analyzed by TEM using an electrostatic precipitator (ESP). The rationale behind depositing only 60 nm nanoparticles was a trade-off suiting all generators with varying distributions and output of the aggregates generated.

A total of 310–604 primary particles for each of the generation method settings were analyzed using ImageJ software (Rasband, 1997–2012). The average (μ) of the cumulative distributions was determined numerically for the number weighted, surface area weighted, and mass weighted primary particle size distributions. Also based on the primary particle distribution the Sauter primary particle size was calculated ($d_{va\text{-}TEM}$):

$$d_{va-TEM} = \frac{\sum \left(N_{pp(d_{pp})} \cdot d_{pp}^3 \right)}{\sum \left(N_{pp(d_{pp})} \cdot d_{pp}^2 \right)} \tag{3}$$

where N_{pp} is the number of primaries quantified.

2.5.2. Primary particle size from DMA–APM

As suggested in Charvet et al. (2014) the primary particle diameter can be estimated by extrapolating the mass–mobility relationship according to a fitted power-law from the bulk density of gold (d_{APM}), Fig. 2. The uncertainty in d_{APM} was also quantified based on the extrapolation.

Eggersdorfer, Groehn, Sorensen, McMurry, and Pratsinis (2012) also suggest a method to determine d_{pp} from DMA–APM data ($d_{va\text{-}APM}$) described in Section 3.2.4. Note that the method suggested in Approach I for estimation of surface area from DMA–APM does only use DMA–APM for mass estimation while TEM-imaging for primary particle size.

2.5.3. Bridging/necking

The degree of bridging between the primary particles was determined for all five conditions investigated. This was performed by measuring the width of the bridge and the two adjacent primary particles (Fig. 3A).

The diameter of the bridge (d_b) was only measured when two clearly identifiable primary particles could be seen on either side, referred to Eq. (4) as d_{pp1} and d_{pp2}. The degree of bridging, the bridging ratio, b_r, was determined as:

$$b_r = \frac{d_b}{\left(\frac{d_{pp1} + d_{pp2}}{2}\right)}. \tag{4}$$

3. Theory and models

This section describe the methodology in quantifying and calculating the mass–mobility relationship, the effective density and the dynamic shape factor. Furthermore, the four approaches used for calculating the surface area for aggregates and for the aggregate distributions are presented. The methods used here are partly based on diffusion limited cluster aggregates (DLCA) according to Eggersdorfer, Groehn, Sorensen, McMurry, and Pratsinis (2012), Lall, Rong, Mädler, and
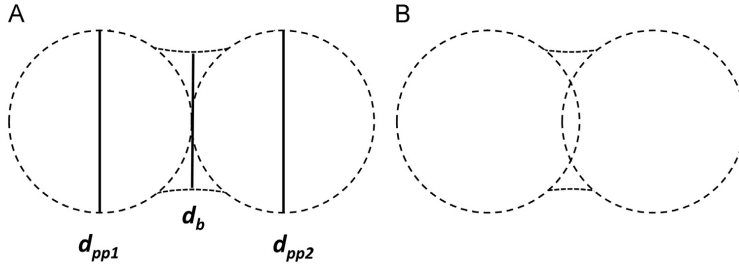
Fig. 3. Principle for bridging determination of the aggregates. (A) and (B) illustrate two ways of approaching the how the bridging between the primaries is formed – either by material condensing after agglomeration (A) or by fusing after agglomeration (B). The two geometries are used in the bridging sensitivity study.

Friedlander (2008) and Sorensen (2011). Furthermore, a method proposed by Rissler et al. (2013) is also used that is not restricted to aggregates formed by DLCA, but would apply to all types of aggregates. In short, this latter approach suggests to estimate the primary particle size is obtained by TEM and combined this with the aggregate mass measured by DMA–APM to calculate its corresponding surface area. This is similar to the method suggested by Bau et al. (2010) with the difference that the aggregate number of primaries (or related to mass when knowing the density of the primary particles) was estimated from aggregation theory.

3.1. The mass–mobility relationship, effective density and shape factor

Numerous studies have shown that the relation between the mobility diameter (d_{me}) and the mass of airborne aggregates formed by diffusion can be described by a power law (such as Park, Kittelson, and McMurry (2004), Rissler et al. (2013)) according to

$$m_{agg}(d_{me}) = k \cdot d_{me}^{D_{mm}} \tag{5}$$

D_{mm} is here referred to as the mass–mobility exponent (in previous studies often referred to as the fractal/mass-fractal dimension), the k in the mass mobility relation is in this study referred to as k-factor.

The effective density (ρ_{eff}) and shape factor (χ) were calculated from the mass–mobility relationship measured by the DMA–APM. The ρ_{eff} is calculated as the ratio of the aggregate mass over the mobility equivalent volume:

$$\rho_{eff} = \frac{6 \cdot m_{agg}(d_{me})}{\pi \cdot d_{me}^3} \tag{6}$$

The χ is calculated as the ratio of the Stokes force (F), or friction factor (f) multiplied by velocity (V), for aggregates (F_{agg}) over volume equivalent spheres (F_{ve}) according to

$$\chi = \frac{F_{agg}}{F_{ve}} = \frac{f_{agg} \cdot V}{f_{ve} \cdot V} = \frac{d_{me} \cdot C_{ve}}{d_{ve} \cdot C_{agg}} \tag{7}$$

The Cunningham slip correction, C, is calculated for the aggregates mobility size, d_{me}, and volume equivalent, d_{ve}, respectively.

3.2. Surface area content

By combining the size dependent surface area of a single aggregate, $SA_{agg}(d_{me})$, (achieved through the three approaches described below) with the mobility number distribution of the corresponding aerosol, the surface area distribution can be calculated:

$$dSA_{agg}/d \log d_{me} = SA_{agg}(d_{me}) \cdot dN/d \log d_{me} \tag{8}$$

The total surface area of the aerosol, SA, is calculated by summing the surface area of each size interval according to

$$SA = \sum \frac{dSA_{agg}(d_{me})}{d \log d_{me}} \cdot d \log d_{me} \tag{9}$$

The total mass of the aerosols can be calculated in the same fashion by replacing SA_{agg} with m_{agg} in Eq. (8) and performing the calculation in Eq. (9).

In addition to the three approaches presented in Sections 3.2.2–3.2.5 the surface area was calculated by assuming the mobility diameter was equal to the geometric diameter i.e. assuming that the particles were spherical. For each method and setting the Au aerosol size distribution was used to calculate the total surface area using the described models/approaches.

3.2.1. Specific surface area – SSA

The specific surface area is in Approaches I and II estimated from analysis of TEM imagery (SSA_{TEM}) using the method proposed in Bau et al. (2010). The method does to the first approximation not consider overlap of the primaries. $d_{va\text{-}TEM}$ is calculated from the primary particle distribution as described in Eq. (3), and SSA_{TEM} according to

$$SSA_{TEM} = \frac{6}{\rho_{Au} \cdot d_{va-TEM}}.$$ (10)

3.2.2. Approach I – Bau and Rissler

By multiplying the TEM-derived specific surface area, SSA_{TEM}, by the size dependent aggregate mass, achieved through the DMA–APM measurements, $SA_{agg}(d_{me})$ is calculated for the aggregates as a function of mobility diameter according to

$$SA_{agg}(d_{me}) = SSA_{TEM} \cdot m_{agg}(d_{me})$$ (11)

The method was first suggest by Rissler et al. (2012) and is not restricted to work for aggregates formed by DLCA, but would apply to all types of aggregates – also those formed by dustiness.

3.2.3. Approach II – Bau and Sorensen

A general theoretical approach is suggested in Sorensen (2011) for the calculation of the primary particle number in aggregates. The primary particle number, as function of mobility size, can then be translated into both mass and surface area.

For fractal aggregates formed by DLCA, as in the experiments of this study, the relationship between the aggregate primary particle numbers N, d_{me} and d_{pp} in the free molecular regime is proposed to be

$$d_{me} = d_{pp} \cdot N^{0.46}$$ (12)

In the slip transition regime for Knudsen number ($0.1 < Kn < 10$) the following relation between d_m, d_{pp} and N is suggested:

$$d_{me} = d_{pp} \cdot \left(10^{-2 \cdot x + 0.92}\right) \cdot N^x$$ (13)

where x is calculated, from the Kn of the mobility diameter and mean free path as

$$x = 0.51 \cdot Kn^{-0.043}$$ (14)

By multiplying the aggregate mass (achieved from the number of primaries multiplied by their individual mass) with SSA_{TEM}, the surface area of the aggregate is calculated as

$$SA_{agg}(d_{me}) = SSA_{TEM} \cdot m_{agg}(d_{me}) = SSA_{TEM} \cdot N(d_{me}) \cdot m_{pp}$$
$$= SSA_{TEM} \cdot N(d_{me}) \cdot \left(\frac{\rho_{AU} \cdot \pi \cdot d_{pp}^3}{6}\right)$$ (15)

For the calculation of primary particle mass, m_{pp}, the surface area weighted, d_{pp}, from the TEM analysis was used, as was the bulk gold density 19.3 g/cm³ (ρ_{AU}).

3.2.4. Approach III – Eggersdorfer

This approach utilize DLCA theory and DMA–APM data to calculate the surface area of the aggregates (Eggersdorfer, Groehn, Sorensen, McMurry, & Pratsinis, 2012). The approach uses the Sauter diameter of the primary particles, $d_{va\text{-}APM}$, calculated as

$$d_{va} = \cdot \left(\frac{k_a \cdot \pi}{6 \cdot v} \cdot d_{me}^{(2 \cdot D_a)}\right)^{1/(2D_a - 3)}$$ (16)

The factors k_a and D_a are based on simulations of DLCA aggregates and are for this study set to 1 and 1.08, respectively. v is the aggregate volume determined from DMA–APM. The SSA_{APM} is then calculated as

$$SSA_{APM} = \frac{6}{\rho_{Au} \cdot d_{va}}$$ (17)

The aggregate surface area is calculated as the product of the SSA_{APM} and the aggregate mass from DMA–APM

$$SA_{agg}(d_{me}) = SSA_{APM} \cdot m_{agg}(d_{me})$$ (18)

The principle of the method is tested and valid for both diffusion limited and ballistic aggregation in the transition regime, it is also valid for degrees of sintering up to compact spheres. However, the constants used in Eq. (16) would then be different. The main assumption of the model is that the projected surface area of the aggregates, in the transition regime, is proportional to the drag force.

3.2.5. Approach IV – Lall and Friedlander mass and surface area

Another theoretical approach suggested for estimating aggregate mass and surface area, based on relating the migration velocity of spheres to that of aggregates with similar mobility, was suggested by Lall and Friedlander (2006) and Lall et al. (2008).

In this approach the total number of primary particles in an aggregate is calculated as

$$N(d_{me}) = \frac{12 \cdot \pi \cdot \lambda \cdot d_{me}}{c* \cdot d_{pp}^2} \tag{19}$$

The aggregate mass is then calculated as the number of primaries multiplied by their individual mass:

$$m_{agg}(d_{me}) = N(d_{me}) \cdot \rho \cdot \frac{\pi \cdot d_{pp}^3}{6} = \frac{2 \cdot \rho \cdot \pi^2 \cdot \lambda \cdot d_{pp} \cdot d_{me}}{c*} \tag{20}$$

Similarly, the aggregate surface is calculated as the number of primaries multiplied by their individual surface area

$$SA_{agg}(d_{me}) = SSA_{TEM} \cdot m_{agg}(d_{me}) = SSA_{TEM} \cdot \frac{2 \cdot \rho \cdot \pi^2 \cdot \lambda \cdot d_{pp} \cdot d_{me}}{c*} \tag{21}$$

The dimensionless drag force is denoted as $c*$. The mass and surface area distributions for the aerosols are then calculated using Eqs. (8) and (9).

The method is described as valid if the primary particle radius is much smaller than the mean free path; also bridging is neglected as well as shielding. Shielding is a phenomenon where part of the primary particles do not contribute to the Stokes drag of an aggregate.

For the calculation of primary particle mass, m_{pp}, the surface area weighted, d_{pp}, from the TEM analysis was used, as was the bulk gold density 19.3 g/cm^3 (ρ_{AU}).

4. Sensitivity analysis of bridging on specific surface area

In Approaches I and II, the calculation of surface area is based on the assumption that the primary particles in the aggregates are at point contact. Thus, the specific surface area is determined solely by the surface area of the primary particles – assuming aggregates following previous definitions (Lövestam et al., 2010). Since TEM images show that there are bridging between the primary particles, this is obviously an erroneous assumption. The ratio between the diameter of the bridge and the diameter of the adjacent primary particles is quantified by TEM image analysis.

To test the effect of bridging when determining the surface area according to Approach I (would result in similar effect in Approach II), described in Section 3.2.2., two geometrical views were compared. In method A we assume that the primary particles collide and that the bridge builds up as material condenses unto the aggregate (Fig. 3A), and in method B we assume that two primary particles collide and "melt" together (Fig. 3B). That means that the mass of the bridge is constituted of mass from the primary particles. It might be that the two methods describe aggregates formed in different processes. Likely gold particles, as used in this study, are described by method B.

5. Results and discussion

5.1. Aggregate characteristics

Results include total surface area and mass output, number size distribution and properties related to the mass–mobility relationships. The mass–mobility relationship is described by fitting D_{mm} and k in the associated power law, Eq. (5). The primary particle analysis is presented regarding size and bridging/necking. A sensitivity analysis of the specific surface area of aggregates is performed with regards to bridging between the primaries.

Examples of typical TEM images are shown in Fig. 4. A first order comparison of the aggregates analyzed show that all the methods and settings produce similar structures.

5.1.1. On-line characterization and surface area

For the SDG$_P$, the aerosol distribution statistics are not greatly affected by a change in the carrier gas flow rate from 2.9 to 3.7 l/min, while retaining the same spark generation frequency. To achieve a noticeable effect on particle size distribution, the carrier gas flow rate has to be increased or decreased to the extent that the coagulation rate is affected (Messing et al., 2009; Tabrizi, Ullmann, Vons, Lafont, & Schmidt-Ott, 2009). For the HT system the carrier gas flow was held constant (at 1.7 l/min) while the generation temperature was either 1625 or 1575 °C. With an increase in generation temperature, the CMD of the aggregate distribution increased, while the width of the distribution remained similar, Table 1. The increase in CMD is explained by an increased evaporation of particle material with temperature, material then available for forming the particles. Accordingly, the output with respect to mass strongly increases with increasing temperature. The mass output here being calculated using DMA–APM data in combination with DMPS. The total aggregate number did not increase as the generation temperature was increased. The HT had a higher output than the SDG$_P$ with regards to both number and mass concentration. The SDG$_C$ system had a similar output as the HT with respect to particle number concentration, while a
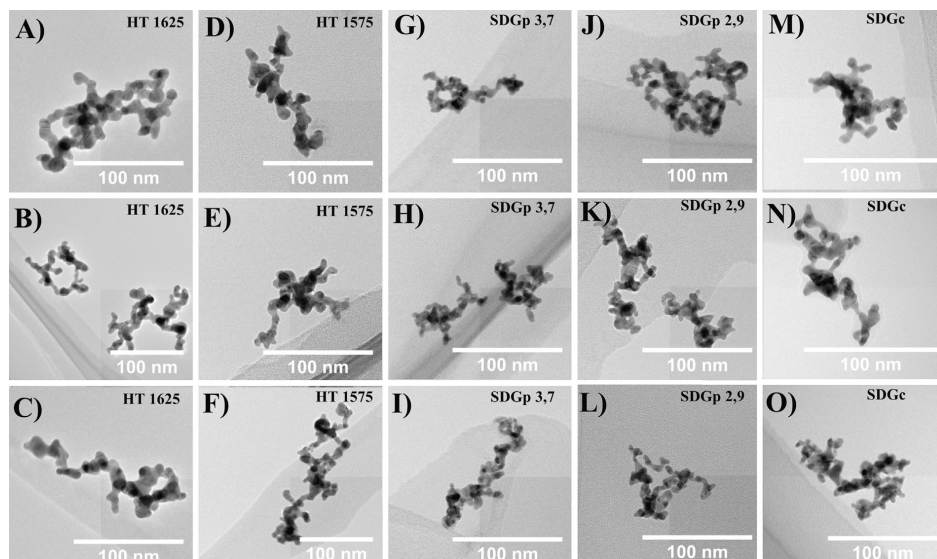
Fig. 4. TEM images of the generated aggregates: (A–C) HT 1625 aggregates, (D–F) HT 1575 aggregates, (G–I) SDG$_P$ 3,7 aggregates, (J–L) SDG$_P$ 2,9 aggregates, and (M–O) SDG$_C$ aggregates.

Table 1
Statistics of the aerosols based on DMPS and DMA–APM measurements. CMD is the count median diameter of the aggregate number size distribution, GSTD the geometric standard deviation and D_{mm} and k fitted parameters to the DMA–APM data (defined in Eq. (5)). The units for mobility diameter and mass used when fitting the parameters in the power law function are [m] and [kg] (SI units). The mass concentration is calculated from the measured number size distribution and mass–mobility relation.

	CMD (nm)	GSTD	Number conc. (#/cm³)	Mass conc. (mg/m³)	D_{mm} (95% CI)	k
HT 1625	74.8	1.80	9.28×10^7	48.1	2.35 (95% CI, 2.17–2.54)	54.7×10^{-3}
HT 1575	53.9	1.79	1.19×10^8	34.3	2.23 (95% CI, 1.93–2.52)	6.83×10^{-3}
SDG$_P$ 3.7	28.3	1.65	2.05×10^8	6.08	2.18 (95% CI, 2.11–2.26)	1.39×10^{-3}
SDG$_P$ 2.9	28.1	1.64	1.91×10^8	6.41	2.22 (95% CI, 2.16–2.28)	2.74×10^{-3}
SDG$_C$	78.4	1.92	8.62×10^7	25.0	2.24 (95% CI, 2.13–2.34)	5.23×10^{-3}

slightly lower mass output. The SDG$_C$ had a higher CMD and GSTD compared to both the SDG$_P$ and the HT systems for either setting. Thus, the lower mass output was mainly explained by the lower effective density of the aggregates (discussed later). One of the goals of the SDG$_C$ was to enable the generation of particles with broader size distributions then a commercially available SDG$_P$, and this result confirms that it is possible. The main reason for this is that the SDG$_C$ allows a higher energy input to each spark discharge. It should be mentioned that the out-put of the SDG$_C$ can be increased further by changing settings of the spark discharge.

The mass–mobility relationships (i.e. aggregate mass as a function of mobility diameter) were obtained for each of the systems and settings tested using the DMA–APM technique, Fig. 5. From the mass–mobility relationship, the effective density and dynamic shape factor was determined, defined in Eqs. (6) and (7), and also presented in Fig. 5.

The mass–mobility relationship of the aggregates could in all cases be described by a power law function, Eq. (5). The D_{mm} exponents ranged between 2.18 and 2.35 and are presented in Table 1. Most exponents found were very similar to that suggested in Sorensen (2011) of ∼2.2. One exception was the exponent of particles generated for HT 1625 with a slightly higher of 2.35. This could possibly be explained by the higher temperature during of the aerosol flow resulting in sintering and restructuration. The exponents did however not show any significant differences (CI 95%) between the methods and settings. The data suggest that in order to narrow the confidence interval of D_{mm}, as determined by DMA–APM, more considerations than simply extending the characterization interval should be taken. This is evident when examining the SDG$_C$, SDG$_P$ and HT D_{mm}, the characterization interval for the SDG$_P$ and HT was from 15 to 80 nm and SDGC from 40 to 300 nm. The characterization interval of the SDC$_C$ is in the order 2–3 times wider than SDG$_P$ and HT, while the width of the confidence intervals remain in the same size range.
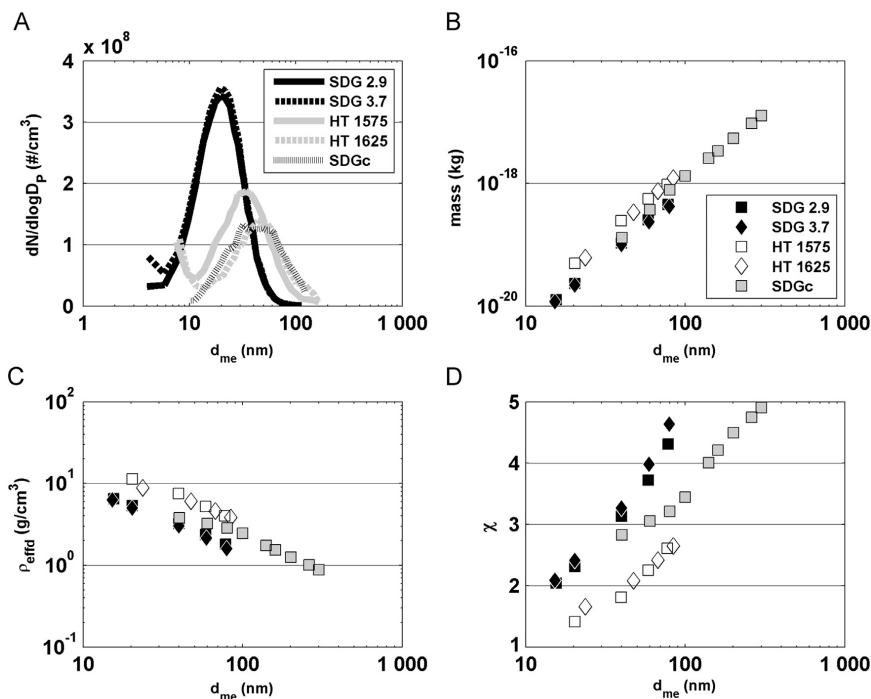
Fig. 5. (A) Aggregate mobility number size distributions for the generated aerosols, (B) mass–mobility relationships for SDGp, HT method and SDGc, (C) effective density, and (D) dynamic shape factor, χ, plotted versus mobility size.

The particle effective density ranged from 15.6 g/cm^3 for the smallest (15 nm) measured aggregates (measured only for the SDG$_P$ system), down to 0.8 g/cm^3 for the 400 nm particles, shown in Fig. 5C. The decrease in effective density over mobility sizes is expected if aggregated particles formed in a diffusion-limited process. Overall, the HT furnace generated more compact aggregates with the highest effective densities. In the size range where HT and SDG$_P$ overlap with SDG$_C$, the SDG$_C$ particle effective densities lay in-between the HT and SDG$_P$ settings (Fig. 5C). The same trends as for effective density is evident in the calculated shape factor (Fig. 5D), defined in Eq. (7).

The total mass of the aggregate distributions were in addition to that previously discussed, DMA–APM in combination with DMPS, calculated by two models based on aggregation theory, as well as when assuming spherical particles of density 19.3 g/cm^3 (gold). The number of primary particles per aggregate was calculated using the theory as described in Sorensen (2011) and that suggested in Lall et al. (2008), as described in Sections 3.2.3 and 3.2.5, and the aggregate mass was calculated as the sum mass of all primary particles in the aggregate. The total aerosol distribution was estimated combining the modeled aggregate mass with the aggregate number size distribution according to the DMPS. In this comparison we expect the DMA–APM derived aerosol mass to be close to the true mass, since based on the measurements only, with no assumptions regarding the aggregate type.

For SDG$_P$ the DMA–APM derived aerosol mass was comparable to that calculated using Sorensen (2011) theory, while the aerosol mass calculated using theory from Lall et al. (2008) was significantly lower for the SDG$_P$. For the HT settings the same trend is evident, DMA-based aerosol mass is the highest followed by that based on Lall et al. (2008) and Sorensen (2011) in declining order. As expected the aerosol mass based on the assumption of spherical particles resulted in the highest mass. This is due to the porous structure of the particles, reflected also in the shape factor and effective density, Fig. 5C and D.

The difference in aerosol mass modeled based on Lall et al. (2008) or on Sorensen (2011) has been observed earlier, and as pointed out in Eggersdorfer, Groehn, Sorensen, McMurry, and Pratsinis (2012) the model suggested in Lall et al. (2008) has several issues. For example, only part of the generated aerosols can be argued to be in the *Kn* regime as required by the Lall and Friedlander theory, that is the free molecular regime.

The differences in modeled aggregate mass based on Sorensen (2011) and the mass estimated based on DMA–APM measurements cannot be fully explained by the occurrence of bridging, explored in Section 5.1.2. Nor can it be explained by

measurement uncertainties of the DMA–APM. One possible explanation for the discrepancy between the DMA–APM based aerosol mass and that of Lall et al. (2008) and Sorensen (2011) could be that the aggregates selected for primary particle image analysis was not representative of the entire aggregate size distribution. Then, since the aggregate number size distributions were different for the different generators, the aggregates analyzed would represent a different fraction of the distributions with regards to primary particle size. This would affect both the Lall et al. (2008) and Sorensen (2011) based aerosol mass since the aggregate mass is the number of primary particles per aggregate, as calculated from the theory, multiplied with the mass of each primary particle (proportional to d_{pp}^3). In this study the TEM images was performed on aggregates of 60 nm mobility size for all methods and settings.

In short, the aggregate surface area was calculated by multiplying the size dependent aggregate mass with the specific surface area, Eqs. (11), (15), (18) and (21). The surface area of the individual aggregates is in turn multiplied with the number of aggregates in the size bin of the number size distribution Eq. (8). Finally, the sum of all bins is the total aerosol surface area of the aerosol, Eq. (9). The surface area of the aerosols were also calculated by assuming the mobility diameter was the true geometrical diameter, as described earlier.

For the SDG$_P$ settings the calculated surface area are similar for Approaches I–III and the approach based on the assumption of spherical particles, while Approach IV predict lower surface areas. For the HT settings and the SDG$_C$ the calculated surface area concentration are more divergent, illustrated in Fig. 6B. Still Approach IV predicts significantly lower values. Approach I predict the highest surface area concentration, followed by Approaches III and II, respectively. The larger differences in predicted surface area is partly explained by the larger size of the aggregates, for which the models differs more than for smaller aggregates.

The difference between Approaches I and III, with regards to total predicted surface area, is explained by the difference in SSA_{TEM} and SSA_{APM}. This is because both approaches use the same size dependent aggregate mass, as determined by DMA–APM. The difference in SSA between Approaches I and III can in turn be traced to the difference in the Sauter primary particle diameter based on TEM and theory (Eggersdorfer, Groehn, Sorensen, McMurry, & Pratsinis, 2012; Eggersdorfer, Kadau, Herrmann, & Pratsinis, 2012), Table 2. When comparing results from Approaches I and III it is clear that even small differences in the Sauter diameter result in substantial differences in total calculated surface area.

In contrast to that described in the previous paragraph, where differences in aerosol surface area could be explained by the used SSA, observed differences between Approaches I, II and IV is explained by the size dependent aggregate mass (as shown in Fig. 6A). Thus, the discussion between the mass predicted by DMA–APM, Lall et al. (2008), and Sorensen (2011) theory is relevant also for the total calculated surface area.

When here applying the surface area Approaches I, II and IV, the same definition of primary particle size is used with regards to SSA. However, it is important to note that depending on how primary particle size is defined, the resulting specific surface area will vary. For primaries of a narrow size distribution this is not an issue. However, most often the primary particles consist of a distribution with some broadening. Thus, how the d_{pp} achieved from the size distribution of primaries (i.e. weighted by nr, area or volume) is critical for the resulting estimate of total surface area. The same holds for estimating the mass of the primaries.

There is no praxis to date as to what weight or derivative from the primary particle distribution that consecutively should be used for surface area calculations, such as Sauter primary particle diameter and SSA.

5.1.2. Primary particle analysis and bridging

The primary particle size and the bridging between the primaries was determined for all generation methods and settings by TEM imagery and subsequent image analysis. Also the Sauter primary particle diameter was calculated from TEM measurements ($d_{va\text{-}TEM}$), Eq. (3). The Sauter diameter was then in its turn used to determine the specific surface area of aggregates (SSA_{TEM}), as presented in previous sections. Results from the primary particle analysis are summarized in Table 2. In addition, a method suggested by Charvet et al. (2014) was tested to predict the d_{pp} from the DMA–APM data as described in Section 2.5.2, here referred to as d_{APM}. Similarly, Eggersdorfer, Groehn, Sorensen, McMurry, and Pratsinis (2012) suggest a method to predict the Sauter primary particle diameter from the DMA–APM data, $d_{va\text{-}APM}$.

There is a clear difference in the diameter of the primaries with regards to the different generation methods, whereas the degree of bridging is similar.

Analysis of the primary particles, based on TEM, shows that the HT method results in the largest primary particles for all types of d_{pp} (nr, area and volume). The temperature of the furnace did not seem to affect the primary particle size to any great extent. The SDG$_P$ generator produced aggregates with a lower primary particle size than the HT method with regards to all approaches determining the primary particle size, and did not change considerably with the carrier gas flow rate in the flow range measured. The primary particle size of the SDG$_C$ by TEM was similar to that of the SDG$_P$ generator.

The primary particle size predicted from DMA–APM data (d_{APM}, $d_{va\text{-}APM}$) in general predict larger differences of the primary particles than what can be observed from the TEM image analysis. It is apparent that the similarity in primary particle size, as determined from TEM, for SDG$_P$ and SDG$_C$ aggregates is not present for d_{APM} and $d_{va\text{-}APM}$. This most likely reflect the effective densities (Fig. 5), where the effective density of the SDG$_C$ lies between that of SDG$_C$ and HT. The Sauter primary particle sizes calculated from DMA–APM, $d_{va\text{-}APM}$, are in general larger than those based on TEM, $d_{va\text{-}TEM}$, for HT and SDG$_C$. A possible explanation could be that the aggregates formed by the HT and SDG$_C$ are of a more compact structure than those formed by SDG$_P$, erroneously interpreted as larger primary particles.
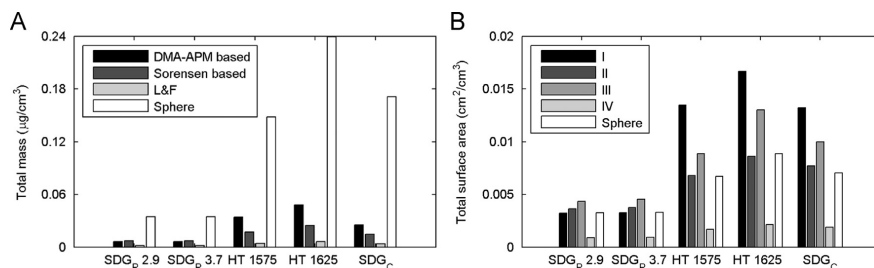
Fig. 6. (A) Comparison of calculated total mass of the characterized aerosols based on DMA–APM measurements to that of modeled using DCLA-theory of Sorensen (2011), Lall et al. (2008) and assuming that the particles are spherical with density 19.3 g/cm³. (B) The total surface area for each method and setting was calculated using each of the Approaches I–IV respectively, the approaches defined in Sections 3.2.2–3.2.5, including a calculation based on the assumption that the mobility diameter is the true physical diameter.

Table 2
Primary particle analysis and specific surface area based on TEM image analysis (i.e. on $d_{va\text{-}TEM}$) and DMA–APM data, as described in material and methods. N_{pp} refer to the number of measured primary particles for each generation method and settings. The average diameter (μ) is estimated both from number, surface area and mass weighted distributions.

Primary particle size, bridging analysis and *SSA* based on TEM

	N_{PP}	μ (nm $\pm$ std)			$d_{va\text{-}TEM}$	SSA_{TEM} (m²/g)	b_r (std)
		Nr	Area	Vol			
HT 1625	482	8.26 $\pm$ 2.07	8.68 $\pm$ 2.29	9.36 $\pm$ 2.26	8.98	34.63	0.70 $\pm$ 0.08
HT 1575	604	7.31 $\pm$ 1.69	7.71 $\pm$ 1.76	8.29 $\pm$ 1.78	7.92	39.24	0.64 $\pm$ 0.09
SDG$_P$ 3.7	373	5.41 $\pm$ 1.34	5.74 $\pm$ 1.41	6.11 $\pm$ 1.41	5.82	53.46	0.64 $\pm$ 0.11
SDG$_P$ 2.9	486	5.79 $\pm$ 1.32	6.11 $\pm$ 1.27	6.36 $\pm$ 1.35	6.20	50.18	0.62 $\pm$ 0.11
SDG$_C$	310	5.55 $\pm$ 1.35	5.83 $\pm$ 1.37	6.17 $\pm$ 1.32	5.89	52.74	0.66 $\pm$ 0.09

Primary particle size derived from DMA–APM data

	d_{APM}[a]		$d_{va\text{-}APM}$[b]	SSA_{APM} (m²/g)[c]
	(nm)	(nm $\pm$ SE)	(nm)	(m²/g)
HT 1625	7.34	$e^{(1.99 \pm 0.13)}$	11.49	27.06
HT 1575	10.74	$e^{(2.37 \pm 0.13)}$	12.01	25.89
SDG$_P$ 3.7	3.92	$e^{(1.37 \pm 0.07)}$	4.18	74.37
SDG$_P$ 2.9	3.92	$e^{(1.37 \pm 0.06)}$	4.58	67.88
SDG$_C$	5.76	$e^{(1.75 \pm 0.17)}$	7.80	39.86

[a] From measured effective density analysis and density of the pure compound according to the method suggested in Charvet et al. (2014).
[b] Method suggested in Eggersdorfer, Groehn, Sorensen, McMurry, and Pratsinis (2012).
[c] Based on $d_{va\text{-}APM}$.

In the model suggested in Charvet et al. (2014) to determine the primary particle size (d_{APM}), the power-law function fitted to the effective density over mobility diameter is extrapolated down to the size of the primary particles (i.e. when the effective density reaches the material crystal density). To our understanding, this assumption is acceptable for aggregates formed by DLCA, but only for $N > 100$ (Sorensen, 2011). Nevertheless, comparing the results of the d_{pp} predicted from DMA–APM they correlate relatively well, with the exception of the HT 1625.

5.1.3. Model sensitivity of bridging

The TEM image analysis shows that the ratio between the diameter of the bridge and adjacent primary particles was similar for all methods and settings tested, around 60–70% (b_r 0.6–0.7). Using this as input in a sensitivity study of bridging on estimated specific surface area, the assumption of point contact lead to an overestimation of specific surface area by ~20% (20% using method A and 22% for B). The effect of the bridging is calculated assuming the two geometries (A and B) resulting from the two assumptions of how the bridging is formed, described in Section 2.5.3. As can be seen the two assumptions resulted in similar values. Assuming the extreme – that the diameter ratio of the bridge and primary particles are unity – will result in an overestimation of the specific surface area by 50%.

Bau et al. (2010) also suggest a method to compensate for bridging in the determination of specific surface area from TEM image analysis by introducing an overlap coefficient. Estimating the corresponding overlap coefficient corresponding to a b_r of 0.6 and 0.7, respectively, assuming that the primary particles fuse together (method B), result in coefficients of 0.096 and

Table 3
Overview of the input needed (empirical or theoretical) for surface area estimations using the four different approaches.

Approach	I	II	III	IV
DMA–APM	X		X	
TEM	X	X		X
DLCA		X	X	X

0.134, respectively. Neglecting this overlap coefficient, results in overestimating the specific surface area by $\sim$14–21% (from the equations given by Bau et al. (2010), which is similar to the 20% achieved from the above approach.

When estimating the aggregate surface area based on aggregation theory using Approach II, the effect on surface area is more complex. The specific surface area will be affected in the same way as described above. However, also when predicting the aggregate mass–mobility relationship from aggregation theory, the bridging will come into account and shift d_{me} compared to that of pure aggregates. If the bridging is formed according to method A, the volume/mass of the aggregates will be underestimated using the assumption of point contact. This is because material condenses onto the aggregates after they have formed according to DLCA. On the other hand, d_{me} will be shifted towards larger sizes during the condensation process, and will counteract the total effect on the mass–mobility relationship. If instead the formation of the bridge is described by method B, the mass of a specific aggregate will be the same as that predicted by the theory; however d_{me} will in this case be shifted towards smaller mobility diameters during the fusing of the primary particles.

5.2. Discussion of surface area approaches

The surface area of individual aggregates as a function of d_{me} are calculated using the four approaches described in Section 2, as well as assuming spherical particles. An overview of the approaches and what they are based on is provided in Table 3.

When choosing an approach to estimate the surface area of an aerosol it is important to consider limitations, pros and cons, and of course the instruments that are available. Regarding Approaches II and IV an advantage is that a DMA–APM measurement is not needed. It does however require a primary particle image analysis, for example by TEM. In contrast, Approach III does not require a primary particle analysis, while it does require DMA–APM measurements of the aerosol.

Approach II is strictly limited to aggregates formed by DLCA with no following restructuring occurring. Approach III is limited to aggregates formed by DLCA and sintered by viscous flow, grain boundary or lattice diffusion. Many aerosol aggregate distributions have large portions that are not in the free molecular regime, for example combustion soot or welding fume, making Approach IV unsuitable. It is unlikely that these approaches (II, III and IV) describe the properties of aggregates formed from abrasion or dustiness, or aggregates that restructure upon, for example, humidification. Approach I requires both DMA–APM and primary particle image analysis. However, it is not limited to the shape of the aggregates and thus applies to aggregates of all forms and not only to aggregates formed by DLCA. Thus, the method can be used for all types of aggregates. In all approaches bridging needs to be considered, as discussed in Section 5.1.3.

6. Conclusions

The characteristics and output of gold aggregates generated by three methods at different settings were tested. The aggregates were investigated using both online techniques (DMPS, DMA–APM) as well as off-line (TEM). The generators used were a new custom-built spark discharge generator (SDG$_C$), a commercially available spark discharge system (SDG$_P$), and a high temperature evaporation furnace (HT). The output of the SDG$_C$, with respect to both mass and surface area was higher than for the SDG$_P$. Furthermore, the distributions were broader than for both the SDG$_P$ and HT. This, together with a compact system design, makes the new system preferable in a number of applications ranging from in vivo and in-vitro tests of toxicity to calibration of in-situ techniques – where it often is required to move the system between sites and in which a high output over a broad size range is preferable to allow tuning.

The mass–mobility relationship indicates that all characterized aerosols are highly aggregated. This is confirmed by TEM image analysis showing a typical diameter of the primary particles of 6–9 nm. The aggregates had clear bridges between the primaries (60–70% of the diameter of the primary particles), similar for all methods and settings tested. Analysis of the mass–mobility relation for the Gold aerosols showed that it can be well described by a power law with mass–mobility exponents in the range of 2.18–2.34. Interestingly the confidence interval (95%) show that they are not significantly distinguished between the methods i.e. no significant difference in D_{mm} can be asserted. With regards to reducing the uncertainty in D_{mm} it is clear that a wider span of DMA–APM characteristics does not on its own narrow the confidence interval.

The HT methods for both settings produce aggregates of a higher mass as compared to the other methods at a given mobility size. This property is also reflected in the effective density and the calculated shape factor. The higher effective densities can partly be explained by larger primary particle sizes. However, when comparing the measured effective densities with that estimated from aggregation theory (DCLA; Sorensen, 2011), it seems that the primary particle size does

not fully explain the observed difference. That the difference is due to difference in bridging can be ruled out and the deviation is larger than the uncertainty in the measured effective density. One hypothesis could be that the aggregates selected for primary particle image analysis is not representing the entire aggregate size distribution and that the primary particle size is not the same over the aggregate size distribution. One could also speculate that the properties of the aggregates formed in the different generator really have a difference in structure.

With regards to the predicted surface area of the characterized aerosols, the difference varied with at most a factor of 2 between the approaches, excluding Approach IV, for one and same generation method and setting. Including Approach IV there was as most a factor of 8 in difference for HT 1625, approach I highest with Approach IV predicting the lowest surface area.

For the SDG$_P$ settings the difference is surprisingly small for the calculated surface areas, excluding Approach IV, and is partly explained by the low CMD of the distributions. For distributions containing larger aggregates the differences is expected to be larger. Approach I predict a slightly lower total surface area for the SDG$_P$ aerosols as compared to Approaches II and III. However, for the HT and SDG$_C$ aerosols Approach I instead predict a considerably higher total surface area. The difference in predicted surface area between Approaches I, II and IV reflects the difference in aggregate mass, since the approaches use the same specific surface area SSA_{TEM} in their method. The difference between Approaches I and III is instead explained by the difference in specific surface, while they both use the same aggregate mass in the calculations.

As expected, since the generated aerosol was shown to be aggregated, the aerosol mass based on the assumption of sphericity was significantly higher as compared to that based on DMA–APM, Lall et al. (2008) and Sorensen (2011). The aerosol surface area based on the same assumption was comparable to the other approaches, especially Approach II.

In order to fully understand and describe the observations a more advanced image analysis technique could be very useful. This is because a large part of the investigated aggregates, as apparent from Fig. 4, cannot be described by primary particles. Furthermore, more TEM-samples would be needed, collected for aggregates of more than one mobility size. A more representative selection could be aggregates of the mobility diameter where each distribution peaks.

7. Data sharing

The data that this study is based upon is publicly available through Swedish National Data Service (www.SND.gu.se/en) by doi:10.5878/002624. Data available are those related to Fig. 5 i.e. mobility to mass/effective density/shape factor. Also data from the primary particle analysis using imageJ is appended for each of the methods.

It is the hope of the authors that the data will be a valuable asset and live on in research to come.

Acknowledgments

References

Aitken, R., Chaudhry, M., Boxall, A., & Hull, M. (2006). Manufacture and use of nanomaterials: current status in the UK and global trends. *Occupational Medicine*, *56*(5), 300–306.

Asbach, C., Fissan, H., Stahlmecke, B., Kuhlbusch, T., & Pui, D. (2009). Conceptual limitations and extensions of lung-deposited Nanoparticle Surface Area Monitor (NSAM). *Journal of Nanoparticle Research*, *11*(1), 101–109.

Barath, S., Mills, N.L., Lundback, M., Tornqvist, H., Lucking, A.J., & Langrish, J.P., et al. (2010). Impaired vascular function after exposure to diesel exhaust generated at urban transient running conditions. *Particle and Fibre Toxicology*, *7*(19), 1–11.

Bau, S., Witschger, O., Gensdarmes, F., Rastoix, O., & Thomas, D. (2010). A TEM-based method as an alternative to the BET method for measuring off-line the specific surface area of nanoaerosols. *Powder Technology*, *200*(3), 190–201.

Brunauer, S., Emmett, P.H., & Teller, E. (1938). Adsorption of gases in multimolecular layers. *Journal of the American Chemical Society*, *60*(2), 309–319.

Chan, P., & Dahneke, B. (1981). Free-molecule drag on straight chains of uniform spheres. *Journal of Applied Physics*, *52*(5), 3106–3110.

Charvet, A., Bau, S., Paez Coy, N., Bémer, D., & Thomas, D. (2014). Characterizing the effective density and primary particle diameter of airborne nanoparticles produced by spark discharge using mobility and mass measurements (tandem DMA/APM). *Journal of Nanoparticle Research*, *16*(5), 1–11.

Dahneke, B. (1982). Viscous resistance of straight-chain aggregates of uniform spheres. *Aerosol Science and Technology*, *1*(2), 179–185.

Deppert, K., Schmidt, F., Krinke, T., Dixkens, J., & Fissan, H. (1996). Electrostatic precipitator for homogeneous deposition of ultrafine particles to create quantum-dot structures. *Journal of Aerosol Science*, *27*(1001), 151–152.

DFG (2013). *Nanomaterials*. Wiley-VCH Verlag GmbH & Co. KGaA: .

Dillon, E., Copley, M., Koos, A.A., Bishop, P., & Grobert, N. (2013). Flame spray pyrolysis generated transition metal oxide nanoparticles as catalysts for the growth of carbon nanotubes. *RSC Advances*, *3*(43), 20040–20045.

Dockery, D.W., Pope, C.A., Xu, X.P., Spengler, J.D., Ware, J.H., & Fay, M.E., et al. (1993). An association between air-pollution and mortality in 6 United-States Cities. *New England Journal of Medicine*, *329*(24), 1753–1759.

Donaldson, K., Borm, P.J.A., Oberdorster, G., Pinkerton, K.E., Stone, V., & Tran, C.L. (2008). Concordance between in vitro and in vivo dosimetry in the proinflammatory effects of low-toxicity, low-solubility particles: The key role of the proximal alveolar region. *Inhalation Toxicology*, *20*(1), 53–62.

Eggersdorfer, M.L., Groehn, A.J., Sorensen, C.M., McMurry, P.H., & Pratsinis, S.E. (2012). Mass-mobility characterization of flame-made ZrO2 aerosols: Primary particle diameter and extent of aggregation. *Journal of Colloid and Interface Science*, *387*, 12–23.

Eggersdorfer, M.L., Kadau, D., Herrmann, H.J., & Pratsinis, S.E. (2012). Aggregate morphology evolution by sintering: number and diameter of primary particles. *Journal of Aerosol Science*, *46*, 7–19.

Ehara, K., Hagwood, C., & Coakley, K.J. (1996). Novel method to classify aerosol particles according to their mass-to-charge ratio – Aerosol particle mass analyser. *Journal of Aerosol Science, 27*(2), 217–234.
Fierz, M., Houle, C., Steigmeier, P., & Burtscher, H. (2011). Design, calibration, and field performance of a miniature diffusion size classifier. *Aerosol Science and Technology, 45*(1), 1–10.
Gopalakrishnan, R., Thajudeen, T., Ouyang, H., & Hogan, C.J. (2013). The unipolar diffusion charging of arbitrary shaped aerosol particles. *Journal of Aerosol Science, 64*, 60–80.
Heurlin, M., Magnusson, M.H., Lindgren, D., Ek, M., Wallenberg, L.R., & Deppert, K., et al. (2012). Continuous gas-phase synthesis of nanowires with tunable properties. *Nature, 492*(7427), 90–94.
Karlsson, M.N.A., Deppert, K., Karlsson, L.S., Magnusson, M.H., Malm, J.O., & Srinivasan, N.S. (2005). Compaction of agglomerates of aerosol nanoparticles: A compilation of experimental data. *Journal of Nanoparticle Research, 7*(1), 43–49.
Knutson, E.O., & Whitby, K.T. (1975). Aerosol classification by electric mobility: apparatus, theory, and applications. *Journal of Aerosol Science, 6*(6), 443–451.
Ku, B.K., & Kulkarni, P. (2012). Comparison of diffusion charging and mobility-based methods for measurement of aerosol agglomerate surface area. *Journal of Aerosol Science, 47*, 100–110.
Ku, B.K., & Maynard, A.D. (2005). Comparing aerosol surface-area measurements of monodisperse ultrafine silver agglomerates by mobility analysis, transmission electron microscopy and diffusion charging. *Journal of Aerosol Science, 36*(9), 1108–1124.
Lall, A.A., & Friedlander, S.K. (2006). On-line measurement of ultrafine aggregate surface area and volume distributions by electrical mobility analysis: I. Theoretical analysis. *Journal of Aerosol Science, 37*(3), 260–271.
Lall, A.A., Rong, W., Mädler, L., & Friedlander, S.K. (2008). Nanoparticle aggregate volume determination by electrical mobility analysis: Test of idealized aggregate theory using aerosol particle mass analyzer measurements. *Journal of Aerosol Science, 39*(5), 403–417.
LeBouf, R.F., Ku, B.K., Chen, B.T., Frazer, D.G., Cumpston, J.L., & Stefaniak, A.B. (2011). Measuring surface area of airborne titanium dioxide powder agglomerates: Relationships between gas adsorption, diffusion and mobility-based methods. *Journal of Nanoparticle Research, 13*(12), 7029–7039.
Lövestam, G., Rauscher, H., Roebben, G., Klüttgen, B.S., Gibson, N., & Putaud, J.-P., et al. (2010). *Considerations on a definition of nanomaterial for regulatory purposes. Joint Research Centre (JRC) Reference Reports.* IHCP: .
McMurry, P.H., Wang, X., Park, K., & Ehara, K. (2002). The relationship between mass and mobility for atmospheric particles: A new technique for measuring particle density. *Aerosol Science and Technology, 36*(2), 227–238.
Meakin, P., Donn, B., & Mulholland, G.W. (1989). Collisions between point masses and fractal aggregates. *Langmuir, 5*(2), 510–518.
Messing, M., Svensson, C.R., Pagels, J., Meuller, B.O., Deppert, K., & Rissler, J. (2012). Gas-borne particles with tunable and highly controlled characteristics for nanotoxicology studies. *Nanotoxicology, 7*(6), 1052–1063.
Messing, M.E., Dick, K.A., Wallenberg, L.R., & Deppert, K. (2009). Generation of size-selected gold nanoparticles by spark discharge – For growth of epitaxial nanowires. *Gold Bulletin, 42*(1), 20–26.
Meuller, B.O., Messing, M.E., Engberg, D.L., Jansson, A.M., Johansson, L.I., & Norlén, S.M., et al. (2012). Review of spark discharge generators for production of nanoparticle aerosols. *Aerosol Science and Technology, 46*(11), 1256–1270.
Ntziachristos, L., Giechaskiel, B., Ristimäki, J., & Keskinen, J. (2004). Use of a corona charger for the characterisation of automotive exhaust aerosol. *Journal of Aerosol Science, 35*(8), 943–963.
Olfert, J., Symonds, J., & Collings, N. (2007). The effective density and fractal dimension of particles emitted from a light-duty diesel vehicle with a diesel oxidation catalyst. *Journal of Aerosol Science, 38*(1), 69–82.
Park, K., Kittelson, D.B., & McMurry, P.H. (2004). Structural properties of diesel exhaust particles measured by transmission electron microscopy (TEM): Relationships to particle mass and mobility. *Aerosol Science and Technology, 38*(9), 881–889.
Rasband, W. (1997–2012). *WS 1997–2012 ImageJ.* US National Institutes of Health: Bethesda, Maryland, USA.
Rissler, J., Messing, M.E., Malik, A.I., Nilsson, P.T., Nordin, E.Z., & Bohgard, M., et al. (2013). Effective density characterization of soot agglomerates from various sources and comparison to aggregation theory. *Aerosol Science and Technology, 47*(7), 792–805.
Rissler, J., Nordin, E.Z., Eriksson, A.C., Nilsson, P.T., Frosch, M., & Sporre, M.K., et al. (2014). Effective density and mixing state of aerosol particles in a near-traffic urban environment. *Environmental Science & Technology, 48*(11), 6300–6308.
Rissler, J., Swietlicki, E., Bengtsson, A., Boman, C., Pagels, J., & Sandström, T., et al. (2012). Experimental determination of deposition of diesel exhaust particles in the human respiratory tract. *Journal of Aerosol Science, 48*, 18–33.
Scheibel, H.G., & Porstendorfer, J. (1983). Generation of monodisperse Ag-aerosol and NaCl-aerosol with particle diameters between 2-N m and 300-N m. *Journal of Aerosol Science, 14*(2), 113–126.
Schwyn, S., Garwin, E., & Schmidtott, A. (1988). Aerosol generation by spark discharge. *Journal of Aerosol Science, 19*(5), 639–642.
Shin, W.G., Mulholland, G.W., Kim, S.C., Wang, J., Emery, M.S., & Pui, D.Y.H. (2009). Friction coefficient and mass of silver agglomerates in the transition regime. *Journal of Aerosol Science, 40*(7), 573–587.
Sorensen, C.M. (2011). The mobility of fractal aggregates: A review. *Aerosol Science and Technology, 45*(7), 765–779.
Svensson, C.R., Messing, M.E., Lundqvist, M., Schollin, A., Deppert, K., & Pagels, J.H., et al. (2013). Direct Deposition of Gas Phase Generated Aerosol Gold Nanoparticles into Biological Fluids-Corona Formation and Particle Size Shifts. *PloS one, 8*(9).
Tabrizi, N., Xu, Q., van der Pers, N., Lafont, U., & Schmidt-Ott, A. (2009). Synthesis of mixed metallic nanoparticles by spark discharge. *Journal of Nanoparticle Research, 11*(5), 1209–1218.
Tabrizi, N., Xu, Q., van der Pers, N., & Schmidt-Ott, A. (2010). Generation of mixed metallic nanoparticles from immiscible metals by spark discharge. *Journal of Nanoparticle Research, 12*(1), 247–259.
Tabrizi, N.S., Ullmann, M., Vons, V., Lafont, U., & Schmidt-Ott, A. (2009). Generation of nanoparticles by spark discharge. *Journal of Nanoparticle Research, 11*(2), 315–332.
Thajudeen, T., Jeon, S., & Hogan, C.J. (2015). The mobilities of flame synthesized aggregates/agglomerates in the transition regime. *Journal of Aerosol Science, 80*, 45–57.
Wang, J., Shin, W., Mertler, M., Sachweh, B., Fissan, H., & Pui, D. (2010). Measurement of nanoparticle agglomerates by combined measurement of electrical mobility and unipolar charging properties. *Aerosol Science and Technology, 44*(2), 97–108.
Waters, K.M., Masiello, L.M., Zangar, R.C., Zangar, R.C., Karin, N.J., & Quesenberry, R.D., et al. (2009). Macrophage responses to silica nanoparticles are highly conserved across particle sizes. *Toxicological Sciences, 107*(2), 553–569.
Wiedensohler, A. (1988). An approximation of the bipolar charge-distribution for particles in the sub-micron size range. *Journal of Aerosol Science, 19*(3), 387–389.

Paper III

Spark Discharge Generation of InSb Nanoparticles

Linus Ludvigsson[1], Knut Deppert[1], Maria E Messing[1]

[1]Solid State Physics and NanoLund, Lund University, Box 118, 221 00 Lund, Sweden

Abstract

Smart nanomaterials based on nanoparticles have the potential to revolutionize applications in electronics and optoelectronics if they can be manufactured on a large scale. Semiconductors are a highly interesting class of materials for nanoscale applications in electronics and optoelectronics. Indium antimonide (InSb) is one candidate material for high speed electronics and infrared detectors due to its excellent properties of extreme electron mobility and small bandgap. Here we present results from successful generation of InSb nanoparticles produced by the spark discharge method. The particles are generated via electrical discharges between pure indium and antimony electrodes. The generated particles are transported in a carrier gas to be further processed via size selection, compaction in a sintering furnace, and a second size selection step. We have investigated the influence of the carrier gas on the process. Gas mixtures of nitrogen, nitrogen + hydrogen, argon, and argon+hydrogen were investigated. In the carrier gases without hydrogen we observed high compaction temperatures indicative of oxide formation. With the addition of 5 % hydrogen the compaction temperature were drastically decreased. This was further confirmed by TEM analysis, in which the quality of the compound InSb particles was assessed. Initial InSb particles had a composition with an excess of Sb, but the Sb content decreased during sintering to reach a ratio close to 1:1 in the completely compacted particles. Monodisperse InSb nanoparticles of high crystalline quality have been produced with the spark discharge generator. With a continuous method of production with less hazardous material it opens up for quantum dot applications in optics and optoelectronics in a broader fashion then before.

Introduction

Large scale production of nanoparticles with controlled size and morphology is vital for the development of new smart nanoparticle-based materials[1]. A particularly interesting class of materials for nanoscale applications, primarily for electronics and optoelectronics, is semiconductors[2]. Semiconductors of extremely high quality can be manufactured in a greatly controlled manner by physical methods both as thin films[3] and nanowires[4], but not in nanoparticle form. Attempts have been made to produce semiconductor nanoparticles by physical methods via laser ablation[5], laser pyrolysis[6], inert gas condensation [k3] and by ball milling of bulk material[7]. In addition to the problem of enabling mass production, which is possible with ball milling but not the other methods, these

1

previous attempts to generate semiconductor nanoparticles have resulted in particles of poor morphology, crystal structure and size control. Size, morphology and crystal structure are properties that largely affect the performance of electronic and optoelectronic semiconductor devices, and hence needs to be fully controlled if the nanoparticles are going to be used for such applications.

Indium antimonide (InSb) is a semiconductor material with extraordinary properties, such as the highest room-temperature electron mobility ($\sim$78,000 cm^2/(Vs)^2) and one of the smallest band gaps ($\sim$0.17 eV at 300 K) which is why it is an excellent candidate for a number of different electronic and optoelectronic applications[8]. To date there are a number of reports on fabrication of InSb thin films[9] and nanowires of high quality[10] but only a few reports on attempts to produce InSb nanoparticles[11,12]. Common problems in these reports are aggregation of particles, poor morphology and crystal structure and non-uniform size. In the one case where physical generation has been used the particles are slightly more uniform in size [k3], but still with poor morphology and crystal structure and with a generation route not suitable for large-scale manufacturing.

Spark discharge generation (SDG) is believed to be one of the most suitable methods for large-scale production[13] of nanoparticles. The first steps towards scaling up this method have already been taken[14] and generation of 2000 mg of material per hour have been demonstrated[15]. SDG was originally a method developed for production of conducting materials but Vons et al.[16] have shown that it is indeed possible to generate semiconductor nanoparticles as well. The silicon particles fabricated by Vons et al. were, however, agglomerated, non-uniform in size and of poor crystal quality but nonetheless an important proof that SDG can be the method of choice also for semiconducting materials.

In this paper, we use the SDG in a setup that enables transformation of the formed agglomerate particles into size-selected compact particles[17] and demonstrates for the first-time production of high quality monodisperse InSb nanoparticles. We show how to control and tune the formation parameters, most importantly the carrier gas, to form pure indium (In), pure antimony (Sb) and InSb particles. Furthermore, we show that it is possible to tune the composition of the final particles while still using only pure mono component material in the used electrodes. This possibility to produce high quality InSb nanoparticles opens up for interesting quantum dot applications.

Methods

In, Sb, and InSb particles were produced using an in house built SDG setup[18]. The setup enables the use of several carrier gas sources and starting materials. The generator and processing scheme can be seen in Figure 1. Material is ablated and evaporated from the two electrodes by discrete electrical discharges. A Technix CCR15-P-150 capacitance charger is used to charge an array of 21 nF high voltage capacitors. The electrodes are connected to the capacitors via a high voltage cable with

2

the grounded return in the coaxial shielding braid. The two electrodes are mounted 2 mm apart from each other. A continuous carrier gas flow of 1.68 slm is put through the chamber during the process. The released electrode material will form singlet particles[19] as the temperature rapidly decrease after the initial discharge. If the concentration of these singlets and residual vapor is high the particles will gather more material via condensation and further coalesce with each other. Eventually agglomeration will take place until the particle concentration is reduced. The discharge characteristics were measured for different capacitances and gas mixtures using a Techtronics high voltage probe (P6015A) connected to the HV and grounded side of the generation chamber, as close to the gap as possible.
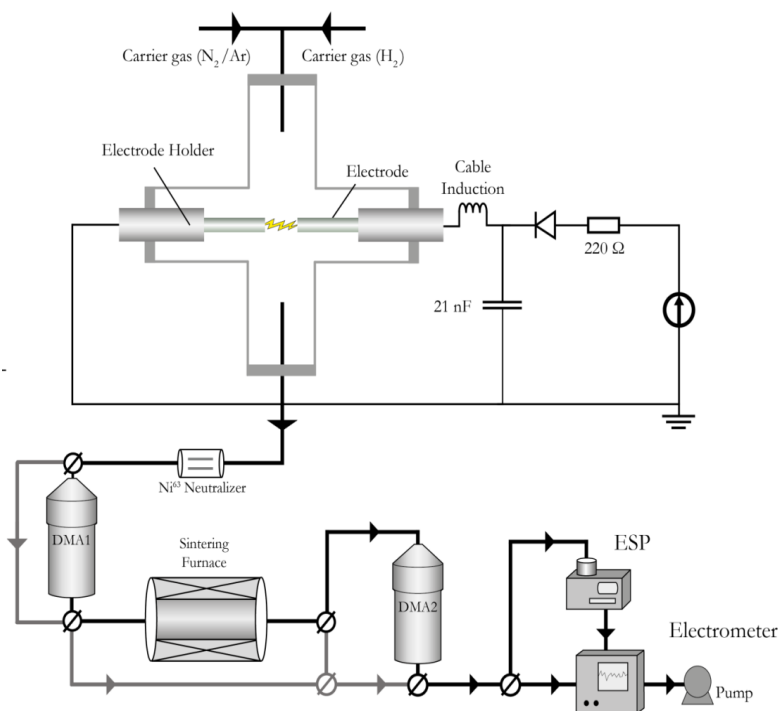
Figure 1 Schematic of the nanoparticle generation setup

The continuous flow of carrier gas through the chamber carries the formed agglomerate particles to a Ni-63 neutralizer and further to a differential mobility analyzer (DMA, TSI. Long). A monodisperse aerosol is selected and this fraction is compacted using a tube furnace (Lenton). As agglomerates of the same mobility diameter can have different amount of material, the compacted particles will have a broader mobility size distribution compared to before compaction. Partially oxidized particles will require a higher temperature to undergo complete compaction and will remain as agglomerates after the sintering furnace. A second DMA (Vienna type[20]) is used to select particles that have undergone complete compaction and that have a specific mobility diameter. Particles are

3

deposited in an electrostatic precipitation chamber onto substrates for further offline analysis. Alternatively, the aerosol stream can be diverted to an electrometer (TSI, Model 3068B) for measurement of the particle concentration.

The carrier gas was changed in a pump-purge process to precondition the system between runs with different gas mixtures or materials. We carried out tests using pure nitrogen (purity 99.999%), pure argon (99.999%) or nitrogen with addition of 1-10 % hydrogen (purity 99.999%). Electrodes used for generation were pure (99.999%, Goodfellow, Huntingdon, England) antimony and indium with diameters 4.7 mm and 3.5 mm respectively. For some runs, hydrogen gas (purity 99.999%) was also introduced at a later stage in the process, namely after generation and the first size selection but before compaction.

For each series of material-gas combination, the compaction behaviour was studied by selecting a mobility diameter of 50 nm in DMA1 and scanning DMA2 for a set of temperatures in the furnace. This creates a size distribution on which a log-norm curve is fitted. The mean mobility diameters from the different fits are then plotted to reveal the compaction behaviour. In addition, samples for scanning electron microscopy (SEM) and transmission electron microscopy (TEM) analysis were deposited at several temperatures onto Si substrates with a 3mm lacy carbon coated Cu grid glued to it to investigate the particle morphology. The final compacted particles were also analyzed with energy dispersive x-ray spectroscopy (EDX) in scanning TEM (STEM) mode to assess the chemical composition.

Settings used in previous studies of metals and metal oxides generated with low frequency SDG [13,21,22] was found to be useful for the materials produced in this study as well, with some modifications. The generation parameters were optimized to ensure that the electrodes would last prolonged generation while the output of particles was as high as possible at the desired mobility diameter. As there is no active cooling in the setup the electrodes will heat up and in the case of In (melting point 430 K) there was a risk of melting the electrode. A gap distance of 2 mm, a carrier gas flow of 1.68 slm, a 21 nF capacitance, and a charging current of 2 mA was found to be optimal and was kept constant for all experiments, with the exception of the measurements of the discharge characteristics where the capacitance was varied.

Results and Discussion

In, Sb and InSb agglomerate particles were successfully generated at the described settings. All materials showed a peak in concentration at a mobility diameter around 60 nm. Although the low charging current slightly limited the production rate and median size of the agglomerate particles, the

yielded number concentrations were in the same range as in previous studies of metal and metal oxides [3, 17, 18].

The discharge characteristics for generation of InSb are shown in Figure 2a, and for all capacitances and gas mixtures the characteristic oscillatory behaviour is measured. An oscillating discharge will erode both electrodes which are especially important when producing compound materials to ensure even mixing of the materials in the final particles. Studies with intrinsic semiconductor electrodes showed damped discharges as opposed to oscillating that are present for metals [4]. However, the electrode materials used in this study, In and Sb, are both metallic in their pure form and hence the oscillatory behaviour is expected. Adding hydrogen to the nitrogen carrier gas is expected to lower the breakdown voltage[23]. This is indeed observed and shown as an increase in frequency, Figure 2b. So,
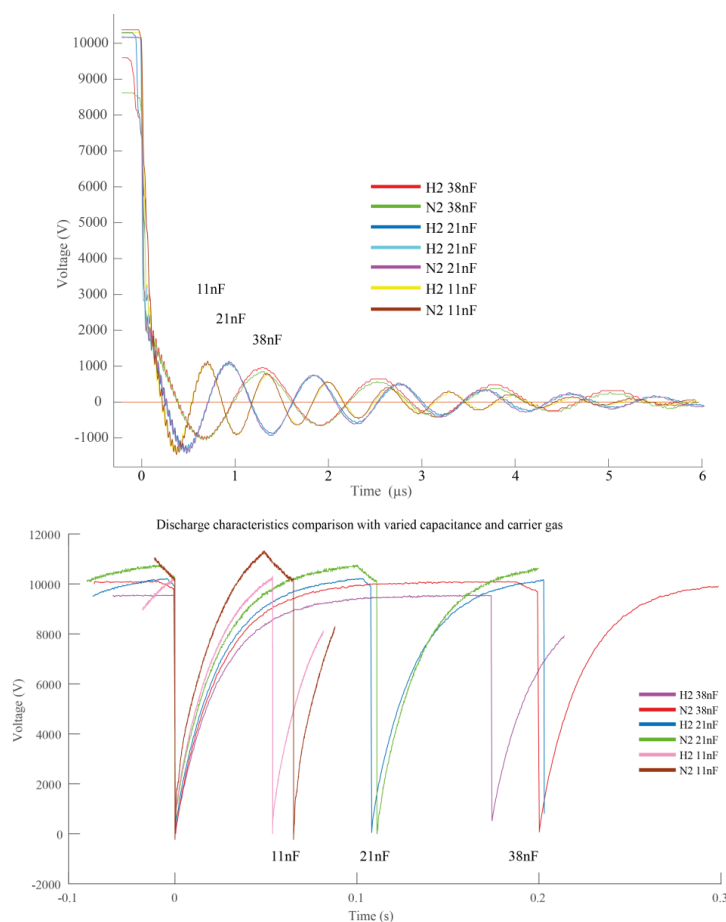

Figure 2 The discharge characteristics for InSb there are minor differences in the discharge characteristics on a short time scale comparing the gas mixtures, but the increase in frequency with the presence of hydrogen is clear when looking at several discharges.

5

although InSb is a compound semiconductor material the actual formation step for InSb is similar to the formation of metal and metal alloy particles reported in previous studies[15,23].

The formed agglomerate particles are, however, not suitable for electronic and optoelectronic applications where morphology, crystal structure and size control are vital for optimal device performance. Therefore, a transformation step where the formed agglomerate particles are heated in a second furnace into compact particles followed by a second size selection (Figure 1) is needed. Very few studies of the compaction behaviour of particles produced by SDG have been reported and among the few that exist most deals with single compound materials that are not highly prone to oxidation, such as gold[24] and palladium[25]. When dealing with materials that are easily oxidized, such as In and Sb, one have to ensure an oxygen free or even reducing environment during the generation and/or heating step. Producing compact compound particles furthermore requires that the vapor pressure of the different compounds is similar to avoid evaporation of one of the compounds during the heating step.

In Figure 3, the compaction as a function of temperature of In, Sb and InSb particles generated and compacted in pure nitrogen and in nitrogen with addition of 5 or 10 % hydrogen is shown. For all materials generated and compacted in nitrogen with addition of hydrogen the diameter is slowly decreasing with increasing temperature until a more rapid drop of the peak mobility diameter occurs. After the more rapid drop the diameter is almost constant or decreases very slowly. A rapid drop of the peak mobility diameter is characteristic of coalescence while a slow decrease could be a sign of evaporation of material from the particles. Compaction via coalescence in nanoparticles is expected to occur below the melting point of the bulk material [20].

6
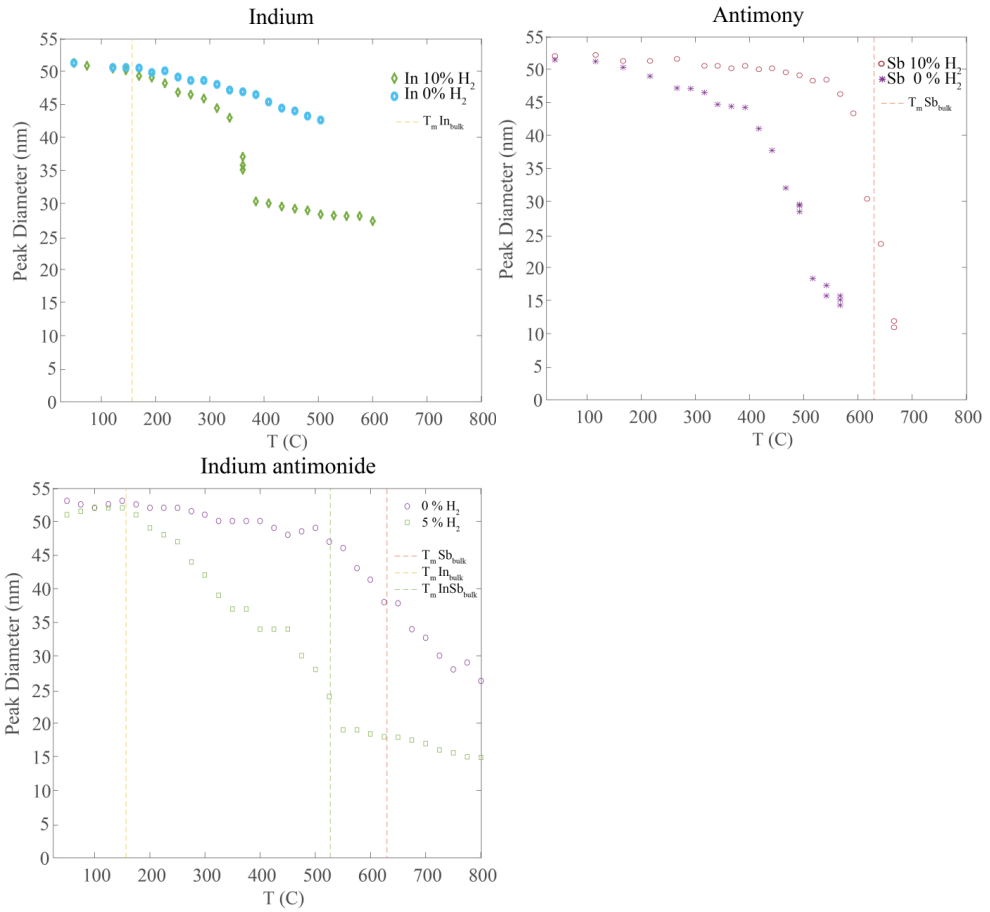
Figure 3 The compaction behavior of a) In, b) Sb and c) InSb.

For pure Sb particles generated in the nitrogen/hydrogen mixture, the rapid diameter drop occurs around 425 $^{\circ}$C (698 K) and the compaction temperature, T_c, i.e. the temperature where almost no further drop in diameter occur is around 500 $^{\circ}$C (773 K), see figure 3 b. This corresponds to about 85 % of the bulk melting point for Sb measured in K and is higher than previous reports of compaction temperatures for metals that are typically in the range of 1/3 to 1/2 of the melting temperature of the bulk metal[26]. For pure In particles generated in nitrogen with 10 % hydrogen, the rapid diameter drop occurs around 300 $^{\circ}$C (Figure 3 a) which is well above the bulk melting point of pure In. Typically, a notable and steep decrease of particle diameter occurs above the bulk melting point of a material due to evaporation[26]. This is clearly not the case for the In particles generated in this study and a strong indication of some kind of oxidation of the particles either during the formation step or due to trace amounts of oxygen in the subsequent parts of the system. The particles are, however, not completely oxidized since a rapid diameter drop occur down to around 20 nm where the diameter starts to decrease much slower. This is only possible when the particles are generated and compacted in

7

nitrogen with 10 % hydrogen. Particles generated and compacted in pure nitrogen or nitrogen with 5 % hydrogen never reach a fully compact state. This behavior is most likely a sign of oxide formation in pure nitrogen and with the addition of hydrogen the small amount of oxygen present in the setup is scavenged. The oxygen levels were measured for the system during operation and was found to be <0.1ppm (Servomex DF-310E), during both operation using only nitrogen and hydrogen.

The decrease in diameter for InSb particles generated with the reducing gas mixture shows a modest decline in diameter over a broad temperature range which could be an indication of evaporation. However, the deposited particles when investigated by TEM (Figure 4) shows that the decline in size follows coalescence of agglomerates in the same fashion as has been observed in other materials[24]. The decline coincides with both pure In and Sb but as the size distributions for each temperature were monodisperse after compaction the possibility that fractions of pure In particles would compact at a lower temperature while Sb particles remain intact is, if present, a limited process. The generated particles behave as a single material and do not show any signs of size fractioning at any temperature. The compaction temperature for InSb is similar to the T_c for Sb, and occurs around the melting temperature of bulk InSb, which is 527 $^\circ$C (800 K). Above this temperature, the diameter decrease is typically more rapid than what is shown here since evaporation is expected to occur. It is plausible that this is an effect of small amounts of oxygen still present in the system, which might be used to form a protective oxide shell around the particles. Such a shell is evident from high resolution TEM images (Figure 5 a), but it is not possible to determine whether the shell is present already during particle formation or if it forms when the particles are exposed to air during TEM sample mounting.
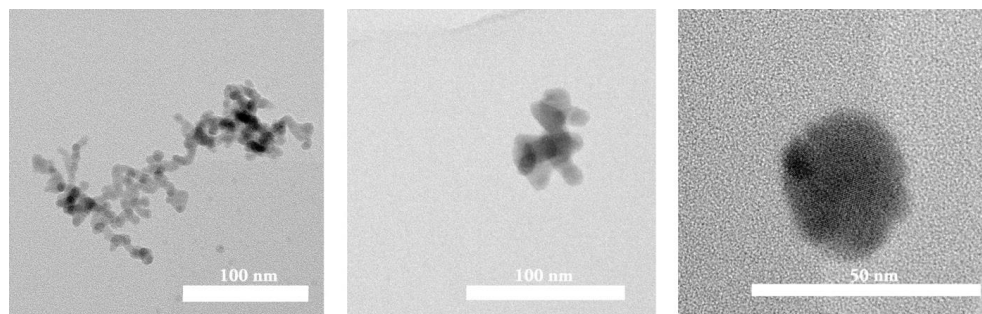
Figure 4 Compaction of 80 nm InSb agglomerates generated in the presence of 5 % H$_2$ with increasing temperature: Room temperature, 400 $^\circ$C, 500 $^\circ$C.

When comparing the diameter decline for all of the three materials when using only nitrogen and nitrogen with hydrogen it is clear that the decrease in diameter occurs at a lower temperature when hydrogen is present. It can also be seen that the overall decline is less prominent without hydrogen indicating that the material is less prone to coalesce/evaporate. This behavior is a clear sign of oxide formation in pure nitrogen, since the compaction temperature is higher for oxides[26], and with the addition of hydrogen a reducing atmosphere is created. The effect of the added hydrogen is present

already at low concentrations but adding more improves the compaction behavior. A final concentration of 5 % H_2 was sufficient to produce particles that compact to form crystalline Sb and InSb particles, whereas 10 % was needed for pure In particles. It is not surprising that more hydrogen is needed in the case of In since In is more prone to oxidation than Sb.

The addition of hydrogen to the nitrogen carrier gas seems to have an effect which is instant and show a low degree of hysteresis in our system. Switching off the hydrogen after a run immediately returns the median diameter back to what it was without hydrogen present. This effect was also prominent after several hours of particle generation, when one can assume that the oxygen levels are lower than during the beginning of the generation. Additional test runs were performed with addition of hydrogen solely at the transformation step to comprehend the effect of a reducing atmosphere during the formation of particles. Introduction of hydrogen during transformation showed no effect on the produced particles, even at levels as high as 10 % H_2 the compaction was identical to compaction in pure nitrogen. This result highlights the importance of the atmosphere already during the spark event when the particles are formed, and clearly demonstrate that for these materials that are highly prone to oxidation, non-oxidized particles could not be achieved solely by a reducing atmosphere during the compaction step.

InSb particles were also generated in argon with an addition of 5 % hydrogen to manifest the reducing effect of hydrogen. While the production rate was different due to the change in discharge voltage between an argon and a nitrogen gas mixture, the compaction behavior of the particles was unaffected by the main carrier gas. The compaction curve was almost identical to the one for nitrogen with addition of 5 % hydrogen. This is a strong indication that the addition of hydrogen is the main reason of the changes in compaction temperature due to its reducing properties.

From the STEM XEDS measurements performed to determine the particle composition it was clear that the In and Sb content in the InSb particles varied with compaction temperature. The particles showed an excess of Sb at lower compaction temperatures which declined as the compaction temperature rose. This might both be a sign of evaporation and a sign of reduction of In oxide. Sb is expected to evaporate to a higher degree than In due to eq. vapor pressure ratio of 10^5 compared with In. At 600C the ratio is almost 1:1 with an uncertainty of +-5% given instrument limitations. High resolution TEM does confirm that a high degree of the fully compacted particles is compound InSb and not amorphous mixtures nor phase segregated. Measurements of the lattice constant are close to the tabulated constants of InSb[10], Figure 5, and confirm the generation of particles with high crystal quality.
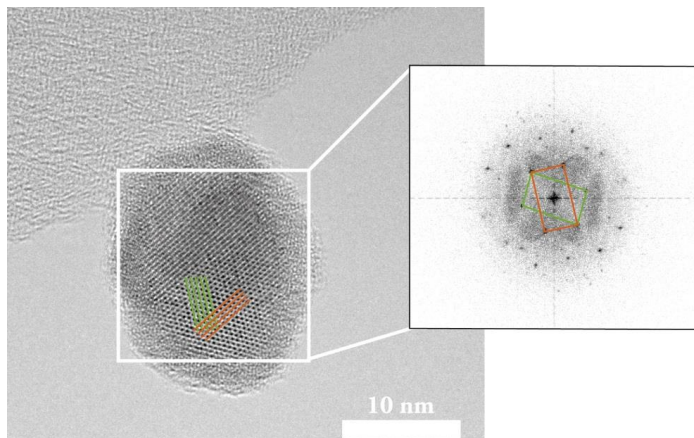
Figure 4 High resolution TEM image of InSb nanoparticle and its FFT with lattice distances corresponding to InSb.

Conclusions

We have successfully produced monodisperse InSb nanoparticles of high crystalline quality using a spark discharge generator. The material is generated under similar formation parameters as previously reported for other metal and metal oxides. We show that there is a need to add amounts of hydrogen to the carrier gas already during generation to prevent oxidation and for the compound particles to fully compact. The transformation step, where the formed agglomerate particles are sintered into size-selected compact particles, is crucial in order to form high quality particles of the desired composition as the initial agglomerate particles does not have a 1:1 ratio between In and Sb. Vapor pressure of the different components play a major role during transformation as it drives the ratio towards unity and compacted compound particles. We can tune composition of the final particles by varying the sintering temperature and thus the evaporation rate of Sb. We demonstrate a continuous method of production, with less hazardous material compared with conventional methods, that may open up for quantum dot applications in optics and optoelectronics in a broader fashion then before.

Acknowledgments

References

1   Messing, M. E. The advantages of spark discharge generation for manufacturing of nanoparticles with tailored properties. *Journal of Green Engineering* **5**, p. 83-96, doi:10.13052/jge1904-4720.5346 (2016).

2   Gudiksen, M. S., Lauhon, L. J., Wang, J., Smith, D. C. & Lieber, C. M. Growth of nanowire superlattice structures for nanoscale photonics and electronics. *Nature* **415**, 617-620, doi:Doi 10.1038/415617a (2002).

3   Morkoc, H. *et al.* Large-Band-Gap Sic, III-V Nitride, and II-VI ZnSe-Based Semiconductor-Device Technologies. *J Appl Phys* **76**, 1363-1398 (1994).

4   Dick, K. A. *et al.* Control of III-V nanowire crystal structure by growth parameter tuning. *Semicond Sci Tech* **25**, doi:10.1088/0268-1242/25/2/024009 (2010).

5   Yoshida, T., Takeyama, S., Yamada, Y. & Mutoh, K. Nanometer-sized silicon crystallites prepared by excimer laser ablation in constant pressure inert gas. *Appl Phys Lett* **68**, 1772-1774, doi:Doi 10.1063/1.116662 (1996).

6   Huisken, F., Ledoux, G., Guillois, O. & Reynaud, C. Light-emitting silicon nanocrystals from laser pyrolysis. *Adv Mater* **14**, 1861-1865, doi:DOI 10.1002/adma.200290021 (2002).

7   Lam, C. *et al.* Large-scale synthesis of ultrafine Si nanoparticles by ball milling. *J Cryst Growth* **220**, 466-470, doi:Doi 10.1016/S0022-0248(00)00882-4 (2000).

8   Aardvark, A., Mason, N. J. & Walker, P. J. The growth of antimonides by MOVPE. *Prog Cryst Growth Ch* **35**, 207-241 (1997).

9   Biefeld, R. M. The metal-organic chemical vapor deposition and properties of III-V antimony-based semiconductor materials. *Mat Sci Eng R* **36**, 105-142, doi:10.1016/S0927-796x(02)00002-5 (2002).

10   Caroff, P. *et al.* InSb heterostructure nanowires: MOVPE growth under extreme lattice mismatch. *Nanotechnology* **20**, doi:10.1088/0957-4484/20/49/495606 (2009).

11   Pandya, S. G. & Kordesch, M. E. Characterization of InSb Nanoparticles Synthesized Using Inert Gas Condensation. *Nanoscale Res Lett* **10**, 1-7, doi:10.1186/S11671-015-0966-4 (2015).

12   Breivik, M., Nilsen, T. A. & Fimland, B. O. Temperature dependent lattice constant of InSb above room temperature. *J Cryst Growth* **381**, 165-168, doi:10.1016/j.jcrysgro.2013.06.034 (2013).

13   Meuller, B. O. *et al.* Review of Spark Discharge Generators for Production of Nanoparticle Aerosols. *Aerosol Science and Technology* **46**, 1256-1270, doi:10.1080/02786826.2012.705448 (2012).

14   Feng, J. *et al.* Scalable and Environmentally Benign Process for Smart Textile Nanofinishing. *ACS Applied Materials & Interfaces* **8**, 14756-14765, doi:10.1021/acsami.6b03632 (2016).

15   Hontanon, E. *et al.* The transition from spark to arc discharge and its implications with respect to nanoparticle production. *J Nanopart Res* **15**, doi:10.1007/S11051-013-1957-Y (2013).

16   Vons, V. A. *et al.* Silicon nanoparticles produced by spark discharge. *J Nanopart Res* **13**, 4867-4879, doi:DOI 10.1007/s11051-011-0466-0 (2011).

17   Svensson, C. R. *et al.* Characteristics of airborne gold aggregates generated by spark discharge and high temperature evaporation furnace: Mass-mobility relationship and surface area. *J Aerosol Sci* **87**, 38-52, doi:10.1016/j.jaerosci.2015.05.004 (2015).

18   Ludvigsson, L., Meuller, B. O. & Messing, M. E. Investigations of initial particle stages during spark discharge. *Journal of Physics D-Applied Physics* **48**, doi:10.1088/0022-3727/48/31/314012 (2015).

19   Feng, J. *et al.* General Approach to the Evolution of Singlet Nanoparticles from a Rapidly Quenched Point Source. *Journal of Physical Chemistry C* **120**, 621-630, doi:10.1021/acs.jpcc.5b06503 (2016).

20   Knutson, E. O. & Whitby, K. T. Anomalous Unipolar Diffusion Charging of Polystyrene Latex Aerosols. *J Colloid Interf Sci* **53**, 493-495, doi:Doi 10.1016/0021-9797(75)90067-3 (1975).

21   Hillerich, K., Messing, M. E., Wallenberg, L. R., Deppert, K. & Dick, K. A. Epitaxial InP nanowire growth from Cu seed particles. *J Cryst Growth* **315**, 134-137, doi:DOI 10.1016/j.jcrysgro.2010.08.016 (2011).

22   Tabrizi, N. S., Xu, Q., van der Pers, N. M., Lafont, U. & Schmidt-Ott, A. Synthesis of mixed metallic nanoparticles by spark discharge. *J Nanopart Res* **11**, 1209-1218, doi:DOI 10.1007/s11051-008-9568-8 (2009).

23   Tabrizi, N. S., Ullmann, M., Vons, V. A., Lafont, U. & Schmidt-Ott, A. Generation of nanoparticles by spark discharge. *J Nanopart Res* **11**, 315-332, doi:DOI 10.1007/s11051-008-9407-y (2009).

24   Messing, M., Dick, K., Wallenberg, L. & Deppert, K. Generation of size-selected gold nanoparticles by spark discharge — for growth of epitaxial nanowires. *Gold Bull* **42**, 20-26, doi:10.1007/bf03214902 (2009).

25   Messing, M. E. *et al.* Generation of Pd Model Catalyst Nanoparticles by Spark Discharge. *Journal of Physical Chemistry C* **114**, 9257-9263, doi:Doi 10.1021/Jp101390a (2010).

26   Karlsson, M. N. A. *et al.* Compaction of agglomerates of aerosol nanoparticles: A compilation of experimental data. *J Nanopart Res* **7**, 43-49, doi:DOI 10.1007/s11051-004-7218-3 (2005).

Paper IV

Optical and particle emission of a spark discharge nanoparticle generator

Attila Kohut[1], Linus Ludvigsson[2], Gábor Galbács[3], Bengt O. Meuller[2], Knut Deppert[2], Maria E. Messing[2], and Zsolt Geretovszky[1] (✉)

[1]Department of Optics and Quantum Electronics, University of Szeged, Dóm tér 9, Szeged H-6720, Hungary
[2]Solid State Physics, Lund University, P.O. Box 118, Lund SE-22100, Sweden
[3]Department of Inorganic and Analytical Chemistry, University of Szeged, Dóm tér 7, Szeged H-6720, Hungary

ABSTRACT

The increased demand for high purity nanoparticles (NPs) of defined geometry necessitates the continuous development of generation routes. One of the most promising physical techniques for producing metal, semiconductor or alloy NPs in the gas phase is spark discharge nanoparticle generation. The simplicity of the technique implies a great potential for up-scaling without altering the particles. Despite the simplicity of the setup, the formation of NPs in a spark discharge generator (SDG) takes place via complex multi-scale processes, which hinders the investigation of NP generation, e.g. the atomization of the electrode material via conventional nanoparticle measurement techniques. In the present work, time-resolved optical emission spectroscopy (OES) was used to provide information on the species present in the spark from as early as approximately 100 ns after the initiation of the discharge. The emission spectra of the spark are also used to identify, among others, the main stages of material erosion and to calculate the quenching rate of the generated metal vapor. We demonstrate that the alteration of key control parameters, that are typically used to optimize NP generation, clearly affect the emission spectra. We found for Cu and Au NPs that the intensity of the spectral lines emitted by metal atoms levels off when the spark energy is increased above a certain energy threshold, suggesting that the maximum concentration of metal vapor produced in the SDG is limited. This explains the size variation observed for the generated nanoparticles. Our results prove a strong correlation between the optical and particle emission of the SDG, which on one hand, demonstrates the suitability of OES as a non-invasive *in-situ* monitoring method, and on the other, allows for a more conscious optimization of NP generation.

1 Introduction

The mass-production of nanoparticles (NPs) by environmentally friendly and cheap means is a key point if nanoparticle-based product development should continue to advance. A suitable route to fulfill these requirements is NP generation by physical methods. In contrast to chemical generation techniques, advantages of manufacturing based on physical methods include continuous generation, higher purity of the NPs and smaller amount of waste [1].

Flame pyrolysis is an established method used for the industrial scale production of metal-oxide particles [2], but unsuitable for the production of pure metal particles. Metal NPs are often formed by material evaporation in an inert gas followed by subsequent nucleation and condensation [3]. Evaporation can be achieved in several ways, e.g. using furnaces [4], glowing wires [5] or laser ablation [6]. These methods are, however, often not energy efficient and their use in mass-production might be problematic. A more energy efficient and up-scalable method for the evaporation of conducting materials is spark discharge generation [7].

The spark discharge generator (SDG) has an appealingly simple design that consists of a leak-tight chamber, housing two electrodes that are separated by a small gap. For creating a high voltage spark discharge between the electrodes, the traditional self-pulsed circuit is typically used, consisting of a capacitor fed by a high voltage DC power supply, which are connected in parallel to the electrode gap. Each spark is initiated by the formation of a conducting channel (spark channel) between the two electrodes in which the charge carriers are (initially) dominated by electrons and ions of the carrier gas. The colloquial term "single spark" actually refers to a damped oscillatory event, the characteristic duration of which damping is determined by the electrical parameters of the discharge loop [8]. The surfaces of the electrodes are heated at local "hot spots" and a vapor plume is formed from the material eroded from the electrodes [9, 10]. In addition, ions both from the anode, cathode and the carrier gas bombard the electrodes leading to further removal of electrode material [11]. When the vapor plume is cooled by adiabatic expansion and mix with the carrier gas nucleation will take place and first atomic clusters are formed. These clusters will grow further into singlet particles by condensation and coalescence and ultimately grow to primary particles that finally may form agglomerate particles [9].

The potential of spark discharge generation for mass-production of NPs is largely based on its relative simplicity. Furthermore, by placing several electrode pairs in parallel, the generation process could be easily and controllably scaled up at low cost and with minimal impact on the environment. In the EU-project BUONAPART-E, 21 partners from both industry and academia worked on this upscaling approach and realized a production rate of 100 kg day^{-1} [12]. Industrial scale productivity not only necessitates the connection of multiple SDGs in parallel, but also the precise, in-line characterization and control of NP properties of each SDG. To this end, it is important to gain detailed knowledge about the particle generation process itself. Although the SDG has been around since 1988 [7], is commercially available [13], and used by several groups [14-21] the fundamentals of the processes leading to particle formation is not yet fully understood.

One reason for this knowledge gap is the difficulty in investigating the initial phase and the different stages of particle formation. Traditionally, there are two main approaches in aerosol science, through which gas-borne particles are characterized or monitored. One of this is NP collection (e.g. collection on various substrates by using electrostatic precipitators, cascade impactors, etc.) followed by off-line electron microscopic analysis. In the other approach, instrumentation, capable of in-flight aerosol measurement, is used, such as the scanning particle mobility sizer (SMPS), aerosol particle mass analyzer (APM), the conventional aerosol mass spectrometer (AMS) or laser-vaporization aerosol mass spectrometer (LV-AMS) [22]. All of these

Address correspondence to gero@physx.u-szeged.hu

methods are only applicable further downstream of the generator spark gap, not in the vicinity of the primary NP formation zone. Invasive methods, such as sampling for electron microscopy has been performed close to the spark gap [23]. This sampling provides integrated information on the early stages of particle formation but during sampling the flow field might be altered and hence the generation process is affected. In addition, such sampling does not provide information on what species present in the gas phase before nucleation.

In this paper, we employ a non-invasive method, namely time resolved optical emission spectroscopy (OES) for gaining information on the first stages of particle formation in the spark without disturbing the examined processes in any ways. This technique allows for the *in-situ* investigation of the spark plasma with a temporal resolution on the nanosecond time-scale. OES provides direct information on the excited atomic and ionic species which are inherently produced during the formation of the energetic spark plasma. Time-resolved emission spectra can further be used to derive important plasma properties, such as the temperature and electron concentration [24]. The outstanding potential of OES for the investigation of electric discharges is well reflected by the fact that the technique has a sound literature in connection with spectroanalytical chemistry [25, 26]. In the present work, time resolved OES was used to provide information on the species present in a single (oscillatory) spark from as early as approximately 100 ns after the initiation of the spark. The temporally resolved optical emission of the spark is used to identify the main stages of the material erosion and to calculate the quenching rate of the generated metal vapor. We also demonstrate that the alteration of key control parameters, that are typically used to optimize nanoparticle generation, e.g. gap size and charging current, clearly affect the emission spectra, although they are specific to the early stages of the process, prior to particle nucleation. In the present study, the effect of the charging current and the size of the electrode gap on the erosion of copper and gold electrodes was investigated by means of OES, while agglomerated

NPs were characterized downstream by an SMPS. Correlations between particle characteristics and the atomic emission are also presented. Our findings contribute significantly to the understanding of the first stages of particle formation in an SDG and will lead to a more conscious optimization of the NP generation.

2 Experimental

The SDG used in this work consists of a Technix CCR15-P-150 capacitance charger high voltage power supply, that charges a 20 nF high voltage capacitor bank. The voltage is carried to the initially anodic electrode via a high voltage cable. The opposite electrode is connected to the ground via a separate cable. Please note that from this point forward, the two electrodes will be identified according to their initial electrical polarity that is anode and cathode. The spark chamber consists of a standard KF40 6-way cross with the gas inlet and outlet on the top and bottom flanges, respectively (Fig. 1). Two horizontal, opposing flanges are used for the electrical feedthroughs, connected internally to the cylindrical electrodes aligned uniaxially. A high voltage feedthrough (for the anode) and a linear motion manipulator (for the cathode), both manufactured by MDC Vacuum Products, was used in the experiments. Gas control was realized by using
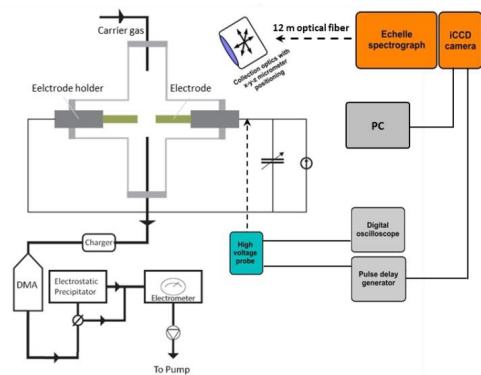

Figure 1 Schematic view of the SDG together with auxiliary instrumentation for particle characterization and time-resolved optical emission spectroscopy.

an AERA FC-7700CU mass flow controller. Pressure control was achieved with a Bronkhorst P-702CV electronic controller. The SDG system is controlled via purpose-made LabView software through a National Instruments cDAQ with a NI-9205 module for analog input, a NI-9264 module for analog output and a NI-9403 module for digital input and output. The discharge voltage is continuously monitored by using a Tektronix P6015A high-voltage probe that has a bandwidth of 75 MHz and capability of measuring voltage peaks up to 40 kV.

The SDG is connected to a scanning mobility particle sizer (SMPS) setup constructed from a particle charger containing a β-emitting ^{63}Ni source and a dynamic mobility analyzer (TSI 3081). An electrostatic precipitator was used to facilitate controlled deposition of NP samples for ex-situ characterization by means of transmission electron microscopy (TEM).

Copper (99.9% purity) and gold (99.9% purity) electrodes with flat surfaces and diameters of 3 mm were eroded via sparking. All measurements were performed under ambient pressure with nitrogen (99.995% purity) as carrier gas at a flow rate of 1.68 slm. The electrode distance and the charging current were varied in the range of 1.0-4.0 mm and 2-15 mA, respectively.
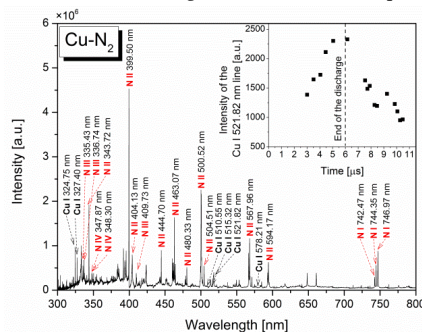
The time-resolved OES measurements were carried out by an Andor Mechelle 5000 fiber-coupled echelle spectrograph equipped with an Andor iStar 734-18F-03 intensified CCD (ICCD) camera. In order to reduce the electromagnetic interference induced by the SDG, the spectroscopic instrumentation was set up in a nearby laboratory and the optical signal was transmitted to the spectrometer using a 12 m long fused silica optical fiber with 50 μm core diameter. The emitted light from the plasma was spatially integrated over a ca. 6 mm diameter circular area (in a direction perpendicular to the axis of the electrodes) by using a quartz collection lens (Avantes COL-UV/VIS). The position of the collecting lens was optimized (to the highest optical signal) before each experimental run. The spectrograph was wavelength and intensity-calibrated and allowed for spectral data collection in the 300-800 nm wavelength range with ~0.125 nm resolution (at 435 nm). The light

acquisition of the ICCD camera was triggered by the sharp negative signal edge (provided by the HV probe) caused by the breakdown of the gas between the electrodes. A Stanford DG535 pulse generator was used to produce a logical signal after the onset of the breakdown and initiated the exposure, i.e. the spectral acquisition. The overall time delay (including insertion delays and signal propagation) of the spectroscopic setup caused is around 100 ns, which thus defines the temporal starting point of our investigations. In order to study the time evolution of the spark, emission spectra of the discharge were acquired at time delays varying from 0 ns to 15 μs. The gate width of the camera, hence the temporal resolution of the measurements, was set to 50 ns. Each spectrum was measured on separate, consecutive sparks and few hundred spectra were accumulated at each experimental setting.

3 Results

3.1 Optical emission of the spark

Erosion of the electrode material in an SDG is driven by the electrical discharge forming in the electrode gap. Due to the high energy input, not only atoms are removed from the electrodes but these atoms will also get excited and, if temperature

Figure 2 Temporally and spatially integrated emission spectrum of the spark acquired during the generation of Cu NPs in nitrogen atmosphere (4 mm gap, 1.68 slm gas flow rate, 10 mA charging current). Inset: temporal evolution of the intensity of the Cu I 521.82 nm line (2 mm gap, 1.68 slm gas flow rate, 15 mA charging current).

permits, ionized. The characteristic optical emission originates from the relaxation of these excited atoms and ions. Figure 2 represents a typical spark emission spectrum acquired by spatially integrating the photons leaving the electrode gap into the acceptance angle of the lens. The spectra acquired by temporal resolution were mathematically summed in order to illustrate the time-averaged spectral character of the spark emission.

As can be seen in Fig. 2, the spectrum is dominated by the emission of the excited species of the gas ambient, namely spectral lines of nitrogen atoms and singly or multiply charged ions. Atomic lines of the electrode material (copper) are also present with much smaller relative intensity. This relation reflects that the number concentration of the gas species exceeds the concentration of the electrode material in the spark gap by several orders of magnitude [24].

As a single spark (oscillatory spark discharge) has a characteristic temporal behavior (alternating voltage and current waveform with exponentially damping amplitude, see e.g. [27]) the quantity and the properties (e.g. temperature) of the eroded material evolves in time as well. This temporal evolution is well reflected in the emitted spectrum. The optical emission of spark discharges used for spectroanalytical purposes has a well-established literature dating back to the last century [25, 28, 29]. The evolution of an electric spark discharge is usually divided into four stages with respect to the emitted light: *i)* pre-breakdown, *ii)* breakdown, *iii)* arc and *iv)* afterglow stages [25]. The pre-breakdown and breakdown stages are responsible for the increase of the charge carriers in the electrode gap, which eventually leads to the formation of a conducting plasma channel that bridges the electrodes [30]. In the arc stage, the spark very much behaves like a transient arc discharge [25, 31]. After the electric current ceased, the spark enters the so-called afterglow regime. The name of this final stage reflects the (experimental) observation that the species emit light for an extended period of time well after the electrode gap stops being conductive.

The pre-breakdown and breakdown stages

have negligible contribution to the erosion of the electrode material which is supported by the fact that these stages are characterized by molecular bands in the emission spectrum when a molecular gas is used as ambient gas [32]. In the typical, i.e. free-running SDG, the breakdown is expected to complete quickly due to the low inductance of the discharge loop [32]. Figure 2 also suggests that the breakdown completes in less than 100 ns, since the spectral acquisition started about 100 ns after the voltage drop between the electrodes, and do not exhibit molecular nitrogen bands. This is in line with the ~50 ns breakdown duration value reported recently in case of an SDG operated under argon atmosphere [24]. This means that practically the breakdown occurs instantly as compared to the timescale of the entire emission process. After the breakdown, alternating current starts to flow in the gap with exponentially dampening amplitude. In this arc stage, the capacitor fully discharges. The erosion of the electrode material takes place mainly during this stage, when electric energy is pumped into the electrodes. The numerous ionic nitrogen lines shown in Fig. 2 correspond to this stage [25], which is the evidence of the high temperature and electron concentration existing in the electrode gap. The duration of the arc stage depends on the resistance, capacitance and inductance of the discharge loop and is about 6 μs for the present SDG. Even though the generation of metal vapor is less significant after this stage, the previously atomized material still has a rather high temperature as evidenced by the prolonged light emission from the spark gap. The intensity evolution of a typical atomic copper line (521.82 nm) is also shown in the inset of Fig. 2. It can be seen that the emission intensity peaks around 6 μs that is about the end of the arc stage and also when material erosion terminates. After this point in time, the intensity of the emission continuously decreases and finally fades away in about 11-12 μs after the onset of the breakdown. The emission spectrum acquired in the afterglow phase is not influenced by erosion, only by the conditions of the discharge-free gap.

In the following, the effect of the gap size and

the charging current will be shown on the excited species of the electrode material and the carrier gas existing in the spark gap. In order to investigate the generality of the optical properties of the process, experiments were performed both by using Au and Cu electrodes which were shown to have very different erosion properties [33]. Even though the monitoring of the emission from the metal atoms is the most important from the point of view of NP generation, the main component of the spark plasma is the carrier gas, so emission of atomic nitrogen is also discussed here. To this end, the intensity (which is defined as the area under the spectral line profile) of selected atomic copper, gold and nitrogen lines (521.82 nm, 746.83 nm and 746.83 nm, respectively) was measured in the afterglow stage of the spark (more precisely, in the temporal window of about 5-15 μs after the onset of the breakdown). The temporally resolved spectra were mathematically summed in the above mentioned temporal window in order to get a
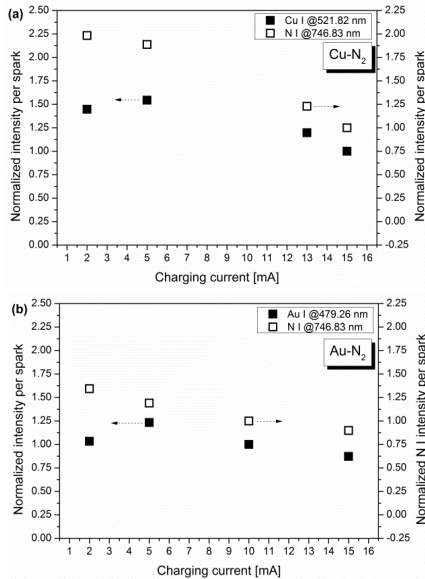
cumulated spectrum representing the afterglow only. Considering the spark repetition rate (SRR) values used in the present study and the length of the afterglow stage we can assume that consecutive sparks are optically independent from each other, so the emission intensity of a single spark does not depend on the SRR. Therefore the emission intensity data here are always shown to be normalized to a single spark.

As can be seen in Fig. 3, the intensity of atomic metal and gas spectral lines follows very similar trends in case of both Cu and Au electrodes. The atomic nitrogen emission decreases monotonously while the emission of the metal atoms varies via a slight maximum when the charging current is increased.

The variation of the gap size results in a different trend. As it is shown in Fig. 4, the intensity of the N I line increases monotonously with the increase of the gap size, while the emission of metal atoms shows saturation for over about 3 mm gap

Figure 3 Normalized intensity of an atomic nitrogen and copper line as a function of the charging current acquired during sparking between Cu (a) and Au (b) electrodes.
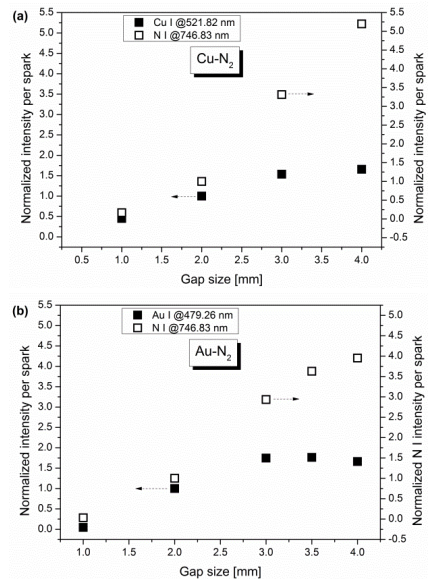(2 mm gap size, 1.68 slm gas flow rate).

Figure 4 Normalized intensity of an atomic nitrogen and copper line as a function of gap size acquired during sparking between Cu (a) and Au (b) electrodes.
(10 mA charging current, 1.68 slm gas flow rate).

sizes for both type of electrodes.

Figure 3 and 4 clearly show that the control parameters of the SDG (such as the gap size and the charging current) affect the optical emission of the spark. These results obtained in nitrogen atmosphere with different metal electrodes exhibit very similar trends, however the emission of atomic nitrogen behaves differently from that of the atomic gold and copper.

3.2 Nanoparticles emitted by the SDG

The nanoparticle production of the SDG was also characterized by using an SMPS. Figure 5 illustrates the effect of charging current on the size distribution of Cu and Au NPs generated in the SDG. The mobility size distribution of the NPs follows log-normal distribution with a modus in the range of 18-30 nm and 21-45 nm for Cu and Au,

respectively. Both the modal diameter and peak concentration increase with the increase of the charging current.

The size distribution of Cu and Au NPs generated at a fixed charging current and varying gap size is shown in Fig. 6. As can be seen in Fig. 6(a), at 1 mm gap the produced Cu NP agglomerates have log-normal size-distribution with a modal diameter of 34 nm. When the gap is increased to 2 mm the modus does not change, only the concentration increases. By further increasing the gap both the modus and the peak concentration shift to smaller values, down to about 19 nm modal diameter at 4 mm gap. A similar trend can be seen during the generation of Au particles (Fig. 6(b)). The modal diameter of the NPs increases from about 32 nm to ~42 nm when the gap is changed from 1 mm to 3 mm and by further increasing the gap the

Figure 5 Mobility size distribution of Cu (a) and Au (b) NP agglomerates generated in nitrogen atmosphere at different charging currents (2 mm gap, 1.68 slm gas flow rate). The log-normal fit of the measured data (squares) is represented by lines.
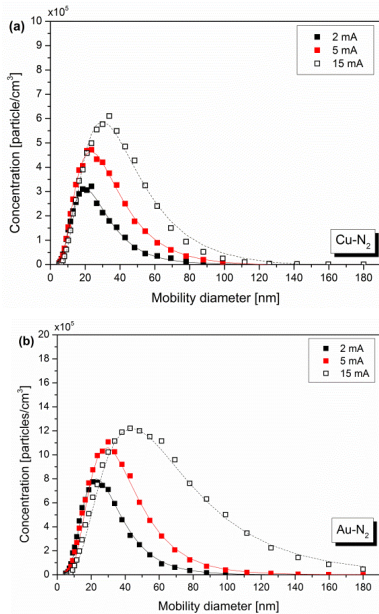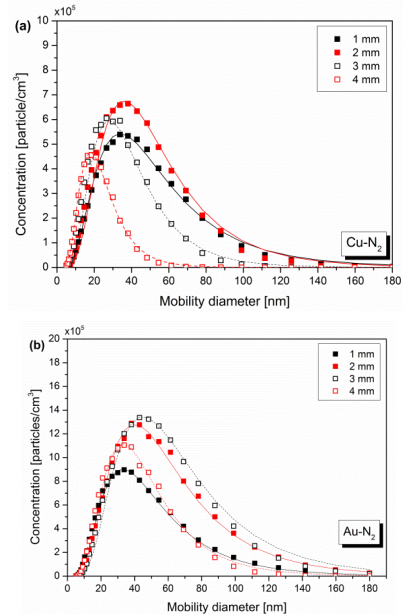

Figure 6 Mobility size distribution of Cu (a) and Au (b) NP agglomerates generated in nitrogen atmosphere at different gaps (10 mA charging current, 1.68 slm gas flow rate). The log-normal fit of the measured data (squares) is represented by lines.

modus of the size distribution shifts to ~32 nm. This means that as opposed to the case of charging current, the gap size variation cannot be used to monotonously tune the size of the NPs generated in the SDG.

4 Discussion

4.1 Quenching rate and particle formation

The intensity of the atomic copper line at 521.82 nm measured as a function of time is replotted in Fig. 7. The temporal evolution of the spectral line intensity suggests that either the concentration or the temperature of the excited species is decreasing. Using the Boltzmann plot method, the plasma temperature can be calculated from the emission spectroscopy data (see the Methods section). As it is shown in Fig. 7 (solid symbols), the peak temperature was found to be about 12000 K, which decreases linearly down to ca. 9000 K in the temporal range where atomic copper emission characterized by a reasonable signal-to-noise ratio. The rate of temperature decrease, the so-called quenching rate, was estimated to be $(5.5\pm0.6)\times10^8$ Ks^{-1}. This value fits into the 10^6-10^9 Ks^{-1} range reported in the literature [34-37]. The fast quenching is believed to be a key component of the exceptional properties of NP generation in SDGs [34].

Our quenching rate value is closer to the higher end of the literature range. Recently Feng *et al.* experimentally estimated the quenching rate in an SDG for gold vapor in nitrogen atmosphere and obtained 7.5×10^6 Ks^{-1} [34], which is almost two orders of magnitude smaller than the value we obtained. They assume that the temperature of the atomic gold vapor is around the boiling point, however as we found it here by evaluating the optical emission spectrum of the spark, the temperature is considerably higher even at the later stages of the spark discharge. Thus we believe that generally the 10^8-10^9 Ks^{-1} values, including our value, are more accurate quenching rate estimates.

Knowing the quenching rate and the peak temperature, one can estimate how long it takes the

metal vapor to cool down to room temperature after the initiation of the breakdown in the gap. This calculation shows that in an SDG producing copper NPs in nitrogen atmosphere –at a gap size of 2 mm, 1.68 slm gas flow rate and charging current of 15 mA – Cu atoms cool down to room temperature in about 25 µs after the onset of breakdown. This is a rough estimate for the end of the cooling stage, which is followed by particle formation. By considering the typical 50-200 Hz SRR values employed in the present study which results in single (oscillatory) spark events in the millisecond characteristic range and the above cooling time which is a few tens of microseconds, one can conclude that NP formation from consecutive single (oscillatory) sparks are independent from each other. By adopting the main mechanisms of particle formation (coagulation, turbulent dilution, turbulent diffusion, laminar diffusion, aggregation) and their respective approximate time ranges from Feng *et al.* [34] the timescale of nanoparticle formation in SDGs starting from the breakdown of the carrier gas can be summarized as it is shown in Fig. 8. The schematic spectra shown at the top of Fig. 8 represents the different emission characteristics typical to the material erosion and the cooling phase. Due to the high energy during the arc stage of the spark the spectrum is dominated by the gas ions while the cooling stage is characterized by atomic copper and nitrogen
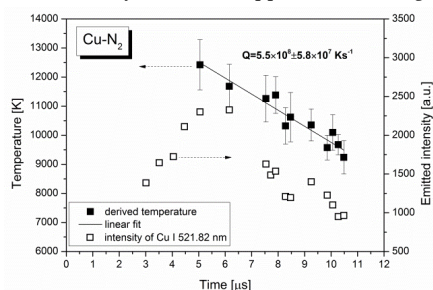

Figure 7 The temporal evolution of the intensity of the Cu I 521.82 nm line (open squares) and the evolution of the temperature of the spark plasma derived from the emission spectra (full squares) (2 mm gap, 1.68 slm gas flow rate, 15 mA charging current).
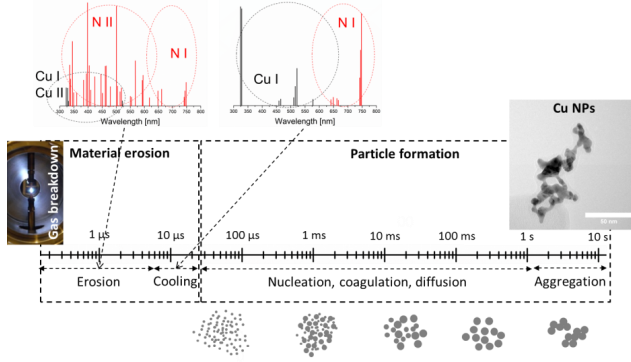
Figure 8 Approximate time scale of NP formation in SDGs from the breakdown of the gap to the formation of NP agglomerates. The typical spectral character of the material erosion is shown together with the main NP formation mechanisms and time-range as adopted from [34]. A typical Cu NP agglomerate is shown in the right inset.

emission. As a result of particle growth steps (schematically shown at the bottom of Fig. 8) aggregated Cu nanoparticles form from the Cu atoms (shown in the right inset of Fig. 8).

4.2 Effect of control parameters

In the conventional SDG setup, the one also used here, the main control parameters are the flow rate of the carrier gas, the distance of the electrodes (gap size) and the capacitor charging current. These parameters affect the NP output of the generator via controlling the energy and the repetition rate of the sparks, and the condensation process [38].

The energy per spark is usually considered to be proportional to the energy stored in the capacitor right before the breakdown [33]. Hence the energy accumulated in the capacitor is:

$$E = \frac{1}{2} C U_{bd}^2 \qquad (1)$$

where C is the total capacitance of the discharge loop and U_{bd} is the breakdown voltage. At a constant pressure and electrode geometry the breakdown voltage predominantly depends on the gap size, hence the energy per spark is mainly determined by the gap size. At a fixed gap, the SRR can be varied by changing the charging current as described by Eq. 2 [33]:

$$SRR = \frac{I_{ch}}{C U_{bd}} \qquad (2)$$

where I_{ch} is the current charging the capacitor, as supplied by the power supply (which will be denoted as charging current). It should be noted that in the present case the increase of SRR results in decreasing breakdown voltage and hence decreasing spark energy. This is most probably due to the "memory effect" of the gap that is charge carriers left behind by the preceding spark are accumulated in the gap thereby lowering breakdown voltage as compared to the single spark (or low frequency) case [39]. The variation of the measured breakdown voltage as a function of the gap size as well as the charging current measured during sparking between Cu electrodes is shown in Fig. 9(a). As can be seen in Fig. 9(a) the breakdown voltage is increasing linearly with the increase of the gap size in qualitative agreement with Paschen's law [40]. The increasing charging current and hence increasing SRR result in a linearly decreasing breakdown voltage. The energy per spark calculated from the breakdown voltage using Eq. 1 and the measured SRR is shown in Fig. 9 (b) and (c), respectively as a function of the gap size and the charging current. As expected from Fig. 9(a) and Eq. 1, the energy per spark increases quadratically with the increase of the gap size and decreases with the increase of the charging current (Fig. 9(b)). The SRR however decreases with an increasing gap and increases quasi linearly with an increasing charging
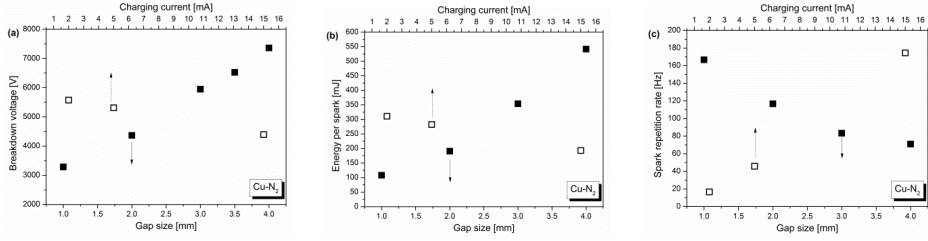
Figure 9 The variation of the breakdown voltage (a), energy per spark (b), and spark repetition rate (c) as a function of gap size at 10 mA charging current and as a function of the charging current at 2 mm gap in case of Cu electrodes in nitrogen atmosphere.

current, as dictated by Eq. 2. Similar behavior was observed for gold electrodes as well.

The tendencies shown in Fig. 9 can be used to interpret the variation of the size distribution of the generated NPs as a function of the charging current. The variation of the charging current results in the variation of the *SRR* (Fig. (9)). Increased *SRR* produces more eroded material per second, which results in higher particle concentration, more pronounced aggregation and larger modal diameter of the generated NPs [33, 41]. This qualitatively explains the trends shown in Fig. 5, namely that both the diameter and the concentration of the generated Au and Cu NPs increases with increasing charging current. The *SRR* depends more strongly on the charging current than spark energy (cf. Fig. 9(b) and (c) which results in an overall increasing trend in the particle diameter.

By changing the gap size at a fixed charging current, both the *SRR* and the energy per spark is changing significantly. As it was shown in Fig. 6, the diameter and the concentration of the generated NPs reach a peak value and start to decrease when the gap size is increased for both Cu and Au electrodes. This behavior is the combined effect of the variation of the *SRR* and the energy per spark at different gaps as shown in Fig. 9(b) and (c). The spark energy strongly increases with increasing gap, while the *SRR* decreases. The higher the energy per spark the more material is eroded from the electrodes [33, 42], which in turn increases the vapor concentration in the gap. This can be seen in

the size distributions measured at 1 mm and 2 mm gaps for Cu, and in the gap range of 1-3 mm for Au (cf. Fig. 6). However, at larger gaps the increased erosion rate caused by the higher energy per spark apparently cannot compensate for the diminishing effect of the decreasing *SRR* (cf. Fig. 9(c)), which decreases the total particle concentration.

On one hand, we suggest that the properties of the NP agglomerates (generated at different conditions) reflect the combined effect of the SRR and the energy per spark. On the other hand, the mass of the metal vapor eroded by a single spark is assumed to be defined by the energy per spark [42] and OES can be used to gain in situ information on the erosion process in this regard. If we assume that the optical emission of the spark plasma depends on the energy per spark, the atomic emission intensities (shown in Fig. 3-4) can be presented together on the same graph regardless of whether the particular energy per spark value was achieved via varying the gap size, the charging current, or both. Since the measured absolute intensity values depend on the actual conditions of the light collection (e.g. the optical system, integration time, gain factor, averaging, etc.) to a great extent the spectra measured in different experimental runs should be scaled in order to make trends comparable. To this end, each measurement series was performed to contain overlapping energy values which could be used to normalize the acquired spectra to the same spark energy.
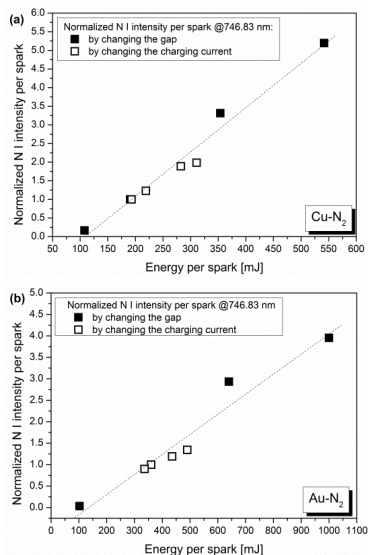
Figure 10 Normalized intensity of an atomic nitrogen line as a function of the energy per spark acquired during sparking between Cu (a) and Au (b) electrodes. (Varying gap and charging current values, 1.68 slm gas flow rate.)

Since the concentration of the atoms of the carrier gas (here nitrogen) exceeds the concentration of the atoms of the electrode material in the spark gap by several orders of magnitude [24], it seems logical to examine the effect of the energy per spark on the emission of nitrogen atoms. The normalized intensity of a typical atomic N line measured at different spark energies during sparking between Cu and Au electrodes is shown in Fig. 10. The points represented by closed symbols were obtained when the spark energy was varied via changing the gap size, while the open symbols represent intensities measured at energy per spark values obtained by the variation of the charging current. As it is illustrated by the fitted dashed line, the overall trend of the emission intensity is linear in the entire energy range studied, meaning that nitrogen atoms emit more light when the spark energy is increased, regardless of whether this increase is realized via adjusting the gap or the charging current. This also justifies our previous assumption on the dependence of the emission

intensity on the spark energy. As can be seen in Fig. 10 (a) and (b) the observed linear correlation applies to both electrode materials studied.

As it is shown in Fig. 11, the emission of metal atoms behaves differently from that of the nitrogen. The emission intensity of Cu I increases roughly linearly up to about 300 mJ (by varying either the gap or the charging current), after which the increasing tendency continues to grow much less steeply, or even saturates (Fig. 11(a)). A similar trend can be seen in Fig. 11(b) for Au electrodes.

The intensity of a spectral line mainly depends on the temperature and the concentration of the given species (see the Methods section). If we assume that the spark is in local thermodynamic equilibrium during the spectral acquisition (it was recently shown that LTE exists in most of the afterglow stage of a spark used for Cu NP generation in Ar atmosphere [24]), it follows that nitrogen and metal atoms exist in the same spatial region have the same temperature. This suggests that the difference between Fig. 10 and 11 should be mainly attributed to the concentration difference of the two species. Nitrogen atoms are present in the spark gap before each spark event at a constant concentration while copper or gold atoms are only produced during sparking. Therefore Fig. 11 suggests that after a certain threshold value, the energy is utilized less efficiently for increasing the concentration of metal atoms. As it is indicated in Fig. 11(a) and Fig. 9(b), this threshold energy is reached when the gap is increased from 2 mm to 3 mm in case of Cu NPs. This correlates well with the total concentration (and the diameter) of the generated particles – as measured by the SMPS – which started to decrease between 2 mm and 3 mm gap sizes despite of the monotonously increasing energy per spark (cf. Fig. 6(a)). Similarly, the breaking point of the linear trend shown in Fig. 11(b) corresponds to a gap of 3 mm in case of Au electrodes, which correlates well with the peak concentration and the modal diameter of the generated Au NPs (cf. Figure 6 b).

Although the eroded metal vapor does not directly correspond to the total particle concentration or diameter, they are related to each
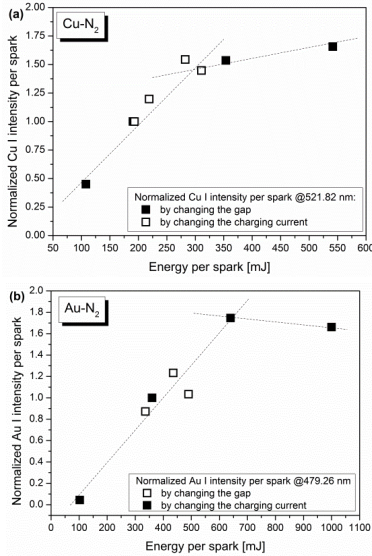
Figure 11 Normalized intensity of an atomic Cu (a) and Au (b) line as a function of the energy per spark acquired during sparking under nitrogen atmosphere. (Varying gap and charging current values, 1.68 slm gas flow rate.)

other. As it was shown e.g. by Byeon *et al.* the more material is eroded in unit time the higher the concentration and the larger the diameter of NPs will be [43].

OES results suggest that the concentration of metal vapor produced in the SDG only can be increased monotonously by increasing the spark gap and hence the energy per spark up to a certain threshold energy. Therefore, it is qualitatively understandable why the total NP concentration and hence the modal diameter follow the *SRR* instead of the more steeply increasing energy per spark curve after a certain gap size. In the present study the above mentioned trends were confirmed both for Cu and Au electrodes – which are known to have substantially different erosion properties [33] – which strengthens the generality of the process. It should be noted that the exact value of the threshold energy depends on the electrode material used. This energy is about 300 mJ for Cu and ~600 mJ for Au (cf. Fig. 11(a) and (b)). Tabrizi *et al.* reported the mass loss of Au electrodes as a

function of the spark energy and reported on a linear trend [33]. However the highest energy value was about 150 mJ in their experiments, which is well below the energy limit derived in the present work, i.e. it is still in the linear domain. Horvath and Gangl investigated the effect of the spark energy on the mass concentration of carbon particles produced in a modified SDG [42]. They observed a tendency similar to that is shown in Fig. 11(a) or (b) exhibiting a threshold energy value after which the mass concentration of the particles starts to saturate. The energy limit corresponding to the saturation was found to be about 10 mJ in their experiments with carbon particles [42]. This suggests that the tendencies of the electrode erosion revealed by OES are consistent with the literature and describe a general process which depends on the exact conditions of the nanoparticle production and the material of the generated NPs.

5 Conclusions

In the present work, we performed optical emission spectroscopic measurements on the plasma of a spark discharge nanoparticle generator (SDG) and complemented those with particle characterization for the generation of copper and gold nanoparticles (NPs) in nitrogen atmosphere.

The emitted light of the spark was spectrally resolved and acquired with 50 ns temporal resolution. The initial stages of the evolution of the spark plasma are characterized by the intense emission of the atoms and ions of the carrier gas. As the current flowing in the spark gap ceases, atomic spectral lines of the electrode material and the gas atmosphere start to dominate the emission spectrum. The erosion of the electrode material takes place in the arc stage of the discharge, more specifically in the first 6 μs and followed by the cooling of the metal vapor in the afterglow stage, which lasts for about 25 μs after the onset of the breakdown. The optical emission of the species in the spark gap collected during the cooling of the metal vapor varies with varying control parameters (i.e. charging current and gap size) of the SDG. More importantly, it was shown that the changes in

the optical emission are determined by the energy per spark, regardless of whether it was achieved via changing the spark gap or the charging current. The intensity of atomic spectral lines of N increases with increasing energy per spark. However, the intensity of emission lines of metal atoms – both Cu and Au – proceeds towards a plateau at a threshold energy. This suggests that the concentration of metal vapor produced in the SDG can only be increased up to a threshold value via increasing the spark energy, above which it levels off.

It was also shown for Cu that time-resolved emission spectra can be used to derive the temporal variation of plasma temperature. From the rate of temperature drop in the cooling (afterglow) phase of the process, the quenching rate of the Cu atoms was derived to be $(5.5\pm0.6)\times10^8$ Ks^{-1}. Such a fast quenching implies that the metal vapor generated in the first approx. 6 µs of the process cools down to about room temperature in as short as ~25 µs after the onset of the breakdown. In other words, this result provides a rough estimate for the temporal starting point of Cu NP generation.

Agglomerated Cu and Au NPs generated during the operation of the SDG were meticulously sampled by an SMPS. The variation of the mobility diameter and the peak concentration of the generated NPs were investigated as a function of two control parameters of the SDG, namely the gap size and the charging current of the capacitor bank. Cu and Au particles with modal diameter in the range of 18-30 nm and 21-45 nm were generated, respectively. Both the peak concentration and the modus of the size distribution of the generated particles increase linearly with increasing charging current via the variation of the spark repetition rate (SRR). The tendencies obtained for the variation of the electrode gap show a peak size at 2 mm and 3 mm with mobility diameters of 34 nm and 42 nm for Cu and Au, respectively, is the result of the combined effect of SRR and spark energy.

The energy corresponding to the gap size at which the mobility diameter and the concentration of the generated NPs peak, coincides neatly with the threshold energy determined from the optical emission of metal atoms. This is our most direct

evidence for the strong correlation between the optical emission of the spark plasma and the properties of the NPs generated in the SDG. This, on one hand, demonstrates the suitability of OES as a non-invasive *in-situ* monitoring method, and on the other, allows for a more conscious optimization of NP generation.

6 Methods

Optical emission spectroscopy (OES) relies on the phenomenon that excited atoms and ions emit a unique emission spectrum when optically de-excite. The emitted intensity of an optical transition between two energy levels (i→j) can be written as:

$$I_{ij} = h\nu_{ij}A_{ij}n_i \qquad (3)$$

where A_{ij} is the transition probability, h is Planck's constant, ν_{ij} is the frequency of the transition, and n_i is the number concentration of the given species in the upper energy level (indicated by index i). As it can be seen in Eq. 3, the emission intensity depends on the population of the upper energy level of the transition. If we can assume that the studied system is in local thermodynamic equilibrium (LTE), which practically means that in a certain spatial point the plasma can be characterized by a single temperature, the population of each excited state obeys the Boltzmann distribution. Consequently, the emitted intensity can be written as:

$$I_{ij} = h\nu_{ij}A_{ij}\frac{1}{Z}g_i n e^{\left(\frac{-E_i}{kT}\right)} \qquad (4)$$

where Z is the partition function, g_i and E_i are the statistical weight and the energy of the excited level, respectively, k is the Boltzmann constant, T is the excitation temperature, and n is the number concentration of the studied species (i.e. the net population of every energy levels). Equation 4 shows that under LTE conditions the intensity of any spectral line belonging to a given species (i.e. atoms or ions) depends on the temperature and the total number concentration of the studied species. This relation can be used to interpret the emission spectra generated in the SDG.

If we rearrange Eq. 4, it becomes apparent that data points for different spectral lines of a selected species should scatter around a straight line when

$\ln\left(\frac{I_{ij}}{\nu_{ij}g_i A_{ij}}\right)$ is plotted as a function of E_i:

$$\ln\left(\frac{I_{ij}}{\nu_{ij}g_i A_{ij}}\right) = \ln\left(\frac{hn}{Z}\right) - \frac{E_i}{kT} \qquad (5)$$

The slope of the line as defined by Eq. 5 can be used to derive the excitation temperature of the given species. This procedure is called the Boltzmann plot method (see e.g. [25, 44]), which is widely used for calculating the so-called excitation temperature of a plasma in LTE. Optically well resolved, interference- and self-absorption-free spectral lines need to be selected for the above calculations. The atomic data of transitions selected for this study were taken from the NIST database [45] and are tabulated in Table 1.

Table 1 Atomic data of selected Cu I transitions; λ_{ij} is the emission wavelength, E_i and g_i are the energy and the statistical weight of the upper level and A_{ij} is the transition probability of the transitions.

Spectrum	λ_{ij} (nm)	E_i (cm^{-1})	g_i	A_{ij} (10^7 s^{-1})
Cu I	521.82	49942	6	7.50
Cu I	465.11	62403	8	3.80
Cu I	510.55	30783	4	0.20
Cu I	515.32	49935	4	6.00
Cu I	578.21	30535	2	0.17
Cu I	458.70	62948	6	3.20

Spectral data processing and calculations were carried out by using Origin (Originlab Co.) and our purpose-made scripts written in MATLAB (MathWorks, Inc.).

Acknowledgements

References

[1] Biskos, G.; Vons, V.; Yurteri, C. U.; Schmidt-Ott A. Generation and sizing of particles for aerosol-based nanotechnology. *KONA Powder Part. J.* **2008**, *26*, 13-35.

[2] Wegner, K.; Pratsinis, S. E. Scale-up of nanoparticle synthesis in diffusion flame reactors. *Chem. Eng. Science*, **2003**, *58*, 4581-4589.

[3] Meuller, B. O.; Messing, M. E.; Engberg, D. L. J.; Jansson, A. M.; Johansson, L. I. M.; Norlén, S. M; Tureson, N.; Deppert, K. Review of spark discharge generators for production of nanoparticle aerosols. *Aerosol Sci. Technol.* **2012**, *46*, 1256-1270.

[4] Magnusson, M. H.; Deppert, K.; Malm, J. O.; Bovin, J. O.; Samuelson, L. Size selected gold nanoparticles by aerosol technology. *Nanostruct. Mater.* **1999**, *12*, 45-48.

[5] Schmidt-Ott, A.; Schurtenberger, P.; Siegmann, H. C. Enormous yield of photoelectrons from small particles. *Phys. Rev. Lett.* **1980**, *45*, 1284-1287.

[6] Kato M. Preparation of ultrafine particles of refractory oxides by gas evaporation method. *Jpn. J. Appl. Phys.* **1976**, *15*, 757-760.

[7] Schwyn, S.; Garwin, E.; Schmidt-Ott, A. Aerosol generation by spark discharge. *J. Aerosol Sci.* **1998**, *19*, 639-642.

[8] Hontanón, E.; Palomares, J. M.; Stein, M.; Guo, X.; Engeln, R.; Nirschl, H.; Kruis, F. E. The transition from spark to arc discharge and its implications with respect to nanoparticle production. *J. Nanopart. Res.* **2013**, *15*, 1957.

[9] Pfeiffer, T. V.; Feng, J.; Schmidt-Ott, A. New developments in spark production of nanoparticles. *Adv. Powder Technol.* **2014**, *25*, 56-70.

[10] Borra, J.-P. Nucleation and aerosol processing in atmospheric pressure electrical discharges: Powders production, coatings and filtration. *J. Phys. D.* **2006**, *39*, R19–R54.

[11] Borra, J.-P.; Goldman, A.; Goldman, M.; Boulaud, D. Electrical discharge regimes and aerosol production in point-to-plane DC high pressure cold plasmas: Aerosol production by electrical discharges. *J. Aerosol Sci.* **1998**, *29*, 661–674.

[12] www.buonapart-e.eu

[13] Helsper, C.; Molter, W.; Löffler, F.; Wadenpohl, C.; Kaufmann, S.; Wenninger, G. Investigations of a new aerosol generator for the production of carbon aggregate particles. *Atmos. Environ. A*, **1993**, *27*, 1271-1275.

[14] Messing, M. E.; Hillerich, K.; Bolinsson, J.; Storm, K.;

Johansson, J.;. Dick, A. K.; Deppert, K. A Comparative Study of the Effect of Gold Seed Particle Preparation Method on Nanowire Growth. *Nano. Res.* **2010**, *3*, 506–519.

[15] Messing, M. E.; Westerström, R.; Meuller, B. O.; Blomberg, S.; Gustafson, J.; Andersen, J. N.; Lundgren, E.; van Rijn, R.; Balmes, O.; H. Bluhm, *et al.* Generation of Pd model catalyst nanoparticles by spark discharge. *J. Phys. Chem. C* **2010**, *114*, 9257-9263

[16] Kala, S.; Theissmann, R.; Rouenhoff, M.; Kruis, F. E. Metal-semiconductor pair nanoparticles by a physical route based on bipolar mixing. *Nanotechnology*, **2016**, *27*, 125604.

[17] Pfeiffer, T. V.; Kedia, P.; Messing, M. E.; Valvo, M.; Schmidt-Ott, A. Precursor-less coating of nanoparticles in the gas phase, *Materials*, **2015**, *8*, 1027-1042.

[18] Bae, Y.; Pikhitsa, P. V.; Cho, H.; Choi, M. Multifurcation Assembly of Charged Aerosols and Its Application to 3D Structured Gas Sensors. *Adv. Mater.* **2017**, *29*, 1604159.

[19] Muntean, A.; Wagner, M.; Meyer, J.; Seipenbusch, M. Generation of copper, nickel, and CuNi alloy nanoparticles by spark discharge. *J. Nanopart. Res.* **2016**, *18*, 229.

[20] Wagner, M.; Kohut, A.; Geretovszky, Zs.; Seipenbusch, M.; Galbacs, G. Observation of fine-ordered patterns on electrode surfaces subjected to extensive erosion in a spark discharge. *J. Aerosol Sci.* **2016**, *93*, 16-20.

[21] Byeon, J. H.; Park, J. H.; Yoon, K. Y.; Hwang, J. Ambient spark generation to synthesize carbon-encapsulated metal nanoparticles in continuous aerosol manner. *Nanoscale,* **2009**, *1*, 339-343.

[22] Nilsson, P. T.; Eriksson, A. C.; Ludvigsson, L.; Messing, M. E.; Nordin, E. Z.; Gudmundsson, A.; Meuller, B. O.; Deppert, K.; Fortner, E. C.; Onasch, T. B., *et al.* In-situ characterization of metal nanoparticles and their organic coatings using laser vaporization aerosol mass spectrometry, *Nano Res.* **2015**, *8,* 3780–3795.

[23] Ludvigsson, L.; Meuller, B. O.; Messing, M. E. Investigations of initial particle stages during spark discharge. *J. Phys. D.* **2015**, *48*, 314012.

[24] Kohut, A.; Galbács, G.; Márton, Zs.; Geretovszky, Zs. Characterization of a copper spark discharge plasma in argon atmosphere used for nanoparticle generation. *Plasma Sources Sci. Technol.* **2017**, *26*, 045001.

[25] Boumans, P. W. J. M. Excitation of spectra. In *Analytical Emission Spectroscopy*. Grove E. L. Ed.; Marcel Dekker: New York, 1972.

[26] Scheeline, A. Sampling Processes in Emission Spectroanalytical Chemistry. *Mikrochim. Acta*, **1990**, *I*, 247-285.

[27] Palomares, J. M.; Kohut, A.; Galbács, G.; Engeln, R.; Geretovszky, Zs. A time-resolved imaging and electrical study on a high current atmospheric pressure spark discharge. *J. Appl. Phys.* **2016**, *118*, 233305.

[28] Walters, J. P. Historical advances in spark emission spectroscopy. *Appl. Spectrosc.* **1969**, *23*, 317-331.

[29] Scheeline, A.; Coleman, D. M. Direct Solids Elemental Analysis: Pulsed Plasma Sources. *Anal. Chem.* **1987**, *59*, 1185-1196.

[30] Raizer, Y. P. *Gas discharge physics;* Springer-Verlag: Berlin Heidelberg, 1991.

[31] Mandelstam, S. Excitation of the spectrum in a spark discharge. *Spectrochim. Acta*, **1959**, *15*, 255-271.

[32] Walters, J. P.; Malmstadt, H. V. Emission Characteristics and Sensitivity in a High-Voltage Spark Discharge. *Anal. Chem.* **1965**, *37*, 1484-1503.

[33] Tabrizi, N. S.; Ullmann, M.; Vons, V. A.; Lafont, U., Schmidt-Ott, A. *J. Nanopart. Res.* **2009**, *11*, 315-332.

[34] Feng, J.; Huang, L.; Ludvigsson, L.; Messing, M. E.; Maisser, A.; Biskos, G.; Schmidt-Ott, A. General Approach to the Evolution of Singlet Nanoparticles from a Rapidly Quenched Point Source. *J. Phys. Chem. C*, **2016**, *120*, 621−630.

[35] Berkowitz, A. E.; Walter, J. L. Spark Erosion: A Method for Producing Rapidly Quenched Fine Powders. *J. Mater. Res.* **1987**, *2*, 277−288.

[36] Jenkins, N. T.; Eagar, T. W. Submicron Particle Chemistry: Vapor Condensation Analogous to Liquid Solidification. *JOM*, **2003**, *55*, 44−47.

[37] Martinen, H.; Tholl, H. Untersuchung Der Temperatur Und Der Expansion von Funkenkanalen in H_2 Bei Variabler Energiezufuhr. *Z. Naturforsch.* **1970**, 25, 430−439.

[38] Feng, J.; Biskos, G.; Schmidt-Ott, A. Toward industrial scale synthesis of ultrapure singlet nanoparticles with controllable sizes in a continuous gas-phase process. *Sci. Rep.* **2015**, *5*, 15788.

[39] Crawford, F. W.; Edels, H. The reignition voltage characteristics of freely recovering arcs. *Proc. IEE*, **1960**, *107*, 202-212.

[40] Fridman, A.; Kennedy, L. A. *Plasma Physics and Engineering (2nd edition)*; CRC Press: Boca Raton, 2011.

[41] Boddu, S. R.; Gutti, V. R.; Ghosh, T. K.; Tompson, R. V.; Loyalka, S. K. Gold, silver, and palladium nanoparticle/nano-agglomerate generation, collection, and

characterization. *J. Nanopart. Res.* **2011**, *13*, 6591–6601.

[42] Horvath, H.; Gangl, M. A low-voltage spark generator for production of carbon particles. *J. Aerosol Sci.* **2003**, *34*, 1581-1588.

[43] Byeon, J. H.; Park, J. H.; Hwang, J. Spark generation of monometallic and bimetallic aerosol nanoparticles. *J. Aerosol Sci.* **2008**, *39*, 888-896.

[44] Aragón, C.; Aguilera, J. A. Characterization of laser induced plasmas by optical emission spectroscopy: A review of experiments and methods. *Spectrochim. Acta B*, **2008**, *63*, 893–916.

[45] http://physics.nist.gov/PhysRefData/ASD/lines_form.html

Paper V

Carbon Nanotube Emissions from Arc Discharge Production: Classification of Particle Types with Electron Microscopy and Comparison with Direct Reading Techniques

Linus Ludvigsson[1,2]*, Christina Isaxon[2], Patrik T. Nilsson[2],
Hakan Tinnerberg[3], Maria E. Messing[1], Jenny Rissler[2], Vidar Skaug[4],
Anders Gudmundsson[2], Mats Bohgard[2], Maria Hedmer[3] and
Joakim Pagels[2]

1.Solid State Physics, Lund University, SE-22100 Lund, Sweden;
2.Ergonomics and Aerosol Technology, Lund University, SE-22100 Lund, Sweden;
3.Occupational and Environmental Medicine, Lund University, SE-22100 Lund, Sweden;
4.National Institute of Occupational Health, P.O. Box 8149 Dep, 0033 Oslo, Norway
*Author to whom correspondence should be addressed. Tel: +46 (0)46 222 7689; fax: +46 (0)46 222 3637;
e-mail: linus.ludvigsson@ftf.lth.se
Submitted 2 October 2014; revised 2 December 2015; revised version accepted 7 December 2015.

ABSTRACT

Introduction: An increased production and use of carbon nanotubes (CNTs) is occurring worldwide. In parallel, a growing concern is emerging on the adverse effects the unintentional inhalation of CNTs can have on humans. There is currently a debate regarding which exposure metrics and measurement strategies are the most relevant to investigate workplace exposures to CNTs. This study investigated workplace CNT emissions using a combination of time-integrated filter sampling for scanning electron microscopy (SEM) and direct reading aerosol instruments (DRIs).

Material and Methods: Field measurements were performed during small-scale manufacturing of multiwalled carbon nanotubes using the arc discharge technique. Measurements with highly time- and size-resolved DRI techniques were carried out both in the emission and background (far-field) zones. Novel classifications and counting criteria were set up for the SEM method. Three classes of CNT-containing particles were defined: type 1: particles with aspect ratio length:width >3:1 (fibrous particles); type 2: particles without fibre characteristics but with high CNT content; and type 3: particles with visible embedded CNTs.

Results: Offline sampling using SEM showed emissions of CNT-containing particles in 5 out of 11 work tasks. The particles were classified into the three classes, of which type 1, fibrous CNT particles contributed 37%. The concentration of all CNT-containing particles and the occurrence of the particle classes varied strongly between work tasks. Based on the emission measurements, it was assessed that more than 85% of the exposure originated from open handling of CNT powder during the *Sieving, mechanical work-up, and packaging* work task. The DRI measurements provided complementary information, which combined with SEM provided information on: (i) the background adjusted emission

concentration from each work task in different particle size ranges, (ii) identification of the key procedures in each work task that lead to emission peaks, (iii) identification of emission events that affect the background, thereby leading to far-field exposure risks for workers other than the operator of the work task, and (iv) the fraction of particles emitted from each source that contains CNTs.

Conclusions: There is an urgent need for a standardized/harmonized method for electron microscopy (EM) analysis of CNTs. The SEM method developed in this study can form the basis for such a harmonized protocol for the counting of CNTs. The size-resolved DRI techniques are commonly not specific enough to selective analysis of CNT-containing particles and thus cannot yet replace offline time-integrated filter sampling followed by SEM. A combination of EM and DRI techniques offers the most complete characterization of workplace emissions of CNTs today.

INTRODUCTION

Carbon nanotubes (CNTs) were discovered in 1991 (Iijima, 1991). Since then they have gained special interest due to their unique properties. CNTs can consist of either a single graphene cylinder (single-walled CNTs or SWCNTs) or multiple graphene cylinders (multi-walled CNTs or MWCNTs). CNTs can improve properties like durability, strength, flexibility, and electrical and thermal conductivities (Köhler *et al.*, 2008; Wohlleben *et al.*, 2011; Liu and Kumar, 2014) and can thus be incorporated in different materials such as composites, rubbers, plastics, concrete, and fabrics. The increasing demand for CNTs means increased handling and, inevitably, increased risk of occupational exposure to workers. CNTs are high aspect ratio nanomaterials with low density, high surface-to-mass ratio, and are biopersistant in the lungs (Muller *et al.*, 2005), all of which are properties of hazardous nanomaterials. The fibre-like morphological similarity of many CNTs with asbestos is apparent and the need for a proactive approach to the potential risks is indisputable (Sanchez *et al.*, 2010; Murphy *et al.*, 2011).

Inhalation has been identified as the major exposure route (Hedmer *et al.*, 2013; Ma-Hock *et al.*, 2009, 2013; Pauluhn, 2010a; Gustavsson *et al.*, 2011). To the best of our knowledge no toxicological data for human exposure to CNTs currently exists, but animal inhalation studies of both long and short MWCNTs have been shown to have adverse effects in the lungs, such as inflammation, granuloma formation, and fibrosis (Mercer *et al.*, 2010; Ma-Hock *et al.*, 2013; Pauluhn, 2010b; Murphy *et al.*, 2011). It has also been shown in animals that inhalation exposure to some forms of MWCNTs can promote lung cancer (Sargent *et al.*, 2014).

No legally enforced occupational exposure limits (OELs) for CNTs exist, but there are proposals for a benchmark exposure limit for airborne fibrous nanomaterials (e.g. CNTs) with high aspect ratios (>3:1 and length >5 µm) set at 0.01 fibre cm⁻³ from national organizations such as the British Standards Institute (BSI, 2007) and the Institute for Occupational Safety and Health of the German Social Accident Insurance (IFA, 2014). An OEL based on elemental carbon (EC) at 1 µg cm⁻³ as a respirable mass 8-h time-weighted average (TWA-8) concentration has been proposed (NIOSH, 2013).

As long as the research community has not agreed on what dose metric best correlates with the toxicological effects of CNTs, it is crucial to use a multi-metric approach for emission and exposure measurements. One important metric is the particle number concentration of CNT-containing particles achieved by filter-based air sampling methods in combination with electron microscopy (EM) analysis. EM has previously been used in exposure assessment studies (Ogura *et al.*, 2011; Takaya *et al.*, 2012), but there are currently no standardized methods for measuring and counting CNTs on filter samples. The methods used for CNT counting so far are based on the ones for asbestos counting initially set up by WHO (1986, 1997), examples of which are the NIOSH methods 7400 and 7402. Some studies have followed the NIOSH method 7402 (Han *et al.*, 2008; Bello *et al.*, 2008; Lee *et al.*, 2010). Dahm *et al.* (2012) used a modified the NIOSH method 7402, by excluding the steps required for asbestos identification in the EM analysis. It is important to make both full-shift personal exposure measurements (for comparison with suggested exposure limits), and work task-based

emission measurements (to identify the processes in which emissions occur) so that a complete and accurate evaluation of the exposure risk can be performed. Methner *et al.* (2010) have suggested the nanoparticle emission assessment technique (NEAT), based on a combination of direct reading instrumentation (DRI) and filter-based air samples that is both source specific and in the personal breathing zone (PBZ).

In this study, we focus on characterizing airborne emissions of CNT-containing particles during different work tasks and we utilize both real-time aerosol instruments and filter-based air sampling methods. With the DRIs, it is possible to differentiate between background and process-related nanoparticles and to identify the part of a work task that leads to emissions, but they are commonly not specific enough to selectively analyze CNT-containing particles.

So far, most CNT emission and exposure measurements have been performed in facilities where CNTs are produced by chemical vapor deposition (CVD) (Maynard *et al.,* 2004; Bello *et al.,* 2008; Han *et al.,* 2008; Tsai *et al.,* 2009; Lee *et al.,* 2010; Kumar and Ando, 2010). Another method for CNT generation is the arc discharge technique, which is an inexpensive way of producing high-quality CNTs without the use of metal catalysts. The drawback is a high amount of graphite impurities. To the best of our knowledge, there are no published studies of workplace emissions and exposures during CNT production with the arc discharge technique.

The objectives of this study were: (i) to develop and apply a method based on EM for the classification of airborne CNT-containing particles including agglomerates, (ii) to characterize the emissions of CNTs during different stages of production with the arc discharge technique and during purification and functionalization, (iii) to investigate added values by combined characterization with the SEM technique and highly time- and size-resolved direct reading techniques

MATERIAL AND METHODS

Study design

Particle emissions and personal exposure were measured at a small-scale manufacturer that produced MWCNTs with the arc discharge technique. Emission measurements with DRIs and filter sampling were carried out during manufacturing divided into 11 work tasks performed at designated locations (numbered 1–11 in Tables 1 and 3 and Fig. 1). The facility was divided into three areas denoted as the *production laboratory*, *sieving laboratory,* and *purification laboratory*. The *production and sieving laboratories* were adjacent, connected by an open door during the measurements. The *purification laboratory* was situated on a different floor. A schematic layout of the workplace is provided in Fig. 1.

The measurements were carried out during two consecutive days, the first day in the *production* and *sieving laboratories* (Work Tasks Nos. 1–6) and the second day in the *purification laboratory* (Work Tasks Nos. 7–11). Emission measurements were carried out in close vicinity of the source (<10 cm; near-field), using both filter samplers and DRIs to measure the immediate emissions. Simultaneous measurements were carried out with the DRIs in the background zone (>3 m from source; far-field). In addition, full-shift personal exposure measurements were carried out, as described in detail by Hedmer *et al.* (2014).

Method of production and description of work tasks

The arc discharge method produces MWCNTs by means of a continuous electrical discharge between two graphite electrodes within a closed reaction chamber (Gamaly and Ebbesen, 1995). The discharge evaporates the electrode material from the anode followed by deposition on the opposite electrode—the cathode or counter electrode. The core of the deposited material contains the CNTs but also high amounts of carbonaceous impurities and needs to be purified.

After the reaction is completed, there is the *Opening of the reactor* (Work Task No. 3 in Fig. 1) and *Cleaning of the reactor* (Work Task No. 4) by blowing high pressure air into it. After removing the CNT-enriched electrodes a table saw is used for *Cleaving of deposits* (Work Task No. 1) and *Harvesting* (Work Task No. 2) of the CNT-rich material is carried out manually.

The core material is further dispersed in the *sieving laboratory* and sorted with a stack sieve. *Sieving, mechanical work-up, and packaging* (Work Task No. 5) is conducted in a room adjacent to the *production laboratory*. The process, which is not enclosed, is performed by automated shaking of the stack of sieves. No pressurized air is used. The fractions of desired size are selected and this material is labeled 'As produced'. In the same room,

Table 1. List of work tasks performed during production and purification of CNTs and sampling time/length of work task

| Work task	Task number/location in Fig. 1	Description of sampled work task	CNT-containing material handled during work task	Sampling time (min)
Cleaving of deposits (morning)	1	Generated deposits/electrodes cleaved with a table saw	Yes	11
Cleaving of deposits (afternoon)	1	Generated deposits/electrodes cleaved with a table saw	Yes	13
Harvesting	2	CNT material is harvested from the cleaved electrodes.	Yes	17
Opening of the reactor	3	The reactor is opened after finished production	Yes	8
Cleaning of the reactor parts I and II	4	High pressure air is blown into the closed reactor. A vacuum cleaner is used to draw air out of the reactor	No	8 + 4
Sieving, mechanical work-up and packaging	5	Harvested material is dispersed and placed in flasks with a magnetic stirrer. The material is then funnelled through a stack sieve. Several iterations are performed	Yes	53
Lathe machining	6	Graphite electrodes are prepared for production using a lathe machine. Visible chunks of graphite are released to air	No	13
Purification part I	7	Chemical purification in several steps; a furnace was opened during the task	Yes	63
Purification part II	8	Activities performed inside a fume hood	Yes	70
Functionalization part I	9	Activities performed inside a fume hood	Yes	13
Functionalization part II	10	Activities performed inside a fume hood	Yes	24
Grinding	11	Coarse functionalized material was ground with mortar and pestle. Ground material was poured into a vial	Yes	35
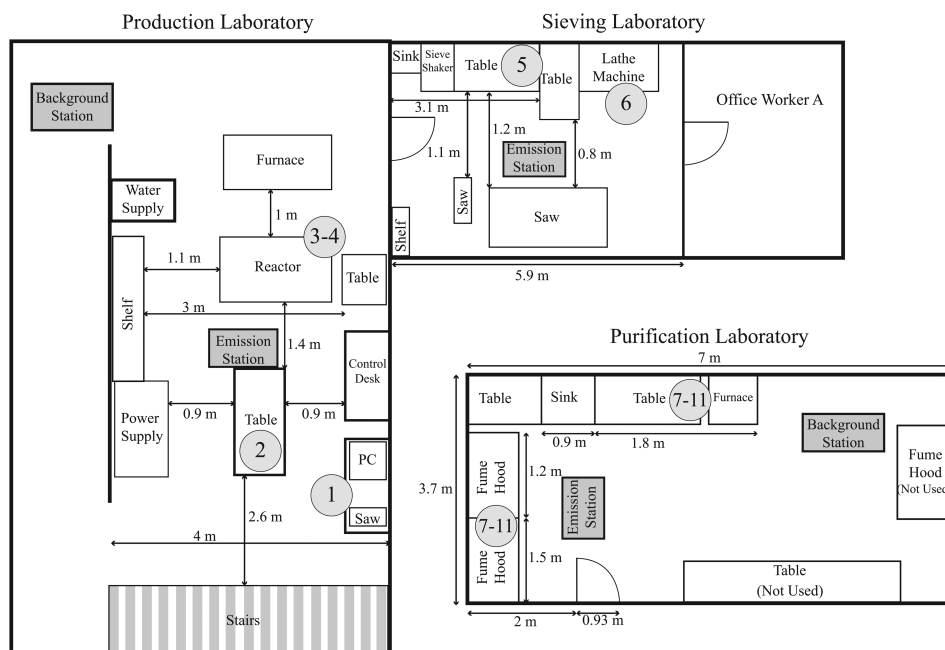
Figure 1   Schematic layout of the facility. Numbers in grey circles correspond to work tasks in Table 1. The production and sieving laboratories were located on a different floor from the purification laboratory.

the graphite electrodes used for the production process are prepared by *Lathe machining* (Work Task No. 6) to fit in electrode holders inside the reactor.

The 'As produced' material is further processed in the *purification laboratory*, where it follows a series of steps from raw material to purified CNTs. The purification process involves dispersion of the material in a liquid and several steps of chemical purification. The material is dried in a furnace. Some of the purified material is used for production of functionalized CNTs. The processes of *Purification I and II, Functionalization I and II,* and *Grinding* are performed on location/Work Tasks Nos. 7–11 in Fig. 1 and Table 1.

Direct reading techniques and filter collection
A summary of the particle sampling techniques and sample locations is given in Table 2. The DRI techniques are described in detail in Table 2 and Supplementary material. Briefly, two aerodynamic particle sizers (APS) were used to measure number concentration and size distributions in the large particles range (dp > 0.5 μm). For the small particle

range (dp > 0.01 μm), a condensation particle counter (CPC) measured the total number concentration in the emission zone, and a scanning mobility particle sizer (SMPS) provided particle size distributions and total particle number concentrations in the background zone. The APS and CPC used a time resolution of 5 s and the SMPS 180 s. The location of the emission and background measurement stations, listed in Table 2, can be seen in the schematic of the facility in Fig. 1. Sampling was carried out continuously in the background station, throughout the work shift.

Respirable fractions of particles in the emission zone were collected for SEM analysis during each work task. Workers also carried filter samplers in the breathing zone for SEM analysis; sampling took place throughout the full work shift. Two full-shift filter samples were collected each day, one from the worker in the *production* and *sieving laboratories*, and one swapped between the two workers in the *purification laboratory*. Further descriptions of the personal exposure measurements and methods are provided by Hedmer *et al.* (2014).

Table 2. List of DRIs and filter-based sampling equipment used in the emission measurements during production and purification of CNTs

Instrument/equipment	Measured/collected size range	Location	Sample flow ($l\,min^{-1}$)
Aerodynamic particle sizer (APS 3321 TSI)	Size distribution: >0.5 μm (aerodynamic diameter)	Emission and background (two units)	1.0 (5.0)
Condensation particle counter (CPC 3022 TSI)	Total nbr. conc. >0.007 μm	Emission	0.3
Respirable sampling on polycarbonate membrane filter followed by SEM analysis	0.04 (geometric diameter)–4 (aerodynamic diameter) μm	Emission, personal breathing zone	2.2
Scanning mobility particle sizer (SMPS Model 3071 TSI)	Size distribution: 0.010–0.51 μm (mobility diameter)	Background	1.0 (sheath air 6.0)

Respirable samples were collected on 37-mm track-etched polycarbonate membrane filters with a pore size of 0.4 μm (Nuclepore™ product no. 225–1609, SKC Inc., Eighty Four, PA, USA) using cyclones (BGI4L, BGI Inc., Waltham, USA) mounted in plastic three-piece filter cassettes. A sample flow rate of 2.2 l min^{-1} was provided by an Escort ELF pump (MSA, Pittsburgh, PA, USA). The flow rate was checked prior to and after sampling by a primary calibrator (TSI Model 4100, TSI Inc., Shoreview, MN, USA).

Sampling of CNTs using cyclones is recommended by NIOSH (2013). Jones (2005) have shown that the sampling of respirable fibres and particles results in accurate and reliable sampling for the cyclone used as penetration, e.g. depends solely on fibre diameter, independent of fibre length through the cyclone and also led to an even distribution on the filter downstream the cyclone. This observation is important because orientation effects can potentially cause large differences in the aerodynamic diameters assigned for different measurement techniques. The use of respirable sampling may result in the exclusion of some larger CNT-containing agglomerate particles that would have had a low probability to reach the target (pulmonary) region.

Data analysis

Background correction and averaging for DRIs
We subtracted the background particles that were not emitted from the work tasks for the DRIs in two different ways. Spatial background subtraction denotes the difference between the instrument in the emission zone and the instrument at the background station for the same measurement period. Temporal background subtraction denotes the difference between the work task period of the measurement and a three minute period before the work task for the same instrument. Spatial background subtraction was only carried out for the APS measurements, while the temporal background subtraction is given for both the APS and the CPC. The negative values as seen in Table 3 should be interpreted as no significant increase of the average concentration; similarly, increases by less than about 20% relative to the background may be due to variability in the background concentration. The values reported from the DRIs are averages of the periods that were defined as work tasks. The periods are marked in Fig. 2.

SEM method for classifying and counting airborne CNTs
Most airborne CNTs do not have the typical fibre dimensions required by WHO (length > 5 μm and length:width ratio >3:1) due to agglomeration (Dahm *et al.*, 2012). Consequently, we decided not to apply the WHO standard fibre counting method and instead develop an electron microscopic method for the analysis of airborne CNTs. We manually counted all CNT-containing particles imaged by SEM. If several fibres were attached to or constituted a particle, it was counted as *one* CNT-containing particle. This differs from how asbestos is counted (OH Learning, 2010).

Table 3. Emission concentrations from DRI instruments and results of SEM analysis from all work tasks. Shaded columns are background corrected; clear columns are total particle concentrations (respirable fractions) including background particles. Temporal background corrected denotes adjustment relative to a background period from the same instrument before the task. Spatial background corrected denotes adjustment relative to the simultaneous background station measurement with an identical instrument

Work Task	Location in [Fig. 1]	Direct reading instruments				SEM analysis		
		>0.01 μm (CPC) temporal background corrected[a]	>0.5 μm (APS) temporal background corrected[a]	>0.5 μm (APS) spatial background corrected[b]	Total (35 nm–4μm)[c]	CNT-containing particles[d]		LOD[e]
						All types	Types (1, 2, 3)%	
		#cm⁻³	#cm⁻³	#cm⁻³	#cm⁻³	#cm⁻³		#cm⁻³
Cleaving of deposits (morning | afternoon)	1	39 (1239) | −110(6185)	53 (1.7) | 93 (4.1)	51(2.3) | 89(3.7)	190 ± 5.0	**1.6 ± 0.40**	12, **6**, 82	0.08
Harvesting	2	−112 (1280)	−0.3 (1.9)	−0.7 (2.3)	2000 ± 40	ND[f]	ND, ND, ND	1.8
Opening of the reactor	3	2278 (3588)	146 (1.9)	142 (6.5)	1100 ± 40	ND	ND, ND, ND	1.0
Cleaning of the reactor[g]	4	—	—	—	600 ± 17	ND	ND, ND, ND	2.1
Sieving, mechanical work-up, and packaging	5	45 (928)	21 (2.8)	19 (4.9)	320 ± 4.7	**11 ± 1.0**	41, **18**, 41	0.04
Lathe machining	6	399 (908)	207 (8.2)	211 (4.6)	770 ± 13	**1.2 ± 0.50**	17, **17**, 66	0.20
Purification part I	7	11 760 (3830)	−1.9 (8.8)	−5.2 (12)	160 ± 3.9	ND	ND, ND, ND	0.28
Purification part II	8	−363 (2948)	−0.1 (6.2)	0.03 (10.1)	190 ± 3.2	**0.46 ± 0.15**	11, **ND**, 89	0.02

Table 3. *Continued*

Work Task	Location in Fig. 1	Direct reading instruments				SEM analysis		LOD[e]
		>0.01 μm (CPC) temporal background corrected[a]	>0.5 μm (APS) temporal background corrected[a]	>0.5 μm (APS) spatial background corrected[b]	Total (35 nm–4μm)[c]	CNT-containing particles[d]		
						All types	Types (1, 2, 3)%	
		$\#cm^{-3}$	$\#cm^{-3}$	$\#cm^{-3}$	$\#cm^{-3}$	$\#cm^{-3}$		$\#cm^{-3}$
Functionalization part I	9	−325 (3194)	−2.1 (12.8)	−0.5 (10.3)	290 ± 6.2	**1.0 ± 0.41**	ND, ND, 100	0.1
Functionalization part II	10	1045 (2888)	−1.2 (8.9)	−5.8 (16.0)	160 ± 4.1	ND	ND, ND, ND	0.11
Grinding	11	−238 (3152)	0.18 (6.7)	−4.0 (10.9)	210 ± 4.1	ND	ND, ND, ND	0.08

[a]Values in parentheses are the averaged measured backgrounds 3 min before the work task. [b]Values in parentheses are the measured concentrations from the background station instrument. [c]All measured particles, size detection limit: 35 nm (geometric)–4 μm (aerodynamic, 50% cut off, respirable curve). [d]Any particle with visible CNT content. [e]Level of detection (LOD), the upper 95% one sided confidence limits (95% CLs) of the number concentrations of particles in the air were calculated by assuming that the number of particles on the filter could be described using the Poisson distribution. The CL where the observed CNT cluster count was zero is considered to be the LOD. The method for calculating the 95% CL was based on ISO 10312 (1995). [f]Not detected. [g]Due to the short sampling time, the same filter was used for both parts I and II.
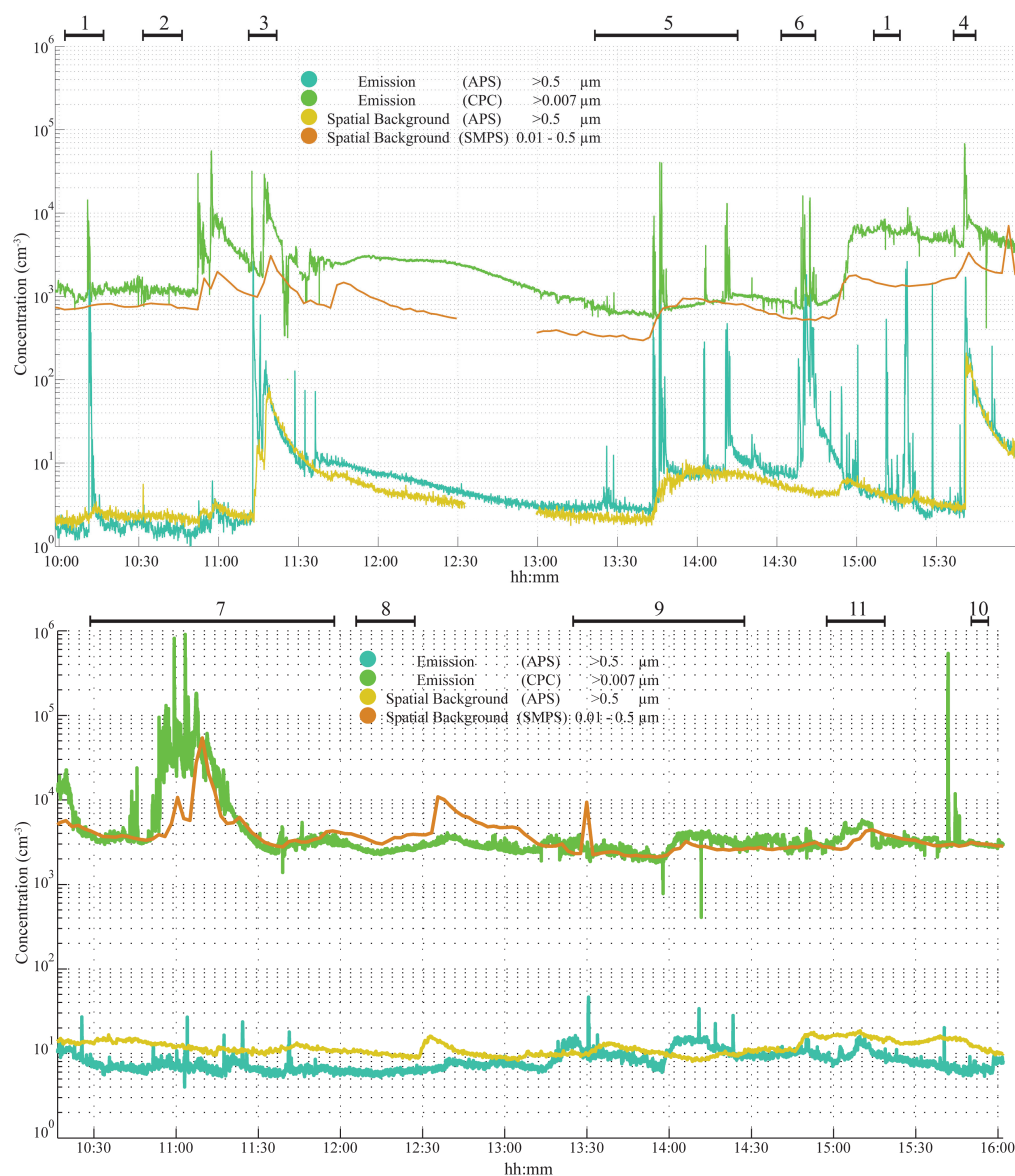
Figure 2   (a) Time series from online instruments measured in the production and sieving laboratories on the first day. Nos. 1–6 refer to Work Tasks: 1. Cleaving of deposits, 2. Harvesting, 3. Opening of the reactor, 4. Cleaning of the reactor, 5. Sieving, 6. Lathe machining. The numbers also refer to the locations in Table 1 and Fig. 1. (b) Time series from online (DRI) instruments measured in the purification laboratory on the second day. Nos. 7–11 refer to Work Tasks: 7. Purification Part I, 8. Purification Part II, 9. Functionalization Part I, 10. Functionalization Part II, 11. Grinding. The numbers also refer to the locations in Fig. 1.

We classified the CNT-containing particles according to three types. To do this, the length and width of the particles were measured. We defined the length as the longest straight path between any two points of a particle, and the width as the longest path between two points perpendicular to the length. Type 1 includes fibre-shaped CNT-containing particles with an aspect ratio >3:1. Type 2 contains one or more CNT fibres sticking out from a lump of impurities. In order to be classified as a type 2 particle, the CNTs protruding from the lump of impurities must be longer than 50% of the width of the lump. Type 3 particles contain mostly impurities and CNTs are typically only visible when embedded in the surface of the particles or when sticking out from a main body of impurities.

The number concentration of CNT-containing particles (in cm^{-3}) was calculated from the sampled air volume. The analysis of unexposed blank filters as well as of field blanks showed that the polycarbonate filters used did not contribute particles/fibres in the analysis. Calculations of the 95% confidence interval of the detection limits were based on ISO 10312 (1995). The SEM analysis was performed using a Focused Ion Beam—Scanning Electron Microscope (FIB-SEM, model Nova Nanolab 600, FEI, Hillsboro, USA) at Lund Nanolab, Lund University with an acceleration voltage of 5 kV and a probe current of 20 μA. The track-etched polycarbonate filters were prepared for SEM analysis after air sampling by mounting approximately a quarter of the filter on a silicon wafer and coating the filter surface with platinum. This sampling procedure gives a homogenous coverage of the surface. The samples were initially screened for anomalies and areas which were not representative for the filter—those close to the cutting fringes and the edge of the filter—were omitted from further analysis. Images were acquired at a resolution of 35 nm per pixel at a magnification of 2500, generating an imaged area of 9050 $μm^2$ per image. The imaged areas were chosen at random, excluding the previously mentioned, non-representative areas.

The images acquired were analysed in *ImageJ* (Rasband, W.S., ImageJ, National Institute of Health, Bethesda, Maryland, USA, 1997–2008. Available: http://rsbweb.nih.gov/ij). Every particle collected in the selected areas was manually measured, regardless of whether it contained CNTs or not. It was noted whether the analyzed particles did or did not contain visible CNTs. The minimum dimension possible to accurately measure was equivalent to the resolution of the imaged area (i.e. the width of one pixel, which is 35 nm). For particles in the range of a few pixels (35–100 nm), the contrast may in some cases be too low to distinguish the particle from the filter surface, limiting the detectable size range. CNT-containing particles were identified by the distinct contrast between the CNTs and the carbon impurities within the same particle. Particles suspected of containing CNTs were individually screened at a higher resolution to confirm that they actually contained CNTs. A minimum of 5 images, or a total count of 1500 particles were characterized for each filter sample.

RESULTS

Time series data from DRI

The time series from the DRIs from both the emission and background zone measurements in the *production* and *sieving laboratories* during day 1 (Work Tasks Nos. 1–6) are shown in Fig. 2a. Peaks from the emission zone DRIs, CPC (>0.01 μm) and APS (>0.5 μm), coincide with work tasks performed by the worker, indicating that the increase in particle number concentration is related to the work tasks performed. In most cases, the peaks appear as transient episodes (less than a minute) after which the concentration returns to approximately the background value. However, in some cases the elevated concentration remains for a much longer time and clearly induces an increased background concentration, with the potential of exposure for workers in the far-field area as well (*For example opening of the reactor*; Work Task No. 3). In the large particle range a few unexplained short-lived peaks were identified. These are most likely due to resuspension of coarse particles by movements of the workers between work tasks. During the lunch break period no workers were present in the facility, and no emission peaks were found.

In the *purification laboratory* (Work Tasks Nos. 7–11), the most apparent increase in concentration for dp > 0.01 μm took place when a furnace was opened at 11:12 during Work Task No. 7 (Fig. 2b). The concentration of the larger particles (>0.5 μm) assessed with the emission and background APSs, showed only small fluctuations. Peak emission concentrations in the *purification laboratory* (>0.5 μm) were about two orders of magnitude lower compared to those in the *production laboratory*.

Quantification and classification of CNT-containing particles using electron microscopy

Using scanning electron microscopy (SEM), airborne CNT-containing particles were detected in three out of six work tasks in the *production* and *sieving laboratories*, and two out of five work tasks in the *purification laboratory* (Table 3). In general, CNT-containing particles were a small fraction of the total number of particles detected with SEM (respirable fraction). The highest emissions of CNT-containing particles in the *production laboratory* were found for Work Task No. 5, *Sieving mechanical work-up and packaging* ($11\,\text{cm}^{-3}$) and in the *purification and sieving laboratory* for Work Task No. 9, *Functionalization Part I* ($1.0\,\text{cm}^{-3}$).

Hedmer *et al.* (2014) carried out full-shift PBZ measurements from each laboratory during the same study and found mean values for 2 days of measurements of $1.3\,\text{cm}^{-3}$ (*production and sieving laboratory*) and $0.07\,\text{cm}^{-3}$ (*purification laboratory*). By adjusting every work task for its duration, we reconstructed full-shift average concentrations from the task-based emission measurements alone. The reconstructed concentrations of CNT-containing particles were 1.5 and $0.2\,\text{cm}^{-3}$. The good agreement in the *production and sieving laboratory* suggests that the concentrations in the emission zone were representative for the breathing zone exposure. A three times higher reconstructed concentration from the emission measurements in the *purification laboratory* compared to the PBZ exposure concentration measured is reasonable, as some of the emission sampling was carried out inside hoods and thus may have overestimated the breathing zone exposure. From this analysis, it was also assessed that Work Task No. 5, *Sieving, mechanical work-up, and packaging*,

was responsible for more than 85% of the full-shift PBZ exposure in terms of number of CNT-containing particles in the *production and sieving laboratory*.

From the SEM analysis, it was clear that the CNT-containing particles occurred in a variety of shapes and sizes. The CNT-containing particles ($N = 338$, sum for full campaign) counted from the measurements were classified into three types based on the general morphology and size of the particle and the amount of CNTs that it contained (Fig. 3). Type 1 consists of fibre-shaped CNT particles with an aspect length:width ratio >3:1. Each of these particles typically contained 1–15 individual CNTs stuck parallel to each other. It should be noted that we included all particles fulfilling this criteria, rather than just particles with a length >5 μm, as in the WHO criteria. The amount of impurities was non-existent or low for this particle type. The average length and width of type 1 particles were 1.66 and 0.26 μm, respectively.

Type 2 contains one or more CNT fibres sticking out from a lump of impurities. In order to be classified as a type 2 particle, the CNTs protruding from the lump of impurities should be longer than 50% of the width of the lump. The average length and width of type 2 particles was 2.05 and 1.02 μm, respectively. These particles typically contained 5–20 individual CNTs.

Type 3 particles contain mostly impurities and CNTs are only visibly embedded in the surface of the particles or sticking out from a main body of impurities. The average length and width of type 3 particles were 2.61 and 1.69 μm, respectively. Type 3 particles contained between 1–30 CNTs.

Based on all the particles counted in the emission samples in the study, the following distribution of particle
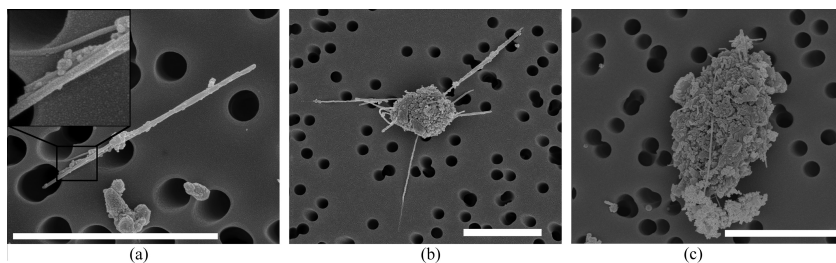

Figure 3   SEM images of different types of airborne CNT-containing particles: (a) type 1 insert shows several strands of CNTs building up the larger structure, (b) type 2, and (c) type 3. The scale bar in each image equals 3 μm. The overall time weighted distribution of the different types was as follows: type 1: 37%; type 2: 22%; type 3: 41%.

types was found: type 1: 37%, type 2: 22%, and type 3: 41%. This was similar to both Task No. 5 *Sieving, mechanical workup, and packaging* (Table 3) and the full-shift breathing zone sample from the production lab. (type 1: 35%, type 2: 22%, and type 3: 43%). There was a strong variation in particle type distribution between work tasks.

In Fig. 4, the particle size distributions from SEM analysis for total number of particles counted and CNT-containing particles is given for the full-shift PBZ sample on day 2 in the *production and sieving laboratory*. The length and width distributions of the total number of respirable particles (including CNT-containing particles) counted are relatively narrow, peaking between 100 and 200 nm. In comparison, the length distribution of CNT-containing particles is shifted towards much larger particles, peaking around 1–2 μm. Thus, the size overlap between the total counted particles and the CNT-containing particles is small: 1.6% of the particles counted with SEM contained CNTs.

Emissions and size distributions from different work tasks and comparison between SEM and DRIs

Table 3 shows average background adjusted emission concentrations from the DRIs for each work task within the two size ranges. These values can be compared with both the total and the CNT-containing number concentrations derived from the SEM analysis (respirable fraction). No background adjustment

was available for SEM. Since the size ranges in which particles detected are different, the absolute numbers differ. The total concentration detected with SEM (>0.03 nm) was typically lower than the total concentration from the CPC (>0.01 μm) which is reasonable, as the detection efficiency using SEM starts to drop below 100 nm.

Size distribution of particle emissions from different work tasks were studied using direct reading measurements (APS; time resolved size distributions in Fig. S1) and offline measurements from filter analysis using SEM. A comparison between the two techniques show relatively good agreement both in terms of particle sizes and absolute concentration in the size range >0.7 μm (Fig. 5a, c, e). A shift towards larger particle sizes indicating high concentrations of mechanically generated particles from the process is found for *Cleaving of deposits* (Work Task No. 2).

Sieving, mechanical work-up, and packaging (Work Task No. 5)

The DRI data shows that the sieving of CNTs resulted in sharp, short-lived (1–10 s) strong emission peaks that could be related to the process both in the small particle range (>0.01 μm) and in the larger particle range (>0.5 μm) (Fig. 2a). For the APS (>0.5 μm), there was also a clear increase in average emission concentration both for spatial and temporal background
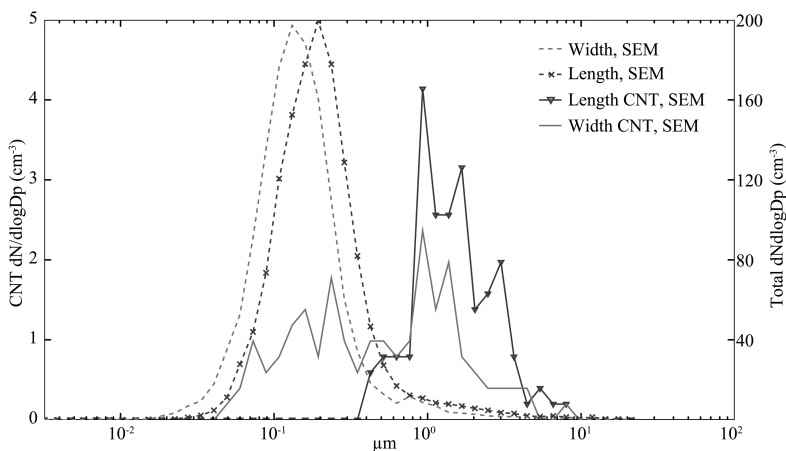

Figure 4   Number size distributions based on particle length and width for SEM total particles and CNT-containing particles (both sampled as respirable fractions). Full-day measurement on day 2 from the worker's breathing zone during work carried out in the production laboratory and sieving laboratories.
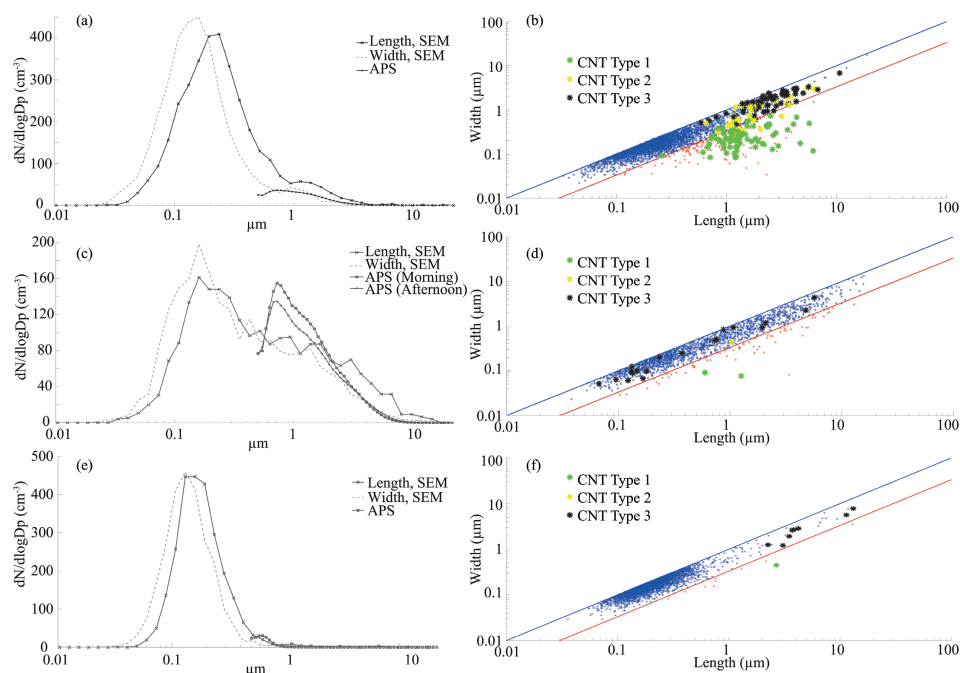
Figure 5   (a, c, and e) Length and width distribution of total particle number concentrations from the SEM analysis and APS aerodynamic particle size distribution. (b, d, and f) Length versus width of measured particles from SEM analysis. Red: non-CNT-containing particles with aspect ratio >3:1; Blue: non-CNT-containing particles with aspect ratio <3:1; Green: CNT-containing particles of type 1; Yellow: CNT-containing particles of type 2; Black: CNT-containing particles of type 3. (a, b) Sieving, mechanical work-up and packaging (Work Task No. 5). (c, d) Cleaving of deposits (Work Task No. 1). (e, f) Purification part II (Work Task No. 8).

adjustment (19 and 21 cm^{-3}, respectively Table 3). The concentration of CNT-containing particles was high 11 cm^{-3} and Type 1 dominated with 40%. The CNT-containing particles (Fig. 5b) occurred almost exclusively as particles with lengths greater than 0.5 μm (up to 10 μm), while their width varied between 0.07 and 2 μm. In this case, the CNT-containing particles were distinctly different from the majority of the non-CNT-containing particles (lengths typically below 0.5 μm).

The fraction of the released particles that contain CNTs can be estimated by comparing the number concentrations of the CNT-containing particles from SEM with the background adjusted concentrations from the DRIs. For this work task, SEM provided a concentration of 11 cm^{-3}, the APS (>0.5 um) 21 cm^{-3}, and the CPC (>0.01 um) 45 cm^{-3}. It is therefore reasonable to assume that a large fraction of the emitted particles from the process contained CNTs.

Cleaving of deposits (Work Task No. 1)

Cleaving of deposits was carried out twice. It resulted in clear emission peaks in the size range >0.5 μm (APS). The temporal background adjusted emission concentrations (>0.5 μm) were 53 and 93 cm^{-3} on the two occasions, respectively. Increases in the smaller particle range (as measured by the CPC) were less obvious. The concentration of CNT-containing particles was 1.6 cm^{-3}. That is, only a small fraction of the emitted particles from the process contained CNTs. The CNT-containing particles (Fig. 5d) were evenly distributed over a large size range (length = 0.07–7 μm, width = 0.05–2 μm) and roughly similar to the distribution of the total counted particles. Type 3 particles dominated these emissions (82%).

Lathe machining (Work Task No. 6)

Lathe machining resulted in the highest emissions of particles >0.5 μm (207 cm^{-3}). The concentration

derived from the SEM filter was relatively high (770 cm⁻³). A moderate concentration of CNT-containing particles (1.2 cm⁻³) was detected on the SEM samples. Although lathe machining did not involve work with material containing CNTs, it is possible that some CNT-containing particles from the high emissions during sieving 30 min earlier were still airborne. Another possibility is that CNT-containing dust was re-suspended during the operations taking place in connection with lathe machining. The fraction of Type 1 CNT particles was lower for lathe machining compared to sieving (17 versus 41%).

Harvesting (Work Task No. 2)

Harvesting did not result in any clear emission peaks in either size range with the DRIs. However, the SEM analysis showed a very high concentration, 2000 cm⁻³. This exceeds the total CPC concentration >0.01 μm and is difficult to explain. No CNT-containing particles were detected at this work task.

Opening and cleaning of the reactor (Work Tasks Nos. 3, 4)

When opening the reactor, high number concentrations of particles in both size ranges were emitted (2278 cm⁻³ for >0.01 μm, 146 cm⁻³ for >0.5 μm). As pointed out previously, these emissions affected the background concentration leading to potential far-field exposures for a long period (Fig. 2a). SEM analysis also showed high concentrations (1100 cm⁻³). Cleaning of the reactor was carried out on day 2 when the DRIs were not available in the production lab, but the SEM analysis showed a high concentration of particles (600 cm⁻³). Even though these two processes resulted in very high emissions, no CNT-containing particles were detected. The filter samples from these work tasks contained almost exclusively porous soot agglomerates with (geometric) sizes ranging from submicrometer to well above 30 μm.

Purification laboratory (Work Tasks Nos. 7–11)

All the work tasks in the *purification laboratory* generated similar size distributions (peaks at around 200 nm, example in Fig. 5e) and similar concentrations in the SEM analysis (150–300 cm⁻³). The background adjusted CPC emission concentrations (>0.01 μm) were negligible for *Functionalization Parts I and II* and *Purification Part II*. It is expected that background

particles, possibly infiltrated from ambient air, were the main source of the particles detected with SEM.

For *Purification Part I* (Work Task No. 7), relatively high emissions were recorded in the >0.01 μm range in connection with turning on a high temperature furnace. Since these particles did not affect either the SEM or the APS concentrations, they can be expected to be mainly <50 nm. For the APS (>0.5 μm), none of the five work tasks showed average concentrations higher than 10% above the background, although very short-lived relatively small peaks above the background concentrations were identified in the emission zone for *Purification Part I* (Work Task No. 7) and *Functionalization Part I* (Work Task No. 9).

CNT-containing particles were only detected from *Functionalization Part I* (Work Task No. 9; 1.0 cm⁻³) and *Purification Part II* (Work Task No. 8; 0.46 cm⁻³). In both these cases, the CNT-containing particles had lengths longer than 1 μm; in that size range they constituted a significant fraction of the detected particles with SEM (Fig. 5f). The most abundant CNT particle type was type 3, constituting 69% of the total amount of CNT particles. Since the emission concentrations from the DRIs were very low for these two work tasks, it is likely that a large fraction of the emitted particles contained CNTs.

DISCUSSION

Emissions of CNT-containing particles from different work tasks

In this study, we carried out detailed investigations of particle emissions from a total of 11 work tasks during arc discharge production of MWCNTs. There were strong variations in the total emitted particle concentrations measured in the two size ranges with the DRIs as well as in the total number of particles and CNT-containing particles collected on filters and analysed offline. Emissions of CNT-containing particles were identified with EM for 5 out of the 11 work tasks investigated. CNT-containing particles were also identified on all PBZ filters. The highest CNT-containing emissions were found during open and manual handling of CNT-containing material (*Sieving, mechanical work-up, and packaging,* Work Task No. 5). This was the work task with the longest duration and the distributions of particle types were similar to the full-day personal exposure sample, clearly indicating that

the majority of the personal exposure came from this source.

We also found respirable emissions of CNT-containing material from two other sources in the *production laboratory* (*Cleaving of deposits* and *Lathe machining*, Work Tasks Nos. 1 and 6) and from two work tasks in the *purification laboratory* (*Functionalization Part I* and *Purification Part II*, Work Tasks Nos. 9 and 8). Our emission data of MWCNTs ranged between <0.20 and 11 cm^{-3}. When compared with the highest emission level reported by others during manufacturing of MWCNTs, our emission data is higher than what Ogura *et al.* (2011) and Dahm *et al.* (2013) found, but lower than the levels reported by Han *et al.* (2008).

Particle types and release mechanisms

Both emission concentrations of CNT-containing particles, and the properties (length, width, degree of purity, etc.) varied strongly between the work tasks. For example, emissions from *Sieving, mechanical work-up, and packaging* had a very high fraction of 'free fibres' (type 1) CNT-containing particles (41%). This is much higher than in several previous studies on CNT emissions from other types of production processes. For example, Tsai *et al.* (2009) reported the release of predominantly clusters of spherical shape with some individual nanoparticles as well as MWCNTs for CVD production of CNTs with a low injector temperature.

On the other hand, *Cleaving of deposits* and *Purification Part II* (Work Tasks Nos. 1 and 8) were dominated by type 2 and type 3 particles, with very few 'free' fibres. However, between these two cases there were also differences. *Cleaving of deposits* included CNT-containing particles distributed over a large size range with lengths and widths similar to the total particles detected with SEM. For *Purification Part II*, though, the emitted CNT-containing particles were much larger in both length and width than the majority of collected particles. Thus, it is hard to draw generalized conclusions regarding the characteristics of the CNT exposures from arc discharge production compared to other manufacturing methods.

It is likely that the material properties and the type of handling affect the amounts of released CNTs as well as the types of particles released. For example, the cleaving of deposits involves high temperatures and

large amounts of energy added to the material, while sieving involves open handling of CNT-containing raw material, with much lower energy input.

Emissions of CNT-containing particles were unexpectedly found during the lathe machining of unreacted graphite (i.e. material that did not contain CNTs). This suggests that the re-suspension of deposited CNT-containing dust may occur. An analysis of surface contamination at this workplace is reported by Hedmer *et al.* (2015).

Knowledge gained by combining DRIs and offline EM-based techniques, influence of background concentration

The EM techniques have higher specificity for exposures containing CNTs compared to the DRIs as also shown by Dahm *et al.* (2013). A similar conclusion was obtained by Hedmer *et al.* (2014) when comparing the SEM technique to EC and total dust as exposure metrics. On the other hand, from the time-integrated filter-based SEM technique, only limited understanding can be gained of what specific actions lead to CNT release during a given work task.

This study gives several examples of added value by using the combination of the SEM and DRI techniques. One benefit of highly time-resolved analysis is the identification of emission peaks. This includes the peak concentration relative to the background and the length of the emission peak. Additionally, we could differentiate between short-lived emission events that did not affect the background, and emission events that affected the background for prolonged time leading to potential far-field exposure risks for workers other than the operator of the work task in question.

It is essential to correct for, and understand, the impact of the background concentration at the workplace. Background particles can infiltrate from outdoors (ambient particles) or be generated by indoor activities not related to the current work task. The background particle concentrations and size distributions are determined by a number of factors such as ventilation rates, infiltration from neighboring laboratories, and ambient air and emissions from multiple sources at the actual workplace. The background number concentration >0.01 μm in the workshop during periods with no activity was 1000–2000 cm^{-3} with no obvious indoor sources. These are likely ambient particles that have penetrated from outdoors.

Temporal and spatial background adjustment was compared for particles larger than 0.5 μm. For strong sources these two approaches showed very good agreement, while for cases where the emission concentration was small compared to the background, they differed more. Emissions more than 20% above background were found for four sources in the size range >0.01 μm; two of these also released CNT-containing particles. Five sources showed emissions clearly above the background in the size range >0.5 μm; four of these led to emissions of CNT-containing particles detected with SEM, suggesting a stronger connection between emissions of particles >0.5 μm and CNT-containing particles compared to emissions in the size range >0.01 μm.

The combined DRI and SEM techniques also provided evidence for particle emissions that did not contain CNTs but were released during the work tasks studied. By comparing the number concentration of CNT-containing particles with the total concentration of emitted particles from each source in the two size ranges from the DRIs (Table 3), we could roughly estimate the fraction of the emitted particles that contained CNTs. For the *Sieving* work task and *Functionalization Part 1* and *Purification Part II* (Work Tasks Nos. 5, 8, and 9), CNT-containing particles may have contributed to a substantial fraction of the emitted particles, possibly as much as ~50%. The uncertainty in this number is quite high due to a high background concentration, particularly for the size range >0.01 μm. For the case of *Cleaving of deposits* (Work Task No. 1), the fraction of CNT-containing particles was <10%. During this task, the majority of released particles may have been generated when cutting through the non-CNT-containing 'shell' of the deposits, or emitted from the saw blade. For *Lathe machining* (Work Task No. 6), the CNT-containing particles were an even smaller fraction, as expected since no CNT-containing material was handled.

Even though *Opening of the reactor* and *Purification Part I* (Work Tasks Nos. 3 and 7) had the highest emissions of >0.01 μm particles, no CNT-containing particles could be detected. In the case of opening the reactor, the emitted particles were soot/graphite particles. In *Purification Part 1*, high concentrations of particles were released (<0.01 μm), but the emitted particles could not be detected with SEM due to their small size. Most likely these ultrafine particles were generated by thermal processes in the case of heating up and opening the oven in the *purification laboratory*.

For very small particles below about 40 nm (geometric diameter), it is only the SMPS and CPC that can detect the particles. The CPC detects the entire particle size range of interest (>0.01 μm), but because of the usually high background in this size range, CNT-containing particles may be hidden in the noise. With the APS in the large particle range (>0.5 μm), emissions are often more clear. It seems that the APS in most of the cases measures particle size distributions and number concentrations above 0.7 μm that are similar to the SEM distributions. The underestimation of particles smaller than about 0.7 μm depends on the decreasing counting efficiency of the APS in this range.

SEM method: implications for legislative limits and exposure metrics

The number concentration of fibre-containing particles is likely the most important exposure metric for fibre-shaped nanoparticles with high aspect ratios. Today there is no consensus on how CNTs collected with a filter-based sampling methodology should be counted in EM analysis. According to the WHO's standard fibre counting criteria that are used, for example, in asbestos counting (1986, 1997), a particle is defined as a fibre if it has a length >5 μm, a width <3 μm, and an aspect ratio >3:1. In addition, fibres are counted separately as if the carrier particles did not exist.

Typically all three particle classes found in this study contained a relatively high number of individual CNTs (1–30) with length <5 μm and we assessed that it was not possible to practically count every single CNT. Thus, we decided not to follow the standard fibre counting criteria. If the length criteria were followed, less than 1% of our total counted CNT-containing particles would have been defined as fibres.

Several previous studies that followed the WHO counting rules quantified no or few CNTs (Bello *et al.*, 2009; Lee *et al.*, 2010 and may therefore have underestimated the presence of CNTs in workplace air. Moreover, shorter MWCNTs (length <5 μm) have been shown to penetrate the visceral pleura in rats (Mercer *et al.*, 2010), to cause pulmonary inflammatory effects and fibrosis (Mercer *et al.*, 2011; Porter *et al.*, 2013) and bronchoalveolar inflammation and

thickening of the alveolus septum in rats, indicative of interstitial fibrosis (Pauluhn, 2010b). These adverse health effects may be caused by other CNT characteristics than fibre lengths, and demonstrate that the standard fibre counting criteria is not applicable for all CNTs. It is not known what happens to the CNT agglomerates deposited in the lungs (e.g. deagglomeration may occur with the subsequent release of single CNTs). More research on lung deposition and particularly the fate of agglomerated CNTs in lung fluid is needed.

Recently it was proposed that EC may be a usable metric for CNT exposure (Dahm *et al.*, 2012; NIOSH, 2013). Our recent publication reported that the EC exposure metric is both too insensitive and unspecific to be used as a generic exposure metric for CNT exposures during arc discharge production (Hedmer *et al.*, 2014). For example in *Cleaning of the reactor* (Work Task No. 4), no CNTs were detected while the EC concentration was very high (550 μg/m^3). SEM analysis is time consuming, expensive, and not at all as commercially available as EC analysis, but it is very important that the analytical method used to quantify exposures to CNTs has high selectivity and sensitivity to CNTs.

A further development of the SEM method is needed to decrease the analysis time and thereby the costs of the analysis. Computer software is available for image analysis with automatic counting of objects in SEM on substrates without pores. There is also ongoing research to develop computer software that automatically can perform the image analysis of fibre-shaped objects on filter samples. Thus, in the near future it will be possible to automatically, quickly, more easily, and inexpensively count CNTs in EM, which will ease the establishment of a standardized protocol for counting criteria of CNTs. The SEM method we developed can be applied for analysis of all fibre-shaped nano-objects, and their aggregates and agglomerates (NOAAs) >100 nm with high aspect ratios that have structural similarities with asbestos (e.g. metal and semiconductor nanowires).

Online techniques for the selective detection of particles from different processes are deeply needed. An example is the application of time-resolved aerosol mass spectrometry for the selective detection of metals and different types of carbonaceous particles (Onasch *et al.*, 2012; Nilsson *et al.*, 2013).

Recommendations to the company

For CNT exposures, the precautionary principle must be applied until the toxicological effects of CNT exposure have been evaluated. In practice, this means enclosed handling in combination with a high level of control measures and a high degree of use of personal protection equipment (PPE). Thus, the workers in the facility were assessed to have higher exposure than necessary due to lack of PPE as well as in engineering controls. Dry CNT powder should not be openly handled in the facility without any engineering controls, such as ventilated enclosures (Schulte *et al.*, 2012). During all open handling of CNTs in the facility, respiratory protection must be used. To protect the workers more efficiently, PPEs such as coveralls, hoods, and shoe protection are needed especially in the *production laboratory* to prevent dermal exposure and to inhibit the CNT dust spreading in the workplace. The engineering controls used were assessed and found not to be sufficient for reducing the CNT exposure. For example, the *production laboratory* was not located in a closed area since it was part of a larger room that was used for other purposes such as storing. The *production laboratory* was connected via stairs to other rooms in the building without any airtight sluice. This means that airborne CNT-containing particles could be present in other rooms in the building and thereby cause exposure to unprotected workers. Moreover, the office used by the production workers was located next to the *sieving laboratory*, and since the same shoes were worn in both the *production laboratory* and *sieving laboratory* as in the office, there could be a high risk that the floor in the office was contaminated with CNT dust.

Limitations

It should be pointed out that the data obtained may not be directly generalizable to other CNT manufacturing methods (such as the more commonly used CVD method) and to workplaces with stricter engineering control systems. Due to the use of respirable particle size selection, this study does not give a full image of the particle emissions that occur during the different work tasks since particles with aerodynamic diameters larger than the respirable size limit are expected to be released into the air as well. This study focuses on the particles with the highest probability to reach the pulmonary region and thus does not consider particles

that most likely are deposited above the pulmonary region, such as large (dae > 4μm) agglomerated particles. Hedmer *et al.* (2015) present microscopy data from cascade impactor sampling without preselection from the same campaign.

CONCLUSIONS

The emissions of CNTs during specific work tasks performed in arc discharge production and purification in a small-scale factory were characterized. In addition, a method for SEM analysis of CNT-containing particles on filter samples was developed that makes it possible to classify CNT-containing particles into different types based on their morphology. Particles containing CNTs were found on emission filter samples from five out of the eleven work tasks investigated. Full-shift PBZ exposures exceeded the proposed OELs. By far, the highest contribution (>85%) was from manual handling of CNTs in powder form during *Sieving, mechanical work-up, and packaging*. The morphology of the CNT-containing particles was diverse; free CNT fibres constituted 37% of the total CNT-containing particles. However, the type distribution and characteristics of the CNT-containing particles varied strongly between work tasks.

Data from DRIs provided complementary information on: (i) the background adjusted emission concentration of total particles from each work task in different particle size ranges, (ii) the identification of the key procedures in each work task that lead to emission peaks, (iii) the identification of emission events that affect the background, thereby leading to potential far-field exposures for workers other than the operator of the work task, and (iv) when combined with SEM analysis, the fraction of particles emitted from each source that contains CNTs could be estimated. Thus, this study confirms that a combination of online time-resolved instrumentation and time-integrated filter sampling methods is needed in order to achieve a full evaluation of particle emissions that occur during the production and purification of CNTs. A standardized/harmonized method for the EM analysis of airborne CNTs is urgently needed since only filter-based sampling methods in combination with EM analysis are currently selective and sensitive enough for measuring CNTs. The SEM method presented in this study could form the basis for such a harmonized protocol for the counting of CNTs.

REFERENCES

Bello D, Hart AJ, Ahn K *et al.* (2008) Particle exposure levels during CVD growth and subsequent handling of vertically-aligned carbon nanotube films. *Carbon*; 46: 974–7.

Bello D, Wardle BL, Yamamoto N *et al.* (2009) Exposure to nanoscale particles and fibers during machining of hybrid advanced composites containing carbon nanotubes. *J Nanoparticle Res*; 11: 231–49.

BSI. (2007) *Nanotechnologies – part 2: guide to safe handling and disposal of manufactured nanomaterials*. London, UK: British Standards Institute.

Dahm MM, Evans DE, Schubauer-Berigan MK *et al.* (2012) Occupational exposure assessment in carbon nanotube and nanofiber primary and secondary manufacturers. *Ann Occup Hyg*; 56: 542–56.

Dahm MM, Evans DE, Schubauer-Berigan MK *et al.* (2013) Occupational exposure assessment in carbon nanotube and nanofiber primary and secondary manufacturers: mobile direct-reading sampling. *Ann Occup Hyg*; 57: 328–44.

Gamaly EG, Ebbesen TW. (1995) Mechanism of Carbon Nanotube Formation in the Arc-Discharge. *Phys Rev B*. 52: 2083–9.

Gustavsson P, Hedmer M, Rissler J. (2011) Carbon nanotubes – Exposure, toxicology and protective measures in the work environment. *Swedish Work Environment Authority* Report 2011.

Han JH, Lee EJ, Lee JH *et al.* (2008) Monitoring multiwalled carbon nanotube exposure in carbon nanotube research facility. *Inhal Toxicol;* 20: 741–9.

Hedmer M, Kåredal M, Gustavsson P *et al.* (2013) The Nordic Expert Group for criteria documentation of health risks from chemicals. 148. Carbon nanotubes. *Arbete och Hälsa*; 47: 1–238.

Hedmer M, Isaxon C, Nilsson PT *et al.* (2014) Exposure and emission measurements during production, purification, and functionalization of arc-discharge-produced multi-walled carbon nanotubes. *Ann. Occup Hyg*; 58: 355.

Hedmer M, Ludvigsson L, Isaxon C *et al.* (2015) Detection of carbon nanotubes and carbon nanodiscs on workplace surfaces in a small-scale producer. *Ann Occup Hyg*; 53: 836.

IFA. (2014). Criteria for assessment of the effectiveness of protective measures. Available at http://www.dguv.de/ifa/Fachinfos/Nanopartikel-am-Arbeitsplatz/Beurteilung-von-Schutzmaßnahmen/index-2.jsp. Accessed 5 October 2015.

Iijima S. (1991) Helical microtubules of graphitic carbon. *Nature*; 354: 56–8.

ISO 10312. (1995) *Ambient air—determination of asbestos fibres—direct transfer transmission electron microscopy method.* Technical Committee ISO/TC 146, Air quality, Subcommittee SC 3, Ambient atmospheres.

Jones AD. (2005) Thoracic size-selective sampling of fibres: performance of four types of thoracic sampler in laboratory tests. *Ann Occup Hyg*; 49: 481–92.

Kumar M, Ando Y. (2010) Chemical vapor deposition of carbon nanotubes: a review on growth mechanism and mass production. *J Nanosci Nanotechnol*; 10: 3739–58.

Köhler A, Som C, Helland A *et al.* (2008) Studying the potential release of carbon nanotubes throughout the application life cycle. *J Clean Prod*; 16: 927–37.

Lee J, Mahendra S, Alvarez PJ. (2010) Nanomaterials in the construction industry: a review of their applications and environmental health and safety considerations. *ACS Nano*; 4: 3580–90.

Liu Y, Kumar S. (2014) Polymer/carbon nanotube nano composite fibers-a review. *ACS Appl Mater Interfaces*; 6: 6069–87.

Ma-Hock L, Strauss V, Treumann S *et al.* (2013) Comparative inhalation toxicity of multi-wall carbon nanotubes, graphene, graphite nanoplatelets and low surface carbon black. *Particle Fibre Toxicol*; 10: 23.

Ma-Hock L, Treumann S, Strauss V *et al.* (2009) Inhalation toxicity of multiwall carbon nanotubes in rats exposed for 3 months. *Toxicol Sci*; 112: 468–81.

Maynard AD, Baron PA, Foley M *et al.* (2004) Exposure to carbon nanotube material: aerosol release during the handling of unrefined single-walled carbon nanotube material. *J Toxicol Environ Health Part A*; 67: 87–107.

Mercer RR, Hubbs AF, Scabilloni JF *et al.* (2011) Pulmonary fibrotic response to aspiration of multi-walled carbon nanotubes. *Particle Fibre Toxicol*; 8: 21.

Mercer RR, Hubbs AF, Scabilloni JF *et al.* (2010) Distribution and persistence of pleural penetrations by multi-walled carbon nanotubes. *Particle Fibre Toxicol*; 7: 28.

Methner M, Hodson L, Geraci C. (2010) Nanoparticle emission assessment technique (NEAT) for the identification and measurement of potential inhalation exposure to engineered nanomaterials--part A. *J Occup Environ Hyg*; 7: 127–32.

Muller J, Huaux F, Moreau N *et al.* (2005) Respiratory toxicity of multi-wall carbon nanotubes. *Toxicol Appl Pharm*; 207: 221–31.

Murphy FA, Poland CA, Duffin R *et al.* (2011) Length-dependent retention of carbon nanotubes in the pleural space of mice initiates sustained inflammation and progressive fibrosis on the parietal pleura. *Am J Pathol*; 178: 2587–600.

Nilsson PT, Isaxon C, Eriksson AC *et al.* (2013). Nano-objects emitted during maintenance of common particle generators: direct chemical characterization with aerosol mass spectrometry and implications for risk assessments. *J Nanoparticle Res*; 15: 2052.

NIOSH. (2013) Current Intelligence Bulletin 65: occupational exposure to carbon nanotubes and nanofibers. Available at http://www.cdc.gov/niosh/docs/2013–145/. Accessed 2 December 2015.

NIOSH. (2013) Occupational exposure to carbon nanotubes and nanofibres. Available at http://www.cdc.gov/niosh/docs/2013–145/pdfs/2013–145.pdf. Accessed 24 May 2013.

Ogura I, Sakurai H, Mizuno K *et al.* (2011) Release potential of single-wall carbon nanotubes produced by super-growth method during manufacturing and handling. *J Nanoparticle Res*; 13: 1265–80.

OH Learning. (2010) W504-fibre counting. Available at http://www.ohlearning.com/Files/Extracted_Files/38/W504coursematerial/JD33%20v1-0%2010Apr10%20W504%20Fibre%20counting.ppt#385,1,W504-fibre-counting. Accessed 16 September 2014.

Onasch TB, Trimborn A, Fortner EC *et al.* (2012). Soot particle aerosol mass spectrometer: development, validation, and initial application. *Aerosol Sci Technol*; 46: 804–17.

Pauluhn J. (2010a) Multi-walled carbon nanotubes (Baytubes): approach for derivation of occupational exposure limit. *Regulatory Toxicol Pharmacol*; 57: 78–89.

Pauluhn J. (2010b) Subchronic 13-week inhalation exposure of rats to multiwalled carbon nanotubes: toxic effects are determined by density of agglomerate structures, not fibrillar structures. *Toxicol Sci*; 113: 226–42.

Porter DW, Hubbs AF, Chen BT *et al.* (2013) Acute pulmonary dose-responses to inhaled multi-walled carbon nanotubes. *Nanotoxicology*; 7: 1179–94.

Sanchez VC, Pietruska JR, Miselis NR *et al.* (2010) Biopersistence and potential adverse health impacts of fibrous nanomaterials: what have we learned from asbestos? *Wiley Interdisciplinary Rev Nanomed Nanobiotechnol*; 1: 511–29.

Sargent LM, Porter DW, Staska LM *et al.* (2014) Promotion of lung adenocarcinoma following inhalation exposure to multi-walled carbon nanotubes. *Particle Fibre Toxicol*; 11: 3.

Schulte PA, Kuempel ED, Zumwalde RD *et al.* (2012) Focused actions to protect carbon nanotube workers. *Am J Ind Med*; 55: 395–411.

Takaya M, Ono-Ogasawara M, Shinohara Y *et al.* (2012) Evaluation of exposure risk in the weaving process of MWCNT-coated yarn with real-time particle concentration measurements and characterization of dust particles. *Ind Health*; 50: 147–55.

Tsai SJ, Hofmann M, Hallock M *et al.* (2009) Characterization and evaluation of nanoparticle release during the synthesis of single-walled and multiwalled carbon nanotubes by chemical vapor deposition. *Environ Sci Technol*; 43: 6017–23.

WHO. (1986) *Asbestos and other natural mineral fibres. Environmental health criteria, no. 53.* Geneva: World Health Organization.

WHO. (1997) *Determination of airborne fibre number concentrations: a recommended method, by phasecontrast optical microscopy (membrane filter method).* Geneva: World Health Organization.

Wohlleben W, Brill S, Meier MW *et al.* (2011) On the lifecycle of nanocomposites: comparing released fragments and their in-vivo hazards from three release mechanisms and four nanocomposites. *Small*; 7: 2384–95.

Paper VI

Exposure and Emission Measurements During Production, Purification, and Functionalization of Arc-Discharge-Produced Multi-walled Carbon Nanotubes

Maria Hedmer[1]*, Christina Isaxon[2], Patrik T. Nilsson[2],
Linus Ludvigsson[2,3], Maria E. Messing[3,4],
Johan Genberg[5], Vidar Skaug[6], Mats Bohgard[2],
Håkan Tinnerberg[1] and Joakim H. Pagels[2]

1.Division of Occupational and Environmental Medicine, Department of Laboratory Medicine, Lund University, PO Box 118, SE-22100 Lund, Sweden
2.Ergonomics and Aerosol Technology, Lund University, PO Box 118, SE-22100 Lund, Sweden
3.Solid State Physics, Lund University, PO Box 118, SE-22100 Lund, Sweden
4.Synchrotron Radiation Research, Lund University, PO Box 118, SE-22100 Lund, Sweden
5.Nuclear Physics, Lund University, PO Box 118, SE-22100 Lund, Sweden
6.National Institute of Occupational Health, PO Box 8149, Dep 0033 Oslo, Norway
*Author to whom correspondence should be addressed. Tel: +4646173193; fax: +4646173180; e-mail: maria.hedmer@med.lu.se
Submitted 4 February 2013; revised version 29 October 2013; accepted 31 October 2013.

ABSTRACT

Background: The production and use of carbon nanotubes (CNTs) is rapidly growing. With increased production, there is potential that the number of occupational exposed workers will rapidly increase. Toxicological studies on rats have shown effects in the lungs, e.g. inflammation, granuloma formation, and fibrosis after repeated inhalation exposure to some forms of multi-walled CNTs (MWCNTs). Still, when it comes to health effects, it is unknown which dose metric is most relevant. Limited exposure data for CNTs exist today and no legally enforced occupational exposure limits are yet established. The aim of this work was to quantify the occupational exposures and emissions during arc discharge production, purification, and functionalization of MWCNTs. The CNT material handled typically had a mean length <5 μm. Since most of the collected airborne CNTs did not fulfil the World Health Organization fibre dimensions (79% of the counted CNT-containing particles) and since no microscopy-based method for counting of CNTs exists, we decided to count all particle that contained CNTs. To investigate correlations between the used exposure metrics, Pearson correlation coefficient was used.

Methods: Exposure measurements were performed at a small-scale producer of MWCNTs and respirable fractions of dust concentrations, elemental carbon (EC) concentrations, and number concentrations of CNT-containing particles were measured in the workers' breathing zones with filter-based methods during work. Additionally, emission measurements near the source were carried out during different work tasks. Respirable dust was gravimetrically determined; EC was analysed with

thermal–optical analysis and the number of CNT-containing particles was analysed with scanning electron microscopy.

Results: For the personal exposure measurements, respirable dust ranged between <73 and 93 µg m^{-3}, EC ranged between <0.08 and 7.4 µg C m^{-3}, and number concentration of CNT-containing particles ranged between 0.04 and 2.0 cm^{-3}. For the emission measurements, respirable dust ranged between <2800 and 6800 µg m^{-3}, EC ranged between 0.05 and 550 µg C m^{-3}, and number concentration of CNT-containing particles ranged between <0.20 and 11 cm^{-3}.

Conclusions: The highest exposure to CNTs occurred during production of CNTs. The highest emitted number concentration of CNT-containing particles occurred in the sieving, mechanical work-up, pouring, weighing, and packaging of CNT powder during the production stage. To be able to quantify exposures and emissions of CNTs, a selective and sensitive method is needed. Limitations with measuring EC and respirable dust are that these exposure metrics do not measure CNTs specifically. Only filter-based methods with electron microscopy analysis are, to date, selective and sensitive enough. This study showed that counting of CNT-containing particles is the method that fulfils those criteria and is therefore the method recommended for future quantification of CNT exposures. However, CNTs could be highly toxic not only because of their length but also because they could contain, for example transition metals and polycyclic aromatic hydrocarbons, or have surface defects. Lack of standardized counting criteria for CNTs to be applied at the electron microscopy analysis is a limiting factor, which makes it difficult to compare exposure data from different studies.

KEYWORDS: carbon nanotube; electron microscopy; elemental carbon; emission; exposure metric; manufactured nanoobject; nanoparticle; occupational exposure

INTRODUCTION

The global production and use of the carbon nanotubes (CNTs) into different products and materials is rapidly growing (Dahm *et al.*, 2012; Gasser *et al.*, 2012; Ono-Ogasawara and Myojo, 2013). CNT is in the paper used as a synonym for multi-walled CNTs. CNTs were discovered in 1991 by Iijima (1991) and are a heterogeneous group of tubes at the nanometre scale consisting of pure graphene layers rolled to form cylinders with high aspect ratios. If the CNT structure consists of one cylinder, it is denoted single-walled carbon nanotube (SWCNT) and if it consists of several cylinders stacked inside each other, they are referred to as multi-walled carbon nanotube (MWCNT).

Use and commercial application

CNTs are usually manufactured by three different methods, which are chemical vapour deposition (CVD), laser ablation, and arc discharge. CVD is the most common and widely used method for CNT production while the arc discharge method is lesser used. However, since arc-discharge-produced MWCNTs with a mean length <5 µm are commercially available, occupational exposure during production with this method also need to be quantified.

CNTs have desirable properties in terms of mechanical strength, chemical inertness, electrical conductivity, optical properties, and thermal properties, and these truly unique properties may make a breakthrough in many vital industries (Barkauskas *et al.*, 2010). Therefore, wide application areas are expected for CNTs in the future in industry sectors such as materials and chemistry, medicine and life science, electronics, information and communication technology, and energy (Köhler *et al.*, 2008; Barkauskas *et al.*, 2010; McIntyre, 2012). Today, CNTs are incorporated into existing materials such as plastics, rubbers, composite materials, textiles, and concrete to make them more durable (strength), lightweight, or more wear-resistant (Schneider *et al.*, 2007; Köhler *et al.*, 2008; Wohlleben *et al.*, 2011). Products on the market today containing CNTs are, e.g. sport equipments, composites for car parts, aircrafts and wind power plants, and solar cells (Hussain *et al.*, 2006; Köhler *et al.*, 2008; Thomas *et al.*, 2009; Tan *et al.*, 2012). Workers exposed to CNTs may be at the highest risks while consumers are unlikely to be exposed to CNTs.

Toxicology and exposure metrics

The properties of CNTs differ depending on, e.g. number of walls, diameter, length, chiral angles, chemical

functionalization, purity, stiffness, and bulk density. CNT materials consist of a complex mixture of different transition metal catalysts, e.g. iron and cobalt, inorganic carbon impurities, and organic impurities, e.g. polycyclic aromatic hydrocarbons, which all could have a critical role in oxidative stress and the toxicology of CNTs (Plata *et al.*, 2008; Hsieh *et al.*, 2012). CNTs have nanoscaled size in two dimensions resulting in fibre-like characteristics and could be referred to as high aspect ratio nanoparticles (Donaldson *et al.*, 2011). The fibre shapes and the small dimensions result in very high surface to mass ratios. The structures of MWCNTs are stiffer compared with the SWCNTs. Membrane piercing of cells is mainly described for long and stiff CNTs with a length >15–20 μm (Nagai *et al.*, 2011; Gasser *et al.*, 2012). Since CNTs are fibre-like in their characteristics, there are structural similarity between them and asbestos fibres. Thus, concern has been raised if some forms of CNTs could induce similar adverse biological effects as asbestos, e.g. mesothelioma (Poland *et al.*, 2008; Donaldson and Poland, 2009; Donaldson *et al.*, 2011; Palomäki *et al.*, 2011). Animal studies have shown serious effects in the lungs, i.e. inflammation, granuloma formation, and fibrosis, after repeated inhalation exposure to MWCNTs (Ma-Hock *et al.*, 2009; Ryman-Rasmussen *et al.*, 2009; Pauluhn 2010; Porter *et al.*, 2013), even at realistic exposures and doses. Studies exposing the abdominal cavity in animals to MWCNTs indicated a certain carcinogenic potential (Poland *et al.*, 2008; Takagi *et al.*, 2008). Furthermore, recent studies clearly demonstrated threshold effects of the fibre length. Silver nanofibres with a length >4 μm were pathogenic and caused acute inflammation when the nanofibres were injected into the pleura (Schinwald *et al.*, 2012b). But if the silver nanofibres instead were administrated by pharyngeal aspiration, the threshold fibre length for acute pulmonary inflammation was between 10 and 14 μm (Schinwald *et al.*, 2012a). Shorter CNTs entangle and coil and are preferentially enclosed by the cells (Nagai *et al.*, 2011). But shorter MWCNTs, for example with a median length of 3.9 μm, have in several studies shown to both penetrate alveolar macrophages, the alveolar wall, and visceral pleura (Mercer *et al.*, 2010) and cause pulmonary inflammatory effects and fibrosis (Mercer *et al.*, 2011; Porter *et al.*, 2013). Also, repeated exposure to very short MWCNTs (0.2–0.3 μm) has in rats shown to cause bronchoalveolar inflammation and thickening

of the alveolus septum indicative of interstitial fibrosis (Pauluhn, 2010). In the future, measurements of biological oxidative damage might be used as a biomarker for CNT exposure (Hsieh *et al.*, 2012). To date, no toxicological data for humans exist. Thus, exposure to all types of CNTs must be avoided as long as the adverse biological effects are not fully understood. Until the relevant dose metrics of CNTs are known, exposure to CNTs should be measured with multiple exposure metrics, for example mass concentration, elemental carbon (EC) mass concentration, and particle number concentration of CNT-containing particles (Brouwer *et al.*, 2012; Dahm *et al.*, 2012; Hedmer *et al.*, 2013).

Methods for measuring CNTs

How to collect and count CNTs on filters with electron microscopy is not obvious today due to a lack of standardized protocols. Based on the similarities between CNTs and asbestos, the method for standard fibre counting from World Health Organization (WHO, 1997) has been applied in a few previous studies of workplace exposure of CNTs (Bello *et al.*, 2009; Lee *et al.*, 2010). According to the WHO method, a fibre is counted if it has a minimum length of 5 μm, a width <3 μm, and length:width ratio >3:1 (WHO, 1997; OH Learning, 2010). Furthermore, if the fibre is attached to a non-CNT carrier particle, the carrier particle is neglected and the fibre is counted if the visible part of the fibre meets the above definition. Also, split fibres, fibre bundles, and ends of fibres partially within imaged area are counted. If >1/8th of the imaged area is covered with dust or particles, the area is rejected for counting and another area is chosen. The workplace studies that follow this method quantified no or few CNTs (Bello *et al.*, 2009; Lee *et al.*, 2010). Most airborne CNTs do not have these typical fibre dimensions due to agglomeration (Schulte *et al.*, 2012). Therefore, we decided to not apply the WHO standard fibre counting criteria and instead we counted every CNT-containing particle regardless of length. Furthermore, it is not clarified what will happen with the agglomerated CNTs that are deposited in the surfactant lining fluid in the lungs.

Workplace exposure

Since the use of CNTs is increasing and is predicted to do so even more strongly in the future, occupational exposure to CNTs can occur during the whole life cycle: production, purification, functionalization, incorporation in

different materials/products, use, repair, disposal, and end of life. Both the occupational exposure in terms of number of exposed workers and airborne concentrations of CNTs may increase if market expands and goes from small-scale production to mass production. Exposure through inhalation has been identified to be the dominating exposure route and potentially entailing the highest risk (Ma-Hock *et al.*, 2009; Pauluhn 2010; Gustavsson *et al.*, 2011; Porter *et al.*, 2013; Hedmer *et al.*, 2013). Thus, airborne exposures of CNTs need to be quantified and controlled, especially in open and manual handling of CNT powder.

Up to now, a limited number of studies have been carried out on workplace exposure to CNTs during production (Maynard *et al.*, 2004; Bello *et al.*, 2008; Han *et al.*, 2008; Lee *et al.*, 2010; Dahm *et al.*, 2012) and even fewer during specific steps in laboratory work such as purification and functionalization (Dahm *et al.*, 2012). Moreover, there are also very limited exposure data on machining of CNT composites (Bello *et al.*, 2009, 2010). To our knowledge, to date, no exposure data for arc-discharge-produced CNTs exist. Thus, the exposure data for airborne CNTs are still limited. In some studies, personal exposure measurements were performed during specific work tasks, e.g. during CVD production of CNTs, harvesting of CNTs, or weighing of CNT powder, and the sampling times were therefore short (Maynard *et al.*, 2004; Bello *et al.*, 2008; Dahm *et al.*, 2012).

Exposure limits

Today, no consensus occupational exposure limits for CNTs exist. The British Standards Institute (BSI) and the Institute for Occupational Safety and Health of the German Social Accident Insurance (IFA) have proposed benchmark exposure limits for fibrous nanomaterials with high aspect ratios (>3:1 and length >5 µm) set at 0.01 fibre cm^{-3} (BSI, 2007; IFA, 2009). In Japan, a mass-based occupational exposure limit of 30 µg m^{-3} was proposed by the Japanese New Energy and Industrial Technology Department Organization (Nakanishi, 2011). The National Institute for Occupational Safety and Health (NIOSH, 2013) has recently proposed a recommended exposure limit for CNTs based on EC of 1 µg C m^{-3} as a respirable mass 8-hr-time-weighted average (TWA-8) concentration.

EC is typically measured with a thermal–optical method to divide the amount of carbonaceous material in a sample into organic carbon and EC. During the EC analysis, a temperature program is used, where the carbonaceous material is oxidized in several temperature steps in the presence of a controlled amount of oxygen (e.g. 2% O$_2$). The amount of EC oxidized at each temperature step is then added together and reported as EC (Birch and Cary, 1996). According to Ono-Ogasawara and Myojo (2013), MWCNTs are mainly oxidized at temperatures >700°C. They also suggested that EC in the two highest temperature classes (700 and 920°C) in their study can be used as qualitative indices of MWCNTs. Furthermore, if the MWCNTs have diameters >20 nm, they were mainly measured in the highest temperature class (920°C). So far, only one study has used EC (inhalable fraction) as an exposure metric for CNTs during personal exposure measurements in production of CNTs (with CVD; Dahm *et al.*, 2012). However, the recommended exposure limit for EC proposed by NIOSH is based on the respirable mass (NIOSH, 2013). No exposure data based on single oxidation temperature classes are available today. In summary, very little information is available for occupational exposure to CNTs, and exposure and emission data from production of CNTs with the arc discharge technique are still missing.

Aim

The objective of this study was to quantify the occupational exposures and emissions to CNTs with a mean length <5 µm and therefore, personal exposure measurements in the breathing zone of workers as well as emission measurements near the expected emission source were performed during production, purification, and functionalization of arc-discharge-produced MWCNTs. Respirable fractions of dust, EC, and number concentrations of CNT-containing particles were measured to obtain multiple exposure metrics for the CNT exposure. An evaluation of the used exposure metrics was also performed by studying the correlations between the investigated metrics.

METHODS

MWCNT producer

In this study, we had the opportunity to investigate occupational exposures and emissions of one of the few small-scale facilities producing MWCNTs using the arc discharge method. Also, other carbonaceous

nanoparticles such as cones and discs were occasionally produced by the company. In the company, three workers were involved in the production, purification, and functionalization work of MWCNTs. Schematic drawings of the production laboratory, sieving laboratory, and purification laboratory can be seen in Fig. 1. A description of the production methods and the work tasks in the production laboratory, sieving laboratory, and purification laboratory is given below.

Production

The production of MWCNTs took place in the production laboratory and sieving laboratory. The company had an arc discharge reactor for the MWCNT production. The arc discharge method is based on application of a high-voltage field over two rods composed of high-purity graphite. The rods serve as electrodes, an anode and a cathode, and a stable arc discharge is formed between them. The MWCNTs grow on the cathode while the anode is consumed. With this production method, no metal catalysts are

required and the metal impurities can therefore be very low. However, non-CNT-containing impurities (e.g. graphite and soot) are produced by this method, so purification steps are challenge when scaling up the production. According to the manufacturer, the produced MWCNTs consisted of 55 wt% CNTs and 45 wt% graphite nanoparticles and other graphitic structures. The produced MWCNTs had diameters between 2 and 50 nm and a typical length of >2 µm according to the producer. According to scanning electron microscopy (SEM) analysis on bulk material obtained from the company during the sampling campaign, the mean length of the individual MWCNTs was 1.7 µm with a distribution ranging from 0.3 to 6.1 µm. Compared with the critical dimensions of fibres, the majority of produced MWCNTs in the studied company had a length <5 µm. The production included the following work tasks: synthesizing of MWCNTs with the enclosed arc discharge reactor, opening of reactor, and collection of reacted graphite deposit (No. 3 in Fig. 1), dry cutting of reacted graphite deposit with a band saw (No. 1 in Fig. 1), manual
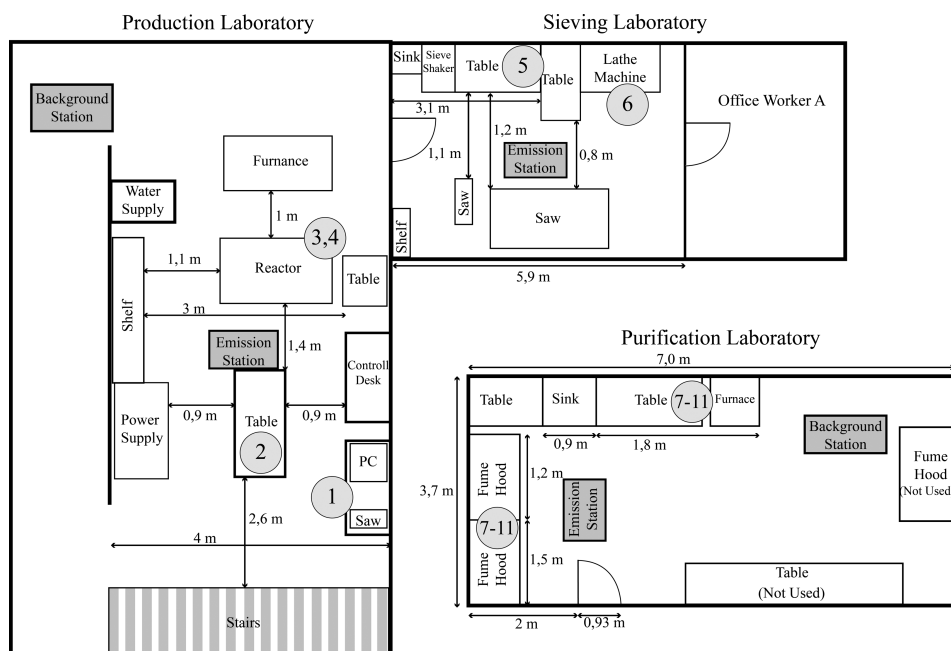
1 Schematic drawing of the facility. The numbers in grey circles correspond to activities in Table 4. The production laboratory and sieving laboratory were located on a different floor than the purification laboratory.

harvesting of produced MWCNTs (No. 2 in Fig. 1), mechanical work-up, sieving, weighing, pouring, and packaging (No. 5 in Fig. 1), lathe machining of graphite rods for the reactor (No. 6 in Fig. 1), and reactor clean out with compressed air and a vacuum cleaner with high efficiency particulate absorption (HEPA) filter (No. 4 in Fig. 1). Worker A was responsible for the above-described work tasks of which several of these included open handling of MWCNT powder.

Purification and functionalization

In the purification laboratory, the produced MWCNTs were purified to remove carbonaceous structures, e.g. graphite and soot. According to the company, the purified MWCNTs consisted of 80 wt% CNTs and 20 wt% graphite nanoparticles and other graphitic structures. Functionalization of purified MWCNTs also took place there. Workers B and C were responsible for the work tasks performed in the purification laboratory. Most work tasks were defined as laboratory work and were performed inside the two fume hoods (No. 7–11 in Fig. 1). Work tasks performed inside the fume hoods were, for example pouring of MWCNT powder, dispersion of MWCNT powder, filtration of MWCNT dispersion, grinding of CNTs (No. 11 in Fig. 1). The workers poured and weighed MWCNT powder, packed MWCNT powder into containers, and dried MWCNT powder in a furnace and these work tasks were performed outside the fume hoods.

Workplace monitoring

Strategy for air sampling

The personal exposure measurements and emission measurements of workplace air were performed in the facility during two consecutive work days, and an overview of the sampling strategy can be seen in Table 1. Three different exposure metrics (respirable fractions of mass concentration, EC, and number concentration of CNT-containing particles) were used.

Personal exposure measurements

Time-integrated sampling with filter-based methods was performed on Workers A–C. The respirable fraction of dust samples (50% cut-off at an aerodynamic equivalent particle diameter of 4 μm), EC samples, and SEM samples were collected in the breathing zone of the workers. Also, sampling with direct-reading personal aerosol monitors was carried out to be able to assess respirable mass concentrations and particle number concentrations. The direct-reading instruments and the EC sampling were used at one department per day (Table 1). Respiratory protection was used by Worker A in the production laboratory and sieving laboratory. Thus, the sampling was performed outside the half-face respirator equipped with particulate filter of Grade P3.

Table 1. The sampling strategy for the exposure and emission measurements at the small-scale producer of MWCNTs

Sampling day	Production laboratory and sieving laboratory		Purification laboratory	
	Personal exposure measurement during the work day	**Short-term emission measurement**	**Personal exposure measurement during the work day**	**Short-term emission measurement**
1	Sampling of: R1, R2, SP, NT	Sampling of: R1, R2 for each work task; EC for select work tasks	Sampling of: R1, R2, EC	—
2	Sampling of: R1, R2, EC	—	Sampling of: R1, R2, SP, NT	Sampling of: R1, R2 for each work task; EC for select work tasks

R1, respirable dust mass concentration by gravimetric analysis; R2, respirable CNT-containing particles by SEM analysis; SP, Sidepak (Photometer), assessment of respirable mass concentration; NT, Nanotracer, assessment of particle number concentration and mean size; EC, respirable elemental carbon by thermal–optical analysis; —, not measured.

Emission measurements of released MWCNTs at the specific work tasks previously described during production, purification, and functionalization work were conducted in the emission zone. The inlet of the sampling line of stainless steel was placed as close as possible to the expected emission source, typically at a few centimetre distance. The sampling line had a diameter of 6 mm and a total length of 1 m. The sampling line was split into three lines and these were connected to three filter cassettes for sampling of respirable dust, EC, and SEM, respectively. This we refer to as the emission station, which was moved for each work task.

Respirable dust samples

Personal samples and static emission samples of respirable dust were collected using cyclones (BGI4L, BGI Inc., Waltham, MA, USA) on 37-mm cellulose fibre filters with a pore size of 0.45 μm (SKC Inc., Eighty Four, PA, USA) mounted in plastic three-piece filter cassettes. An Escort ELF pump (MSA, Pittsburgh, PA, USA) set at 2.2 l min^{-1} provided sample flow. The air flow rate was before, during, and after the sampling regularly checked with a primary calibrator (TSI Model 4199, TSI Inc., Shoreview, MN, USA). The filters were preweighed and postweighed using an analytical balance (XP105 DeltaRange Excellence Plus, Mettler Toledo, Greifensee, Switzerland). The balance was located in a temperature- and humidity-controlled room. A 24-h equilibration period was applied before weighting. The limit of detection (LOD) of the gravimetric analysis was determined to 50 μg collected material per sample.

EC samples

Personal samples and static emission samples of respirable EC were collected according to the same procedure as described for respirable dust samples. However, preheated (at 800°C) 37-mm quartz filters (SKC Inc., Eighty Four, PA, USA) were used. Flow control and checks were carried out in the same way as described for respirable dust samples. Bulk samples of purified MWCNTs and the filters from the air sampling were analysed according to the NIOSH NMAM 5040 protocol with thermal–optical analysis (DRI Model 2001 OC/EC Carbon Analyzer from Atmoslytic Inc., Calabasas, CA, USA) (Birch and Cary, 1996). The

following temperature steps were used: 680°C (EC1), 750°C (EC2), and 900°C (EC3). However, the method was modified with a prolonged oxidation time, 150 s instead of 30 s, at the highest reached temperature, 900°C, to strive for complete oxidation of all carbonaceous compounds. The carbon mass detected in each temperature step was denoted EC1–EC3 as described above. Typical thermograms for the bulk material and a filter sample are shown in Supplementary Figure S1 (available at *Annals of Occupational Hygiene* online). Since the emitted MWCNTs mainly had diameters >20 nm and thereby could be expected to be mainly measured as EC3, we also chose to report the measured EC3 values (900°C). For the bulk samples, on average, 57% of the EC was measured as part of EC3. The LOD for EC was determined to be 0.06 μg C sample^{-1} (about 0.08 μg C m^{-3} for a 6-h sample)

Electron microscopy samples

Personal samples and static emission samples of respirable dust were collected on 37-mm non-fibrous polycarbonate membrane filters with a pore size of 0.4 μm (SKC Inc., Eighty Four, PA, USA) mounted in plastic three-piece filter cassettes. The same sampling procedure as described above was used. Analysis was performed with SEM (FEI Nova Nanolab 600, FEI Company, Hillsboro, OR, USA). With the used SEM method, a piece corresponding to approximately a quarter of the polycarbonate filter was mounted on a silicon wafer and coated with platinum. The visible LOD was >35 nm (1 pixel) but during the SEM analysis, it was possible to see particles with sizes >10 nm if a higher magnification was used, and this will be discussed further on. The SEM analysis was done at images with a standard resolution of 3584×3301 pixels. At least five but up to 29 areas per filter were randomly chosen for image acquisition. Each imaged area was 9050 μm^2. The standard deviation of the derived concentrations of CNT-containing particles varied between ±10 and ±50% for the reported samples. All CNT-containing particles imaged by the SEM were manually counted and defined as any particle with visible CNT content. In comparison with SEM analysis of asbestos according to the WHO method, we counted both fibres that fulfilled the asbestos counting criteria (length of >5 μm, width <3 μm, and length:width ratio >3:1) and those which did not

(WHO, 1997). If several fibres were attached to a particle, it was counted as one CNT-containing particle. This differs to how asbestos is counted; if the asbestos fibre is attached to a particle, it is then assessed as if the particle does not exist and is counted if the visible part of the fibre meet the above definition (OH Learning, 2010). Based on the sampled air volume, the number of CNT-containing particle cm^{-3} could be calculated. Analysis of blank filters as well as of field blanks showed that the used polycarbonate filters did not contribute with matrix particles/fibres. The calculation of the 95% confidence limits was based on ISO 10312 (1995). The elemental composition of the CNTs was analysed using an transmission electron microscopy with energy dispersive X-ray analyser (TEM/EDX; Jeol 3000F, Tokyo, Japan, and SDD XEDS, Oxford Instruments, Oxfordshire, UK).

Direct-reading instruments

Two direct-reading instruments commonly used in occupational hygiene were used for personal monitoring in the workers' breathing zone. A Nanotracer (Philips Aerasense, Eindhoven, The Netherlands) that was based on detection of electrical charges carried by particles, which have passed a unipolar corona charger in the device was used to monitor particle number concentrations. From this, the particle number concentration (10–300 nm) and mean particle (mobility) diameters were derived. The sampling flow rate was 0.24 l min^{-1}. A 0.51-m tubing was applied to be able to place the inlet of the Nanotracer in the breathing zone. Data were logged every 16 s. Additionally, a Photometer (model SidePak Model AM510, TSI Inc., Shoreview, MN, USA) equipped with a 0.91-m tubing connected to a 10-mm Dorr-Oliver cyclone (50% cut-off of 4 µm) was used to assess the respirable mass concentration by illuminating a particle containing space and detect the light scattered against the particles. The SidePak used in the study was calibrated by the manufacturer using the respirable size fraction of Arizona test dust. Thus, the mass concentrations from measurements of non-spherical particles with unknown refractory index should be considered as indicative only. The air flow rate was set to 1.7 l min^{-1} with a primary calibrator (Model 4199, TSI Inc., Shoreview, MN, USA) and the instrument was set to log data every 1 s. Moreover, a condensation particle counter (Model CPC 3022, TSI Inc., Shoreview, MN, USA)

also simultaneously monitored the particle number concentration in the size range 0.01 and >3 µm in the emission zone (<10 cm from the source).

Statistics

The correlation between the different exposure metrics was evaluated. The correlations were described with the Pearson correlation coefficient, r. Values below the LOD were given the value of half the LOD. The correlation between direct-reading instruments in the breathing zone (Nanotracer) and in the emission zone (CPC) was investigated. The sampling line residence time, which is not the same for the two instruments, was corrected for, and averages were calculated for the CPC data (data sampled every 1 s) to match the sampling time of the Nanotracer (every 16 s). Pearson correlation coefficients between the two data sets were calculated on log-transformed data as:

$$r = \frac{1}{n-1} \sum_{i=1}^{n} \left(\frac{X_i - \overline{X}}{s_X} \right) \left(\frac{Y_i - \overline{Y}}{s_Y} \right)$$

where X and Y are the data set from the Nanotracer and CPC, respectively, n is the number of data points in one set, $\overline{X}$ and $\overline{Y}$ are the sample means, and s_X and s_Y are the sample standard deviations.

RESULTS

Personal exposure measurements

Personal exposure measurements during production and laboratory work with MWCNTs were conducted, and the mean sampling time was 5.7 h (range 5.2–6.7 h). The measured concentrations of respirable dust, respirable EC, and number concentrations of CNT-containing particles (respirable fractions) are presented in Table 2. Arithmetic means of the respirable dust concentrations during the production of MWCNTs were 86 µg m^{-3} (range 93 and 79 µg m^{-3}) and <73 µg m^{-3} during purification and functionalization work, respectively. Respirable EC was measured during one of the two sampling days and EC was only quantified during work in the production and sieving laboratory (7.4 µg C m^{-3}).

The personal exposure measurements showed that both workers in the production laboratory and sieving laboratory as well as in the purification laboratory were

Table 2. Results from the personal sampling in the breathing zone of respirable dust, EC, and number concentration of CNT-containing particles. The sampled air volumes ranged between 680 and 890 l. EC is the actual concentration and EC3 is the amount found for the highest oxidation temperature step (900°C)

| Worker	Location	Sampling day	Sampling time (min)	Respirable dust concentration ($\mu g\,m^{-3}$)	Respirable EC concentration ($\mu g\,C\,m^{-3}$)		CNT-containing particles ($\#\,cm^{-3}$)
					EC	EC3	
A	Production laboratory and sieving laboratory	1	341	93	—	—	0.6
A	Production laboratory and sieving laboratory	2	405	79	7.4	6.3	2.0
B + C[a]	Purification laboratory	1	324	<71[b]	<0.08	<0.08	0.04
B + C	Purification laboratory	2	313	<73[b]	—	—	0.1

—, not sampled.

[a]The two workers in the purification laboratory worked there only partly during a shift. They did only occasionally work there at the same time. Therefore, one sampler was used and swapped between Workers B and C.

[b]LOD.

exposed to MWCNTs. The worker in production was exposed to the highest number concentration of CNT-containing particles, in mean $1.3\,cm^{-3}$ CNT-containing particles (range 0.6–2.0). The workers in the purification laboratory work had a mean exposure of $0.07\,cm^{-3}$ CNT-containing particles (range 0.04–0.1). Thus, the MWCNT exposure during production was about an order of magnitude higher in comparison with the laboratory work. In Fig. 2, two types of common airborne CNT-containing particles are shown.

The highest personal respirable dust concentration ($93\,\mu g\,m^{-3}$) was not measured during the same day as the highest number concentration of CNT-containing particles. Thus, emission sources releasing other types of particles than CNTs contribute with particle mass. SEM analysis of the polycarbonate filters showed that airborne particles other than CNT-containing ones dominated by number in the respirable size range. The sampled particles consisted of pure soot agglomerates, raw production materials (graphite), particles from the sieve (containing CNTs), and a large amount of small particles ($<0.3\,\mu m$) that may be partly infiltrated from ambient air. Unfortunately, no EC sample was collected parallel to this SEM sample. EDX analysis of the CNT material in this study showed that the material did not contained any transition metal catalysts.

A summary of the respirable mass concentrations, particle number concentration, and mean particle size obtained from the personal exposure measurements with the direct-reading instruments can be seen in Table 3. A time series from the measurement of assessed respirable mass concentration in the production laboratory is shown in Fig. 3. The direct-reading instrument (Sidepak) showed the highest peak exposure during the reactor clean out Part I. However, the filter-based SEM sample collected during this specific work task showed no presence of CNT-containing particles, indicating that the emitted particles from the clean out consisted of other carbonaceous particles, such as soot and graphite. The direct-reading instrument used for personal exposure measurements of particle number concentration (Nanotracer) measured the highest peak concentration during lathe machining of graphite rods, up to 34 000 particles cm^{-3} (Fig. 4a). The mean diameter of the particles released during lathe machining was small, ~30–40 nm. Sampling in the purification laboratory during Day 2 showed a much higher background concentration, on average 11 000 particles cm^{-3} a.m., compared with the average concentrations between 1800 and 2500 particles cm^{-3} in the production laboratory and sieving laboratory (Table 3). It is possible that thermal sources such as a furnace that was
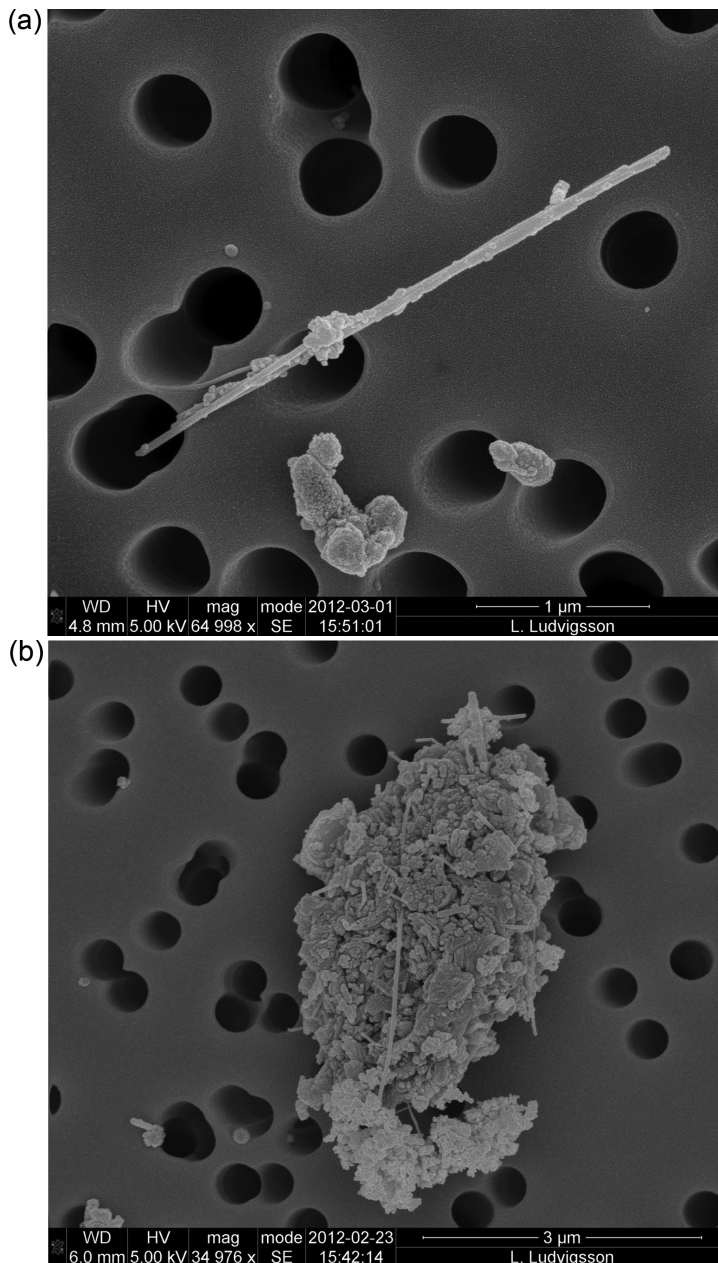
2 Two different types of airborne CNT-containing particles in the collected respirable dust fractions. (a) Individual CNTs were found in 21% of the counted particles. (b) The most frequent counted type of CNT-containing particles; large agglomerates (59%).

Table 3. Summary of the personal sampling with direct-reading instruments

Sampling day	Location	Respirable mass concentration[a] (arbitrary units)			Particle number concentration[b] (# cm^{-3})			Average particle size[b] (nm)		
		Arithmetic mean	Min	Max	Arithmetic mean	Min	Max	Arithmetic mean	Min	Max
1 (a.m.)	Production laboratory and sieving laboratory	0.04	ND	1.7	1800	500	12 000	59	40	86
1 (p.m.)	Production laboratory and sieving laboratory	0.23	ND	5.6	2500	500	34 000	65	32	92
2 (a.m.)	Purification laboratory	0.10	ND	3.2	11 000	2400	280 000	50	22	70
2 (p.m.)	Purification laboratory	0.06	ND	2.8	3800	1700	3800	64	42	86

ND, not detected.
[a]Sidepak (Photometer); the reported concentration is the respirable mass concentration assuming that the workplace aerosol has the same instrument response as the calibration aerosol (Arizona test dust).
[b]Nanotracer (based on unipolar electrical charging and size classification by electrical mobility, 10–300 nm).
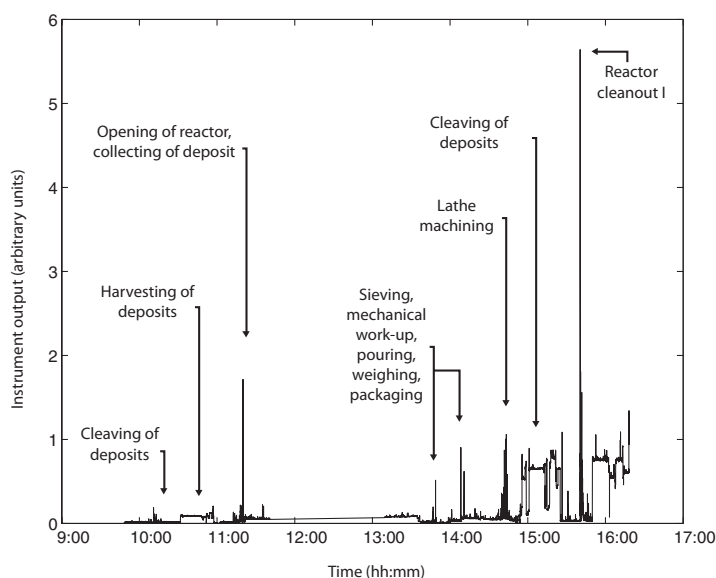
3 Personal sampling of respirable dust with direct-reading instrument (Sidepak) on Worker A during production of MWCNTs.

(a)

(b)
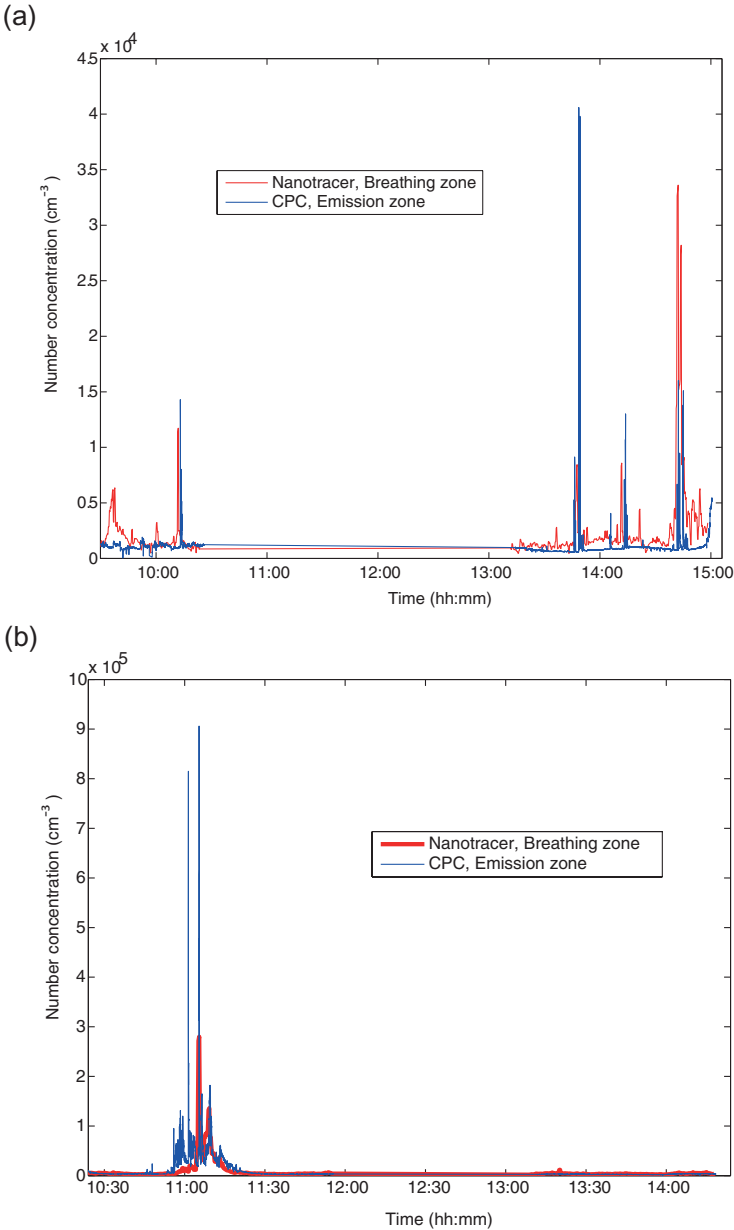
4 Personal sampling with direct-reading instrument (Nanotracer) and emission sampling with CPC during (a) production work and (b) purification and functionalization work of MWCNTs. (c) The distribution of the real-time data from the Nanotracer and CPC (reference instrument) shows that the correlation between the two instruments is higher for higher number concentrations. Nanotracer assesses the particle number concentration using a diffusion charging technique while the CPC allows a direct counting of individual particles (up to $10\,000\,\mathrm{cm}^{-3}$).

(c)
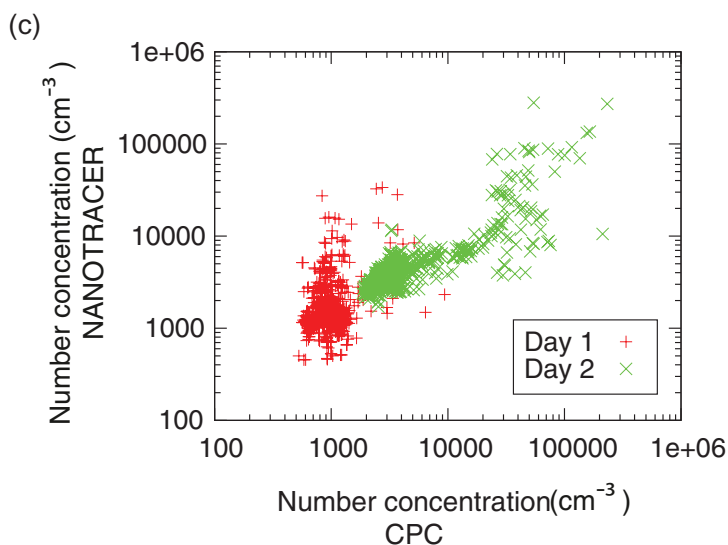
4 *Continued*

continuously forming non-CNT-containing particles from, for example heating of insulation etc. contributes to the high background in the purification laboratory. The highest release of nanometre-sized particles in the purification laboratory was measured during weighing of MWCNTs followed by opening of the furnace (Fig. 4b). The arithmetic mean diameter of these particles was ~20–30 nm. The measured particle number concentration from the personal exposure sampling (Nanotracer) was compared with emission data from a stationary CPC in the emission zone and the Pearson correlation coefficient was $r = 0.30$ for the measurements performed in the production laboratory and sieving laboratory (Fig. 4a). The corresponding value in the purification laboratory was 0.84 (Fig. 4b). The correlation of the real-time data from the Nanotracer (breathing zone) and CPC (emission zone) can be seen in Fig. 4c. With increased particle number concentrations, a stronger correlation between the instruments can be seen. A personal instrument (Nanotracer) could be used if the expected particle number concentrations in the work environment are not too low. But particle number concentrations measured by the CPC in the emission zone could also work as a proxy for the personal exposure.

Emission measurements

Emission measurements were performed at 12 different work tasks during production, purification, and functionalization work in the facility (Table 4). The sampling time ranged between 4 and 70 min. By sampling close to the emission source during different work tasks, important information of the emitted concentrations of each work task was obtained. In only one out of 12 emission samples from the emission zone could the respirable dust concentration be quantified above LOD. This was during a 4-min clean out of the arc discharge reactor with compressed air and vacuum cleaning (use of a vacuum cleaner equipped with HEPA filter) and a dust concentration of 6800 $\mu g\,m^{-3}$ was measured. Also, the highest concentration of EC was measured during the clean out of the reactor. However, the SEM analysis showed no emission of CNT-containing particles during this work task. Most likely, the emitted particles consisted of other carbonaceous materials such as soot and amorphous carbon. The EC concentration measured at different work tasks ranged between 0.05 and 550 $\mu g\,C\,m^{-3}$. The number concentration of CNT-containing particles released during production ranged between 0 and 11 CNT-containing particles cm^{-3}. The highest emission concentrations of CNT-containing

Table 4. Results from the emission measurements of respirable fractions of dust, EC, and number concentration of CNT-containing particles during different work tasks. EC is the total elemental carbon concentration and EC3 is the EC concentration found at the highest oxidation temperature step (900°C)

Work tasks	Location number in Fig. 1	Use of engineering controls/personal protective equipment	Respirable dust samples		Respirable EC samples			Microscopy samples		Calculated TWA (# cm⁻³)
			Air volume sampled[a] (l)	Mass concentration (µg m⁻³)	Air volume sampled[a] (l)	Mass concentration (µg C m⁻³) EC	EC3	Air volume sampled[a] (l)	CNT-containing particles[b] (# cm⁻³)	Calculated TWA (# cm⁻³)
Production laboratory and sieving laboratory										
Opening of reactor, collecting the deposits	3	Local exhaust/half-face respirator[c], nitrile gloves, protecting overall	24	<2100	18	140	91	18	ND (<1.0)	—
Cleaving of deposits	1	None/half-face respirator, nitrile gloves, protecting overall	26	<1900	20	470	460	24	1.6	—
Harvesting of MWCNTs from deposits	2	Local exhaust/half-face respirator, nitrile gloves, protecting overall	40	<1300	42	<1.4	<1.4	37	ND (<1.8)	—
Sieving, mechanical work-up, pouring, weighing, packaging	5	None/half-face respirator, nitrile gloves, protecting overall	117	<430	196[d]	250[d]	240[d]	117	11	8.2[d]

Table 4. *Continued*

Work tasks	Location number in Fig. 1	Use of engineering controls/personal protective equipment	Respirable dust samples		Respirable EC samples			Microscopy samples		
			Air volume sampled[a] (l)	Mass concentration (μg m⁻³)	Air volume sampled[a] (l)	Mass concentration (μg C m⁻³) EC	EC3	Air volume sampled[a] (l)	CNT-containing particles[b] (# cm⁻³)	Calculated TWA (# cm⁻³)
Lathe machining of graphite electrode	6	Local exhaust/half-face respirator, nitrile gloves, protecting overall	29	<1700				29	1.2	
Reactor clean out Part I	4	Local exhaust/half-face respirator, nitrile gloves, protecting overall	18	<2800				18	ND (<0.20)	
Reactor clean out Part II	4	Local exhaust/half-face respirator, nitrile gloves, protecting overall	9	6800	9	550	190	9	ND (<2.1)	—
Purification laboratory										
Purification Part I	7	Fume hood/nitrile gloves, protecting overall	139	<360	464[e]	0.05[e]	0.05[e]	139	ND (<0.28)	0.2[e]
Purification Part II	8	Fume hood/nitrile gloves, protecting overall	154	<320				154	0.46	

Table 4. *Continued*

Work tasks	Location number in Fig. 1	Use of engineering controls/ personal protective equipment	Respirable dust samples		Respirable EC samples			Microscopy samples		
			Air volume sampled[a] (l)	Mass concentration (µg m^{-3})	Air volume sampled[a] (l)	Mass concentration (µg C m^{-3}) EC	EC3	Air volume sampled[a] (l)	CNT-containing particles[b] (# cm^{-3})	Calculated TWA (# cm^{-3})
Functionalization Part I	9	Fume hood/ nitrile gloves, protecting overall	29	<1700				29	1.0	
Functionalization Part II	10	Fume hood/ nitrile gloves, protecting overall	55	<910				53	ND (<0.34)	
Grinding	11	Fume hood/ nitrile gloves, protecting overall	81	<620				77	ND (<0.23)	

ND, not detected; —, not calculated.
[a]The used airflow was 2.2 l min^{-1}.
[b]The upper 95% one-sided confidence limits (95% CLs) of the number concentrations of CNT clusters in the air were calculated by assuming that the number of CNT-containing particles on the filter could be described using the Poisson distribution. The CL where the observed CNT cluster count was zero could be considered to be the LOD. The method for calculating the 95% CL was based on ISO 10312 (1995).
[c]Equipped with filter Type P3.
[d]Include sieving, weighing, pouring, packaging, lathe machining, and reactor clean out Part I.
[e]Include all purification and functionalization parts and grinding.

particles occurred during sieving, mechanical work-up, weighing, pouring, and packaging. These were the work steps where MWCNT powder was openly handled. For example, MWCNT powder was poured from a container into the sieve or from a beaker into a small glass container with plastic lid. On the contrary only, a low concentration of EC and EC3 could be measured during the work tasks in the purification laboratory $(0.05 \, \mu g \, C \, m^{-3})$.

The correlation between respirable EC and number concentration of CNT-containing particles had a Pearson correlation coefficient of 0.088 (Fig. 5). The correlation between respirable EC3 and number concentration of CNT-containing particles had a Pearson correlation coefficient of 0.33 (Fig. 6).

DISCUSSION

This study investigated the feasibility and relative performance of three exposure metrics for exposure and emission to short CNTs (<5 μm) during arc discharge production, purification, and functionalization of MWCNTs. Parallel measurements of respirable dust,
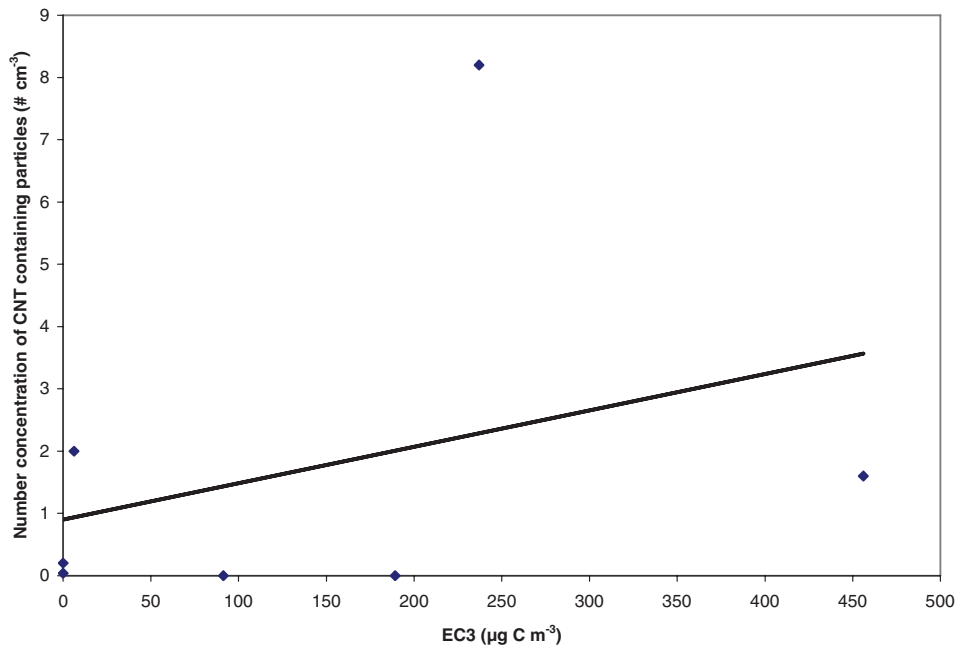
respirable EC, and number concentration of CNT-containing particles were performed during both personal exposure measurements and emission measurements for each work task. Thus, we have valuable exposure data and can thereby assess the occupational exposure as well as evaluate the used exposure metrics. Based on the exposure data in this study, we consider the exposure metric number concentration of CNT-containing particles to be the best marker for occupational exposure to CNTs since it was the only exposure metric that was selective and could specifically quantify the exposure to CNTs.

Analysis of CNT-containing particles with SEM

To date, there is no standardized method for sampling of airborne CNT-containing particles. In this study, we collected MWCNTs on polycarbonate membrane filters in combination with SEM analysis, and particles with a size >35 nm were visible and thus counted. Similar methods were utilized by Ogura *et al.* (2011) and Takaya *et al.* (2012). But other studies have instead used methods developed for asbestos for
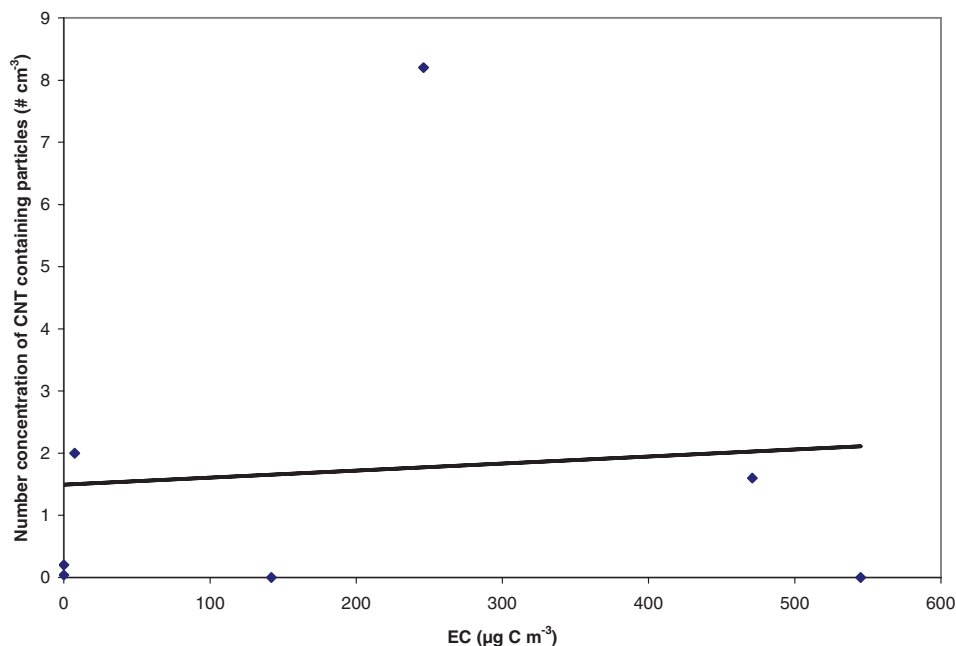
5 Correlation of number concentration of CNT-containing particles and EC (respirable fractions). The Pearson correlation coefficient was 0.088 with linear regression. Non-detect samples were given the value of half the LOD.

6 Correlation of number concentration of CNT-containing particles and EC3 (respirable fractions). The Pearson correlation coefficient was 0.33 with linear regression. Non-detect samples were given the value of half the LOD.

sampling of CNTs, where CNTs were collected on cellulose fibre filters in combination with TEM analysis (Bello *et al.*, 2008, 2009, 2010; Han *et al.*, 2008; Lee *et al.*, 2010; Dahm *et al.*, 2012). However, it is not only the sampling methods that contribute to difficulties to quantify CNT exposures, but it is also the absence of counting rules for CNTs at the electron microscopy analysis. So far, no standardized electron microscopy–based method for counting CNTs has been developed. Thus, to date, it is not clear how CNTs on filter samples should be counted (Brouwer *et al.*, 2012; Schulte *et al.*, 2012). A harmonization of the counting of CNTs in electron microscopy analysis will make it possible to compare exposure data for different workplace measurements.

According to the standard fibre counting criteria by the WHO (1986, 1997), a particle is defined as a fibre if it has a length of >5 μm, a width <3 μm, and >3:1 aspect ratio. These criteria are applied, for example in asbestos exposure quantification. Airborne CNTs appear to be heterogeneous in their shapes and structures as well as they more often are agglomerated

compared with asbestos. Since CNTs often not have the typical fibre dimensions, the standard fibre counting criteria cannot be applied (Schulte *et al.*, 2012). Our collected CNT-containing particles had often not the fibre dimensions and the length of the particles was commonly <5 μm. If we had followed the standard fibre counting criteria by WHO during the CNT counting, very few CNTs would then have been counted. Thus, the standard fibre counting criteria could not be followed, and instead, we chose to count every CNT-containing particle that was imaged with SEM. This is in accordance with how Dahm *et al.* (2012) counted CNTs who also found that their airborne CNT-containing particles were heterogeneous in their shapes and structures ranging from single CNTs to large agglomerates. Most of the counted CNT-containing particles in our study did not consist of individual tubes (79%). The CNTs were instead entangled or embedded in impurities and were thus larger in size compared with the individual tubes (Fig. 2b) but were nevertheless in the respirable size range. Thus, the detected airborne

CNT-containing particles could be classified into different particle types.

There is very limited knowledge of how the different types of CNT-containing particles will act after deposition in the lungs. For example, de-agglomeration of fibre bundles or fibres and carrier particles may take place (Wong *et al.*, 2009). Thus, we find it is important to report all detected airborne CNT-containing particles. With the SEM method, distinction was made between CNT structures and other types of particles, e.g. impurities and background particles. One limitation with SEM analysis is a potential high particle load on the filter if the exposure concentration is high when personal exposure measurements are conducted over extended time (for example full shift measurements). Overlap of deposited particles complicates the manual counting of CNT-containing particles with SEM. Furthermore, it was not straight forward to automatize the counting of particles with SEM due to interference of the pores in the membrane filters, and thereby the SEM analysis was time consuming and expensive. In one study, CNT clusters > ~3 and 0.3 µm were counted at the 1000 and 10 000 magnification, respectively (Ogura *et al.*, 2011). With our SEM method, we could identify and measure individual and small bundles of CNTs down to the nanometre size range (Fig. 2a,b). We also noted that particles with diameters <35 nm were present in our samples. During the SEM analysis, it was possible to use higher magnification and thus, smaller particles down to ~10 nm could be identified and it could be investigated if these particles contained CNTs or not. However, this was only performed on a small number of particles with diameters <35 nm.

Toxicological effects of CNTs have mainly been discussed for CNTs with a length 10–20 µm due to frustrated phagocytosis (Brown *et al.*, 2007; Donaldson *et al.*, 2010; Murphy *et al.*, 2012). However, CNTs with <5 µm have also shown to have effects *in vivo* (Pauluhn, 2010). It is not clarified how small bundles of CNTs or CNT-containing particles as shown in Fig. 2b will act when deposited in the surfactant lining fluid in the lungs. For example, the worst-case scenario for shorter CNTs (<5 µm) would be if the CNTs attached to particles dissolved and detached from the particles and became free individual CNTs inside cells in the respiratory tract. Shorter CNTs will not behave like longer CNTs (>14 µm) *in vivo* and cause frustrated phagocytosis. Shorter CNTs have in animal studies shown to cause adverse effects such as pulmonary inflammation and fibrosis (Mercer *et al.*, 2010, 2011; Pauluhn, 2010; Porter *et al.*, 2013). Based on the fact that longer CNTs could cause frustrated phagocytosis, the nanotechnology industry may design safer materials by using shorter CNTs to avoid critical human effects, and the production of CNTs might then change towards production of shorter CNTs. Thus, it is very important to know how to best measure occupational exposures and emissions of shorter CNTs.

Respirable dust

From the exposure data in Tables 2 and 4, it is obvious that respirable dust is not suitable as an exposure metric for CNT exposure. For the majority of the measurements of respirable dust, the mass concentrations were below the detection limit, while SEM analysis detected a significant number of airborne CNT-containing particles. Similar results have also been reported previously (Johnson *et al.*, 2010; Methner *et al.*, 2012). Also the opposite result was obtained when the respirable dust measurement indicated a high mass concentration during reactor clean out Part II, and the SEM analysis showed no exposure to airborne CNT-containing particles. Thus, the exposure metric respirable dust had low sensitivity and specificity to measure and quantify exposures to CNTs. With this method, no distinction could be made between CNT structures and other types of particles, e.g. impurities and background particles.

Elemental carbon

EC is a selective exposure metric for carbonaceous compounds including CNTs, amorphous carbon, graphite, and soot, but it does not specifically measure CNT exposure. NIOSH has recommended that occupational exposures to all types of CNTs should be monitored by a mass-based airborne concentration until additional data are available to determine if other exposure metrics or techniques would be more effective in protecting workers health (NIOSH, 2010). Furthermore, exposure measurements of CNT exposure should according to NIOSH include measurements of EC and a recommended exposure limit of 1 µg m^{-3} has been proposed (NIOSH, 2013). From the parallel measurements in this study, it was shown

that EC does not correlate with the number concentration of CNT-containing particles (Fig. 5). The correlation between EC3 and number concentration of CNT-containing particles was higher but still low. A correlation between EC and number concentration of CNT structures counted by TEM was shown by Dahm *et al.* (2012). The correlation coefficient was reported to be 0.44, which corresponds to a $R2$ of 0.19. This means that only 19% of the variability in the CNT exposure could be explained by the EC measurements. Also, some of the EC values in that study showed no or very low mass concentrations, while a significant number of CNT structures were counted by TEM analysis, thus indicating false negative values and that EC had low sensitivity for CNT exposures.

Furthermore, from the parallel personal exposure measurements of the workers in the purification laboratory, EC was not detected while a TWA of 0.04–0.1 CNT-containing particles cm^{-3} could be measured. Thus, it was clearly shown that also purification laboratory work with CNTs causes occupational exposure. We considered the exposure metric EC to be both too insensitive and unspecific to be used as a generic exposure metric for CNT exposures during arc discharge production. SEM analysis is time consuming, expensive, and not at all as commercially available as EC analysis, but it is very important that the analytical method used to quantify exposures to CNTs has high selectivity and sensitivity to CNTs.

In this study, the emission measurements were performed for work tasks handling carbonaceous material with different CNT content. If measurements were performed repeatedly for the same work task, it would probably give high correlation between CNT and EC given that the same type of CNT material was used. With material dependence, EC could be used as a proxy for CNTs for the specific work task if the correlation is known. However, the correlation between EC or EC3 and CNTs would differ significantly between different tasks due to variations in the CNT matrix composition. This assumption is based on a specific CNT material's ability to agglomerate as well as the purity of the material, and the correlation is expected to be better between the same manufacturer of MWCNT as opposed to a different manufacturer of MWCNT. Finally, it should be pointed out that manufacturing of CNTs with the arc discharge method may represent a worst case scenario as large amounts of non-CNT carbonaceous by-products

may be emitted, a substantial fraction of which is classified as EC with the thermal–optical method.

According to Ono-Ogasawara and Myojo (2013), EC3 (carbon mass oxidized at 920°C) could be a more selective exposure metric to CNT exposure than EC since the MWCNTs thereby could be separated from other carbonaceous substances with smaller geometrical dimensions that oxidize at lower temperatures in the EC method. From the parallel samples collected during reactor clean out Part II, no CNT structures were detected but the highest EC concentration was measured indicating release of other carbonaceous compounds than CNTs. EC analysis showed that the EC3 fraction of total EC was only 35% for this task, while it was up to 96% of total EC for work tasks where the emitted concentrations of CNTs were high. This indicates that oxidation of other carbonaceous compounds than CNTs preferentially occurs at lower temperatures. The correlation between EC3 and the number concentration of CNT-containing particles was low and only 6% of the variability in CNT exposure could be explained by the EC3 measure. Thus, our limited data do to some extent support the results presented by Ono-Ogasawara and Myojo (2013), but the explained part of the variability by the EC3 measurement is still very small.

The EC method does not distinguish between CNT structures and other types of carbonaceous particles, e.g. impurities and background particles. One limitation with the EC measurements was that we used 37-mm filters instead of 25-mm filters, which caused a slightly higher LOD. Another limitation in the EC sampling in our study was the lack of sampling outdoors to be able to assess the extent of anthropogenic sources of infiltrated EC contamination inside the facility. However, in the nearby rural background site 65 km to the east of the location of the company, the 1-week average concentration of EC was 0.32 ± 0.03 µg C m^{-3} at the time of the exposure measurements. Further, three out of the eight analysed EC samples were below the detection limit; this suggests that infiltrated EC from ambient air was only very weakly affecting our results.

Another more general problem with EC analysis is that there are several different EC protocols available (with large variations in oxidation temperatures used, oxidation time at each step, different strategies to correct for positive or negative artefacts from organic

carbon etc.). So, there is a need for a standardized and specific 'CNT protocol' for EC analysis of CNT material to be set up as soon as possible. A harmonization of the EC analysis of CNTs will make it possible to compare exposure data for different workplace measurements. Based on our data, it is clear that the CNT-specific protocol needs to include temperatures with prolonged oxidation time up to at least 900°C, as CNTs may require higher oxidation temperatures compared with most other carbonaceous materials.

Occupational exposure to CNTs

The personal exposure measurements were performed during both production and laboratory work. The highest exposure was measured during production work with sieving, mechanical work-up, pouring, weighing, and packaging of CNT powder in the sieving laboratory; unfortunately, we could not with the used sampling strategy estimate the different emissions for these different tasks because they were integrated with each other and the sampling time would otherwise have been too short. However, Worker A in the production laboratory and sieving laboratory used a negative-pressure half-face respirator with particulate filter of Class P3 at the different work tasks, but Worker A did not use the half-face respirator between the work tasks. For practical reasons, the personal exposure measurements were performed outside the half-face respirator. However, Workers B and C in the purification laboratory were also exposed to CNTs and they did not use any respiratory personal protective equipment (PPE). Their exposures were 6–50 times lower in comparison with the worker in production.

The proposed benchmark exposure limits for fibrous nanomaterials with high aspect ratios (>3:1 and length >5 µm) of 0.01 fibre cm^{-3} (BSI, 2007; IFA, 2009) cannot be used for CNT exposures as described here due to the heterogeneous structures of CNTs, their agglomeration and CNTs not having the typical fibre dimensions (aspect ratio). Thus, it is difficult to compare our number concentrations from the SEM analysis with other studies due to differences in how the CNTs were counted. For example, two previous studies followed the WHO counting criteria for asbestos in combination with analysis with phase contrast microscopy (NIOSH Method 7400, 1994) with a visible LOD >250 nm and reported no or few CNT fibres (Bello *et al.*, 2009; Lee *et al.*, 2010). In the study by

Dahm *et al.* (2012), a method for asbestos was used for quantification (NIOSH Method 7402) but the method was modified and the steps required for asbestos identification were eliminated. The personal exposure measurements ($N = 7$) in that study performed at different work tasks during CNT production and laboratory work, ranged from 0.003 to 0.4 CNT structures cm^{-3} and ND-1.6 CNT structures cm^{-3}, respectively (Dahm *et al.*, 2012). Furthermore, one of our two personal exposure measurements exceeded the proposed recommended exposure limit of EC (1 µg C m^{-3}). Dahm *et al.* (2012) also measured levels of EC (0.68–5.25 µg C m^{-3}) at different work tasks during CNT production exceeding the recommended exposure limit for EC. Thus, the measured number and EC concentrations in our study are in the same order as reported by Dahm *et al.* (2012). The exposure sources differ in the studies. We measured exposure to arc-discharge-produced MWCNTs while Dahm *et al.* (2012) measured exposure to both SWCNTs and MWCNTs mainly from the CVD method. Both types of production methods produce CNTs that can have a high content of carbonaceous impurities, 40–45% (Popov 2004; Köhler *et al.*, 2008). Thus, production of MWCNTs with arc discharge and CVD seems to cause occupational exposure within the same range, but of course, other parameters in the workplaces, e.g. protective measures also have influence on the exposure. During the arc discharge production in the studied facility, no metal catalysts were used. Thus, surrogates for CNT exposure based on metal content cannot be used in this case. Metal surrogates such as Fe and Ni have been reported for CNT production with CVD and laser ablation (Maynard *et al.*, 2004).

In this study, the measured personal respirable dust concentrations were up to almost 100 µg m^{-3}. Thus, it is in the same concentration range as reported by Ma-Hock *et al.* (2009) to cause mild granulomatous inflammation in the lung and in lung-associated lymph nodes in rats. It is therefore possible that unprotected work during production could cause similar adverse health effects to the worker. However, the properties of the CNT materials differ, for example in terms of tube length and purity, and as previously discussed, total dust is not at all a specific exposure metric for CNTs.

In the fields of occupational hygiene, direct-reading instruments to measure, e.g. mass concentration or particle number concentration are often used to

monitor exposure. This type of direct-reading instrument is often pre-calibrated against a specific type of particles by the manufacturer and thus, the measured concentrations should only be used as indicative. To the Nanotracer monitor, we applied 0.51-m tubing and the measured average particle sizes ranged between ~50 and 65 nm. We calculated the diffusion losses in the tubing with the used flow rate of 0.24 l min^{-1}, and for 50-nm-sized particles, 99.8% of the sampled particles reached the instrument and the corresponding value for 100-nm-sized particles was 99.9%. Thus, diffusion losses in the tubing during the samplings were very low. As long as the particles are not too small in size (e.g. <10 nm), the deposition in the tubing can be neglected in relation to the accuracy of the instrument (Asbach *et al.*, 2012). In this study, it was shown that the usefulness of the direct-reading instruments was limited because they were too unspecific to measure exposures to CNTs, which is in accordance with what Dahm *et al.* (2013) also reported. For CNT exposures, selective and sensitive methods must be used to quantify exposures. The results from more sophisticated stationary direct-reading instruments and the comparison of size distributions determined by these devices (for example an Aerodynamic Particle Sizer) and the size distribution of both CNT containing and 'total' concentration of particles detected by SEM will be presented elsewhere. A comparison between personal sampling (Nanotracer) and sampling in the emission zone (CPC) of particle number concentrations showed a correlation in the purification laboratory although that the measurement points had different distance to the emission source ($r = 0.84$). The particle number concentration data from the two direct-reading approaches in the production laboratory and sieving laboratory did not correlate that well, which might be due to that the worker was more mobile in his work than the workers in the purification laboratory ($r = 0.30$).

Clearly, a direct-reading instrument that shows a reasonable degree of specificity for CNTs would be highly desirable to use in the future, particularly in research-oriented emission studies of CNTs. This would complement the SEM analysis that is per default offline and has limited time resolution. Highly time-resolved instruments give strongly superior possibilities both to identify sources and effectively mitigate emissions.

Candidates to be investigated include filter-based direct-reading instruments such as Aethalometers or Particle Soot Absorption Photometers that measure black carbon based on the wavelength-dependent light-absorption properties and more sophisticated direct-reading aerosol mass spectrometers (Onasch *et al.*, 2012, Nilsson *et al.*, 2013)

It is noteworthy that some non-authority institutions have proposed mass-based occupational exposure limits for CNTs, for example NIOSH and Bayer, but up to now, no country has adopted occupational exposure limits for CNTs. This study gives support to the complexity authorities are facing when discussing occupational exposure limits for CNTs.

PPE and engineering controls

The used PPE and engineering controls in the facility can be seen in Table 4. The worker in the production laboratory and sieving laboratory used a half-face respirator with particulate filter of Grade P3 as PPE during the different work tasks. The workers in the purification laboratory did not use any respiratory protection at all. To protect the workers from dermal exposure to CNTs, protection gloves made of nitrile and laboratory coats were used. The handling of CNTs in the facility was open both during work in the production laboratory and sieving laboratory as well as in the purification laboratory. The open handling of CNT powder contributed to increased airborne exposure but also to dermal exposure due to surface contamination with dust on different surfaces in the workplace. For CNT exposures, the precautionary principle must be applied until the toxicological effects of CNT exposure have been evaluated. In practice, this means closed handling in combination with a high level of control measures and a high degree of use of PPE. Thus, the workers in the facility were assessed to have higher exposure than necessary due to lack in the PPE as well as in the engineering controls. Dry CNT powder should not be openly handled in the facility without any engineering controls, e.g. ventilated enclosures (Schulte *et al.*, 2012). During all open handling of CNTs in the facility, respiratory protection must be used. To protect the workers more efficiently, PPEs such as coveralls, hoods, and shoe protection were needed especially in the production laboratory to prevent dermal exposure and to inhibit the CNT dust to be spread in the workplace. Furthermore, the

used engineering controls were assessed to not be enough for controlling the CNT exposure. For example, the production laboratory was not located in a closed area since it was part of a larger room that was used for other purposes such as storing; see Fig. 1 for the layout of the facility. The production laboratory was connected via stairs to other rooms in the building without any airtight sluice. This means that airborne CNT-containing particles could be present in other rooms in the building and thereby cause exposure to other unprotected workers. Also, the office used by production workers was located next to the sieving laboratory, and since the same shoes were used in both the production laboratory and sieving laboratory as in the office, there might be a high risk that the floor in the office was contaminated with CNT dust.

CONCLUSIONS

The occupational exposures as well as the emissions during specific work tasks, performed in a small-scale factory producing MWCNTs by arc discharge, have been quantified. The highest exposure to CNTs occurred during work with producing CNTs. The highest measured concentration in the emission zone, 11 CNT-containing particles cm^{-3}, was measured at open handling of CNT powder during work tasks as sieving, mechanical work-up, pouring, weighing, and packaging. To be able to quantify exposures and emissions of shorter as well as longer CNTs, a selective and sensitive method is needed. To date, only filter-based methods in combination with SEM/TEM analysis can be selective and sensitive enough. Furthermore, a standardized protocol for counting criteria of CNTs must be set up as soon as possible. A harmonization of the electron microscopy analysis will make it possible to compare exposure data for different workplace measurements.

SUPPLEMENTARY DATA

Supplementary data can be found at http://annhyg.oxfordjournals.org/.

FUNDING

REFERENCES

Asbach C, Kaminski H, Von Barany D *et al.* (2012) Comparability of portable nanoparticle exposure monitors. Ann Occup Hyg; 56: 606–21.

Barkauskas J, Stankeviciene I, Selskis A. (2010) A novel purification method of carbon nanotubes by high-temperature treatment with tetrachloromethane. Separ Purif Technol; 71: 331–6.

Bello D, Hart AJ, Ahn K *et al.* (2008) Particle exposure levels during CVD growth and subsequent handling of vertically-aligned carbon nanotube films. Carbon; 46: 974–7.

Bello D, Wardle BL, Yamamoto N *et al.* (2009) Exposure to nanoscale particles and fibers during machining of hybrid advanced composites containing carbon nanotubes. J Nanopart Res; 11: 231–49.

Bello D, Wardle BL, Zhang J *et al.* (2010) Characterization of exposures to nanoscale particles and fibers during solid core drilling of hybrid carbon nanotube advanced composites. Int J Occup Environ Health; 16: 434–50.

Birch ME, Cary RA. (1996) Elemental carbon-based method for monitoring occupational exposures to particulate diesel exhaust. Aerosol Sci Technol; 25: 221–41.

Brouwer D, Berges M, Virji MA *et al.* (2012) Harmonization of measurement strategies for exposure to manufactured nano-objects; report of a workshop. Ann Occup Hyg; 56: 1–9.

Brown DM, Kinloch IA, Bangert U *et al.* (2007) An in vitro study of the potential of carbon nanotubes and nanofibres to induce inflammatory mediators and frustrated phagocytosis. Carbon; 45: 1743–56.

BSI. (2007) Nanotechnologies – part 2: guide to safe handling and disposal of manufactured nanomaterials, London: British Standards. PD 6699-2:2007.

Dahm MM, Evans DE, Schubauer-Berigan MK *et al.* (2012) Occupational exposure assessment in carbon nanotube and nanofiber primary and secondary manufacturers. Ann Occup Hyg; 56: 542–56.

Dahm MM, Evans DE, Schubauer-Berigan MK *et al.* (2013) Occupational exposure assessment in carbon nanotube and nanofiber primary and secondary manufacturers: mobile direct-reading sampling. Ann Occup Hyg; 57: 328–44.

Donaldson K, Murphy FA, Duffin R *et al.* (2010) Asbestos, carbon nanotubes and the pleural mesothelium: a review of the hypothesis regarding the role of long fibre retention in the parietal pleura, inflammation and mesothelioma. Part Fibre Toxicol; 7: 5.

Donaldson K, Murphy F, Schinwald A *et al.* (2011) Review: identifying the pulmonary hazard of high aspect ratio nanoparticles to enable their safety-by-design. Nanomedicine; 6: 143–56.

Donaldson K, Poland CA. (2009) Nanotoxicology: new insights into nanotubes. Nat Nanotechnol; 4: 708–10.

Gasser M, Wick P, Clift MJD *et al.* (2012) Pulmonary surfactant coating of multi-walled carbon nanotubes (MWCNTs) influences their oxidative and pro-inflammatory potential in vitro. Part Fibre Toxicol; 9: 17

Gustavsson P, Hedmer M, Rissler J. (2011) Carbon nanotubes – exposure, toxicology and protective measures in the work environment. Report 2011:1. Stockholm, Sweden: Swedish Work Environment Authority.

Han JH, Lee EJ, Lee JH *et al.* (2008) Monitoring multiwalled carbon nanotube exposure in carbon nanotube research facility. Inhal Toxicol; 20: 741–9.

Hedmer M, Kåredal M, Gustavsson P *et al.* (2013) The Nordic Expert Group for criteria documentation of health risks from chemicals. 148. Carbon nanotubes. Arbete och Hälsa; 47(5): 1-238. ISBN 978-91-85971-46-6, University of Gothenburg, Sweden. Available at: http://hdl.handle.net/2077/34499. Accessed 28 November 2013.

Hsieh SF, Bello D, Schmidt DF *et al.* (2012) Biological oxidative damage by carbon nanotubes: fingerprint or footprint? Nanotoxicology; 6: 61–76.

Hussain F, Hojjati M, Okamoto M *et al.* (2006) Polymer-matrix nanocomposites, processing, manufacturing, and application. J Compos Mater; 40: 1511–75.

IFA. Criteria for assessment of the effectiveness of protective measures. Available at: http://www.dguv.de/ifa/Fachinfos/Nanopartikel-am-Arbeitsplatz/Beurteilung-von-Schutzma%C3%9Fnahmen/index-2.jsp. Accessed 12 June 2013.

Iijima S. (1991) Helical microtubules of graphitic carbon. Nature; 354: 56–8.

ISO 10312. (1995) Ambient air—determination of asbestos fibres—direct transfer transmission electron microscopy method.

Johnson DR, Methner MM, Kennedy AJ *et al.* (2010) Potential for occupational exposure to engineered carbon-based nanomaterials in environmental laboratory studies. Environ Health Perspect; 118: 49–54.

Köhler AR, Som C, Helland A *et al.* (2008) Studying the potential release of carbon nanotubes throught the application life cycle. J Clean Prod; 16: 927–37.

Lee JH, Lee SB, Bae GN *et al.* (2010) Exposure assessment of carbon nanotube manufacturing workplaces. Inhal Toxicol; 22: 369–81.

Ma-Hock L, Treumann S, Strauss V *et al.* (2009) Inhalation toxicity of multiwall carbon nanotubes in rats exposed for 3 months. Toxicol Sci; 112: 468–81.

Maynard AD, Baron PA, Foley M *et al.* (2004) Exposure to carbon nanotube material: aerosol release during the handling of unrefined single walled carbon nanotube. J Toxicol Environ Health A; 67: 87–107.

McIntyre RA. (2012) Common nano-materials and their use in real world applications. Sci Prog; 95 (Pt. 1): 1–22.

Mercer RR, Hubbs AF, Scabilloni JF *et al.* (2010) Distribution and persistence of pleural penetrations by multi-walled carbon nanotubes. Part Fibre Toxicol; 7: 28.

Mercer RR, Hubbs AF, Scabilloni JF *et al.* (2011) Pulmonary fibrotic response to aspiration of multi-walled carbon nanotubes. Part Fibre Toxicol; 8: 21.

Methner M, Crawford C, Geraci C. (2012) Evaluation of the potential airborne release of carbon nanofibers during the preparation, grinding, and cutting of epoxy-based nanocomposite material. J Occup Environ Hyg; 9: 308–18.

Murphy FA, Schinwald A, Poland CA *et al.* (2012) The mechanism of pleural inflammation by long carbon nanotubes: interaction of long fibres with macrophages stimulates them to amplify pro-inflammatory responses in mesothelial cells. Part Fibre Toxicol; 9: 8.

Nagai H, Okazaki Y, Chew SH *et al.* (2011) Diameter and rigidity of multiwalled carbon nanotubes are critical factors in mesothelial injury and carcinogenesis. Proc Natl Acad Sci USA; 108: E1330–8.

Nakanishi J, editor. (2011) Risk assessment of manufactured nanomaterials: carbon nanotubes (CNT). NEDO project (P06041) Research and development of nanoparticle characterization methods. Final report issued on 17 August 2011.

Nilsson PT, Isaxon C, Eriksson AC *et al.* (2013) Manufactured nano objects emitted during maintenance of common particle generators. J Nanopart Res; 15: 2052.

NIOSH. (2010) Draft current intelligence bulletin occupational exposure to carbon nanotubes and nanofibers. Cincinnati, OH: US Department of Health and Human Services, Centers for Disease Control, National Institute for Occupational safety and Health. DHHS (NIOSH), NIOSH Docket Number: NIOSH 161-A. Available at http://www.cdc.gov/niosh/docket/review/docket161A/. Accessed 21 June 2011.

NIOSH. (2013) Occupational exposure to carbon nanotubes and nanofibers. Current intelligence bulletin 65, publication no. 2013-145. Available at http://www.cdc.gov/niosh/docs/2013–145/pdfs/2013-145.pdf. Accessed 24 May 2013.

Ogura I, Sakurai H, Mizuno K *et al.* (2011) Release potential of single-wall carbon nanotubes produced by super-growth method during manufacturing and handling. J Nanopart Res; 13: 1265–80.

OH Learning. (2010) W504 – fibre counting. Available at http://www.ohlearning.com/Files/Extracted_Files/38/W504coursematerial/JD33%20v1-0%2010Apr10%20W504%20Fibre%20counting.ppt#385,1,W504 – fibre counting. Accessed 15 October 2013.

Onasch TB, Trimborn A, Fortner EC *et al.* (2012) Soot particle aerosol mass spectrometer: development, validation, and initial application. Aerosol Sci Technol; 46: 804–17.

Ono-Ogasawara M, Myojo T. (2013) Characteristics of multi-walled carbon nanotubes and background aerosols by carbon analysis; particle size and oxidation temperature. Adv Powder Technol; 24: 263–9.

Palomäki J, Välimäki E, Sund J *et al.* (2011) Long, needle-like carbon nanotubes and asbestos activate the NLRP3 inflammasome through a similar mechanism. ACS Nano; 5: 6861–70.

Pauluhn J. (2010) Subchronic 13-week inhalation exposure of rats to multiwalled carbon nanotubes: toxic effects are determined by density of agglomerate structures, not fibrillar structures. Toxicol Sci; 113: 226–42.

Plata DL, Gschwend PM, Reddy CM. (2008) Industrially synthesized single-walled carbon nanotubes: compositional data for users, environmental risk assessments, and source apportionment. Nanotechnology; 19: 185706.

Poland CA, Duffin R, Kinloch I *et al.* (2008) Carbon nanotubes introduced into the abdominal cavity of mice show asbestos-like pathogenicity in a pilot study. Nature Nanotechnol; 3: 423–28.

Popov VN. (2004) Carbon nanotubes: properties and application. Materials Sci Eng Rep; 43: 61–102.

Porter, DW, Hubbs AF, Chen BT *et al.* (2013) Acute pulmonary dose-responses to inhaled multi-walled carbon nanotubes. Nanotoxicology; 7: 1179–94.

Ryman-Rasmussen JP, Tewksbury EW, Moss OR *et al.* (2009) Inhaled multiwalled carbon nanotubes potentiate airway fibrosis in murine allergic asthma. Am J Respir Cell Mol Biol; 40: 349–58.

Schinwald A, Chernova T, Donaldson K. (2012a) Use of silver nanowires to determine thresholds for fibre length-dependent pulmonary inflammation and inhibition of macrophage migration in vitro. Part Fibre Toxicol; 9: 47.

Schinwald A, Murphy FA, Prina-Mello A *et al.* (2012b) The threshold length for fiber-induced acute pleural inflammation: shedding light on the early events in asbestos-induced mesothelioma. Toxicol Sci; 128: 461–70.

Schneider T *et al.* (2007) Evaluation and control of occupational health risks from nanoparticles. TemaNord 2007:581. Copenhagen: Nordic Council of Ministers.

Schulte PA, Kuempel ED, Zumwalde RD *et al.* (2012) Focused actions to protect carbon nanotube workers. Am J Industr Med; 55: 395–411.

Takagi A, Hirose A, Nishimura T *et al.* (2008) Induction of mesothelioma in p53+/- mouse by intraperitoneal application of multi-wall carbon nanotube. J Toxicol Sci; 33: 105–16.

Takaya M, Ono-Ogasawara M, Shinohara Y *et al.* (2012) Evaluation of exposure risk in the weaving process of MWCNT-coated yarn with real-time particle concentration measurements and characterization of dust particles. Ind Health; 50: 147–55.

Tan CW, Tan KH, Ong YT *et al.* (2012) Carbon nanotubes applications: solar and fuel cells, hydrogen storage, lithium batteries, supercapacitors, nanocomposites, gas, pathogens, dyes, heavy metals and pesticides, Chaper 1. In Lichtfouse E, Schwarzbauer J, Robert D, editors. Environmental chemistry for a sustainable world: Volume 1: Nanotechnology and health risk. Netherlands: Springer. pp. 3–46.

Thomas T, Bahadori T, Savage N *et al.* (2009) Moving toward exposure and risk evaluation of nanomaterials: challenges and future directions. Wiley Interdiscip Rev Nanomed Nanotechnol; 1: 426–33.

WHO. (1986) Asbestos and other natural mineral fibres. Environmental health criteria, no. 53. Geneva: World Health Organization.

WHO. (1997) Determination of airborne fibre number concentrations: a recommended method, by phasecontrast optical microscopy (membrane filter method). Geneva: World Health Organization. ISBN 92 4 154496 1.

Wohlleben W, Brill S, Meier MW *et al.* (2011) On the lifecycle of nanocomposites: comparing released fragments and their in-vivo hazards from three release mechanisms and four nanocomposites. Small; 7: 2384–95.

Wong BA, Nash DG, Moss OR. (2009) Generation of nanoparticle agglomerates and their dispersion in lung serum simulant or water. J Phys Conf Ser; 151:012036. doi:10.1088/1742-6596/151/1/012036

Paper VII

BOHS
The Chartered Society for
Worker Health Protection

Detection of Multi-walled Carbon Nanotubes and Carbon Nanodiscs on Workplace Surfaces at a Small-Scale Producer

Maria Hedmer[1][*], Linus Ludvigsson[2], Christina Isaxon[3], Patrik T. Nilsson[3], Vidar Skaug[4], Mats Bohgard[3], Joakim H. Pagels[3], Maria E. Messing[2] and Håkan Tinnerberg[1]

1.Division of Occupational and Environmental Medicine, Institute of Laboratory Medicine, Lund University, PO Box 118, SE-22100, Lund, Sweden
2.Solid State Physics, Lund University, PO Box 118, SE-22100, Lund, Sweden
3.Ergonomics and Aerosol Technology, Lund University, PO Box 118, SE-22100 Lund, Sweden
4.National Institute of Occupational Health, PO Box 8149, Dep, N-0033 Oslo, Norway
*Author to whom correspondence should be addressed. Tel: +46-46173193; e-mail: maria.hedmer@med.lu.se
Submitted 22 May 2014; revised 21 March 2015; revised version accepted 23 March 2015.

ABSTRACT

Background: The industrial use of novel-manufactured nanomaterials such as carbon nanotubes and carbon nanodiscs is increasing globally. Occupational exposure can occur during production, downstream use, and disposal. The health effects of many nanomaterials are not yet fully characterized and to handle nano-objects, their aggregates and agglomerates >100 nm (NOAA), a high degree of control measures and personal protective equipment are required. The emission of airborne NOAA during production and handling can contaminate workplace surfaces with dust, which can be resuspended resulting in secondary inhalation exposures and dermal exposures. This study surveys the presence of carbon-based nanomaterials, such as multi-walled carbon nanotubes (MWCNTs) and carbon nanodiscs, as surface contamination at a small-scale producer using a novel tape sampling method.
Methods: Eighteen different surfaces at a small-scale producer were sampled with an adhesive tape sampling method. The surfaces selected were associated with the production and handling of MWCNT powder in the near-field zone. Surfaces in the far-field zone were also sampled. In addition, tape stripping of the skin was performed on one worker. The tape samples were analysed with scanning electron microscopy to detect the carbon-based NOAA. Air sampling with a personal impactor was also performed on a worker who was producing MWCNTs the same day as the tape samples were collected.
Results: MWCNTs were detected in 50% of the collected tape samples and carbon nanodiscs in 17%. MWCNTs and carbon nanodiscs were identified in all parts of the workplace, thus, increasing the risk for secondary inhalation and dermal exposure of the workers. Both airborne MWCNTs and carbon nanodiscs were detected in the personal impactor samples. The tape-strip samples from the worker showed no presence of carbon-containing nanoparticles.
Conclusions: Tape sampling is a functional method for detecting surface contamination of carbon-based NOAA and for exposure control during production at potentially any workplace that produces or handles such manufactured nanomaterials. With the tape method, it is possible to monitor if a potential

for secondary inhalation exposure or dermal exposure exists through resuspension of dust deposited on workplace surfaces. By means of air sampling, we could confirm that carbon nanodiscs were resuspended into the air at the workplace even though they were not handled during that particular work shift. MWCNTs were detected in the air samples, but can have been derived from either resuspension or from the work tasks with MWCNTs that were performed during the air sampling. Tape sampling is a complementary method to air sampling and together these two methods provide a better view of the hygienic situation in workplaces where NOAA can be emitted into work environments.

INTRODUCTION

Several different types of carbon-based nanomaterials such as carbon nanotubes (CNTs), carbon nanofibres, carbon black, graphene nanoplatelets, carbon nanodiscs, and carbon nanocones, are commercially manufactured. CNTs are mainly incorporated in composite materials for reinforcement (e.g. plastics, polymerics, ceramics, metallics, rubber, and concrete), and in fabrics, batteries, and paints (Lam *et al.*, 2006; Köhler *et al.*, 2008; Wohlleben *et al.*, 2011; Liu and Kumar, 2014). Carbon nanofibres are mainly used in composite materials. Carbon black has long been used in industrial applications as a colouring agent in ink, paints, resin and film, and as an electric conductive agent. Graphene nanoplatelets, carbon nanodiscs, and carbon nanocones are relatively new carbon-based nanomaterials attracting substantial scientific interest. Graphene nanoplatelets may have the potential to be used as a component in, e.g. composites, batteries, ultracapacitors, coatings, and adhesives (Pumera, 2009; Shen *et al.*, 2013; Kim *et al.*, 2013). Carbon nanodiscs and carbon nanocones have the potential to be used as additives for making plastics electrically or thermally conductive, possibly as substrates in sensor systems or as miniature electrodes (Garberg *et al.*, 2008).

Occupational exposure to nano-objects, and their aggregates and agglomerates >100 nm (NOAA) (Aggregates and agglomerates <100 nm are to be considered as nano-objects.) can occur at each stage of the life cycle (ISO/TS 12901-1, 2012), such as production, downstream use (e.g. formulation, industrial use), and disposal. It is the dustiness of powders that determines the emission potential, and dustiness testing of powdered nanomaterials provides information about the propensity of a material to aerosolize during its handling. To limit the unwanted occupational exposure to airborne NOAA, it is important to avoid free airborne nanoparticles. For most work processes and handling operations, the emission of NOAA into the air in general can be controlled through different types of conventional safety and protection devices such as equipment for encapsulation of emission sources, enclosures, fume hoods, draw benches, process ventilation, and local exhaust ventilation (Methner *et al.*, 2010). If the safety and protection devices are designed to fit gaseous substances, or are effective against respirable dust in general, they are also suitable and efficient enough to capture NOAA and thereby provide acceptable inhaled air quality (IFA, 2009; NIOSH, 2009). If the exposure to NOAA is not sufficiently controlled during work processes or handling operations, nanoparticles can be emitted into the workplace air and cause primary inhalation exposure to the workers. The emitted airborne NOAA can also be deposited on different surfaces in the workplace, outer clothing of the workers and on their skin contaminant layer, all of which constitute potential secondary sources of airborne NOAA (Schneider *et al.*, 2000; Schneider and Jensen, 2009). The mechanism for contaminating surfaces vary depending on gravitational settling and Brownian and turbulent diffusion if the NOAA are in the size range <100 nm or >1 µm (Schneider *et al.*, 2011). Surface deposition of NOAA can result in both near-field and far-field surface contamination.

Resuspension or reaerosolization of particles deposited on different workplace surfaces will usually result in particles with sizes >1 µm. Resuspension of NOAA from surfaces to the air can result in secondary emission sources. Resuspension to the workplace air can occur by human indoor work activities, such as walking and cleaning (Schneider *et al.*, 1999, Schneider *et al.* 2000). There are also strong suggestions that normal laboratory work can cause wind movement on

workplace surfaces which could resuspend nano-sized particles deposited there as dust, and thus cause secondary inhalation exposure (Schneider and Jensen, 2009; Tsai *et al.*, 2008). It was shown, e.g. that water-based cleaning of surfaces in a laboratory where manufactured nano-objects were handled greatly reduced the background concentrations of airborne particles in the size range 30–100 nm (Tsai *et al.*, 2008).

Many NOAA, such as the carbon-based ones, have low bulk densities, which results in considerable dusting during handling (Hedmer *et al.*, 2013). Dermal exposures from contaminated surfaces can also occur through transfer on contact.

According to Schneider and Jensen (2009), surface contamination by NOAA should be systematically studied for both production and user scenarios as it is a potential secondary source of airborne NOAA. However, to date, the documentation is still scarce of NOAA as surface contamination in workplaces and the potential for inhalation and dermal exposure. During manufacturing of CNTs, e.g. it has previously been shown that CNT-containing dust was emitted into the air during different work processes and handling operations (Han *et al.*, 2008; Lee *et al.*, 2010; Dahm *et al.*, 2012; Hedmer *et al.*, 2014). A previous study has shown the presence of CNT surface contamination by means of wipe sampling during weaving (Takaya *et al.*, 2012). Another study showed the potential for dermal exposure of single-walled CNTs during manufacturing and handling by using cotton gloves as a surrogate for the skin (Maynard *et al.*, 2004). Knowledge of the occupational dermal exposures to other types of manufactured carbon-based nanomaterial is in general limited.

Inhalation has been identified to be the exposure route of highest concern for carbon-based nanomaterials (Donaldson *et al.*, 2011; Schinwald *et al.*, 2012; Hedmer *et al.*, 2013; Ma-Hock *et al.*, 2013). Rodents repeatedly exposed to realistic concentrations of longer (>10 μm) or shorter (<4 μm) multi-walled CNTs (MWCNTs) have been shown to have pulmonary inflammatory effects and fibrosis (Ma-Hock *et al.*, 2009; Ryman-Rasmussen *et al.*, 2009; Pauluhn, 2010; Mercer *et al.*, 2011; Porter *et al.*, 2013). Recently, it was also shown that the inhalation exposure of animals to one type of MWCNT promotes lung cancer (Sargent *et al.*, 2014).

There are methods available to sample surface contamination originating from airborne dust, such as wipe sampling, micro-vacuuming, and adhesive tape sampling (Ness, 1994). Previously, adhesive tape sampling has been used for assessing surface contamination of fibrous dust such as asbestos (Ness, 1994) and manmade vitreous fibres (Salonen *et al.*, 2009). Wheeler and Stancliffe (1998) tested different surface contamination sampling methods based on removal and found that the adhesive tape method was the most effective for collecting settled dust in a reproducible manner. There is also a standard practice available for sampling a surface to determine the presence of particulate contamination by tape lift (ASTM E1216 - 11). No one has previously reported surface contamination of carbon-based NOAA using tape sampling. Based on these results, we decided that the adhesive tape method—an indirect method to estimate the potential for exposure—could be used to monitor deposited NOAA on different surfaces in a workplace where carbon-based nanomaterials are produced and handled. In addition, there are methods available for assessing the presence of particulate matter and fibres on human skin, such as tape stripping followed by scanning electron microscopy (SEM) analysis (van der Molen *et al.*, 1997; Hsieh *et al.*, 2001). Tape stripping was thus performed on one worker to assess the skin exposure to MWCNTs during production.

The objective of the study presented in this article was to survey the presence of MWCNTs, carbon nanodiscs, and nanocones as surface contamination at a small-scale producer of such carbon-based nanomaterials. Tape stripping was performed on a worker exposed to MWCNTs during their production. We wanted to assess the potential for secondary inhalation exposure and dermal exposure. Tape sampling on different surface locations in the workplace was performed to assess surface contamination of carbon-based NOAA. The collected tape samples were analysed with SEM to detect the occurrence of surface contamination of carbon-based NOAA in the workplace. Airborne particles were also collected with a personal impactor to study if resuspension of the nanoparticles to the air occurred at the workplace.

METHODS

Industrial setting

The tape samples were collected during the same sampling campaign where air sampling was being

conducted at a small-scale producer of MWCNTs, carbon nanodiscs, and carbon nanocones (Hedmer *et al.*, 2014). In the facility assessed, the tape samples were collected from surfaces related to the production and purification of MWCNTs that were in the near-field zone of the exposure source. To survey how widespread the surface contamination of NOAA in the facility was, we also sampled surfaces in the far-field zone of the exposure sources. This workplace has recently been described elsewhere (Hedmer *et al.*, 2014) but a short description will follow. In the company, there were three different laboratories, and Fig. 1 presents a schematic drawing of the layout of the facility. In the production laboratory, MWCNTs were synthesized with an enclosed arc discharge reactor. The reacted graphite deposit was collected and then dry cut with a band saw and manually harvested. In the sieving laboratory, the as-produced MWCNTs were mechanically worked-up to pulverize the powder, which was then sieved, weighed, and packaged in glass

containers. The as-produced MWCNTs consisted of 55 wt% MWCNTs and 45 wt% carbonaceous impurities. In the purification laboratory, the MWCNTs were purified to remove carbonaceous structures (e.g. graphite and soot) and functionalized. On average, the company produce ~75 g of as-produced MWCNTs per day. Three workers in the company were involved in the production, purification, and functionalization work of MWCNTs.

The company also produced and handled another carbon-based nanomaterial consisting of ~80% graphitic nanodiscs and ~20% graphitic nanocones. However, this nanomaterial had not been produced recently but was occasionally handled in the production laboratory, e.g. in the transfer of the powder from a big barrel to smaller bottles (packaging) before shipping to the customer.

The floors in the production and sieving laboratories were on average swabbed once a week and washed once a month. On the floor where the production and
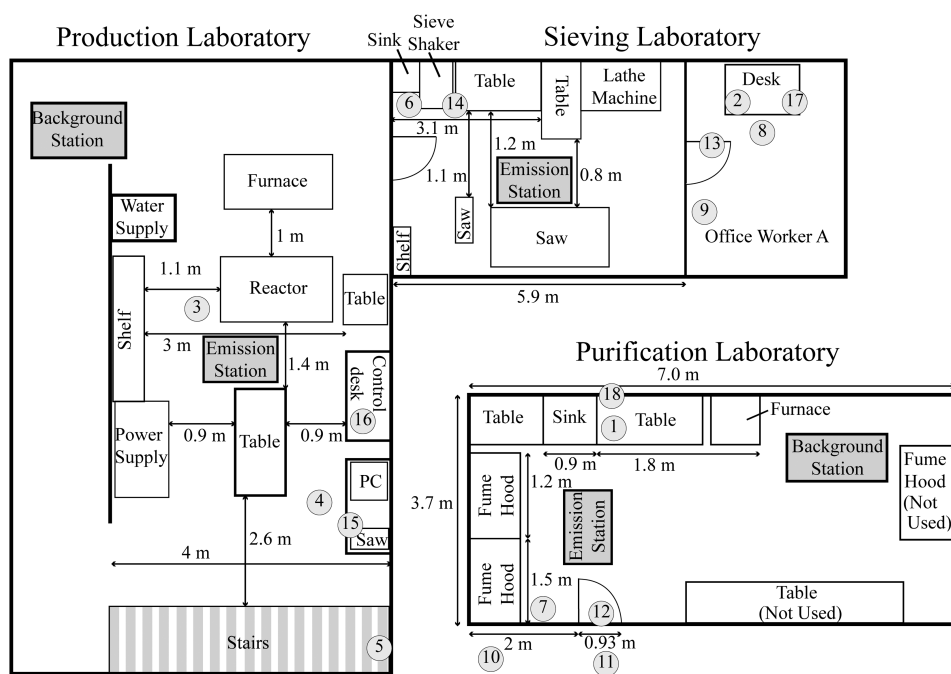

Figure 1   Schematic drawing of the small-scale production facility. The numbers in grey circles correspond to the 18 surface locations that were tape-sampled. The production and sieving laboratories were located on a different floor than the purification laboratory, and the distance between was ~25 m. There was also a closed door between the floors.

sieving laboratories were located, a sticky mat was placed at the base of the stairs to collect dust from the shoe soles so as not to spread it to other floors. The floor in the purification laboratory was swabbed every day. Disposable surface covers were used on most work areas in the company and the work areas were usually cleaned after the work activity. The work areas in the production laboratory and sieving laboratory were vacuum cleaned on a daily basis. The waste handling was open and waste contaminated with MWCNTs was not sealed before disposal. The waste bins were emptied on a daily basis. No other sources of carbon-based NOAA were identified in or near the factory.

Sampling strategy

Tape sampling is a useful method for assessing surface contamination of fibrous dust including asbestos (Ness, 1994). Thus, it has the potential to monitor the occurrence of carbon-based dust containing MWCNTs, nanodiscs, and nanocones as surface contamination. The tape sampling method used conformed to the standardized one (ASTM E1216 - 11). On the day when the tape samplings were performed, MWCNTs were produced and handled in the workplace. According to the company management, ~300 g of powder containing carbon nanodiscs and nanocones were handled in the production laboratory 10 days before the sampling campaign. Packaging of powder into smaller bottles was carried out under local exhaust ventilation in the production laboratory. At the time of the sampling campaign, according to the company, carbon-based nanodiscs and nanocones were also handled in the purification laboratory to functionalize them. All tape samples were collected at the company after work had ended for the day, and thus, there were no work activities in progress in the laboratories at the time of sampling.

To obtain information of what types of airborne carbon-containing nanoparticles were present in the workplace air, a Sioutas Personal Cascade Impactor was used to conduct sampling in the personal breathing zone of the worker in the production laboratory.

Sampling of surface contamination

In total, 18 tape samples and 2 field blanks were collected from surfaces at the workplace. The sampled surfaces were made of metal, plastic, concrete, laminate, and wood. The nature of the sampled surface locations are presented in Table 1 and where they are situated in the company are shown in Fig. 1. To collect a sample, ordinary transparent adhesive tape (Staples Europe B.V., Amsterdam, the Netherlands) was used with a width of 15 mm, length of ~15 cm, with ends folded. Single tape samples were collected from each surface location. The sticky surface of the tape was pressed against the workplace surface to be sampled, and rubbed lightly to assure adhesion to dust deposited on the surface. Then, the tape was pulled off with a fluent and decisive movement, and placed with the sticky side down on a new sheet of plastic film and labelled. The plastic film was placed in a new plastic cover for storage until SEM analysis. A new pair of nitrile gloves was used for each collected tape sample.

Tape stripping

With tape stripping, the cell layers of the stratum corneum from the human skin were removed by use of adhesive tape (van der Molen *et al.*, 1997). The worker in the production laboratory was assessed in advance to be the one with the highest risk of being dermally exposed to carbon-based nanomaterial in the company. The worker used a laboratory coat and protective nitrile gloves during the work activities, but no dermal protection was used in the facial region. The worker did however use a half-face respirator during the different work activities, but the respiratory protection was not used between the activities which meant that it was taken on and off frequently during the workday. This could have contributed to the blackening found on the worker's skin. Tape stripping was performed on this worker who had given informed consent to participate in the study. The tape strips were collected after a full-shift workday and were taken from the skin of his forefinger, cheek and forehead because visual traces of black dust were seen on these areas. The tape was applied to the skin, and the same procedure as described for the surfaces was followed. The tape stripping seemed to remove some of the blackening from the skin.

Sampling of airborne carbon-based NOAA

The personal size-resolved sampling was carried out with a Sioutas Personal Cascade Impactor (SKC, Eighty Four, PA, USA), with cut-off diameters of 2.5, 1.0, 0.50, and 0.25 μm. The impactor was equipped with four 25-mm polycarbonate membrane filters and

Table 1. An overview of the 18 tape-sampled surface locations and the presence of MWCNTs and carbon nanodiscs on different surfaces in the company producing and handling different carbon-based nanomaterials.

Sampling location		Unit	Description of the sampled surfaces/distance to the expected exposure source	Cleaning rate	Surface characteristics		No. of tape sampling location in Fig. 1	SEM analysis	
					Material	Approx. indication of surface roughness		Detection of carbonaceous nanomaterial (yes/no)	Type of carbon-based nanomaterial
Work areas	Table	Purification laboratory	Close to the balance where MWCNT powder was openly weighed/in the near-field zone	Regularly[a]	Laminate	Smooth	1	Yes	MWCNTs
	Desk	Office located next to the sieving laboratory	Belonging to the production worker/in the far-field zone	Seldom[b]	Coated wood	Smooth	2	No	—[c]
Floors	Next to the arc discharge reactor	Production laboratory	Close to the reactor/in the near-field zone	Regularly	Concrete	Rough	3	Yes	MWCNTs
	Between the band saw and the table	Production laboratory	Close to two MWCNT sources: dry cutting and manual harvesting/in the near-field zone	Regularly	Concrete	Rough	4	Yes	MWCNTs
	Top step on the stairs down to the production laboratory	Production laboratory	At almost the same floor as the purification laboratory/In the far-field zone	Regularly	Stone	Rough	5	No	—

Table 1. *Continued*

Sampling location	Unit	Description of the sampled surfaces/distance to the expected exposure source	Cleaning rate	Surface characteristics		No. of tape sampling location in Fig. 1	SEM analysis	
				Material	Approx. indication of surface roughness		Detection of carbonaceous nanomaterial (yes/no)	Type of carbon-based nanomaterial
Sieve shaker	Sieving laboratory	Sieving of as-produced MWCNT powder/in the near-field zone	Regularly	Concrete	Rough	6	Yes	MWCNTs
Next to the fume hood	Purification laboratory	Close to the fume hood where MWCNT powder was handled/in the near-field zone	Regularly	Plastic flooring	Rough	7	No	—
Next to the table	Office for the production worker	Located next to the sieving laboratory/in the far-field zone	Regularly	Concrete	Rough	8	Yes	MWCNTs
Next to the door	Office for the production worker	Located next to the sieving laboratory/in the far-field zone	Regularly	Concrete	Rough	9	No	—
Corridor	Located next to the production laboratory	—/in the far-field zone	Regularly	Plastic flooring	Rough	10	No	—

Table 1. *Continued*

Sampling location		Unit	Description of the sampled surfaces/distance to the expected exposure source	Cleaning rate	Surface characteristics		No. of tape sampling location in Fig 1	SEM analysis	
					Material	Approx. indication of surface roughness		Detection of carbonaceous nanomaterial (yes/no)	Type of carbon-based nanomaterial
Handles	Door handle 1	Door between purification laboratory and corridor	Corridor side/in the far-field zone	Seldom	Metal	Smooth	11	No	—
	Door handle 2	Door between purification laboratory and corridor	Purification laboratory side/in the far-field zone	Seldom	Metal	Smooth	12	No	—
	Door handle	Door between sieving laboratory and office for the production worker	Sieving laboratory side/in the far-field zone	Seldom	Metal	Smooth	13	No	—
Other surfaces	Sieve shaker	Sieving laboratory	On the sieve shaker/in the near-field zone	Regularly	Metal	Smooth	14	Yes	MWCNTs, nanodiscs
	Band saw	Production laboratory	On the band saw/in the near-field zone	Regularly	Metal	Smooth	15	Yes	MWCNTs, nanodiscs

Table 1. *Continued*

Sampling location	Unit	Description of the sampled surfaces/distance to the expected exposure source	Cleaning rate	Surface characteristics		No. of tape sampling location in Fig. 1	SEM analysis	
				Material	Approx. indication of surface roughness		Detection of carbonaceous nanomaterial (yes/no)	Type of carbon-based nanomaterial
Computer mouse next to the arc discharge reactor	Production laboratory	On the computer mouse/in the near-field zone	Seldom	Plastic	Almost smooth	16	Yes	MWCNTs
Computer mouse	Office for the production worker	On the computer mouse/in the far-field zone	Seldom	Plastic	Almost smooth	17	No	—
Cable channel	Purification laboratory	Close to the balance where MWCNT powder was openly weighed/in the near-field zone	Seldom	Metal	Smooth	18	Yes	MWCNTs, nanodiscs

[a]Regular cleaning (e.g. daily or weekly).
[b]No regular cleaning.
[c]No manufactured nanomaterial was detected.

one 37-mm PTFE after filter to capture particles with an aerodynamic diameter smaller than 0.25 um. To avoid bounce-off effects, the filters were sprayed with impactor grease (DS-515 Collection Substrate Spray, Dekati Ltd., Tampere, Finland). The impactor was connected to a Leland Legacy Sample Pump (SKC) that provided an air flow of 9 l min⁻¹, regularly checked before, during and after the sampling with the primary calibrator (TSI 4100 Series, USA). The same day as the tape samples were collected and the tape stripping was performed, the worker in the production laboratory carried the impactor for 403 min while working with activities such as the synthesizing of MWCNTs with the enclosed arc discharge reactor, opening of the reactor and collection of the reacted graphite deposit, dry cutting of the reacted graphite deposit with a band saw, manual harvesting of the MWCNTs produced, mechanically worked-up, sieving, weighing, pouring, and packaging, lathe machining of graphite rods for the reactor, and reactor clean out with compressed air and a vacuum cleaner with a high efficiency particulate absorption (HEPA) filter. The filters from one impactor sample were analysed with the SEM method described below.

SEM analysis of tape samples

The tape samples were prepared for SEM analysis by removing the plastic film and mounting a piece of the tape (~1 cm in size) on a silicon wafer. The nonconductive tape was then coated with a thin layer of platinum on the glue side to avoid charging artefacts in the electron microscope image. The tape samples were qualitatively analysed by SEM (FEI Nova Nanolab 600, FEI Company, USA) at a magnification of ×5000. Each sample was manually investigated for roughly 2 h giving a level of detection of 70 NOAA cm⁻². In all tape samples except one, we assessed the occurrence of NOAA to be low, in the order of 1 out of 100 totally collected particles.

If the SEM analysis showed—based on size, shape, and elemental composition—particle characteristics of an MWCNT (fibrous nature) or of a nanodisc, a closer investigation was performed at a higher magnification to verify the detection. No MWCNTs or nanodiscs or other surface contaminants were detected in the analysis of the field blank tape samples. A recent SEM analysis of bulk material of MWCNTs from the company showed that the MWCNTs on average

had a length of 1.7 μm (range 0.3–6.1 μm) (Hedmer *et al.*, 2014). The elemental composition of the carbon nanodiscs in the field samples was analysed using an energy dispersive X-ray analysis (EDX; SDDXEDS, Oxford Instruments, Oxfordshire, UK).

SEM analysis of the personal impactor samples

A piece corresponding to approximately a quarter of the filter from all the collected impactor samples was mounted on a silicon wafer and coated with platinum. The SEM analysis was performed according to a procedure recently described by Hedmer *et al.* (2014).

RESULTS

Surface contamination

The results from the SEM analysis of the tape samples are presented in Table 1. Carbon-based nanoparticles were detected in 9 of the 18 tape samples collected on different surface locations at the workplace. MWCNTs were detected in 50% of the tape samples ($N = 9$). MWCNT contamination was found on four of the five sampled surfaces in the production laboratory, on both sampled surfaces in the sieving laboratory, on two of the three sampled surfaces in the purification laboratory, and on one of the four sampled surfaces in the office of the production worker. The SEM analysis showed that the MWCNTs present on the workplace surfaces were larger heterogeneous agglomerates with an average length and width of 15–100 μm. The agglomerates were also built up of other carbonaceous compounds such as soot and graphite. Carbon nanodiscs were detected in 17% of the tape samples ($N = 3$) and were also found on surfaces in all three laboratories in the company. These three tape samples also contained MWCNTs and were all collected from surfaces assessed to be seldom cleaned in the 'other surfaces' sampling location. The detected nanodiscs had on average a diameter of 1.5 ± 0.5 μm and a thickness of 60 ± 14 nm. Elemental analysis showed that the nanodiscs in the field samples consisted of 95–98% carbon and a few percentage of oxygen. No carbon nanocones could be identified on the tape samples. Typical SEM images of the detected surface contamination of MWCNTs and carbon nanodiscs in the workplace can be seen in Fig. 2a–d. Soot aggregates present in the MWCNT powder as an impurity can also be seen in the SEM images. We assessed the
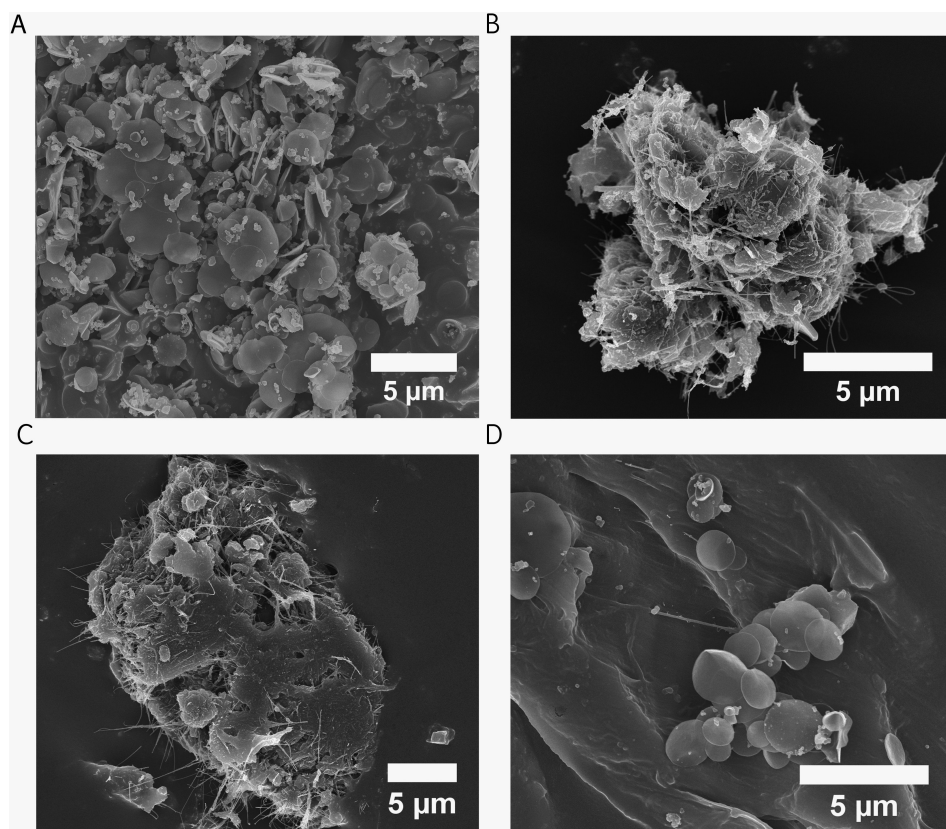
Figure 2   SEM images of surface contamination of carbon-based nanomaterials. (a) Carbon nanodiscs in a tape sample by the band saw in the production laboratory. (b) MWCNT agglomerates detected near the band saw in the production laboratory. (c) An agglomerated MWCNT particle detected on the sieve shaker in the sieving laboratory. (d) Carbon nanodiscs found on the sieve shaker.

occurrence of nanoparticles to be low in all tape samples except one: in sample no. 15 there were numerous carbon nanodiscs present (Fig. 2a), but in the same sample only a few MWCNTs were found (Fig. 2b).

Dermal contamination

The tape strips collected from the worker's skin showed no presence of MWCNTs, carbon nanodiscs, nanocones, other carbon dust, or any other non-carbon particles. The SEM analysis indicated that only skin cells appeared to be collected on the tape strips. Thus, the collected skin cell layer may have obscured the view of possible skin contaminants.

Airborne carbon-based NOAA

The analysis showed that both MWCNTs and carbon nanodiscs were present in the workplace air. Analysis of the different personal impactor stages showed that the airborne MWCNT-containing particles collected consisted most of heterogeneous agglomerates (Fig. 3a–e) but also of individual MWCNTs.

Airborne carbon nanodiscs were detected in the impactor sample: in stage A collecting particles >2.5 μm, in stage C collecting particles between 1.0 and 0.50 μm (Fig. 3c), in stage D collecting particles between 0.50 and 0.25 μm (Fig. 3d), and on the after filter, that is, the stage collecting particles < 0.25 μm
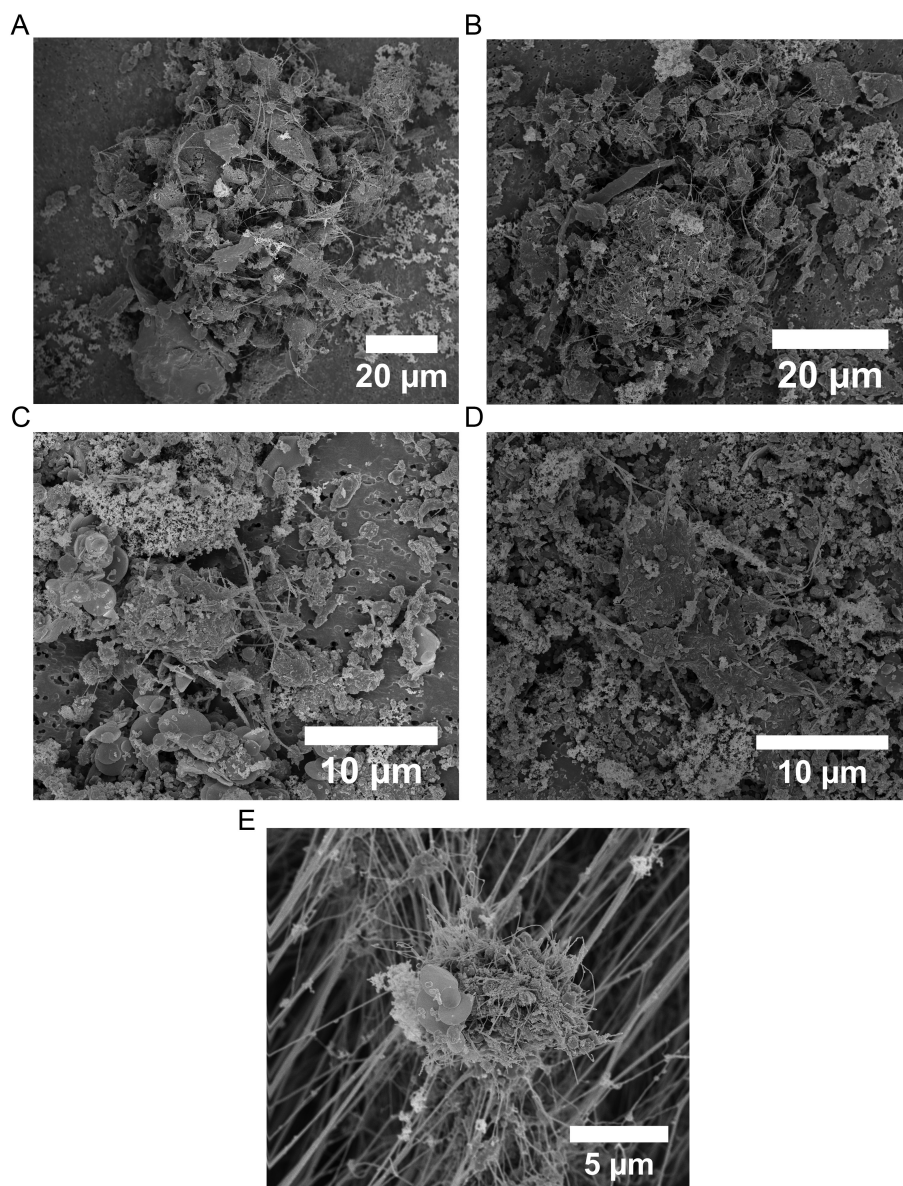
Figure 3   SEM images of airborne agglomerates of MWCNTs collected in the breathing zone of the worker in the production laboratory with a Siorutas Personal Cascade Impactor. Typical particles from the different stages are presented. Soot aggregates present in the MWCNT powder as an impurity can also be seen in the SEM images. (a) MWCNT-containing particles collected at the stage >2.5 μm. (b) MWCNT-containing particles collected at the stage 2.5–1.0 μm. (c) MWCNT-containing particles and carbon nanodiscs collected at the stage 1.0–0.50 μm. (d) MWCNT-containing particles and carbon nanodiscs collected at the stage 0.50–0.25 μm. (e) Carbon nanodiscs collected on the after filter (<0.25 μm) made of polytetrafluoroethylene (PTFE, Teflon). An airborne agglomerated MWCNT particle is also visible in the image.

(Fig. 3e). Numerous of carbon nanodiscs were collected in stage C.

DISCUSSION

To our knowledge, this is the first published study showing the occurrence of carbon-based nanomaterials as surface contamination in a workplace by means of adhesive tape sampling. With this method, it is possible to detect if carbon-based NOAA are present as surface contamination in work environments. MWCNTs were produced on the sampling occasion, and thus it was expected that only MWCNT contamination would be detected on the surfaces in the company. The tape samples, however, also showed the presence of carbon nanodiscs, a nanomaterial that the company occasionally handled. According to the company management, carbon nanodiscs were handled in the purification laboratory in the facility at the time of the tape sampling. Tape samples were collected from both frequently cleaned surfaces (e.g. work areas and floors) and seldom cleaned surfaces (e.g. band saw, cable channels, and computer mouse). The surface contamination of MWCNTs and carbon nanodiscs was widely spread and found in all parts of the facility: production laboratory, sieving laboratory, purification laboratory, and office. Surface contamination of MWCNTs was found on both frequently and seldom cleaned surfaces. However, carbon nanodiscs were only found on surfaces that were seldom cleaned. The tape sampling also showed that carbonaceous nanoparticle contamination was not widely spread to surfaces located outside the laboratories in the company (e.g. floor in corridor, stairs, handles, desks).

The handling of MWCNT materials in the company during the production, purification and functionalization was open, and air sampling performed during the different work tasks in the emission zone showed emission of MWCNTs into the air (Hedmer *et al.*, 2014). Since MWCNTs and carbon nanodiscs were detected on 50% of the sampled surfaces in the workplace, this indicates that the NOAA were not sufficiently controlled during the work processes and handling operations. Furthermore, it is of importance that workplace surfaces are cleaned at regular intervals to prevent them from becoming secondary sources of NOAA (Schneider and Jensen, 2009).

In the SEM analysis of the filters from the personal impactor sampling, both MWCNTs and carbon nanodiscs were detected. The airborne MWCNTs could have originated from either work-related emissions during the sampling or from resuspension of MWCNT-containing dust on surfaces. But the collected airborne carbon nanodiscs could only have originated from resuspension of the carbon nanodisc dust deposited on workplace surfaces, since this nanomaterial was not handled in the production and sieving laboratories during the sampling campaign. At the time of the sampling campaign, carbon nanodiscs were being handled in the purification laboratory, but we did not detect any airborne carbon nanodiscs in the personal and stationary air samples collected in this laboratory (Hedmer *et al.*, 2014).

Heterogeneous MWCNT-containing particles were, e.g. collected at all stages of the personal impactor. Larger agglomerated MWCNT-containing particles collected in the impactor in the stage >2.5 µm (Fig. 3a) were found to a much greater extent compared to the filter samples (respirable fractions). This is most likely due to aerodynamic equivalent particle diameters larger than 4 µm, which was the cut-off for the cyclones used (recently published by Hedmer *et al.*, 2014). Particles with aerodynamic diameters larger than 4 um have a low probability reach and deposit in the alveolar region of the lung.

Many MWCNT-containing particles collected in the impactor stages < 2.5 µm were in the size range of approximately tens of µm. One explanation is that these particles had aerodynamic diameters much smaller than their geometric size, which is expected for porous particles with complex shapes. Another possible explanation could be particle bounce, where particles bounce from one stage to the next. If larger agglomerated MWCNT-containing particles bounced-off and re-entered the airstream, although use of impactor grease, and were collected on later stages they potentially contaminated the analysis. Long sampling time combined with high air concentration of MWCNT might have contributed to the particle bounce. However, from the impactor sampling we received knowledge about MWCNT-containing particles also existed in other size ranges not included in the respirable fraction sampling.

The detected airborne carbon nanodiscs in the production and sieving laboratories could have originated from surfaces in both laboratories, since the door between these was normally open. Only

one worker was working in the production and sieving laboratories and he moved around in all parts of the two laboratories during a normal workday. The detected airborne carbon nanodiscs could have been emitted from the sampled surfaces where carbon nanodiscs were found as contaminants. However, the detected airborne carbon nanodiscs could also have originated from other contaminated surfaces in the production and sieving laboratories not included in the tape sampling survey. The purification laboratory was located on a different floor than the production and sieving laboratories and the distance between was >25 m including a closed door. Thus, it not realistic to believe that the inhalation exposure had drifted in from elsewhere in the facility.

Smaller particles (<1 μm) deposited on surfaces are held by strong forces. The forces responsible for the particles' adhesion to a surface are also the same forces responsible for the particles' adhesion to each other (Ziskind *et al.*, 1995; Ostiguy *et al.*, 2006). The smaller the particles, the more difficult it will be for them to detach from the surface and resuspend into the air. In general, resuspension seems only relevant for particle sizes >1 μm, and the resuspension rate increases for particles increasing in size from 1 to >10 μm (Qian and Ferro, 2008; Schneider and Jensen, 2009). The detected surface contamination of MWCNT agglomerates in sizes between 15 and 100 μm found on surface locations in this study can thus be considered to have the potential for resuspension. The carbon nanodiscs found on some surface locations also could be resuspended because their sizes were >1 μm.

The characteristics of the surface also play an important role. For example, surface roughness can greatly reduce the force of adhesion of a particle, which can contribute to increased resuspension (Ziskind *et al.*, 1995). From the results presented in Table 1 almost half of the samples surfaces, 44% (8 out of 18), were assessed to be rough. Carbon-based nanomaterial was detected on 50% of these types of surfaces (4/8). Based on the results, it is difficult to draw any conclusions. However, it is obvious that surfaces closer to the emission sources (near-field surfaces) were contaminated to a higher extent than surfaces at a farther distance (far-field surfaces). To avoid the risk for resuspension of NOAA, the removal of dust deposited on the floors and work surfaces must be performed regularly (e.g. cleaning) (Ostiguy *et al.*, 2006).

Thus, our findings in the study confirm that surface dust containing carbon-based nanoparticles can resuspend into the workplace air. Our findings can be explained by inadequate routines for cleaning in combination with a lack of adequate engineering controls of the airborne exposure to MWCNTs and carbon nanodiscs during the different work processes, or handling operations. This has recently been described elsewhere (Hedmer *et al.*, 2014).

Since dust containing both MWCNTs and carbon nanodiscs was present on surfaces in the workplace, there was a potential for the workers to be exposed to uncontrolled secondary inhalation of MWCNTs or carbon nanodiscs via resuspension. This exposure could occur anytime, not only during the work activities per se. A half-face respirator with particulate filter of grade P3 was used by the worker in the production and sieving laboratories during the different work tasks, but not between the work tasks. However, the two workers in the purification laboratory did not use any respiratory protection at all. There is reason for concern as toxicological studies have shown that inhalation of MWCNTs with lengths similar to those found on the tape samples (<4 μm) cause adverse effects, such as pulmonary inflammation and fibrosis in animal studies (Pauluhn, 2010; Mercer *et al.*, 2010, Mercer *et al.* 2011; Porter *et al.*, 2013).

The morphology of the detected carbon nanodiscs resembles that of graphene nanoplatelets, which in general have nanoscaled thickness (Donaldson *et al.*, 2013). It has recently been shown that nanoplatelets with a diameter <30 μm were respirable due to their aerodynamic properties, which allows them to deposit in the lower respiratory tract. We found carbon nanodiscs in almost all stages of the personal cascade impactor including the after filter; thus their aerodynamic equivalent diameter could be <0.25 um. This means that they have a very high probability to penetrate down into the alveolar region of the respiratory tract. Graphene nanoplatelets deposited in the pleura space can cause frustrated phagocytosis, inflammation, and have further adverse effects (Schinwald *et al.*, 2012; Donaldson *et al.*, 2013). With similar size and shape, there is potential for carbon nanodiscs with a diameter >4 μm to be respirable and affect the lungs. However, the nanodiscs in this study were very thin (thickness around ~60 nm) and had an average diameter of 1.5 μm, thus allowing for complete phagocytosis

by alveolar macrophages in the pulmonary alveoli. The risk for adverse health effects seems to be less if the nanodiscs are < 15 μm, similar to what Schinwald et al. (2012) suggested for nanoplatelets to minimize human adverse health effects.

MWCNT was found on one of the tape samples collected from the floor of the office next to the sieving laboratory. MWCNT was also detected on the floors in the sieving laboratory and production laboratory (Fig. 1). Since the laboratories in the company where carbon-based nanomaterials were produced and handled were not separated from the rest of the facility, and since no shoe protection was used in the workplace and the same shoes were used in the whole facility, we expected to find MWCNT dust on the floor in the office next to the sieving laboratory. Our air sampling showed that the work activities performed in the sieving laboratory emitted higher concentrations of MWCNTs to the air than any of the other work activities (Hedmer et al., 2014). Thus, the floor in the sieving laboratory may have been one of the most contaminated surfaces in the workplace.

MWCNT was also found on the computer mouse in the production laboratory, indicating the potential of dermal exposure in the workplace. However, protective gloves made of nitrile and laboratory coats were used to reduce dermal exposure. As there are no data on skin penetration and health effects following dermal deposition of MWCNTs, the precautionary principle must be applied and efficient skin protection is needed to prevent and minimize the dermal exposure to MWCNTs. Coveralls, hoods, and shoe protection must be used to more efficiently protect the workers in the company from dermal exposure to carbon-based nanomaterials.

An advantage with the adhesive tape sampling method is that it is inexpensive and easy to use and can be set up rapidly in the field. The collection of a representative number of tape samples in a workplace is rather quickly carried out. Another advantage is that the tape samples can be analysed by SEM without any complicated sample preparation. According to Holopainen et al. (2002), the tape method is useful in places where the dust lies loosely on the surface and where the amount of dust is fairly small. Disadvantages with this tape sampling method are that only qualitative data are obtained, and that the SEM analysis is expensive and time consuming.

The efficiency of any method for sampling dust particles is an important factor. The tape sampling method used in this study, however, has not been validated and as a result, we have no data about its removal efficiency on different types of surfaces. Tape sampling of very rough surfaces could result in false-negative values because the tape does not always adhere to NOAA deposited on such surfaces. In our sampling, though, carbon-based NOAA were detected on 50% of the surfaces assessed to be rough. This indicates that the surface sampling in this study seemed to work. Of course, one should in the first case choose to sample surfaces with a smooth finish to avoid problems with the removal efficiency. In addition, tape sampling has been used successfully for other types of particulate contamination (Salonen et al., 2009), and should also work for agglomerates and aggregates of nanoparticles with sizes >1 μm. Even though the method used was only indicative, it has still been very informative and useful. Further developments of this method should include validation as well as refinement and standardization for quantitative assessments.

Tape stripping is a technique that removes deposited particles and also some of the stratum corneum cells (Lundgren et al., 2006). However, the tape strips did not confirm the presence of carbon-based NOAA contamination on the skin of the worker. In other studies, the method used showed the presence of, e.g. singular glass fibres and particles of TiO_2 on human skin (van der Molen et al., 1997; Hsieh et al., 2001). A possible explanation why we were unable to image any carbon-based NOAA could be due to poor visibility among the many dermal cells that were involuntarily collected on the tape strips. We were only able to analyse the tape strips with the sticky side up because with the other side up, the electron beam could not penetrate the tape due to its thickness. Future developments should also address this issue.

CONCLUSIONS

This study has demonstrated that tape sampling is a useful method for the detection of surface contamination of carbon-based NOAA at workplaces and for assessing if the NOAA exposure at a workplace is sufficiently controlled. With the tape method, it is possible to monitor the potential for secondary inhalation and dermal exposures. Combined with the air sampling data, we could confirm that carbon-based

nanomaterial was resuspended into the air in the workplace, allowing for secondary inhalation exposure to the workers. Thus, this study showed that there was potential for both secondary inhalation exposure and dermal exposure due to the presence of MWCNTs and carbon nanodiscs on different surfaces throughout the workplace. We suggest tape sampling as a complementary method to air sampling. These two methods combined could, with advantage, provide a better overview of the hygienic situation in workplaces where carbon-based NOAA are emitted into work environments.

DISCLAIMER

The authors declare no conflict of interest. The study sponsors have only contributed financially, and have not participated in preparing the research material, writing, reviewing, or approving the submitted manuscript. The carbon-based nanomaterial producer, where the measurements were performed, have read and approved the final version of the manuscript without any corrections.

REFERENCES

ASTM E1216 - 11. Standard Practice for Sampling for Particulate Contamination by Tape Lift. Active Standard ASTM E1216 | Developed by Subcommittee: E21.05. Book of Standards Volume: 15.03. Published October 2011. doi: 10.1520/E1216-11.

Dahm MM, Evans DE, Schubauer-Berigan MK *et al.* (2012) Occupational exposure assessment in carbon nanotube and nanofiber primary and secondary manufacturers. *Ann Occup Hyg*; 56: 542–56.

Donaldson K, Murphy F, Schinwald A *et al.* (2011) Identifying the pulmonary hazard of high aspect ratio nanoparticles to enable their safety-by-design. *Nanomedicine (Lond)*; 6: 143–56.

Donaldson K, Schinwald A, Murphy F *et al.* (2013) The biologically effective dose in inhalation nanotoxicology. *Acc Chem Res*; 46: 723–32.

Garberg T, Naess SN, Helgesen G *et al.* (2008) A transmission electron microscope and electron diffraction study of carbon nanodisks. *Carbon*; 46: 1535–43.

Han JH, Lee EJ, Lee JH *et al.* (2008) Monitoring multiwalled carbon nanotube exposure in carbon nanotube research facility. *Inhal Toxicol*; 20: 741–9.

Hedmer M, Kåredal M, Gustavsson P *et al.* (2013) The Nordic Expert Group for criteria documentation of health risks from chemicals. 148. Carbon nanotubes. *Arbete och Hälsa*; 47: 1–238. http://hdl.handle.net/2077/34499.

Hedmer M, Isaxon C, Nilsson P *et al.* (2014) Exposure and emission measurements during production, purification and functionalization of arc-discharge produced multi-walled carbon nanotubes. *Ann Occup Hyg*; 58: 355–79.

Holopainen R, Asikainen V, Pasanen P *et al.* (2002) The field comparison of three measuring techniques for evaluation of the surface dust level in ventilation ducts. *Indoor Air*; 12: 47–54.

Hsieh MY, Guo YL, Shiao JS *et al.* (2001) Morphology of glass fibers in electronics workers with fiberglass dermatitis–a scanning electron microscopy study. *Int J Dermatol*; 40: 258–61.

IFA. (2009) Criteria for assessment of the effectiveness of protective measures. Available at http://www.dguv.de/ifa/en/fac/nanopartikel/beurteilungsmassstaebe/index.jsp. Accessed 3 September 2010.

ISO/TS 12901-1:2012. (2012) *Nanotechnologies – occupational risk management applied to engineered nanomaterials – part 1: Principles and approaches*. Geneva, Switzerland: International Organization for Standardization.

Kim H, Lim H-D, Kim S-W *et al.* (2013) Scalable functionalized graphene nano-platelets as tunable cathodes for high-performance lithium rechargeable batteries. www.nature.com/scientificreports 3: 1506. Accessed 16 December 2014.

Köhler AR, Som C, Helland A *et al.* (2008) Studying the potential release of carbon nanotubes through the application life cycle. *J Clean Prod*; 16: 927–37.

Lam CW, James JT, McCluskey R *et al.* (2006) A review of carbon nanotube toxicity and assessment of potential occupational and environmental health risks. *Crit Rev Toxicol*; 36: 189–217.

Lee JH, Lee SB, Bae GN *et al.* (2010) Exposure assessment of carbon nanotube manufacturing workplaces. *Inhal Toxicol*; 22: 369–81.

Liu Y, Kumar S. (2014) Polymer/carbon nanotube nano composite fibers–a review. *ACS Appl Mater Interfaces*; 6: 6069–87.

Lundgren L, Skare L, Lidén C. (2006) Measuring dust on skin with a small vacuuming sampler–a comparison with other sampling techniques. *Ann Occup Hyg*; 50: 95–103.

Ma-Hock L, Treumann S, Strauss V *et al*. (2009) Inhalation toxicity of multiwall carbon nanotubes in rats exposed for 3 months. *Toxicol Sci*; 112: 468–81.

Ma-Hock L, Strauss V, Treumann S *et al*. (2013) Comparative inhalation toxicity of multi-wall carbon nanotubes, graphene, graphite nanoplatelets and low surface carbon black. *Part Fibre Toxicol*; 10: 23.

Maynard AD, Baron PA, Foley M *et al*. (2004) Exposure to carbon nanotube material: aerosol release during the handling of unrefined single-walled carbon nanotube material. *J Toxicol Environ Health A*; 67: 87–107.

Mercer RR, Hubbs AF, Scabilloni JF *et al*. (2010) Distribution and persistence of pleural penetrations by multi-walled carbon nanotubes. *Part Fibre Toxicol*; 7: 28.

Mercer RR, Hubbs AF, Scabilloni JF *et al*. (2011) Pulmonary fibrotic response to aspiration of multi-walled carbon nanotubes. *Part Fibre Toxicol*; 8: 21.

Methner M, Hodson L, Dames A *et al*. (2010) Nanoparticle Emission Assessment Technique (NEAT) for the identification and measurement of potential inhalation exposure to engineered nanomaterials–Part B: Results from 12 field studies. *J Occup Environ Hyg*; 7: 163–76.

Ness SA. (1994) *Surface and dermal monitoring for toxic exposures*. New York: Van Nostrand Reinhold. ISBN 0-442-01465-1.

NIOSH. (2009) Approaches to safe nanotechnology. Managing the Health and Safety Concerns Associated with Engineered Nanomaterials. National Institute for Occupational Safety and Health. Available at www.cdc.gov/niosh.

Ostiguy C, Lapointe G, Ménard L *et al*. (2006), Nanoparticles: actual knowledge about occupational health and safety risks and prevention measures. Available at www.irsst.qc.ca/media/documents/PubIRSST/R-470.pdf. Accessed 29 August 2014.

Pauluhn J. (2010) Multi-walled carbon nanotubes (Baytubes): approach for derivation of occupational exposure limit. *Regul Toxicol Pharmacol*; 57: 78–89.

Porter DW, Hubbs AF, Chen BT *et al*. (2013) Acute pulmonary dose-responses to inhaled multi-walled carbon nanotubes. *Nanotoxicology*; 7: 1179–94.

Pumera M. (2009) Electrochemistry of graphene: new horizons for sensing and energy storage. *Chem Rec*; 9: 211–23.

Qian J, Ferro AR. (2008) Resuspension of dust particles in a chamber and associated environmental factors. *Aerosol Sci Technol*; 42: 566–78.

Ryman-Rasmussen JP, Tewksbury EW, Moss OR *et al*. (2009) Inhaled multiwalled carbon nanotubes potentiate airway fibrosis in murine allergic asthma. *Am J Respir Cell Mol Biol*; 40: 349–58.

Salonen HJ, Lappalainen SK, Riuttala HM *et al*. (2009) Man-made vitreous fibers in office buildings in the Helsinki area. *J Occup Environ Hyg*; 6: 624–31.

Sargent LM, Porter DW, Staska LM *et al*. (2014) Promotion of lung adenocarcinoma following inhalation exposure to multi-walled carbon nanotubes. *Part Fibre Toxicol*; 11: 3.

Schinwald A, Murphy FA, Jones A *et al*. (2012) Graphene-based nanoplatelets: a new risk to the respiratory system as a consequence of their unusual aerodynamic properties. *ACS Nano*; 6: 736–46.

Schneider T, Vermeulen R, Brouwer DH *et al*. (1999) Conceptual model for assessment of dermal exposure. *Occup Environ Med*; 56: 765–73.

Schneider T, Cherrie JW, Vermeulen R *et al*. (2000) Dermal exposure assessment. *Ann Occup Hyg*; 44: 493–9.

Schneider T, Jensen KA. (2009) Relevance of aerosoldynamics and dustiness for personal exposure to manufactured nanoparticles. *J Nanopart Res*; 11: 1637–50.

Schneider T, Brouwer DH, Koponen IK *et al*. (2011) Conceptual model for assessment of inhalation exposure to manufactured nanoparticles. *J Expo Sci Environ Epidemiol*; 21: 450–63.

Shen M-Y, Chang T-Y, Hsieh T-H *et al*. (2013) Mechanical properties and tensile fatigue of graphene nanoplatelets reinforced polymer nanocomposites. *J Nanomater*; 2013: 9.

Takaya M, Ono-Ogasawara M, Shinohara Y *et al*. (2012) Evaluation of exposure risk in the weaving process of MWCNT-coated yarn with real-time particle concentration measurements and characterization of dust particles. *Ind Health*; 50: 147–55.

Tsai S-J, Ashter A, Ada E, *et al*. (2008) Control of airborne nanoparticles release during compounding of polymer nanocomposites. *NANO* 3: 301–9.

van der Molen RG, Spies F, van 't Noordende JM *et al*. (1997) Tape stripping of human stratum corneum yields cell layers that originate from various depths because of furrows in the skin. *Arch Dermatol Res*; 289: 514–8.

Wheeler JP, Stancliffe JD. (1998) Comparison of methods for monitoring solid particulate surface contamination in the workplace. *Ann Occup Hyg*; 42: 477–88.

Wohlleben W, Brill S, Meier MW *et al*. (2011) On the lifecycle of nanocomposites: comparing released fragments and their in-vivo hazards from three release mechanisms and four nanocomposites. *Small*; 7: 2384–95.

Ziskind G, Fichman M, Gutfinger C. (1995) Resuspension of particulates from surfaces to turbulent flow – review and analysis. *J Aerosol Sci*; 26: 613–44.